DESIGN OF HEAT-RESISTANT STEELS FOR SMALL POWER PLANT

By
David Graham Cole

Darwin College, Cambridge

University of Cambridge
Department of Materials Science and Metallurgy
Pembroke Street, Cambridge, CB2 3QZ.

A dissertation submitted for the degree of Doctor of Philosophy at the University of Cambridge

September 2000

PREFACE

This dissertation is submitted for the degree of Doctor of Philosophy at the University of Cambridge. The research described herein was conducted under the supervision of Professor H. K. D. H. Bhadeshia in the Department of Materials Science and Metallurgy, University of Cambridge, between October 1997 and September 2000.

This work is, to the best of my knowledge, original, except where acknowledgements and references are made to previous work. Neither this, nor any substantially similar dissertation has been or is being submitted for any degree, diploma or other qualification at any other university. The work has been presented in the following publications so far:

Cole, D., Martin-Moran, C., Sheard, A. G., Bhadeshia, H. K. D. H. and MacKay, D. J. C., Modelling creep rupture strength of ferritic steel welds, Science and Technology of Welding and Joining, Vol. 15, No. 2 (2000) 81–89

Cole, D., Bhadeshia, H. K. D. H. and MacKay, D. J. C., Calculation of creep rupture stress of ferritic power plant steels as a function of chemical composition, heat treatment, temperature and time, Materials Algorithms Project: http://www.msm.cam.ac.uk/map

Cole, D. and Bhadeshia, H. K. D. H., Optimisation of creep and oxidation resistance of ferritic steels, The 10th Iketani Conf. on Materials research towards the 21st century, Symposium on Iron and Steel, Karuizawa, Japan (2000) 43–44

David Cole
September 2000

ACKNOWLEDGEMENTS

I would like to thank Professor A. H. Windle for the provision of laboratory facilities in the Department of Materials Science and Metallurgy at the University of Cambridge.

I am indebted to my supervisor Professor Harry Bhadeshia who has provided unparalleled support, encouragement and inspiration throughout the course of this work.

Many thanks are due to the members of the Phase Transformations and Complex Properties Group, past and present. In particular I would like to mention Joe Robson, Mike Lord, Steve Cardie, Catherine Pitt, Gareth Hopkin, Chris and Dot Downs, Philippe Opdenacker, Carlos and Francisca Capdevila Montes, Franck Tancret, Thomas Sourmail, Sree Harsha Lalam, John Street and others too numerous to mention.

I would also like to thank the members of Industry and Academia world-wide who have taken interest in and aided this work. This includes the members of the Foresight Challenge Project, in particular Rod Vanstone and Phil Clarke. I must also thank Fujio Abe for his advice and enthusiasm regarding this research and great thanks must go to my sponsors, Allen Power Engineering and Rolls-Royce, especially to Geoff Sheard, Charles Martin-Moran and Steve Humphries.

Many thanks must also go to Mr John Harris and The Worshipful Company of Ironmongers for their interest and generous scholarship.

Great acknowledgements must be paid to the friends who have supported me and sometimes even listened to me talk about my work. This includes, of course, the greatest inhabitants of Romsey Town; Will, Nick, Rob, Rich and Fred, let us never forget The Jubilee. It gives me great pleasure to also thank many friends in London, north, south and sometimes both. There are others scattered throughout the world whom I would also like to thank; Tom Needham, Ian Mosburger Martin, Conor Farrell and Eric are amongst them.

Finally I would like to thank my family; my parents Graham and Barbara, my brother Tim and his wife Gilly, my sister Sarah and her husband Roger. Greatest thanks must go to Sally for her patience and support in times of strife. This thesis is dedicated to these people, without whom there would be no thesis.

ABSTRACT

Creep resistant steels must be reliable over long periods of time in severe environments. Their microstructures have to be stable, both in the wrought and in the welded states. This thesis deals with the use and development of quantitative methods for the design of steels for elevated temperature applications. The methods include phase stability calculations, the estimation of complex precipitation reactions occurring over periods extending many tens of years, and a non–linear analysis of the creep rupture life of ferritic steels as a function of a large number of variables. A considerable effort has also been expended in the validation of the theoretical work.

A key technological goal of the work was to propose by calculation, a novel ferritic stainless steel capable of long term service (100 000 h) at 650 °C and under a continuous stress of 100 MPa. The thesis therefore begins with a review of the physical metallurgy and the mechanisms of creep deformation in ferritic power–plant steels. The immense knowledge that exists in the published literature revealed trends, for example, the effects of nickel and silicon, which have been exploited later in the thesis. The exercise also served to collate experimental data which were either used to validate models or to boost experimental databases used in the creation of models.

There are no obvious physical models capable of estimating anything but the simplest of mechanical properties, certainly nothing as far as the creep rupture stress is concerned. Linear regression is too limited in its form. A neural network is capable of realising a greater variety of nonlinear relationships of considerable complexity. The essence of the method is reviewed in Chapter 3 which includes particularly the theory developed by MacKay which properly allows for uncertainties that depend on the position in the input space.

The development and testing of a comprehensive neural network model for the creep rupture strength as a function of the detailed chemical composition and heat treatments forms the basis of Chapters 4 and 5. It is demonstrated first that an earlier model (Brun and co–workers) does not make adequate predictions, by comparing new experimental data against their theoretical work. A new model based on more comprehensive data is then demonstrated to perform with greater precision. This model for steel plates was also adapted to welding alloys and was successful in predicting new data to 40 000 h without doing any experiments.

Bearing in mind the need to design an alloy for service at 650 °C, a literature review on the

oxidation of ferritic steels is presented in Chapter 6. Although knowledge about oxidation resistance is largely qualitative, it proved possible to extract sufficient detail to introduce oxidation resistance in the alloy design procedures.

The range of optimised models and qualitative knowledge were all used to propose a new alloy which should have the required properties, ought to be easy to manufacture and process and which is not particularly expensive in its use of alloying elements. The material has now been manufactured and is undergoing tests which will take some years to complete. There is nevertheless considerable confidence in the alloy given the extensive validation of the models against data in the open literature.

Chapter 8 deals with microstructural studies related to the stability; the work confirms trends reported in the literature review, but in particular highlights the role of nickel in accelerating the coarsening of the microstructure.

The thesis finishes with conclusions, suggestions for future work, a list of references and appendices dealing with the sources of data and with an analysis of a specific commercial alloy using the models created in this work. Most of these models are available freely over the world wide web.

CHAPTER 1

CHAPTER 2

CHAPTER 3

CHAPTER 4

CHAPTER 9

CHAPTER 1

Introduction to Ferritic Power Plant Steels

1.1 Technology Overview

There are strong economic and environmental reasons for improving the efficiency of steam power plant. There has been a continuous increase in the performance of such plant so that in 1990, the mean fuel mass required to generate one kilowatt-hour of electricity was approximately half that required in 1950 (Wachter and Ennis, 1995). Increased concern over rising fuel costs and availability, coupled with a drive to reduce emissions of gases such as CO_2 and SO_2 has further emphasised the importance of increasing plant efficiency. U.S.A. greenhouse gas emissions totalled 1.27 billion tonnes of carbon in 1994 and are rising at a rate of 1% per annum. The world-wide annual carbon emissions from fossil fuel combustion total over 5.4 billion tonnes (Armor, 1998).

The most significant increases in steam turbine efficiency may be obtained by raising the steam temperature. An increase in steam conditions from 538 °C at a pressure of 30 MPa to 650 °C at 40 MPa is expected to raise turbine efficiency by 8% (Takeda and Masuyama, 1991). Details of the service conditions required of steels for steam power plant are shown in Table 1.1. They are compared with the requirements demanded of nickel-based alloys used in aeroengines. In both cases the service conditions are severe, but this is especially so for steels where the service life can be many decades.

Property	Aeroengine	Power Plant
Temperature	>1000 °C	540-570 °C
Pressure	≈ 3 bar	160-370 bar
Design life	10^4 h	2.5×10^5 h
$\sigma_{100000h}$	10 MPa	100 MPa
Coating	Yes	No
Forced Cooling	Yes	No
Single Crystal	Yes	No

Table 1.1: Comparison of service conditions for a component in the hottest part of a power plant and the hot part of an aeroengine. Lower bound conditions for power plant are representative of current technology. The stress is a 100 000 hour creep rupture strength (Bhadeshia, 1999a).

Other factors need to be taken into account when designing and manufacturing steam power plant, especially the requirement for a reliable service life, which may be in excess of thirty years for steam turbines (Berger *et al.*, 1993; Viswanathan, 1989). Many critical components in power plant are made of steels developed to resist deformation in the range 450-600 °C and 15-100 MPa for the entire service life (Evans and Wilshire, 1985; Pickering, 1997). With such a long service life required, the typical tolerable creep strain rate may be about $3\times10^{-11}\mathrm{s}^{-1}$, approximately 2% elongation over thirty years (Bhadeshia *et al.*, 1998). The creep rupture strength of the components must therefore be high enough to prevent failure during the service life.

These steels are able to survive such a long service life because the operating temperature is only about half the absolute melting temperature, thus making the migration of atoms very slow. However, significant changes do occur over the service life, albeit at a very slow rate. This is in spite of the fact that they have a very stable microstructure due to the severe tempering heat treatment that they are generally given before entering service.

These factors, along with other important degradation mechanisms such as oxidation and thermal fatigue, must be considered if the efficiency of the steam turbine is to be increased.

1.2 Power Plant Operation

A steam power plant converts heat energy from the combustion of a fuel into mechanical work energy of shaft rotation which is converted to electrical energy by a generator. Such a plant operates on a thermodynamic cycle which is a closed loop of processes. It is then possible to determine a thermal efficiency for such a cycle using the first and second laws of thermodynamics, defining how well a cycle converts heat into work. The *Carnot efficiency* is based on an ideal cycle and is given by

$$\eta_C = \frac{T_1 - T_2}{T_1}\times100\% \tag{1.1}$$

where T_1 is the absolute temperature at the engine inlet and T_2 is the absolute temperature at the exhaust. This equation shows that the wider the gap between inlet and outlet temperature, the more efficient is the cycle. In practice T_2 is not below 300 K and the maximum temperature T_1 is also limited by the materials available for the highly stressed parts of the plant, such as the boiler tubes and turbine blades. No engine using fluid at T_1 and exhausting at T_2 can have a higher efficiency than this and in practice they all have much lower ones. The temperature T_1 is sometimes referred to as the *metallurgical limit.* To maximise efficiency the steam turbine has to be operated near this limit, usually achieved by superheating the steam.

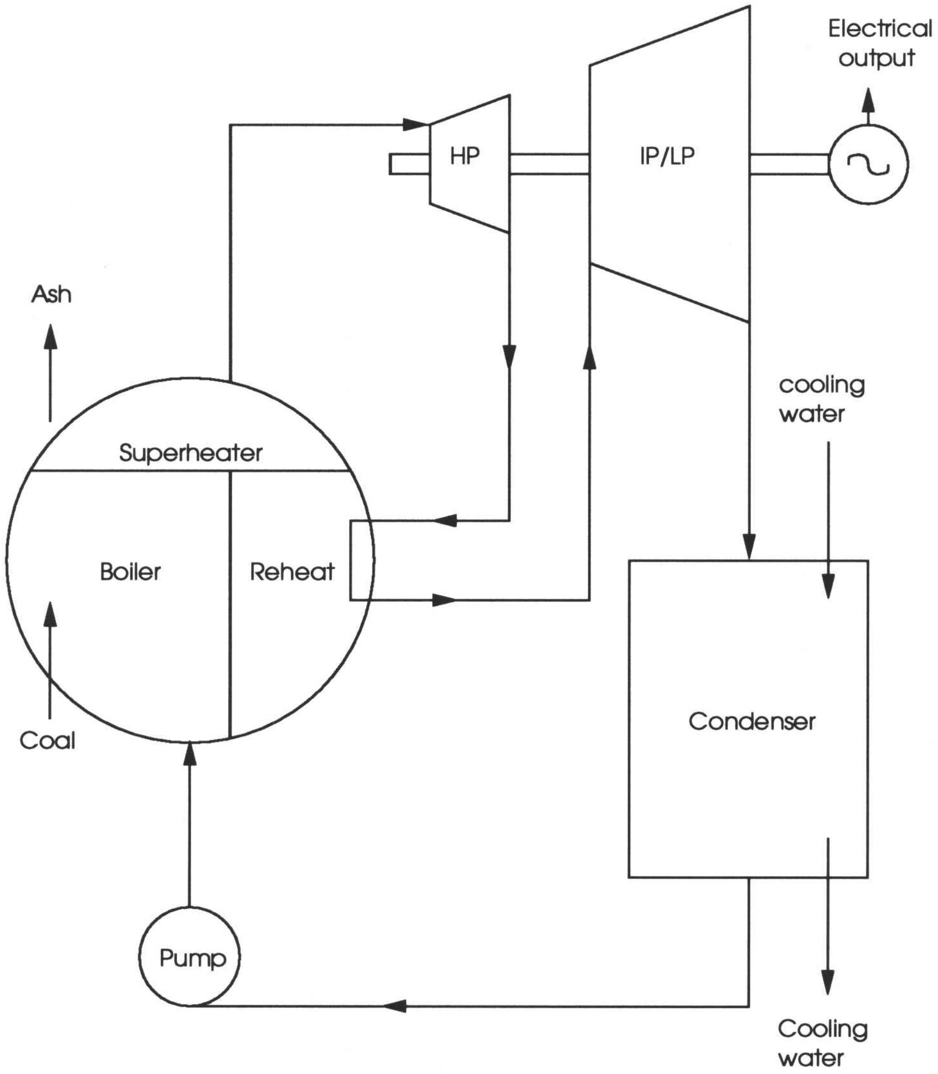

Fig. 1.1 Power plant operating on steam cycle with superheat and reheat.

Fig. 1.1 shows schematically a route for steam and water in a power plant incorporating a "*superheat*" and a "*reheat*". Water is first pumped into a boiler where it is turned into steam and then superheated close to the metallurgical temperature limit. The superheater may be integral with the boiler or may be a separate unit. The steam then enters the high pressure (HP) turbine where it is directed through nozzles onto the turbine blades. The steam is allowed to expand to an intermediate pressure and is then returned to the boiler where it is reheated back to a high temperature at near-constant pressure. The reheated steam can then be passed into an intermediate pressure (IP) turbine from which the exhaust is passed directly into a low pressure (LP) turbine. This allows the steam to expand down to the condenser pressure. The various pressure turbines are coupled together to drive the rotor of the generator to produce electrical power. Table 1.2 gives some example conditions in a turbine generator set for each pressure stage. Fig. 1.2 shows a bladed HP/IP rotor with a man stood beside to indicate the scale of this machinery.

Stage	**Entry Pressure**	**Entry Temp.**	**Exit Pressure**	**Exit Temp.**
HP	16 MPa	565 °C	4MPa	420 °C
IP	4 MPa	565 °C	0.6 MPa	250 °C
LP	0.6 MPa	250 °C	0.1 MPa	100 °C

Table 1.2: An example of steam conditions in a turbine generator set. The terms HP. IP and LP stand for high, intermediate and low pressure respectively.

1.3 Materials for Power Plant

Research and development of power plant steels has spanned many decades, giving rise to a large variety of steels which can be used for different purposes. These steels are rapidly becoming more complex. Table 1.3 shows the compositions of a selection of ferritic power plant steels (Masuyama, 1999).

There are three main groups shown in Table 1.3: 2, 9 and 12 wt%Cr steels. The 9-12 wt%Cr steels are currently undergoing the most research and development due to their high strength and good corrosion resistance. Fig. 1.3 shows the progress of ferritic steels in terms of increasing the 10^5 h creep rupture strength at 600 °C. The improvements have mainly been achieved by the addition of alloying elements. EM12, Tempaloy F-9 and T91 are modified 9 wt%Cr steels whose strengths have been enhanced by the addition of carbide forming elements such as V an Nb.

NF616 has the highest allowable stress of the 9 wt%Cr steels. The design was based on the reduction of Mo to 0.5 wt% and increasing W to 1.8 wt%. This has been shown to have a 30 % increase on 100 000 hour creep rupture strength at 600 °C (Ohgami *et al.*, 1997). The 9 wt%Cr steels have been developed with high creep rupture strength but are limited to service below 625 °C due to problems with oxidation and corrosion resistance.

In terms of the 12 wt%Cr group of steels, HT91 has been used in Europe for extensive periods for superheater tubes, headers and steam pipes. However, due to the high carbon content the steel has poor weldability and it has been found to not have very good creep strength. Improved 12 wt%Cr steels such as HCM12 and HCM12A do have higher creep rupture strengths and lower carbon contents. HCM12 contains δ-ferrite which is detrimental

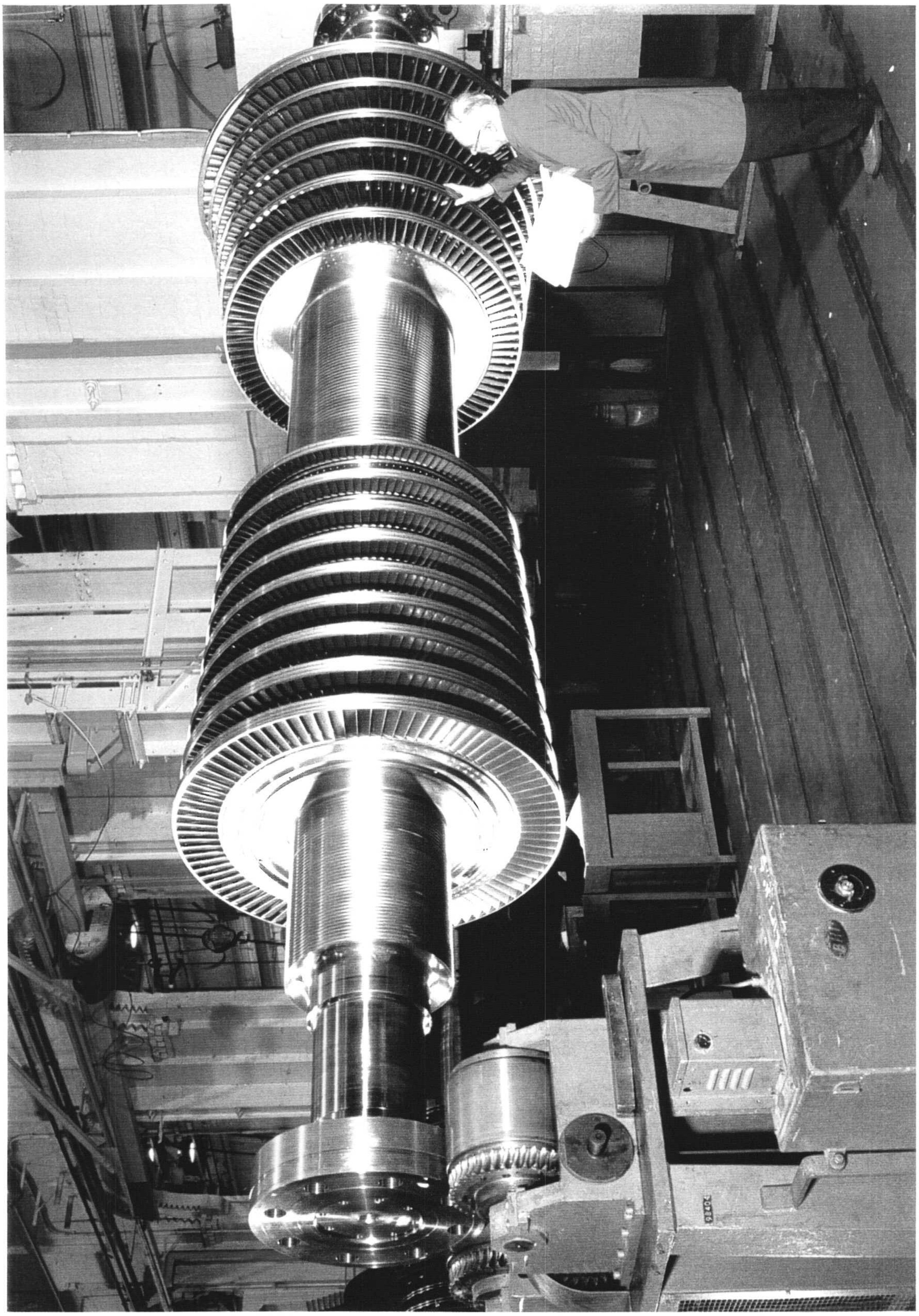

Fig. 1.2 HP/IP rotor for steam turbine (Image courtesy of ALSTOM Power, Rugby; Ref. Taylor and Thornton, 1997).

	Steels	C	Si	Mn	Cr	Mo	W	Co	V	Nb	B	N	Others
2Cr	T22	0.12	0.3	0.45	2.25	1.0	-	-	-	-	-	-	-
	HCM2S	0.06	0.2	0.45	2.25	0.1	1.6	-	0.25	0.05	0.003	-	-
9Cr	T9	0.12	0.6	0.45	9.0	1.0	-	-	-	-	-	-	-
	HCM9M	0.07	0.3	0.45	9.0	2.0	-	-	-	-	-	-	-
	T91	0.10	0.4	0.45	9.0	1.0	-	-	0.20	0.08	-	0.05	-
	NF616	0.07	0.06	0.45	9.0	0.5	1.8	-	0.20	0.05	0.004	0.06	-
	Tempaloy F-9	0.06	0.5	0.60	9.0	1.0	-	-	0.25	0.40	0.005	-	-
	EM12	0.10	0.4	0.10	9.0	2.0	-	-	0.30	0.40	-	-	-
12Cr	HT91	0.20	0.4	0.60	12.0	1.0	-	-	0.25	-	-	-	0.5Ni
	HT9	0.20	0.4	0.60	12.0	1.0	0.5	-	0.25	-	-	-	0.5Ni
	HCM12	0.10	0.3	0.55	12.0	1.0	1.0	-	0.25	0.05	-	0.03	-
	HCM12A	0.11	0.1	0.60	12.0	0.4	2.0	-	0.20	0.05	0.003	0.06	1.0Cu
	NF12	0.08	0.2	0.50	11.0	0.2	2.6	2.5	0.20	0.07	0.004	0.05	-
	SAVE12	0.10	0.3	0.20	11.0	-	3.0	3.0	0.20	0.07	-	0.04	0.07Ta 0.04Nd

Table 1.3: Nominal chemical compositions (wt%) of ferritic steels.

to creep rupture properties and so is limited to thin wall applications such as pipes. HCM12A is the improved version of HCM12 where δ-ferrite has been eliminated, enhancing the toughness so the material may be used for thicker wall applications. The 12 wt%Cr steels in the 180 MPa class are under development and contain increased tungsten contents and additions of cobalt. The cobalt addition can help prevent δ-ferrite formation which then allows the increase in tungsten.

However, most fossil fired power plant in the world are constructed from low alloy steels containing Cr, Mo and V as the major alloying elements. These include such steels as $\frac{1}{2}$Cr$\frac{1}{2}$Mo$\frac{1}{4}$V and 2$\frac{1}{4}$Cr1Mo, the compositions of which are given in Table 1.4, along with some other common creep-resistant steels. The use of these materials places limitations on the operating temperature and pressure which the plant may be run at. For example, in 1993, the maximum steam conditions of 565 °C at 30 MPa were employed in the U.K. (Gooch, 1993). To operate above these conditions requires the use of materials with higher creep strength and oxidation resistance.

Fig. 1.4 shows a comparison of a variety of alloys with 10^5 h creep rupture strength against temperature. It is clear that to obtain higher operating conditions it is necessary to go

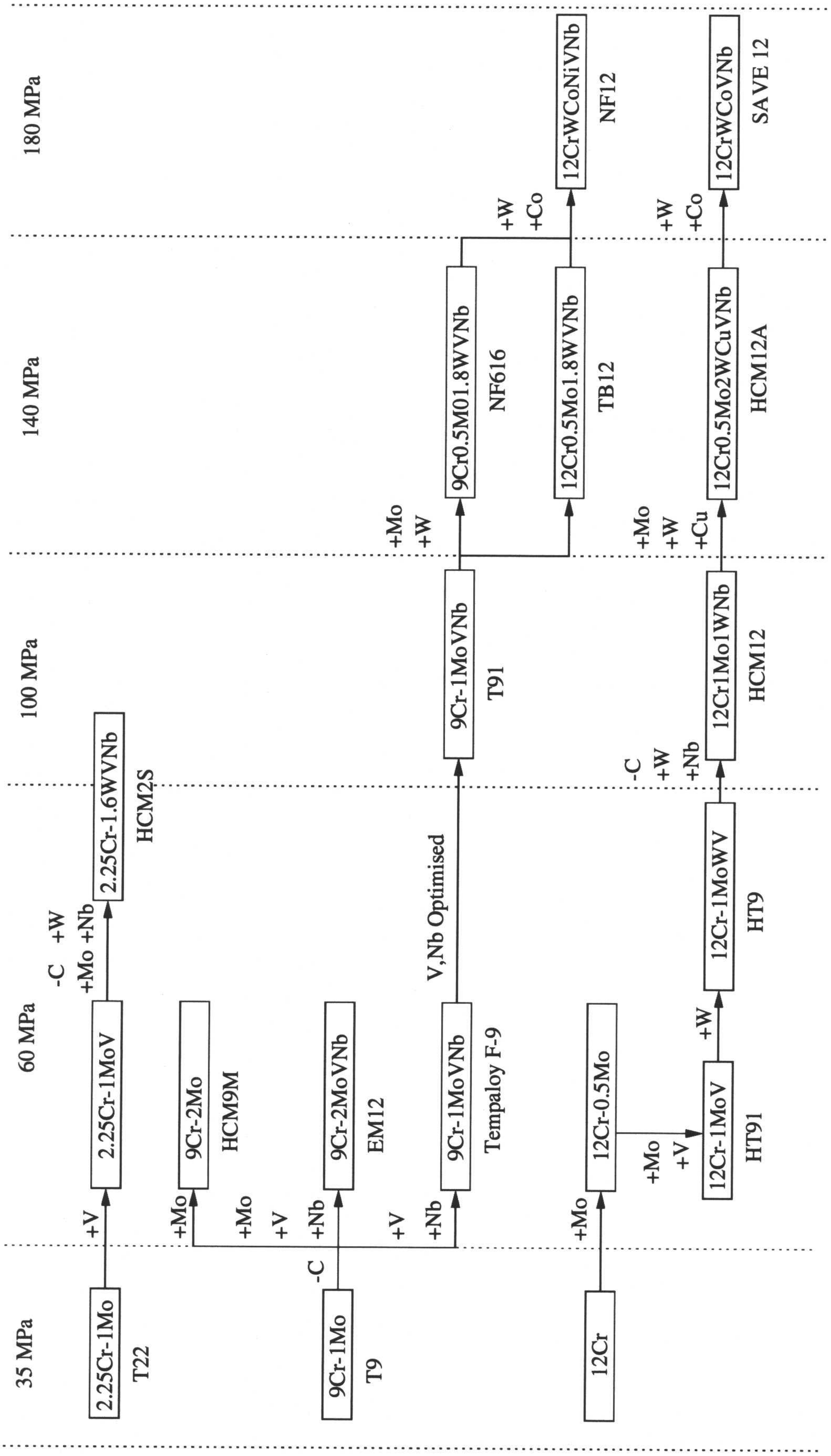

Fig. 1.3 Development progress of ferritic steels (adapted from Masuyama, 1999).

Designation	C	Si	Mn	Ni	Mo	Cr	V
1Cr$\frac{1}{2}$Mo	0.15	0.25	0.50	-	0.6	0.95	-
$\frac{1}{4}$CrMoV	0.15	0.25	0.50	0.05	0.50	0.30	0.25
$\frac{1}{2}$Cr$\frac{1}{2}$Mo$\frac{1}{4}$V	0.12	0.25	0.50	-	0.6	0.45	0.25
1CrMoV	0.25	0.25	0.75	0.70	1.00	1.10	0.35
2$\frac{1}{4}$Cr1Mo	0.15	0.25	0.50	0.10	1.00	2.30	0.00

Table 1.4: Chemical compositions (wt%) of some low-alloy creep-resistant steels for power plant.

to higher alloy content steels or maybe even use certain nickel-based gas turbine alloys. The creep rupture strength of the nickel-based super alloys is very good at high temperatures but they can cost 6-10 times more than low alloy steels, depending on the alloy composition and market prices of alloying elements (Vanstone, 2000). In addition, nickel-based super alloys are more expensive to weld and machine.

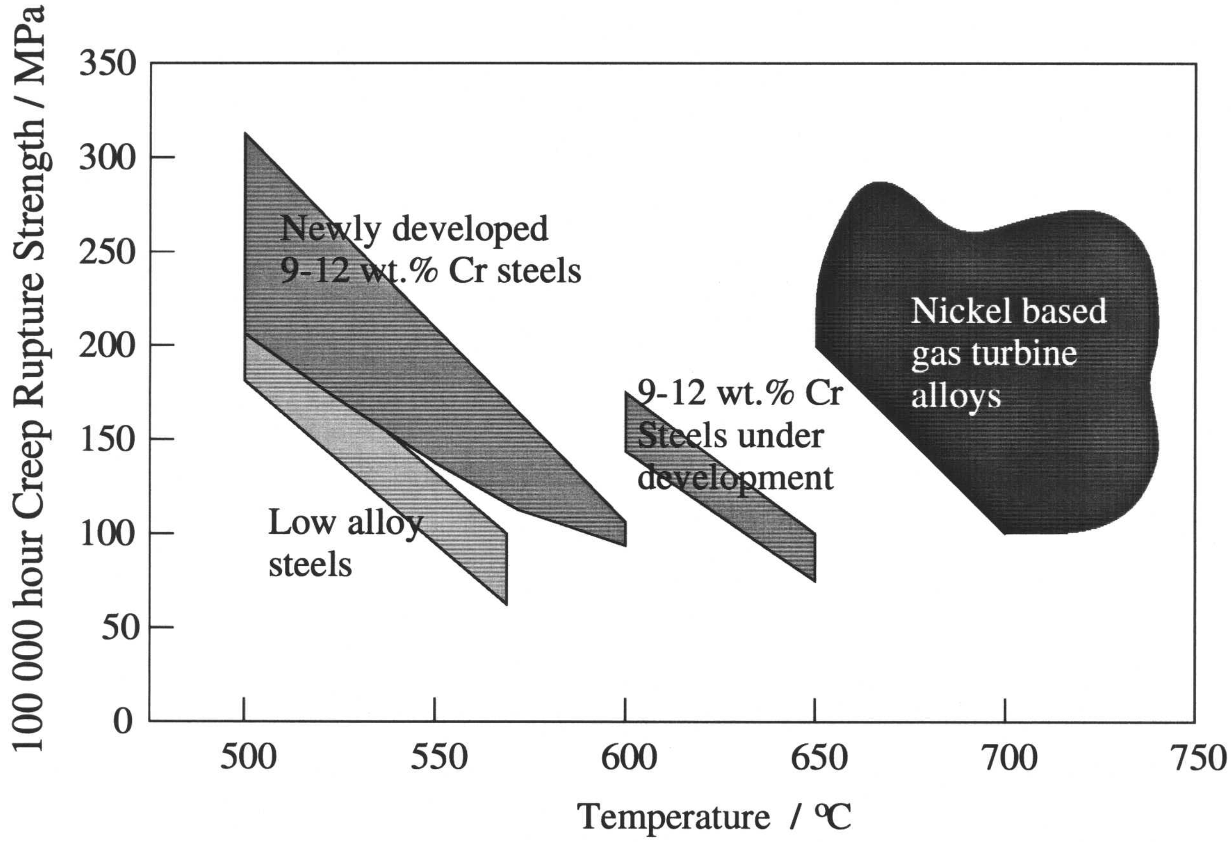

Fig. 1.4 Comparison of creep rupture strength at 100000 hours for a variety of steels (adapted from Vanstone & Thornton, 1997).

Austenitic steels also exhibit high creep rupture strength, but it is likely that they would only offer marginal advantages over advanced 12 wt%Cr steels and at a higher cost (Vanstone & Thornton, 1997). The austenitic steels also have a higher coefficient of thermal expansion and low conductivity compared with ferritic steels, as shown in Table 1.5. This is a problem since steam turbines are often turned off and on during their service life and this thermal cycling can cause fatigue in austenitic steels.

Steel	CTE/μm^{-1}K^{-1}	Thermal Conductivity/Wm^{-1}K^{-1}
Ferritic	9.9	24.9
Austenitic	17.3	16.3

Steel	AISI Type	C	Mn	P	S	Si	Cr	Ni
Ferritic	403	0.15	1.00	0.04	0.03	0.50	11.5-13.0	-
Austenitic	305	0.12	2.0	0.045	0.030	1.0	17-19	10.5-13.0

Table 1.5: Comparison of the coefficient of thermal expansion (CTE) and thermal conductivity for a ferritic and austenitic steel at 100 °C. The compositions (wt%) of the steels are also given (Harvey, 1982).

The purpose of the work reported here is to improve the long-term high temperature properties of these steels. The aim is to design a novel alloy which will have a service life of over 100 000 hours at 650 °C exposed to a stress of 100 MPa.

As previously stated, the limiting factor in use of a material at elevated temperatures is generally its creep strength and resistance to degradation. These factors are related to the microstructural stability of the alloy. In summary, the general requirements for an alloy are as follows:

- high creep strength at high temperature
- high toughness and resistance to embrittlement
- resistance to steam oxidation and corrosion
- ease of fabrication and weldability.

The focus of achieving this goal is on modifying the composition and heat treatment of power plant steels to try and produce these properties. This is to be done by modelling the long term creep properties of these alloys, whilst also utilising information reported in literature and elsewhere.

CHAPTER 2

Creep and the Physical Metallurgy of Power Plant Steels

Creep may be described as the time dependent and permanent deformation of a material when exposed to a constant load, which is below the ordinary yield strength as measured in a tensile test. Creep deformation is a thermally activated process and the rate of deformation is temperature sensitive. In the case of power plant steels the creep strength is affected by the composition of the steel and also the heat treatments applied to them. These variables control the microstructure of the alloy, including precipitation of carbides, which shall be examined in this chapter. We shall begin with an examination of the process of creep.

2.1 Creep

Creep behaviour can simply be demonstrated by plotting the general relationship between strain and time, Fig. 2.1.

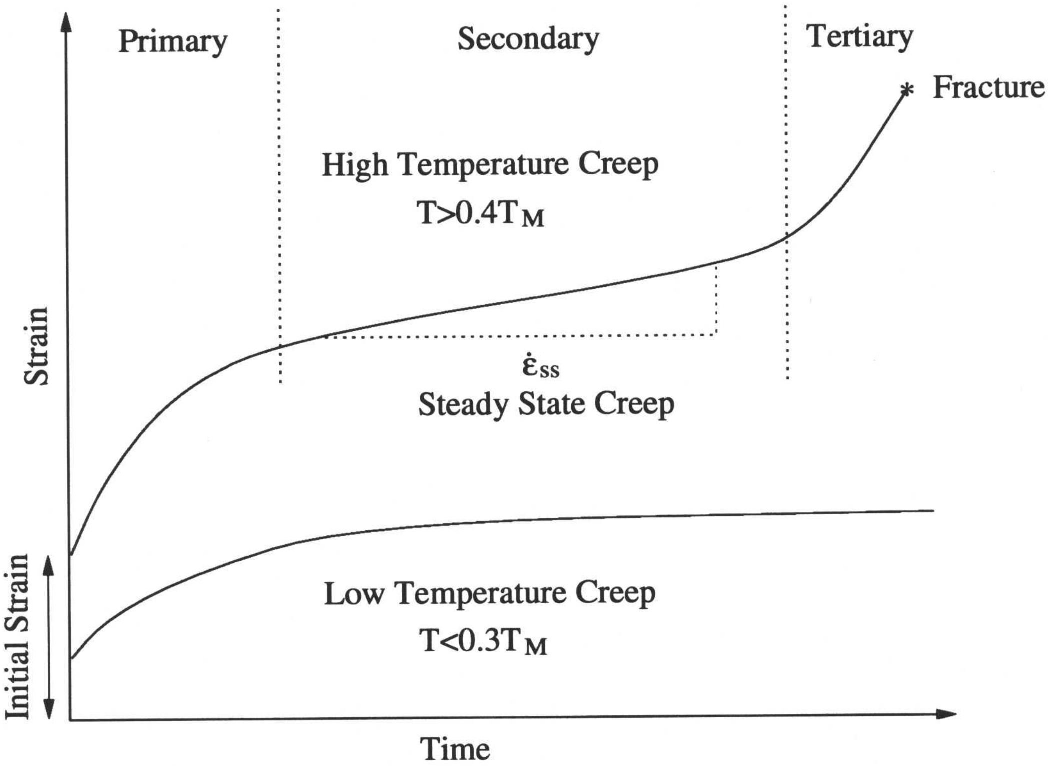

Fig. 2.1 General relationship between strain and time, showing behaviour at low and high temperatures as a function of T_M, the melting temperature of the material.

The plots shown in Fig. 2.1 indicate the temperature dependence of creep. At low temperatures dimensional changes due to creep are usually very small, rarely leading to failure. At higher temperatures creep becomes an important mechanism, likely to cause serious deformations and fracture. Fig. 2.1 shows the temperature as a function of the melting temperature of the material, T_M(K). The general rule for determining if creep will occur in metals or not is:

$$T > 0.3 - 0.4T_M \tag{2.1}$$

Pure iron melts at 1536 °C and so from this generalised rule it can be seen that pure iron would start to creep at approximately 270 °C. This is far too low to be used in steam power plant and is the reason for alloying iron to improve its creep properties. A simpler solution to the problem could be to use metals with such high melting temperatures that creep is not a problem. Tungsten has a melting temperature of 3407 °C but because its oxide (WO_3) sublimes (Petty, 1968), it is not a practical solution.

At high temperature, the details of the creep curve, for example the extent of primary creep or even the existence of a steady-state regime, depend on material and microstructure. After an initial strain on loading the creep rate usually decays in the primary region. Beyond the primary regime, the material enters a steady state region referred to as secondary creep which in the case of steels can be the longest stage of the creep deformation process. This constant creep rate is due mainly to a balance between work hardening and recovery processes.

After this stage the creep rate increases again due to damage and this is called the tertiary stage. For alloys which may be used as power plant steels the curve may be more complex because microstructural changes occur throughout the working life. These changes can include the precipitation of secondary phases which enhance creep resistance or there may also be a depletion of solute in the matrix by the precipitation of coarse phases, which would in turn be expected to be detrimental to creep resistance.

Creep damage occurs in the form of internal cavities on grain surfaces, which can accumulate. These holes first become significantly visible at the start of the tertiary creep stage, and as they grow, the material section decreases. This causes an increase in the stress experienced by the material and since the creep rate is proportional to a power of the stress the damage leads to the tertiary creep stage.

Some examples of actual creep curves are shown in Fig. 2.2 (Argent *et al.*, 1970). Fig. 2.2a shows the creep curve for a low alloy steel tested at 600 °C. A large strain occurs in the primary creep region, followed quickly by the tertiary region. A higher alloy content steel in shown in Fig. 2.2b, showing some initial strain in the primary region but then only a slow increase in strain as the material enters a prolonged steady-state region. Carbides and nitrides provide the precipitation hardening for steel alloys, whilst other alloying elements in the matrix provide solution hardening.

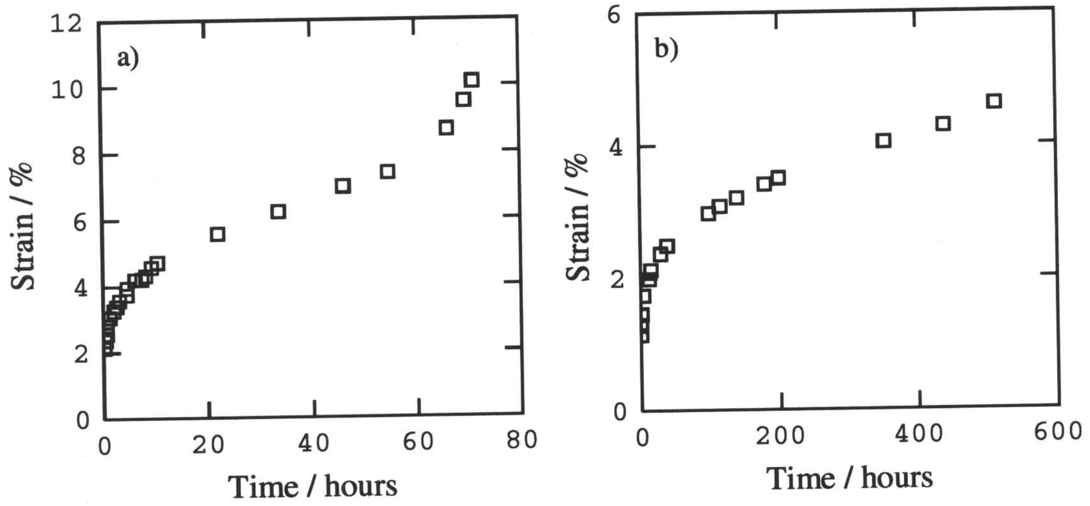

Fig. 2.2 Creep curves for ferritic alloys tested at 600 °C by Argent *et al.* (1970). A low alloy steel is shown in a), containing 0.21 wt% C, 0.07 Cr and 0.52 V. Figure b) shows a higher alloy content steel of composition 0.16 wt% C, 2.41 Cr and 1.25 V.

The creep resistance of a material as measured by fracture is usually termed the ***rupture strength.*** This may be defined as the stress to cause fracture in a given time at a given temperature. The elongation at fracture is usually called the ***rupture ductility.*** For many applications, such as superheater tubing, large deformations in creep can sometimes be tolerated. Thus, when elongation is not vitally important and provided the metal is not deficient in creep ductility, it suffices to use the rupture stress for design calculations. Stress is related to the steady state creep rate ($\dot{\varepsilon}_{ss}$) as follows (Ashby & Jones, 1989):

$$\dot{\varepsilon}_{ss} = B\sigma^n \tag{2.2}$$

where n is the creep exponent between 1 and 8, and B is a constant. At high stresses a mechanism described as *"power-law" creep* occurs and n is of a value between 3 and 8. At low stresses *"linear-viscous" creep* can occur and $n \approx 1$. These mechanisms will be discussed in more detail in section 2.2.

The temperature dependence of the steady-state creep is given by (Ashby & Jones, 1989):

$$\dot{\varepsilon}_{ss} = Ce^{-(Q/\overline{R}T)} \tag{2.3}$$

where $\overline{R}$ is the Universal Gas Constant (8.31 J mol^{-1} K^{-1}), C is a constant and Q is called the ***activation energy for creep*** with units of J mol^{-1}.

Combining the two relationships shown in equations 2.2 and 2.3 gives:

$$\dot{\varepsilon}_{ss} = A\sigma^n e^{-(Q/\overline{R}T)} \tag{2.4}$$

where A is the creep constant. The values of A, n and Q vary with material and have to be found experimentally. The values of n and Q also vary in different stress-temperature regimes, this is due to different mechanisms determining the creep behaviour. An example of this is shown in Table 2.1, where values of n and Q are compared for a matrix of ferrite and a *particle-hardened* alloy at high stresses. The values of n and Q are much higher than expected for the particle-hardened alloy compared to the matrix at stresses greater than ≈130 MPa. This anomalous behaviour has not yet been explained and demonstrates that the values for these equations are all empirical.

Matrix material	n	Q	Particle-hardened alloy	n	Q
Ferrite	≈5	≈260	$\frac{1}{2}$Cr$\frac{1}{2}$Mo$\frac{1}{4}$V	≈12	≈600

Table 2.1: Values of n and Q (kJmol^{-1}) for a single phase matrix and a corresponding particle-hardened alloy at high stresses (Evans & Wilshire, 1993).

The various mechanisms are described in the following section and will start to show why material and microstructure are important for resisting certain types of creep mechanism.

2.2 Creep Mechanisms

There are two main mechanisms by which creep can occur in popular engineering materials:

- Dislocation creep - power law behaviour ($3 \leq n \leq 8$)
- Diffusion creep - linear viscous creep ($n \simeq 1$)

These different regimes of creep may be conveniently represented on a deformation mechanism map (Fig. 2.3). The axes have been normalised by the shear modulus (G) for the stress and by the absolute melting temperature (T$_M$) for temperature. Each region represents a dominant physical mechanism controlling flow, although near the edge of each region, more than one mechanism will contribute.

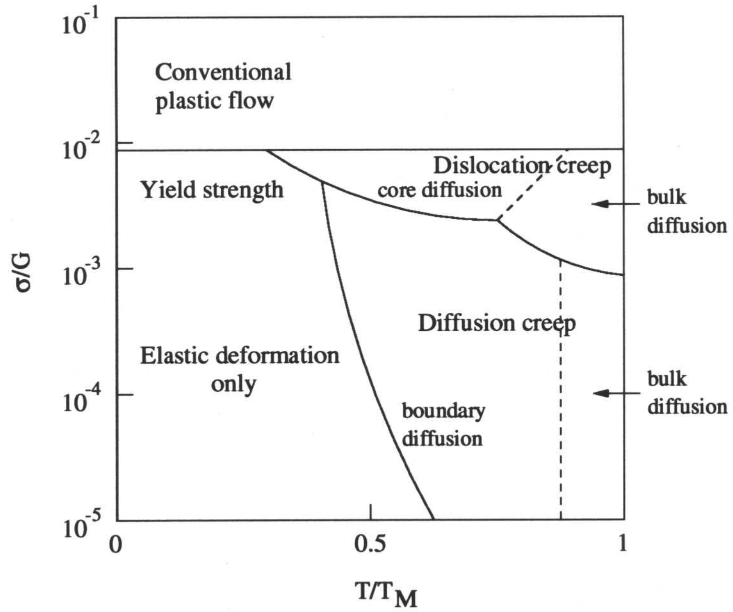

Fig. 2.3 Deformation mechanisms, varying stress and temperature (adapted from Ashby and Jones, 1989).

The two major creep regimes may be further divided:

- Dislocation creep (high stresses)
  - Bulk diffusion
  - Core diffusion
- Diffusion creep (low stresses)
  - Bulk diffusion
  - Boundary diffusion

In each regime, the values of A, n and Q from equation 2.4 are constant, but they change value between regimes. Deformation maps vary for different materials, an example is shown of a 1 CrMoV power plant steel in Fig. 2.4. As will be shown, alloys such as this often depend on precipitation hardening for creep strength, which will vary during over-ageing in service. This means that the boundaries of the deformation map could move during service as the mechanical strength of the alloy changes. The composition of the steel tested is shown in Table 2.2.

Bulk diffusion occurs through the bulk of the crystal in two ways, interstitial diffusion and vacancy diffusion. Interstitial diffusion occurs by the movement of small atoms through the *interstices* of the crystal lattice, which are the small gaps between atoms. Small atoms such as

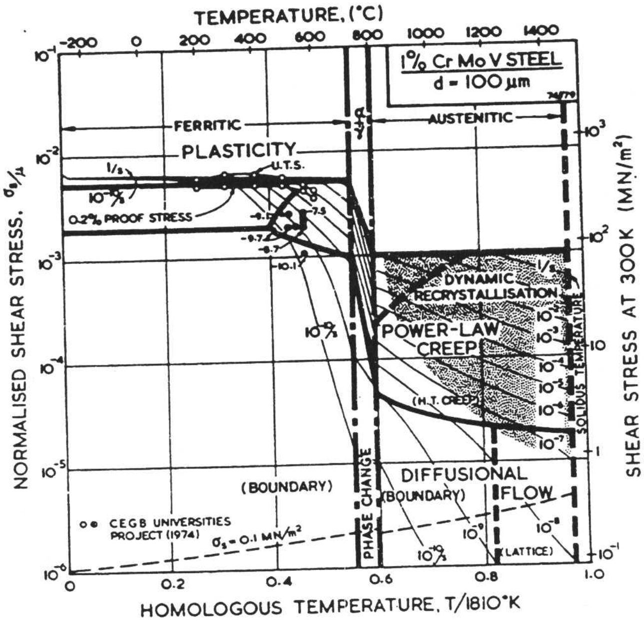

Fig. 2.4 Deformation map of a 1 % Cr-Mo-V steel of grain size 100 μm (Frost & Ashby, 1982).

C (wt%)	Si	Mn	Ni	Cr	Mo	V	S	P
0.24	0.29	0.64	0.21	1.02	0.57	0.29	0.10	0.16

Table 2.2: Chemical composition of 1 % Cr-Mo-V steel.

carbon can do this, as well as such elements as O, N, B, and H. This mechanism is shown in Fig. 2.5a. Vacancy diffusion occurs with atoms which are too large to fit into the interstices, such as an iron atom or other elements such as W and Mo. The atom can only move when a vacancy is available for it to fill, as shown in Fig. 2.5b.

The process of vacancy diffusion is shown in more detail in Fig. 2.6. An atom can move to the site of a vacancy provided that it has sufficient thermal energy. The diagram shows the energy associated with different atom locations, with equilibrium sites at A and C. The mid point between equilibrium sites is shown as B which is a high energy position. The energy needed for the atom to *squeeze* through the lattice can be shown as the difference between B and the equilibrium sites. Vacancy movement is the dominant diffusion mechanism in most metals and alloys.

Core diffusion and boundary diffusion are sometimes described as short-circuiting bulk diffusion, providing routes with low energy barriers for atoms to move along. In core diffusion

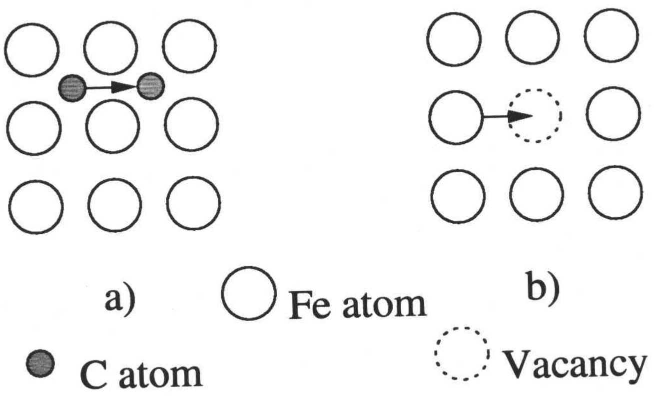

Fig. 2.5 Schematics of a) Interstitial diffusion b) Vacancy diffusion.

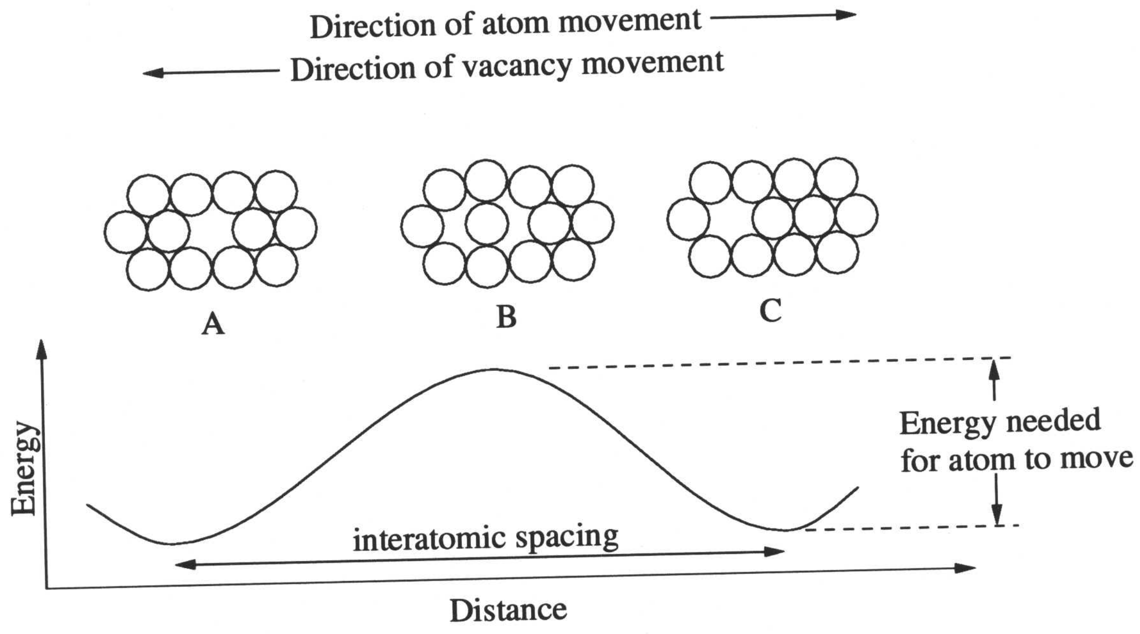

Fig. 2.6 Representation of diffusion as a result of the movement of vacancies. The diagram shows the energy required as an atom "squeezes" between adjacent atoms to reach the new equilibrium site (adapted from Evans & Wilshire, 1985).

a dislocation acts as pathway for atomic diffusion, approximately of the size $(2d)^2$, where d is the atom size. The atoms travel through the distortion caused by the dislocation, as shown in Fig. 2.7a.

In boundary diffusion, grain boundaries act as channels, about 2 atoms wide, creating a fast route with a low energy barrier. Fig. 2.7b shows that incoherent packing creates larger gaps for atoms to fit through.

Because the activation energy is large for bulk diffusion compared with core or boundary

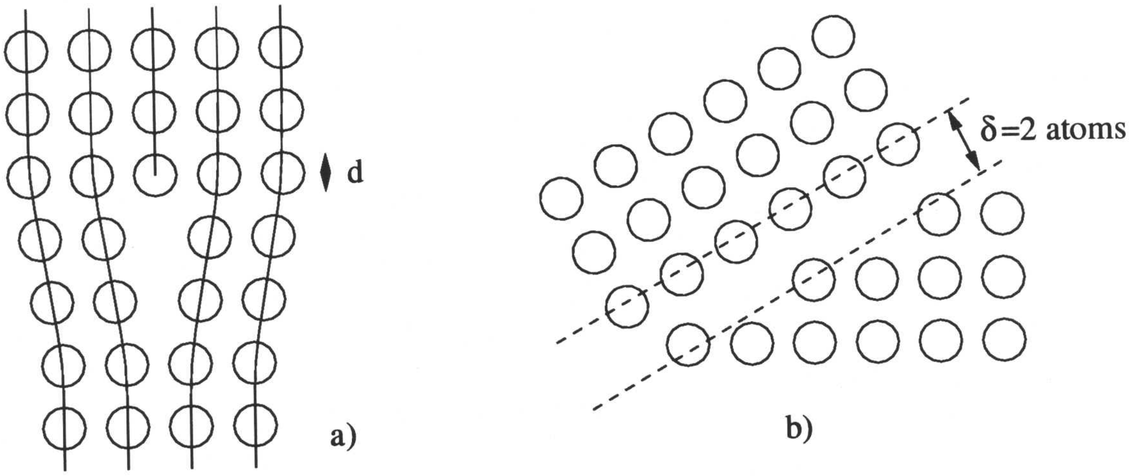

Fig. 2.7 Schematics of a) Dislocation core path for diffusion b) Boundary diffusion.

diffusion, it only starts to occur at higher temperatures. However, the volume over which bulk diffusion can occur is larger, therefore more atoms can diffuse per second and so the mechanism dominates at higher temperatures.

2.2.1 Dislocation Creep

Dislocation movement is impeded by particles, grain boundaries and other dislocations. The precipitates are overcome by the dislocation "climbing" over them, a process which is controlled by diffusion. Atomic diffusion can help to "unlock" dislocations from obstacles in their path and the subsequent movement of these dislocations under the applied stress leads to dislocation creep.

Fig. 2.8 shows a dislocation which cannot glide because its path is blocked by a precipitate. The glide force is balanced by the reaction force from the particle and unless the dislocation hits the precipitate at its mid-plane, there is a component of force left over. This component is the climb force which tries to push the dislocation up out of its slip plane. However, the dislocation cannot glide up by shearing atom planes, instead atoms diffuse away from the loaded areas, allowing the dislocation to climb.

The mechanical forces provide the driving force for diffusion which is the rate controlling process for climb to occur. Diffusion is also reliant on temperature and only occurs at a perceptible rate in normal materials if the temperature exceeds 0.3 T_M (melting temperature). At lower homologous temperatures such as 0.3-0.5 T_M, core diffusion tends to be the dominant mechanism but at higher temperatures bulk diffusion becomes dominant.

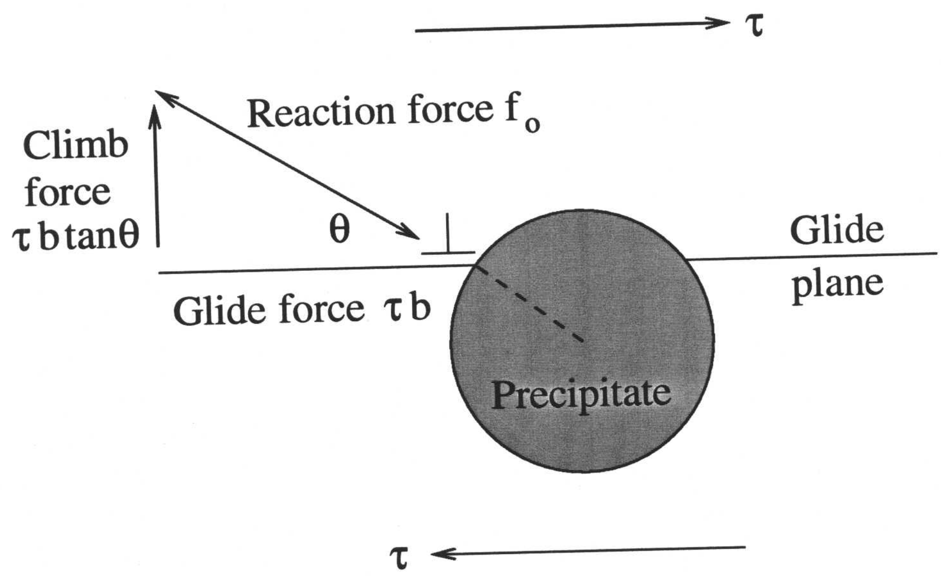

Fig. 2.8 Climb force on a dislocation.

2.2.2 Diffusion Creep

As the stress is reduced the power-law creep mechanism is replaced by diffusion creep, where the applied stress is relieved by grain elongation, caused by diffusion of atoms from one side of the grain to the other (Fig. 2.9). Again, this can happen by two mechanisms, depending on the temperature. At high temperatures the main mechanism is bulk diffusion, where atoms move through the grain itself. At lower temperatures, where bulk diffusion becomes slow, grain boundary diffusion becomes dominant. As before, the rate of creep is dependent on diffusion, stress and temperature but now it is also controlled by grain size. Creep varies as the reciprocal of the square of the grain diameter and so is reduced as the grain increases in size, since matter has to diffuse further to cause elongation. To prevent the formation of holes forming between the grains, grain boundary sliding is required. An example of where increasing grain size has been used to reduce diffusion creep is the manufacture of single crystal blades for gas turbines, often using nickel-based alloys. Gas turbines experience much lower stresses than steam turbines and so power-law creep effects are negligible.

2.2.3 Creep as Applied to Power Plant Steels

In the case of power plant steels the stress levels are relatively high in service and the temperatures are relatively low compared to the melting temperature. With these conditions creep deformation is controlled primarily by dislocation movement as can be shown by the deformation map for the 1 CrMoV steel. For a service temperature of 550 °C (the homologous temperature is approximately 0.45) and high stress the deformation map shows that power-law creep will dominate. This produces a long secondary creep region for steels where work

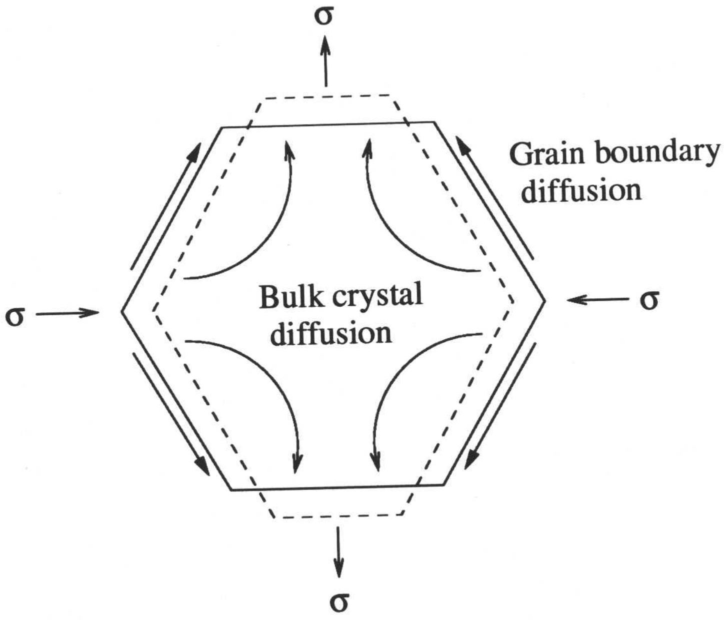

Fig. 2.9 How creep can cause grain elongation.

hardening and recovery produce a steady state creep rate. As creep occurs at high temperatures the movement and generation of dislocations results in strain hardening. Recovery processes such as climb allow dislocations to be annihilated or to re-arrange into low energy positions.

In this case the most effective way to inhibit creep rate is by forming a suitable distribution of particles which may act as a barrier to dislocation motion. Grain size can also have an effect on the motion of dislocations. Low alloy content steels such as $2\frac{1}{4}$CrMo and 1CrMoV are essentially bainitic in microstructure. Higher alloy content steels such as the 9-12 wt% Cr steels are martensitic. Both these microstructures contain grains which are very small, of the order of a quarter of a micron, which provide additional opposition to the movement of dislocations. If diffusion creep were prevalent in this material, a large grain size would be desirable to increase the energy required for diffusion between and through grains. Since the microstructure of power plant steels is important in terms of creep strength, it is useful to examine the physical metallurgy which affects them.

2.3 Physical Metallurgy of Power Plant Steels

The complexity of the alloys produced for steam power plant mean that it is extremely difficult to model the alloys and predict their mechanical properties. This is demonstrated by the flow chart of the development of power plant steels in Chapter 1. Alloy compositions have only had small changes made to them due to the difficulties inherent in design. The problem is further complicated by the large variety of heat-resistant steels now in existence,

Designation	C	Si	Mn	Ni	Mo	Cr	V
1Cr$\frac{1}{2}$Mo	0.15	0.25	0.50	-	0.6	0.95	
$\frac{1}{4}$CrMoV	0.15	0.25	0.50	0.05	0.50	0.30	0.25
$\frac{1}{2}$Cr$\frac{1}{2}$Mo$\frac{1}{4}$V	0.12	0.25	0.50	-	0.6	0.45	0.25
1CrMoV	0.25	0.25	0.75	0.70	1.00	1.10	0.35
2$\frac{1}{4}$Cr1Mo	0.15	0.25	0.50	0.10	1.00	2.30	0.00
Mod. 2$\frac{1}{4}$Cr1Mo	0.1	0.05	0.5	0.16	1.00	2.30	0.25
						Ti=0.03	B=0.0024
3.0Cr1.5Mo	0.1	0.2	1.0	0.1	1.5	3.0	0.1
3.5NiCrMoV	0.24	0.01	0.20	3.50	0.45	1.70	0.10
9Cr1Mo	0.10	0.60	0.40	-	1.00	9.00	-
Mod. 9Cr1Mo	0.1	0.35	0.40	0.05	0.95	8.75	0.22
					Nb=0.08	N=0.05	Al<0.04
9Cr$\frac{1}{2}$MoWV	0.11	0.04	0.45	0.05	0.50	9.00	0.20
					W=1.84	Nb=0.07	N=0.05
12CrMoV	0.20	0.25	0.50	0.50	1.00	11.25	0.30
12CrMoVW	0.20	0.25	0.50	0.50	1.00	11.25	0.30
							W=0.35
12CrMoVNb	0.15	0.20	0.80	0.75	0.55	11.50	0.28
						Nb=0.30	N=0.06

Table 2.3: Typical compositions (wt%) of a selection of creep-resistant steels.

some examples of which are listed in Table 2.3.

The large number of alloying elements in each steel produces a huge variety of microstructures where the matrix can differ as well as the composition and distribution of precipitates. Many of the precipitates formed in power plant steels are carbides and nitrides and their composition may be made up of many elements. In order to describe the chemical formula a simple notation system is used with 'M' representing the metal content and 'X' representing the carbon and nitrogen content.

An example of a carbide often found in these alloys is $M_{23}C_6$ and this was found in steels examined by Abe and Nakazawa (1992). The chromium content of simple 2 wt% W steels was varied and the effect on the microstructure examined (Table 2.4). Carbides M_6C and M_2C were found in the low chromium alloy. The various precipitates and their effect on the mechanical properties of the alloys will be discussed later, as well as certain phases of power plant steels. These experiments demonstrate how easy it is to change the microstructure of the steels, in this case by only varying one element. As the chromium content is increased the microstructure changes from bainitic to martensitic and then to a dual phase matrix of martensite and δ-ferrite. The phase δ-ferrite can form during the solidification of ferritic steels. It is coarse and soft and consequently detrimental to creep strength. Heat-resisting steels with low solute concentrations may also contain substantial quantities of allotriomorphic ferrite and pearlite.

Steel	Quenching treatment	Tempering treatment	Phases	Precipitates after tempering
2Cr-2W	1203 K / 1 h, WQ	1003 K / 1 h, AC	Bainite	$M_{23}C_6$, M_6C, M_2C
5Cr-2W	1203 K / 1 h, WQ	1023 K / 1 h, AC	Bainite	$M_{23}C_6$
9Cr-2W	1223 K / 1 h, WQ	1023 K / 1 h, AC	Martensite	$M_{23}C_6$
12Cr-2W	1273 K / 1 h, WQ	1023 K / 1 h, AC	Martensite +δ-ferrite (0.16)	$M_{23}C_6$
15Cr-2W	1323 K / 1 h, WQ	1023 K / 1 h, AC	Martensite +δ-ferrite (0.16)	$M_{23}C_6$

Table 2.4: Heat treatment conditions, matrix phase and precipitates for steels of varying chromium content. WQ represents a water quench, AC represents an air cool and the volume fraction of δ-ferrite are given in brackets (Abe & Nakazawa, 1992).

The situation can be further complicated by the heat treatments applied to the steel, which can have a large effect on the microstructure and the mechanical properties. In summary the precipitates, phases and composition of a steel and the heat treatments applied to it are all important and interacting factors affecting creep properties. All of these will be discussed in this chapter, beginning with precipitates observed in power plant steels.

2.3.1 Precipitates and Phases observed in Power Plant Steels

Power plant steels are tempered prior to service in order to produce carbides and precipitates and also to relieve stress. The known precipitates are listed in Fig. 2.10; they determine the microstructure and are crucial in the development of creep strain. It is important to note that many of the precipitates are metastable and so do not represent the lowest free energy state. They form because they nucleate easily and they may also dissolve as the material approaches equilibrium with time. Therefore, the first alloy carbide to form is generally not the

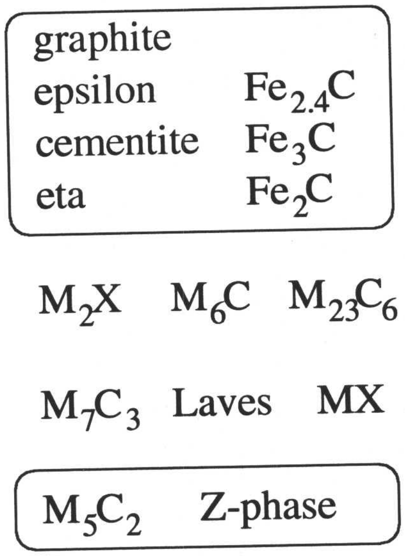

Fig. 2.10 Types of precipitates which can be found in power plant steels. Iron rich carbides such as cementite form rapidly whereas graphite forms incredibly slowly since it is difficult to nucleate. M_5C_2 and Z-phase are recent discoveries in ferritic power plant steels (Mann *et al.*, 1995; Strang & Vodárek, 1996).

equilibrium carbide, leading to precipitations sequences which produce more stable carbides.

A large amount of information on the composition, structure, morphologies and orientation relationships of various precipitates have been obtained (e.g. Goldschmidt, 1948; Kuo, 1953; Shaw & Quarrel, 1957; Baker & Nutting, 1959; Woodhead & Quarrel, 1965; Jack & Jack; 1973; Yakel, 1985). Some information concerning relevant precipitates is presented here.

- **M_3C** - This phase can be referred to as *cementite* and has an orthorhombic structure. Its structure is often Fe_3C but other metal elements may substitute for iron in alloy steels. Kuo (1953) found that chromium may replace iron by up to 18 wt% in Fe_3C. Mn can dissolve in large quantities in M_3C as determined by Woodhead and Quarrell (1965). They also found that Ni and Co can dissolve in M_3C but both partition preferentially to ferrite. Quantities of Mo and Cr have been found in 2.25Cr-1Mo steels by Yang *et al.* (1993). The M_3C composition was found to be 82.2Fe-15.3Cr-2.5Mo (wt%) for the steel composition shown in Table 2.5. The carbide was found in the form of lamellae within a pearlite colony.

M_3C carbides were also analysed by Du *et al.* (1992) for a $\frac{1}{2}$Cr$\frac{1}{2}$Mo$\frac{1}{4}$V steel (Table 2.6). It was found to contain V, Cr, Mn, Mo and C. The chromium content was found to increase with time at high temperature. Mn diffused into the cementite faster than Cr and saturated at higher temperatures. The chemical composition ranges of the M_3C carbide are; 0.8-1.0 wt% V, 2.3-9.0 Cr, 2.4-12 Mn and 1.3-2.0 Mo.

Cr	Mo	C	Mn	P	S	Si	Ni	Cu
2.17	0.80	0.11	0.40	0.027	0.015	0.29	0.055	0.015

Table 2.5: Composition (wt%) of 2.25Cr-1Mo steel examined by Yang *et al.* (1993).

C	Si	Mn	P	S	Cr	Mo	V	Ni	Cu
0.14	0.23	0.61	0.007	0.023	0.36	0.66	0.26	0.21	0.13

Table 2.6: Composition (wt%) of $\frac{1}{2}$Cr$\frac{1}{2}$Mo$\frac{1}{4}$V steel examined by Du *et al.* (1992).

Work on a 2.25Cr-1Mo steel was carried out by Thomson and Bhadeshia (1994a, 1994b) to determine the changes of chemical composition of carbides during tempering. The chemical composition of the steel analysed is shown in Table 2.7. They found that with tempering times of 180 hours at 565 °C that up to 30 wt% of chromium could be detected in M_3C. These few examples show that the chemical composition of carbides depends greatly on the actual composition of the alloy in which they have formed.

C	Si	Mn	P	S	Cr	Mo	Ni	Al	As	Co	Cu	Sn	V
0.15	0.29	0.49	0.01	0.025	2.20	0.96	0.14	<0.01	0.03	0.02	0.18	0.02	0.01

Table 2.7: Composition (wt%) of 2.25Cr-1Mo steel examined by Thomson and Bhadeshia (1994a, 1994b).

Tempering causes the enrichment of cementite and it will approach its equilibrium composition. The rate of enrichment is fastest when the particles are of small size and the ferrite is saturated in carbide forming solute atoms (Bhadeshia, 1992). In low chromium steels the cementite will enrich slowly and is unlikely to reach its equilibrium composition in the component lifetime. In high chromium and high alloy steels the cementite enriches rapidly and then dissolves as other alloy carbides precipitate. This phenomenon is the basis of *secondary hardening* in these steels. It is possible to form more stable carbides, nitrides and borides than cementite. These may form by the dissolution of a relatively coarse cementite dispersion which is replaced by a finer alloy carbide dispersion (Honeycombe & Bhadeshia, 1995). The steel softens as the cementite forms and removes carbon from solid solution, but is then hardened by the alloy carbides which interact with dislocations, thus giving secondary hardening.

It could be expected that when strong carbide forming elements are present that alloy carbides would form in preference to cementite. However, alloy carbides do not form until the steels are tempered in the range 500-600 °C because the metallic alloying elements cannot diffuse sufficiently rapidly to allow the alloy carbides to nucleate. Carbon, like nitrogen, can diffuse much more rapidly since it moves interstitially through the iron lattice, thus iron carbide tends to be the first precipitates formed in these steels. In many cases M_2X type precipitates are the first to form after cementite.

M_2X - This has a hexagonal crystal structure which has been studied by Andrews and Hughes (1959). In this case M represents one or more of the transition metals V, Cr, Mn, Fe, Ni, Nb, Mo, Ta and W, X represents C or N. It has been determined that in complex steels the phase is best regarded as $(Cr, Mo,V)_2(C,N)$ (Woodhouse & Quarrell, 1965). In molybdenum containing steels with a low chromium content and no nitrogen, such as a 2.25Cr-1Mo steel, M_2X is often close to Mo_2C (Baker & Nutting, 1959). However, in 9-12 wt% Cr steels containing nitrogen the composition of M_2X is found to be closer to Cr_2N (Sanderson, 1977).

Yang *et al.* (1993) found the composition of M_2C in a 2.25Cr-1Mo steel (Table 2.5) to be 40.4Fe-23.1Cr-36.5Mo (wt%). Vodárek and Strang (1997) also examined the composition of the M_2X phase in a 12 CrMoV steel (Table 2.8).

Cast	C	Si	Mn	Cr	Mo	V	N	Ni
A	0.13	0.20	0.70	12.32	0.62	0.17	0.04	0.32
D	0.12	0.27	0.65	12.32	0.60	0.18	0.03	1.28

Table 2.8: Chemical compositions (wt%) of 12 CrMoV steel tested by Vodárek and Strang (1997).

It was found that the M_2X existed as fine needle-like particles dispersed throughout the matrix. The composition of the phase is recorded in Table 2.9 and was found to be close to Cr_2N. It was also found that increasing nickel contents decreased the stability of the M_2X phase.

M_2X is generally considered to nucleate on dislocations and martensite lath boundaries (Raynor *et al.*, 1966). Edmonds and Honeycombe (1973) also observed needles and fibres of Mo_2C phase in a Fe-4Mo-0.2C (wt%) steel. The fibres were found to grow normal to the austenite/ferrite interface during transformation.

Cast	V	Cr	Fe	Ni	Mo
A	11.6±2.0	78.1±2.6	2.6±0.9	0.9±0.5	6.8±1.6
D	14.1±3.4	76.3±2.8	2.3±0.7	0.9±0.6	6.5±0.7

Table 2.9: Chemical compositions (wt%) of the metal content of M_2X phase as found in casts A and D (Vodárek and Strang, 1997). The casts were subjected to normalisation at 1150 °C (air cool) and then tempered for 4 hours at 675 °C and air cooled.

Precipitation of M_2X often causes secondary hardening, which is particularly important for low alloy steels where M_2X plays a major role in the creep strength of the alloy. Stabilisation of a chromium-rich M_2X phase in 12 wt% Cr steels can also cause secondary hardening (Irvine *et al.*, 1960). Overaging is accompanied by the formation of $M_{23}C_6$ and dissolution of M_2X. Unfortunately the elements which stabilise M_2X such as Cr and Mo can cause the formation of δ-ferrite, a phase detrimental to creep properties, so limiting the quantities which may be added. It is then often found that M_2X dissolves after long-term exposure at high temperature in 9-12 wt% Cr steels and so does not improve the long-term creep resistance (Vanstone, 1994). However, its precipitation may influence the carbides which form subsequently.

M_7C_3 - M_7C_3 is a chromium-rich carbide which has a trigonal crystal structure, forming after M_2X (Baker & Nutting, 1959), or after cementite formation, without any M_2X being observed (Janovec *et al.*, 1994). Fe dissolves in M_7C_3 with smaller solubilities for Mn, V and Mo respectively. It has been found that M_7C_3 tends to nucleate in the vicinity of cementite, probably at the interface between the carbide and the ferrite matrix of a 2.25Cr-1Mo steel (Baker & Nutting, 1959). This work was supported by that of Kuo (1953), who pointed out that separate nucleation would be unlikely in a matrix already impoverished in chromium. Woodhead and Quarrell (1965) also stated that M_7C_3 would only be observed if a sufficient chromium concentration was available. The dissolution of cementite may provide an area sufficiently rich in chromium for such a precipitation (Beech & Warrington, 1966).

Yang *et al.* (1993) found M_7C_3 in the 2.25Cr-1Mo steel (Table 2.5) which they examined. It had formed as lamellae in pearlite colonies and found to contain more chromium than the neighbouring M_3C carbide, the composition of M_7C_3 being 63.5(wt%)Fe-31.5Cr-5.0Mo.

Yong Wey *et al.* (1981) discovered that M_7C_3 coarsened rapidly and gave no beneficial contribution to creep rupture strength. Beech and Warrington (1966) worked on the M_7C_3 to $M_{23}C_6$ transformation in chromium containing steels. They determined that the transformation occurs by separate competitive nucleation at 700 °C. It was also found that vanadium stabilizes M_7C_3 and so decreases the rate of release into the matrix of carbon and chromium for the growth of $M_{23}C_6$.

- **$M_{23}C_6$** - $M_{23}C_6$ is a chromium-rich carbide which has a face-centred cubic structure. This precipitate may also contain W, Mo, V and Ni (Woodhead & Quarrell, 1965). It forms after either M_7C_3 or M_2X in 9-12 wt% Cr steels, is often the equilibrium carbide and is predominant after tempering. The nucleation of this phase may occur on the prior austenite grain boundaries, martensite lath boundaries (Senior, 1989) or adjacent to M_7C_3 (Nutting, 1999).

Yang *et al.* (1993) examined the composition of $M_{23}C_6$ in two 2.25Cr-1Mo steels (Table 2.10). Microanalysis showed that $M_{23}C_6$ particles in the ferrite matrix of steel 1 (five years service) were enriched in Fe with a high chromium content with some low Mo content, 76.2Fe-21.7Cr-2.1Mo (wt%). Steel 2 was examined after eighteen years service and was found to contain a much more chromium-rich $M_{23}C_6$, of composition 44.3Fe-49.4Cr-6.3Mo (wt%).

Steel	Cr	Mo	C	Mn	P	S	Si	Ni	Cu	Service / hours
1	2.15	0.85	0.15	0.36	0.024	0.024	0.33	0.015	0.012	49700
2	2.10	0.80	0.11	0.40	0.015	0.014	0.25	0.15	0.047	162000

Table 2.10: Composition (wt%) of two 2.25Cr-1Mo steels examined by Yang *et al.* (1993). In service as pipe sections at a temperature 542 °C.

The composition of $M_{23}C_6$ was examined in a 9 wt%Cr steel was determined by Orr *et al.* (1993). The specified composition range of the alloy examined is shown in Table 2.11. The composition of the $M_{23}C_6$ precipitate was found to contain 32Fe-64Cr-4Mo wt%.

C	Si	Mn	P	S	Cr	Mo	Ni	Al	N	Nb	V
0.08-0.12	0.2-0.5	0.3-0.6	0.04	0.03	8.0-9.5	0.85-1.05	0.40	0.040	0.03-0.07	0.06-0.10	0.18-0.25

Table 2.11: Composition range (wt%) of the 9Cr steel examined by Orr *et al.* (1993).

Vodárek and Strang (1997) determined the metal content of $M_{23}C_6$ in the 12Cr steels described in Table 2.8. The results of their analysis are shown in Table 2.12.

$M_{23}C_6$ forms as large particles and is not thought to contribute directly to creep strength, although it has been suggested that $M_{23}C_6$ carbides may stabilise lath boundaries and retard

Cast	V	Cr	Fe	Ni	Mo
A	0.8±0.1	68.3±0.4	24.1±1.0	0.3±0.1	6.5±0.6
D	1.0±0.2	67.1±0.6	23.7±0.7	1.0±0.2	7.2±0.8

Table 2.12: Chemical compositions (wt%) of the metal content of $M_{23}C_6$ phase as found in casts A and D (Vodárek and Strang, 1997). The casts were subjected to normalisation at 1150 °C (air cool) and then tempered for 4 hours at 675 °C and air cooled.

grain growth (Bjärbo, 1994).

- **M_6C** - This can be the equilibrium carbide in steels containing molybdenum and relatively low levels of chromium (Edmonds & Honeycombe, 1973; Tillman & Edmonds, 1974). It has a face-centred cubic structure frequently containing Mo and Fe but not high in Cr. Nucleation can occur on the M_2X and $M_{23}C_6$ interphase boundaries (Kurzydlowski & Zieliński, 1984), prior austenite boundaries or martensite lath boundaries. Recent work reported by Nutting (1999) indicates that this phase may not nucleate from existing carbides, but as the carbides dissolve, solutes are transferred to M_6C by diffusion. It forms at grain boundaries, growing rapidly at the expense of surrounding carbides. The carbide is often coarse and since it causes the dissolution of less stable fine carbides M_6C can cause a reduction in creep strength. It has been shown that the coarsening rate of M_6C is greater than that of $M_{23}C_6$ and so is a particularly undesirable phase (Vodárek and Strang, 1997).

M_6C carbides were found by Du *et al.* (1992) in the $\frac{1}{2}$Cr$\frac{1}{2}$Mo$\frac{1}{4}$V steel described previously in Table 2.6. As Table 2.13 shows, the carbide was found to be mainly rich in Mo.

V	Cr	Mn	Mo	C
2.0-3.0	5.5-8.0	6.0-8.0	16.0-20.0	14.3

Table 2.13: Chemical composition (at.%) of M_6C carbide in $\frac{1}{2}$Cr$\frac{1}{2}$Mo$\frac{1}{4}$V steel (Du *et al.* 1992).

M_6C was also found to precipitate in 12CrMoV steels with high nickel content by Vodárek and Strang (1997). The two high Ni steels examined are recorded in Table 2.14. The chemical compositions of the precipitated M_6C are shown in Table 2.15. In this system M_6C has a high Ni content which increases with time. M_6C was not found to form in the lower Ni content steels. It was found the increased precipitation of M_6C caused an increase in the rate of dissolution

Cast	C	Si	Mn	Cr	Mo	V	N	Ni
C	0.13	0.32	0.65	12.35	0.58	0.17	0.03	0.97
D	0.12	0.27	0.65	12.32	0.60	0.18	0.03	1.28

Table 2.14: Chemical compositions (wt%) of 12 CrMoV steel tested by Vodárek and Strang (1997).

Steel	Life / h	Si	V	Cr	Fe	Ni	Mo
C	3053	7.0±0.9	6.0±0.5	34.5±1.3	9.2±1.1	24.7±1.5	18.6±1.2
C	15643	7.5±1.2	6.8±0.5	33.4±3.2	7.8±1.2	26.2±1.8	18.3±2.0
D	1253	6.7±0.4	5.4±0.4	35.1±1.0	7.6±0.4	26.5±0.8	18.7±0.5
D	14731	7.0±0.9	6.6±0.4	33.1±1.9	6.6±0.7	28.3±0.9	18.4±1.4

Table 2.15 Chemical compositions (wt%) of the metal content of M_6C as found by Vodárek and Strang (1997) in Ni containing 12CrMoV steel tested at 550 °C.

of the finer M_2X type carbide.

- **MX** - Carbonitrides of this form may be observed in power plant steels. They can be of the form MX which often has a cubic structure like NaCl (Woodhead & Quarrell, 1965). This carbide is often rich in vanadium, although NbC and TiC have also been found to form. The vanadium carbide structure is basically VC but extends to V_4C_3 by formation of a defect lattice. There is also some solubility of Fe, Cr and Mo in these MC. The carbides MoC and WC have hexagonal structures.

Other precipitates of this form such as VN are desirable since they form a fine distribution of small and stable particles which are beneficial to creep strength. If the austenitising heat treatment is high enough, these stable nitrides should dissolve and reform on cooling. Janovec *et al.* (1994) found them to be present after the first heat treatment and after tempering in a 12wt%Cr steel. During the tempering process they were enriched in vanadium.

Hofer *et al.* (1998) found formation of VN and NbC in a 12wt%Cr steel containing V and Nb. VN was found as a plate-like phase and NbC was found in a more spheroidal form. These precipitates were also found merged together in 'propellor' particles or in a 'V-wing' morphology (Nickel *et al.*, 1995).

The composition of MX type precipitates were determined by Orr *et al.* (1993) for the 9wt%Cr steel described in Table 2.11. Their results are shown in Table 2.16. Only a small amount of these type of precipitates were reported in this system. VN precipitates were also found.

Precipitate	Cr	Fe	Nb	V
NbC	-	-	87	13
V_4C_3	30	11	3	56

Table 2.16: Chemical composition (wt%) of the metal content of MX type precipitates found in 9wt%Cr steel by Orr *et al.* (1993).

- **Laves phase** - Laves phase has the general composition Fe_2M, where the alloy content may be W, Mo or a combination of both. It has often been observed in 9-12wt%Cr steels containing W or Mo after long exposure to elevated temperatures. It was reported by Senior (1989) that the composition of Laves phase in 9Cr1Mo steel is approximately 11 wt% Si, 44 wt% Mo, 17 wt% Cr and 28 wt% Fe. It was also noted that the formation of Laves phase occurred preferentially in chromium-depleted regions. These regions were found to be comparatively rich in Mo, implying that a principal kinetic constraint on Laves phase formation is the diffusion of molybdenum atoms. The diffusion of Si is also a constraint on formation.

Hosoi *et al.* (1986) found that increasing Si content had a profound effect on Laves phase precipitation in a 9Cr-2Mo steel. Considerable amounts of Laves phase was found to form in the alloy containing 0.67 wt% Si but only small amounts were observed when the silicon content was reduced to 0.008 wt%. It was also determined that the maximum amount of Laves phase formed in a temperature range of 600-640 °C, with drastic reductions above 720 °C and below 460 °C. It was found that Mn additions were useful in retarding the formation of Laves phase, which was delayed in a sample containing 1.17 wt% Mn, compared to a similar alloy with an addition of 0.58 wt% Mn.

Fujitsuna *et al.* (2000) also found that Si additions accelerated the formation of Laves phase and increased the main particle size in 8.5Cr-2W-VNb steels. It was determined that a decrease in creep rate was caused by precipitation of Laves phase on lath boundaries, suppressing the recovery of the microstructure. A silicon content of 0.3 wt% was found to provide the best balance between recovery of the microstructure and coarsening of the precipitate. Ishii *et al.* (1998) determined that formation of Laves phase at grain boundaries and martensitic lath interfaces was an important factor in maintaining creep rupture strength. Precipitation strengthening by Laves phase was also suggested by Hald (1995) for tungsten containing steels, attributing more beneficial effect for creep strength to the precipitate than to solid solution strengthening by tungsten. Laves phase containing W is found to be much more thermally stable than Fe_2Mo but the coarsening rate of the particles after precipitation is still high (Kubon *et al.*, 1997). This gives large Laves phase precipitates after several thousand hours of creep exposure, indicating that the beneficial effects for creep strength would not last into the long-term.

Laves phase has been found to initially form on prior austenite grain boundaries, followed by precipitation on lath boundaries and finally some precipitation within the laths (Senior, 1989). It may also profit from nucleation on existing phases such as $M_{23}C_6$.

- **Z-phase** - Z phase is a complex nitride phase containing chromium, vanadium and niobium. It has been found in 12CrMoVNb steels at temperatures greater than 550 °C and it appears that it forms in close association with dissolving NbX particles (Strang & Vodárek, 1996). As this phase grows it gradually replaces less stable MX and M_2X nitrogen rich phases which improve the creep rupture strength. Therefore Z phase directly contributes to a reduction in the creep rupture strength of the observed 12CrMoVNb steel. However this alloy did contain a very large concentration of niobium (0.29 wt%) which should enhance the precipitation of Z phase.

- **M_5C_2** - M_5C_2 has recently been identified in ex-service 1Cr-0.5Mo steels by Mann *et al.* (1995). It has also been known as the Hägg or χ-carbide and is a monoclinic phase which has not previously been identified in creep-resistant Cr-Mo steels. The precipitates were found to be rod-shaped and appeared to nucleate heterogeneously on M_2C and remain in ferrite regions from which M_2C had disappeared, suggesting that M_5C_2 is more stable than M_2X. The average composition of the carbide was found to be in the range 48 to 56 at.% Fe, 32 to 42 at.% Cr, 8 to 12 at.% Mn and about 1 at.% Mo.

- **μ-phase** - Precipitation of μ-phase of the type Fe_7W_6 has been found to be beneficial for high creep rupture strength at temperatures over 600 °C (Igarashi & Sawaragi, 1997).

It can clearly be seen that many carbides and precipitates can form in creep-resistant alloys and that these phases have a direct effect on the properties of the steel. The composition and heat treatments are very important in determining which precipitates will form in the alloy. Fig. 2.11 summarizes the composition range found in a selection of carbides, showing some of the elements which are important in their formation.

As the composition of alloys become increasingly more complicated the task of predicting

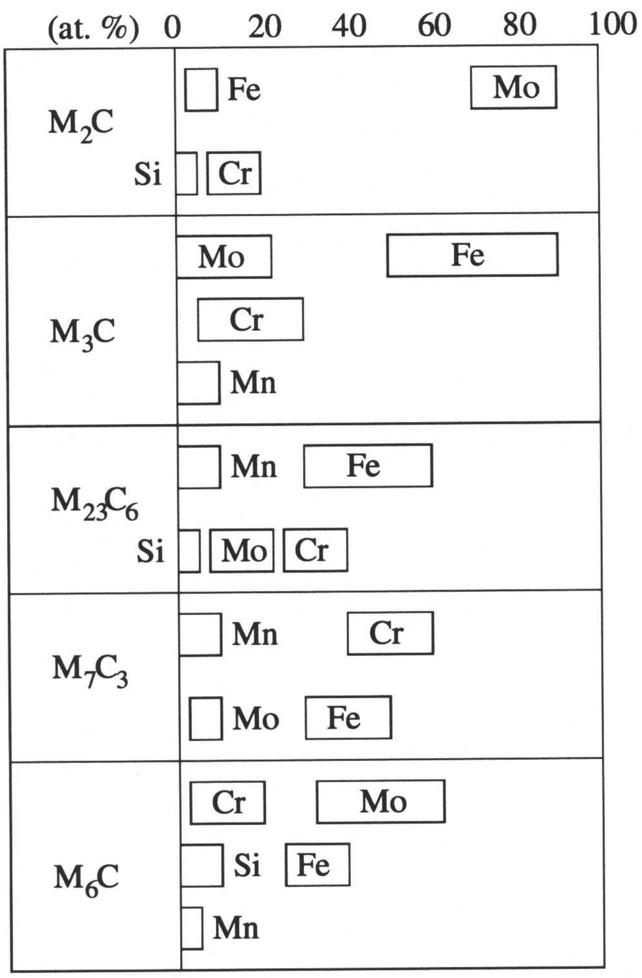

Fig. 2.11 Chemical compositions (at.%) of metallic constituent of carbides in Cr-Mo steels (Janovec *et al.*, 1994).

equilibrium phases gets formidable. Equilibrium diagrams can only give a rough guide to the structures likely to be encountered. It is possible to construct a diagram to show expected phases for a group of steels at a certain temperature. For example, Shaw and Quarrell (1957) constructed a carbide constitution diagram for a 0.2 wt% C steel at 700 °C, varying chromium and vanadium (Fig. 2.12). It is interesting to note that cementite is only stable up to 1.5 wt% chromium or 0.6 wt% vanadium.

Fortunately, the study of phase equilibria has been simplified by the recent advent of computer programs capable of estimating the equilibrium state of multi-component, multi-phase systems. In this work the National Physics Laboratory's Metallurgical and Thermodynamic Data Bank (MTDATA) has been used (Hodson, 1989). It works by combining experimental data for unary, binary and ternary systems and then uses thermodynamic theory to estimate what happens in larger systems. MTDATA calculates the compositions and volume fractions of the phases present by minimising the Gibbs free energy whilst conserving mass. The reli-

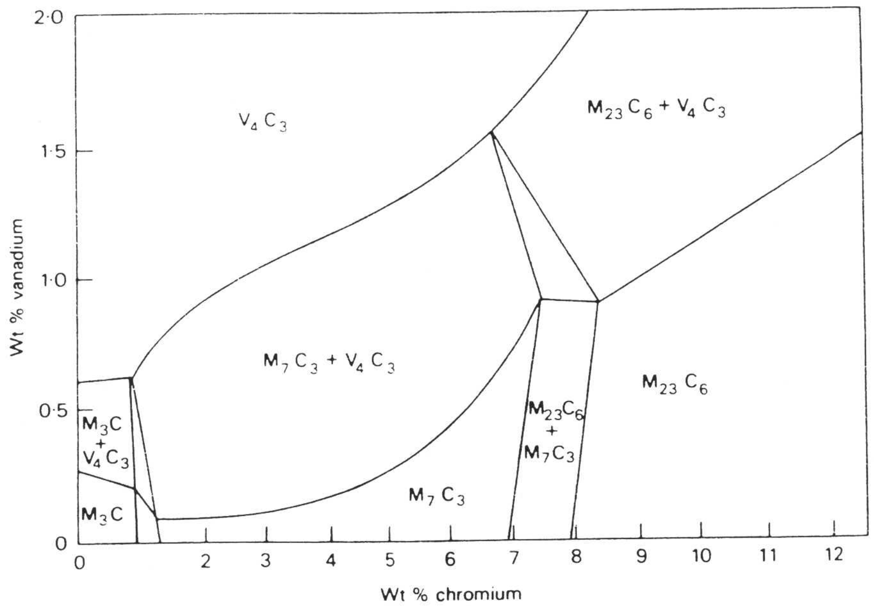

Fig. 2.12 Carbide constitution at 700 °C in a 0.20 wt% carbon chromium vanadium steel (Shaw & Quarrell, 1957).

ability of the results given is dependent on the availability of data for all sub-systems. Using this model equilibrium fractions of carbides in power plant steels can calculated, as shown in Table 2.17. MTDATA can also be used to determine the chemical composition of each of the equilibrium precipitates.

	$M_{23}C_6$	M_2X	M_6C	M_7C_3	Laves
1CrMoV	2.59	0.005	0	0	0
$2\frac{1}{4}$CrMoV	1.11	0	0.43	0	0
3.5NiCrMoV	2.12	0	0	1.52	0
9Cr1Mo	1.95	0	0	0	0
9Cr$\frac{1}{2}$MoWV	2.139	0	0	0	2.509
12CrMoVW	3.89	0	0	0	0.15

Table 2.17: Equilibrium fractions (wt%) of carbides in some common power plant steels, as calculated using MTDATA at 565 °C (838 K). Small amounts of VN and NbN are present in some of the steels but have not been shown. For example, 9Cr$\frac{1}{2}$MoWV and 12CrMoVW both contain 0.23 wt% VN. The phases allowed in the calculation are shown in Table 2.18.

Ferrite	M_2X	M_7C_3
Austenite	$M_{23}C_6$	M_6C
Cementite	M_5C_2	VN
Laves phase		

Table 2.18: Phases included in MTDATA analysis on common power plant steels.

2.3.2 Precipitation Sequences

Although the information provided by MTDATA is extremely useful, it can only tell us about the phases in the alloy at equilibrium. Since power plant steels do not reach the equilibrium state for a long time it is also useful to examine what phases are formed during the alloys service life. One method of achieving this is by determining the carbide precipitation sequence.

The order in which the precipitates are formed is controlled by the composition of the alloy and the heat treatments applied to it. A carbide stability diagram shown in Fig. 2.13 demonstrates the sequence in a $2\frac{1}{4}$Cr1Mo steel (Nutting, 1999). This is an updated version of the analysis carried out by Baker and Nutting in 1959, using improved microanalytical techniques.

This sequence can then be summarised as shown in Fig. 2.14. Precipitation sequences similar to these are observed in 9-12 wt% Cr steels. The rate of precipitation is much faster than in $2\frac{1}{4}$Cr1Mo steels due to the high concentration of carbide forming elements. M_6C is only observed if the steel is tempered at temperatures above 760 °C (Briggs & Parker, 1965) whereas at lower temperatures $M_{23}C_6$ is the main carbide observed. Often with this class of steels the vanadium and molybdenum levels are high enough to stop the formation of M_7C_3 leading to the precipitation of $M_{23}C_6$ directly after M_2X.

Variations of this sequence can also occur. If Laves phase is an equilibrium precipitate, it will form after the illustrated sequence. MX forms stable precipitates which may remain unchanged in the alloy throughout the entire sequence.

2.3.3 Effect of Alloying Elements

As we have seen, the composition of the alloy has a great bearing on the phases formed and the sequences of precipitation. It is useful to examine the effect of each of the constituents of the composition on the alloy properties.

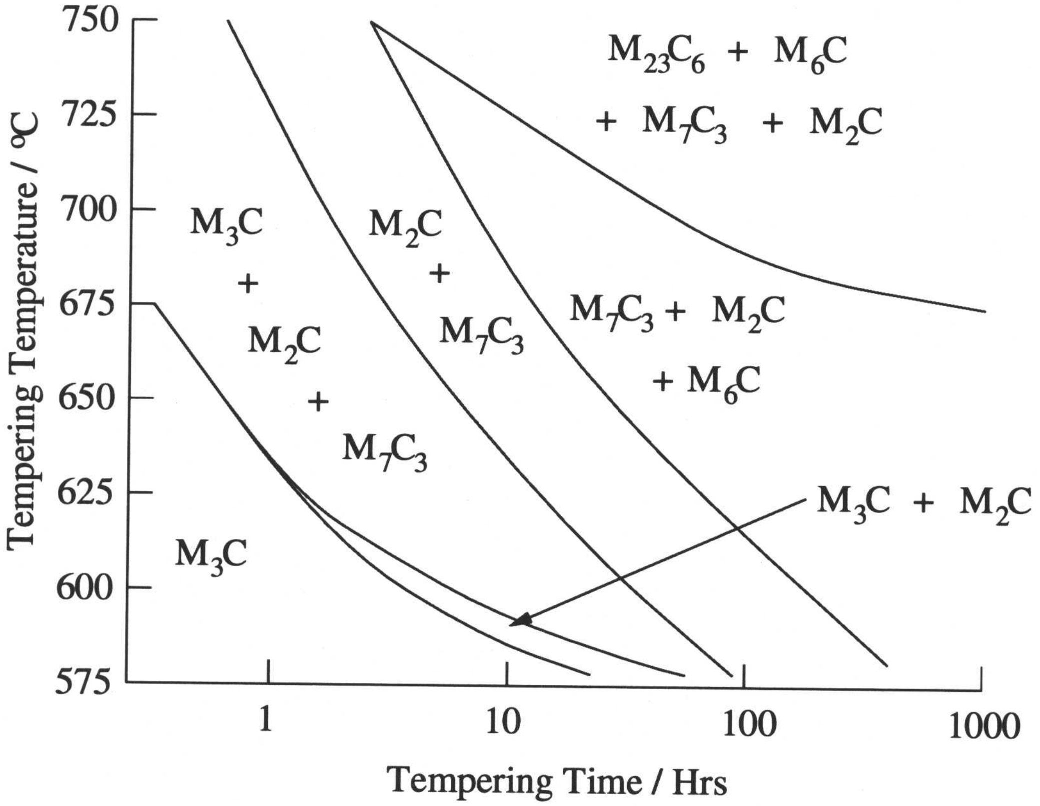

Fig. 2.13 Isothermal diagram showing the sequence of carbide formation in a $2\frac{1}{4}$Cr1Mo steel (adapted from Nutting, 1999).

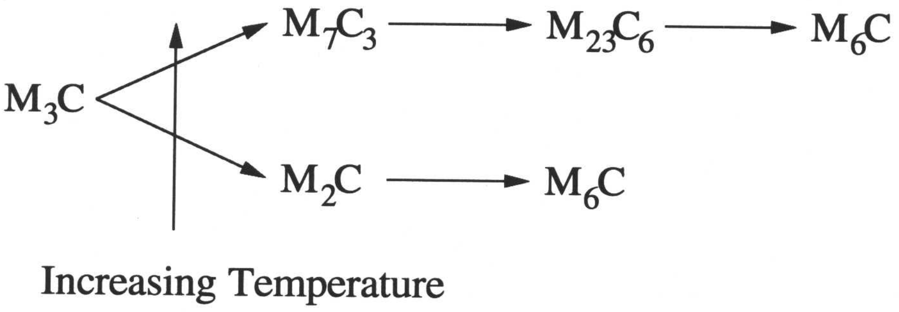

Fig. 2.14 Summary of carbide precipitation sequence (adapted from Nutting, 1999).

It is possible to consider the known effects of each single element on power plant steels even though the problem becomes extremely complicated due to element interactions. The elements used to make up the composition of these steels are added for a variety of reasons. Most are added to stabilise phases which are beneficial to creep resistance or to suppress phases which are detrimental. Some are added for long-term solid solution strengthening or to improve the resistance of the alloy to corrosion. The known characteristics of some of the elements are listed as follows:

- **Aluminium** - The addition of aluminium is thought to be detrimental to the creep rupture strength since it leads to the formation of AlN instead of VN or NbN. AlN is a coarse phase and not useful to creep strength, whilst the others are fine and dispersed and so improve creep properties.

- **Boron** - Boron additions are generally considered to be beneficial to high temperature strength. For example, the effect of boron on long-term creep rupture strength was examined by Ernst *et al.* (1986). Their results are shown in Fig. 2.15, the analysis was carried out on a steel of composition 0.15 wt% C, 10 Cr, 2 Mo, 0.25 V and 0.05 Nb. It can be seen that their is a clear improvement in creep rupture life with B additions up to approximately 0.01 wt%. There appears to be no benefit to creep rupture properties at higher boron percentages. This result is closely backed up by Hidaka *et al.* (1998), who examined the effect of boron in a 12wt% CrWCoB steel.

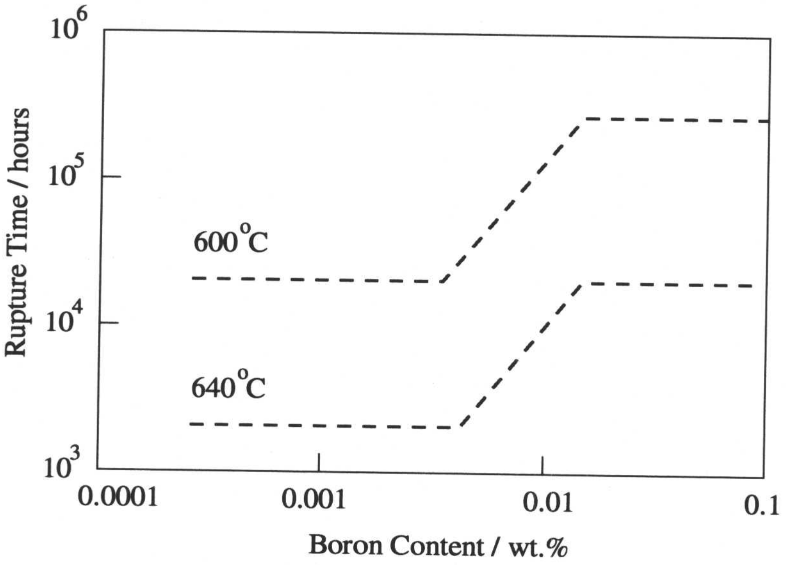

Fig. 2.15 Schematic illustration of long-term creep rupture data for 10 wt% CrMoVNb steel (adapted from Ernst *et al.*, 1986).

Many researchers have attributed this increase in creep rupture strength to boron stabilising $M_{23}C_6$ at grain boundaries, retarding the coarsening of the precipitate and preventing grain boundary sliding, and thereby dynamic recrystallization (Park & Fujita, 1982; Miyata *et al.*, 1999; Hättestrand & Andrén, 1999; Abe, 2000a). However, increased levels of boron may lead to problems with weldability and forgeability (Vanstone, 1999). Excessive levels of boron can also combine with nitrogen to form quite coarse BN precipitates. This may reduce the amount of finer nitrides in the alloy such as VN, which can have beneficial effects on creep rupture properties. BN may also degrade mechanical properties, such as ductility (Hidaka *et al.*, 1997).

- **Carbon** - Carbon occupies interstitial sites in both austenite and ferrite, with a greater solubility in austenite, which it stabilises relative to ferrite. It is essential for the formation of carbides which cause the secondary hardening of power plant steels. Irvine *et al.* (1960) found that a level of 0.15 wt% C was optimum in 12 wt% Cr steels and that greater levels of carbon may lead to unacceptable reductions in mechanical properties such as toughness. However, Fujita and Asakura (1986), examined the effect of carbon on creep rupture strength of a 9-10%Cr-2Mo-V-Nb steel. It was found that the rupture strength increases with C content for a 10 Cr steel (0.05-0.23 wt% C range tested), but there was no discernible increase with C for the 9 Cr steel (0.02-0.14 wt% C range).

  High levels of carbon may cause cracking after normalisation and also after welding.

- **Chromium** - This is a ferrite stabilising element and a carbide former. Large chromium additions of 9-12 wt% provide hardenability, good creep strength and resistance to corrosion. Levels of greater than 11 wt% chromium were found to markedly increase corrosion resistance at 650 °C (Ennis *et al.*, 1998). However, at high concentrations chromium promotes the formation of undesirable δ-ferrite. This is demonstrated in Fig. 2.16 where the time to rupture of a Cr-2W steel increases with Cr content up to 10 wt%, after which there is a decline due to δ-ferrite formation (Abe & Nakazawa, 1992).

- **Cobalt** - This element is useful as an austenite former and, unlike manganese and nickel, does not tend to coarsen the microstructure. Cobalt strengthens the martensitic matrix and enhances the stability of fine precipitates such as MX and μ-phase (Igarashi & Sawaragi, 1997). Cobalt was found to remain in solid solution in 12 % Cr steels, even with concentrations of up to 10 wt% (Irvine *et al.*, 1960). Hidaka *et al.* (1998) carried out creep tests at 650 °C on a 12 % CrWCoB steel with varying levels of cobalt (Fig. 2.17). Their results show a beneficial effect on the creep rupture strength from cobalt addition. Large additions of cobalt (up to 6 wt%) have been used in some gas turbine alloys, they have a high 10 000 hour creep rupture strength at 600 °C which then falls rapidly (Vanstone, 1999).

- **Copper** - Copper is often used as an addition to power plant steels to retard δ-ferrite formation since it stabilises the austenite phase. High copper additions, up to 2 wt%, have

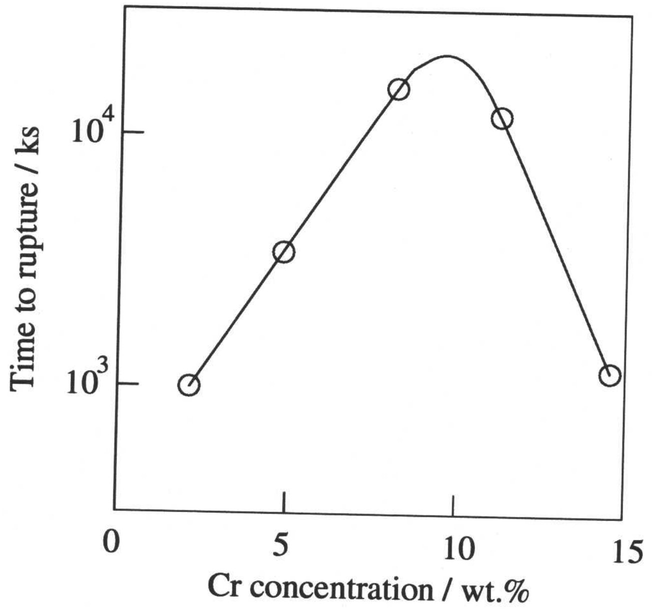

Fig. 2.16 Time to rupture of Cr-2W steels at 600 °C and under a stress of 108 MPa as a function of the Cr concentration (Abe & Nakazawa, 1992).

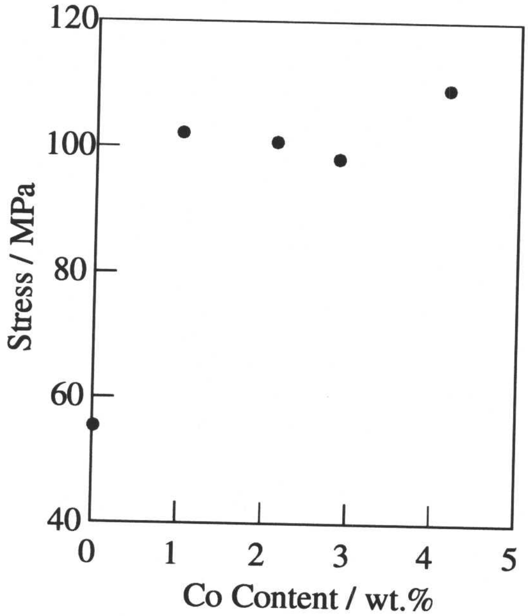

Fig. 2.17 650 °C × 10^5 hrs creep rupture strength as a function of Co content for a 12 wt% CrWCoB steel (Hidaka *et al.*, 1998).

been found to cause the precipitation of fine Cu particles on martensite lath boundaries in a 0.1C-11Cr-2W-0.4Mo-1Cu steel (Iseda *et al.*, 1992). Tsuchiyama *et al.* (2000) found that Cu additions to 9Cr martensitic steels caused Cu particles to precipitate on lath boundaries, pinning them and retarding the recovery of the martensite. It was also observed that copper additions caused refinement of the prior-austenite grain size. One concern with large copper additions is that it may precipitate and become removed from the alloy during heat treatment.

- **Manganese** - Manganese stabilises austenite but is often found to have an adverse effect on the creep strength of power plant steel. Tsuchida *et al.* (1990) examined the effect of manganese on 0.08C-9Cr-1.4Mo-0.2V-0.04Nb-0.05N (wt%) steel and confirmed the detrimental effect on creep properties. This phenomenon was attributed to the retention of austenite which will be rich in carbon and nitrogen and so reducing the effects of secondary hardening. It has also been found that increasing Mn content may increase the growth rate of M_6C, an undesirable and coarse phase which can remove W from solid solution and cause the dissolution of other more desirable precipitates (Miyata *et al.*, 1999).

- **Molybdenum** - This element forms stable carbides and also remains in ferrite, contributing to solid solution strengthening. Additions of Mo can stabilise M_2X phase and $M_{23}C_6$ phase (Baker & Nutting, 1959). Larger additions (greater than 1 wt%) have been found to promote formation of M_6C, Laves phase and δ-ferrite in 9 wt% Cr steels (Foldyna, 1991). This behaviour is very similar to that of tungsten and it is useful to examine the effect of combined additions of these two elements rather than individually. Thus Naoi *et al.* (1994) reported on the effect of W and Mo on 9Cr alloys and found that concentrations of greater than 1.8 wt% W and less than 0.5 wt% Mo improved the creep rupture strength. This is just one example of the many interactions between variables which make alloy design extremely difficult.

- **Nickel** - Nickel is an austenite stabilising element which can cause a substantial drop in creep properties of power plant alloys. This effect has been attributed to nickel accelerating the precipitation and coarsening of carbide phases such as Laves phase (Iseda *et al.*, 1992). It was found that nickel concentrations greater than 0.4 wt% in a 11Cr-2W-0.4Mo-1Cu steel deteriorated the creep strength appreciably (Fig. 2.18). The copper concentrations were also varied in this system and were found to have no effect on the creep rupture strength.

Vodárek and Strang (1998) examined the effect of Ni on the precipitation process in a 12CrMoV steel at 550 °C. Their studies confirmed that Ni additions had a detrimental effect on alloy from the point of view of creep rupture strength. It was found that Ni increased the rate of dissolution of M_2X as a consequence of precipitation of M_6X phase. Nickel was found to be a major constituent of M_6X and the rate of precipitation increased with Ni content. The coarsening of M_6X in ferritic steels is much greater than that of $M_{23}C_6$ and so can partly substitute them (Cahn *et al.*, 1994). Even though only small concentrations of Ni have been

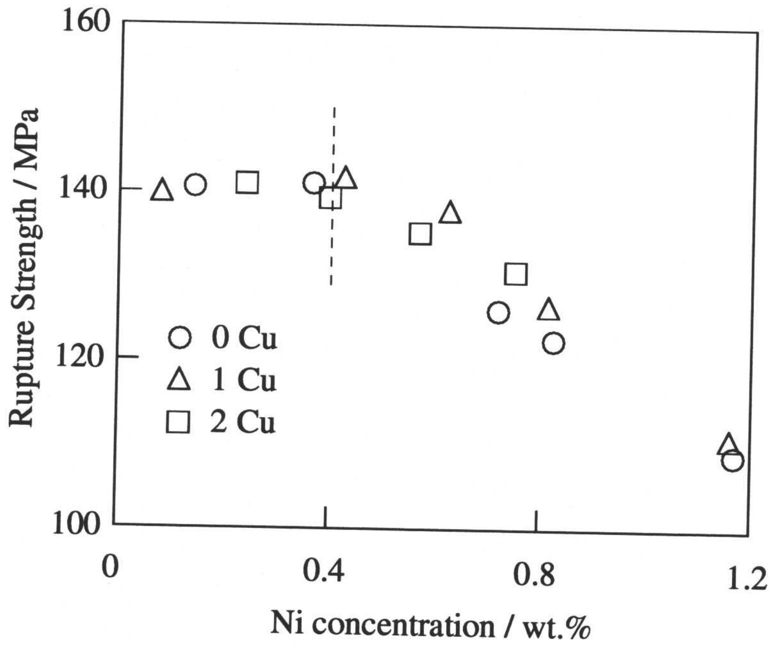

Fig. 2.18 Effects of Ni and Cu on the extrapolated 10^5 h creep rupture strength of 0.1C-11Cr-2W-0.4Mo-Cu steels at 600 °C (Iseda *et al.*, 1992).

found in $M_{23}C_6$, it has been found to increase the coarsening rate of the carbide (Vodárek & Strang, 1997).

- **Niobium** - The addition of niobium gives MX carbides and nitrides which are small and stable. These precipitates help pin grain boundaries and prevent grain growth (Fujita *et al.*, 1981). The effectiveness of this mechanism relies on dissolving Nb during austenitisation, otherwise insoluble NbC remains, causing coalescence of the precipitates, coarsening them and accelerating recovery. Increased levels of Nb may also cause the formation of undesirable Z-phase (Strang & Vodárek, 1996).

- **Nitrogen** - Nitrogen, like carbon, is small enough to occupy interstitial sites in the iron lattice and stabilises austenite relative to ferrite. It has been found to stabilise M_2X precipitate in 12Cr steels, probably of the composition Cr_2N, and this has been one of the reasons suggested why N additions may increase creep strength (Irvine *et al.*, 1960). Nitrogen additions also aid the formation of MX type precipitates, such as VN and NbN, which are fine and generally desirable for creep strength. N and Nb additions to a 12 wt% Cr steel were examined by Masuyama and Ohgami (1993), rises in creep strength were reported with increases in concentration of both elements. However, the addition of nitrogen to boron containing steels may prove problematic due to the formation of BN, which can offset the beneficial effects of both B and N. This has

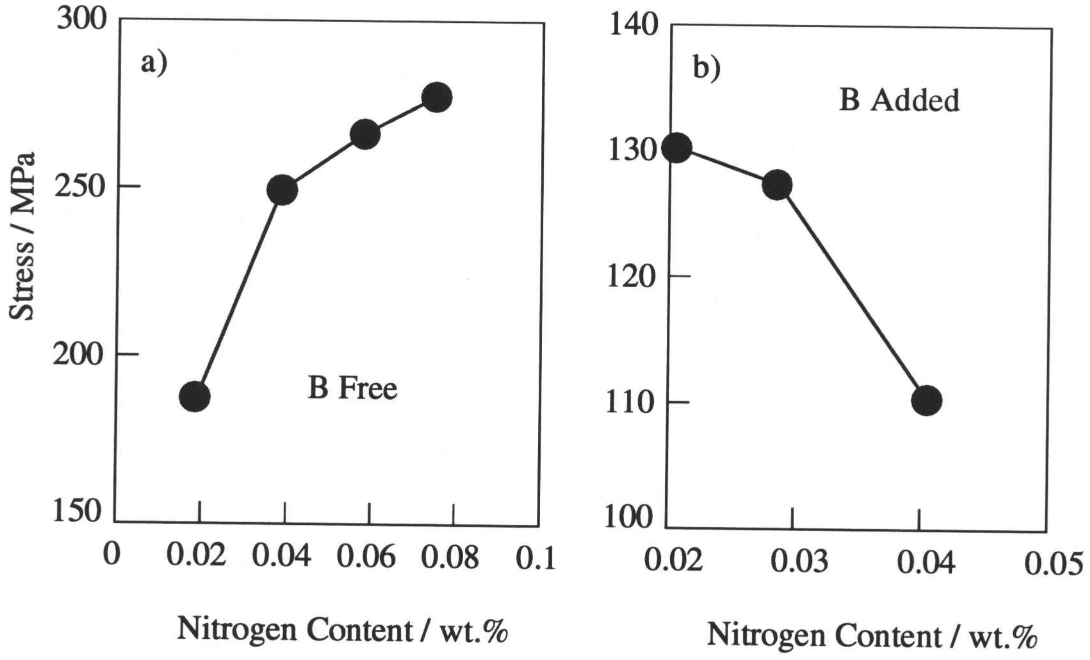

Fig. 2.19 Creep rupture strength of a 12 wt% Cr steel as a function of N content (Hidaka *et al.*, 1998). a) shows the behaviour of a steel free of boron at 550 °C. b) shows a B added, high W content 12%CrCoB steel at 650 °C.

been demonstrated by Hidaka *et al.* (1998) as shown in Fig. 2.19.

It is not easy to increase the nitrogen content of ferritic steels above approximately 0.08 wt% without pressurising the cast in a nitrogen atmosphere (Masuyama & Ohgami, 1993). This must be taken into account when designing alloys because of the cost involved with such a process.

- **Phosphorus** - Significant levels of phosphorus can lead to segregation to grain boundaries and embrittle the alloy. Pilling *et al.* (1982) showed that P increases in a 2.25 wt%Cr-1%Mo steel caused a rise in the creep rate. This was explained by a reduction in the volume fraction of M_2X precipitates. This is caused by the segregation of Mo to prior austenite grain boundaries, driven by interactions with the segregating phosphorus. Phosphorus additions to a 9Cr-1Mo steel have also been found to lead to a significant loss of ductility (Noble *et al.*, 1990).

- **Silicon** - Silicon is a ferrite stabilising element and can influence the kinetics of carbide precipitation (Woodhead & Quarrell, 1965). Silicon additions to 9Cr steels have been found to accelerate the precipitation and coarsening of Laves phase (Hosoi *et al.*, 1986; Fujitsuna *et al.*, 2000). Silicon additions can also cause problems by promoting the formation of undesirable δ-ferrite phase and austenite stabilising elements are often added purely to counteract this effect (Abe *et al.*, 1998). However, silicon can be very important in the formation of protective oxidation layers (Robertson *et al.*, 1989). These characteristics need to be balanced when designing ferritic alloys with significant silicon contents.

- **Sulphur** - Formation of sulphides, such as MnS, can provide preferential nucleation sites for cavitation. Precipitation occurs on prior austenite grain boundaries when cooling from the austenite phase (Cane & Middleton, 1981; Gooch, 1982). The cavitation is caused by the low interfacial adhesion between MnS and the ferrite matrix (Nutting, 1999).

- **Tantalum (and Neodymium)** - Igarashi and Sawaragi (1997) found additions of Ta and Nd to be beneficial to the creep rupture strength of weld joints in a 0.1C-11Cr-3W-3Co-V-Nb-N steel. This effect was attributed to the formation of TaN and NdN precipitates. These nitrides were found to be extremely stable and to not coarsen appreciably during welding and the subsequent heat treatment.

- **Titanium** - Titanium is a strong nitride and carbide former and can improve the creep rupture strength of ferritic steels. This was demonstrated by Pilling *et al.* (1983) on a 2.25Cr1Mo steel, adding titanium additions of up to 0.038 wt%. However, titanium increases may result in a large reduction in rupture ductility due to titanium based inclusions preventing deformation at grain boundaries (Fujita, 1978).

- **Tungsten** - Tungsten is a strong carbide former and also stabilises the ferrite phase. Like Mo, it stabilises M_2X but is less effective. Tungsten promotes the formation of Laves phase and much of the alloy content will go into this phase if it forms (Hald, 1995). Tungsten can also be found as a constituent of $M_{23}C_6$. High contents of W may lead to the formation of undesirable δ-ferrite.

W additions have been found to generally improve the creep rupture strength of ferritic heat-resistant steels. Ohgami *et al.* (1992) found that increasing tungsten content of a 9Cr-0.5Mo steel significantly improved creep strength. This effect was attributed to solid solution hardening and by precipitation strengthening due to $M_{23}C_6$ and Laves phase. Ishii *et al.* (1998) found that only 0.5 wt% W was required to provide the maximum solid solution strengthening effect in 12 wt% Cr steels, regardless of initial tungsten content. Formation of Laves phase and $M_{23}C_6$ at grain boundaries were attributed as the main factors maintaining creep rupture strength. A low carbon 2.25Cr alloy with a high tungsten content has recently been developed (Komai *et al.*, 1998). This alloy contains 1.6 wt% W and is reported to have excellent creep properties and weldability.

Abe (1999) reported that increased W concentrations in a 9Cr alloy reduced the coarsening rate of $M_{23}C_6$ precipitates. In turn, this reduced the coarsening of martensite laths due to the pinning effects of $M_{23}C_6$, thus delaying recovery. Abe also reported that the coarsening rate of Laves phase was very large in these alloys. Bhadeshia (2000) has shown that, contrary to experimental results, tungsten should cause an increase in the coarsening rate of $M_{23}C_6$. The problem is explained by taking account of all phases at the same time. It was found that the flux of solute from small Laves phase particles will not only go to larger ones, but also to small and large $M_{23}C_6$ particles as well. Small precipitates of $M_{23}C_6$ are then maintained for longer periods in the alloy.

- **Vanadium** - This is a strong carbide former and a ferrite stabilising element. Vanadium stabilises M_2X phase and also MX. Vanadium addition to 10-12 wt% Cr steels have been found to significantly improve the long term creep strength (Fujita & Takahashi, 1979; Fujita *et al.*, 1981). The strengthening effect of vanadium may also be enhanced by the removal of available carbon into vanadium carbides, thus leaving molybdenum in the matrix where it contributes to solid solution strengthening (Gooch, 1982).

2.3.4 Heat Treatment of Power Plant Steels

The phases formed in these alloy steels are not only dependent on the elements that make up their composition, but also on the heat treatments applied to the components before they go into service. An examination of the effect of these treatments on power plant steels is therefore useful.

Heat treatments are applied to power plant steels prior to service in order to optimise the mechanical properties of the alloy. Generally, two types of heat treatment are applied, a *normalisation* treatment and a *tempering* treatment.

Normalisation is carried out at a high temperature in order to form the austenite phase and dissolve many of the alloying elements into solid solution. The temperature has to be high enough to dissolve stable precipitates such as carbides and VN so that on cooling they can precipitate as a fine dispersion of particles. Pickering and Vassilou (1980) found that $M_{23}C_6$ precipitates were undissolved in a 9Cr-1Mo steel up to 1020 °C. Nb(C,N) precipitates were found to have not dissolved during normalisation in a 9Cr0.5Mo1.8W steel but these particles do not coarsen rapidly and remain as a fine dispersion in the matrix (Nickel *et al.*, 1995). However, if the normalisation temperature is too high, undesirable δ-ferrite phase can form. This was found to occur at 1200 °C in the 9Cr-1Mo steel examined by Pickering and Vassilou (1980). The normalisation temperature has to be carefully controlled and should vary for different alloy compositions. Barraclough and Gooch (1985) showed that a low normalisation temperature for a 12Cr-Mo-V steel resulted in a loss of creep rupture strength due to incomplete carbide dissolution.

Also important for the normalisation heat treatment is the speed at which the alloy is allowed to cool. The cooling rate will determine the phases which are formed on cooling from austenite. This can cause problems for large components, such as a turbine rotor, as the cooling rate on the surface will be greater than that at the centre of the body. This problem was examined by Norton and Strang (1969) for a rotor forging fabricated out of a 1Cr-Mo-V steel. Fig. 2.20 shows the continuous-cooling transformation diagram for this steel. It can be seen that most cooling rates produce the desired phase, in this case upper bainite. However, cooling at the rotor core is so slow that some undesirable ferrite will form. Formation of ferrite, or lower bainite if the cooling is too fast, will result in an unsatisfactory distribution of carbides, affecting creep properties. Solutions suggested include modifying the alloying content to change the hardenability or using a suitable cooling medium to minimise differences between cooling rates.

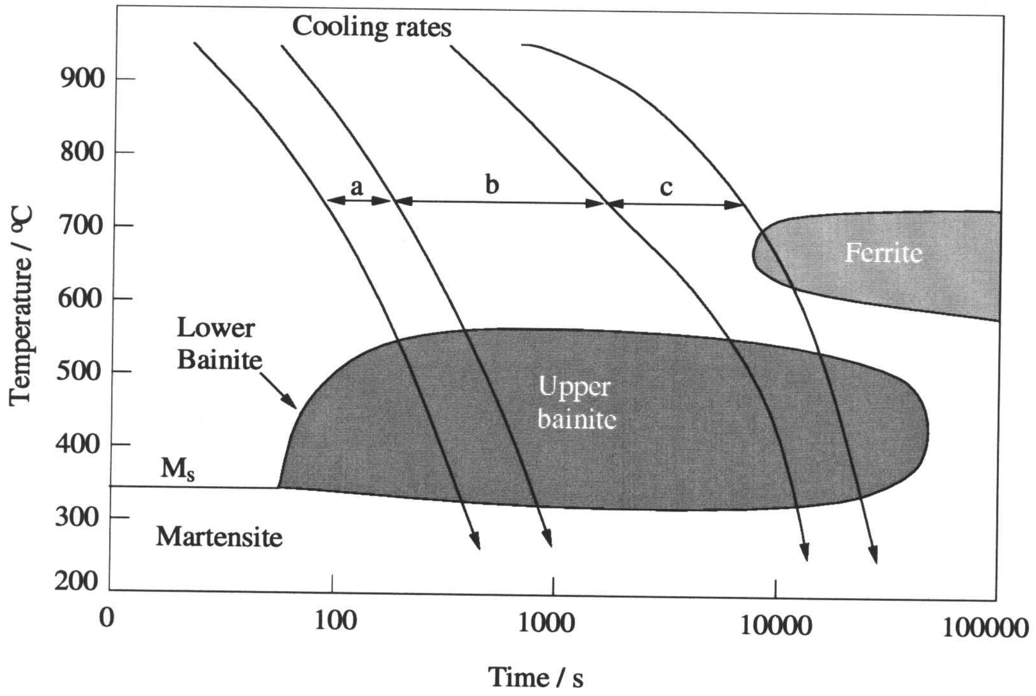

Fig. 2.20 Idealized continuous cooling diagram for 1%Cr-Mo-V rotor forgings (Norton & Strang, 1969). The range of cooling rates shown by a indicate those relating to the rim of the rotor. Range b corresponds to rates between the rim and the rotor core and c demonstrates the rates for the core.

Higher alloy content steels, such as 9-12 wt% Cr steels, tend to be martensitic on cooling rather than bainitic. This is because the larger alloy content causes an increase in the hardenability of the steel, to the point where it cannot transform to bainite. This is illustrated by the time-temperature transformation diagrams for 2.3, 4.3 and 9.3 wt% chromium steels shown in Fig. 2.21. In general, 9-12 wt% Cr steels are fully air hardenable, meaning that the microstructure formed on air cooling from normalising is completely martensitic. The cooling from normalisation is usually followed by a tempering heat treatment to obtain the required mechanical properties.

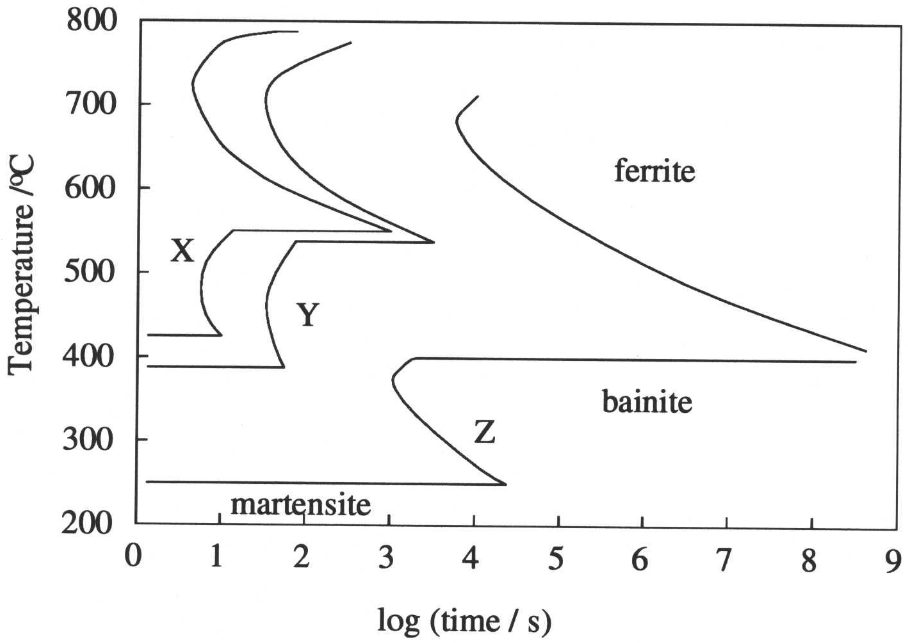

Fig. 2.21 Calculated time-temperature transformation diagrams for steels of composition X (0.15C-0.25Si-0.5Mn-1Mo-2.3Cr wt%), Y (4.3Cr) and Z(9.3Cr). The transformation curves refer to zero percent reaction. In each case the upper curve represents diffusion transformation whereas the lower curve represents bainite (adapted from Bhadeshia, 1999a).

Tempering is carried out at a lower temperature so that there is no transformation to austenite. It is applied to power plant steels to nucleate precipitates and for stress relief. The initial precipitates formed are those for which nucleation is easiest. At longer times more stable phases may form with the complimentary dissolution of the less stable carbides (Section 2.3.2). Although the nucleation of these phases is more difficult, their formation leads to a reduction in the free energy of the system and so is thermodynamically preferable.

Tempering heat treatments are carried out at a temperature in excess of 500 °C in order to allow the diffusion of substitutional atoms over the dimensions of precipitate growth in a reasonable period of time. The conditions chosen can have a clear effect on precipitate size and creep properties. Janovec *et al.* (1994) examined the effect of tempering temperature on the particle size of carbides in a 2.6Cr-0.7Mo-0.3V (wt%) steel. Fig. 2.22 clearly shows that all the particles increase in size with temperature. This growth is undesirable for creep properties since a dispersion of fine particles is desired.

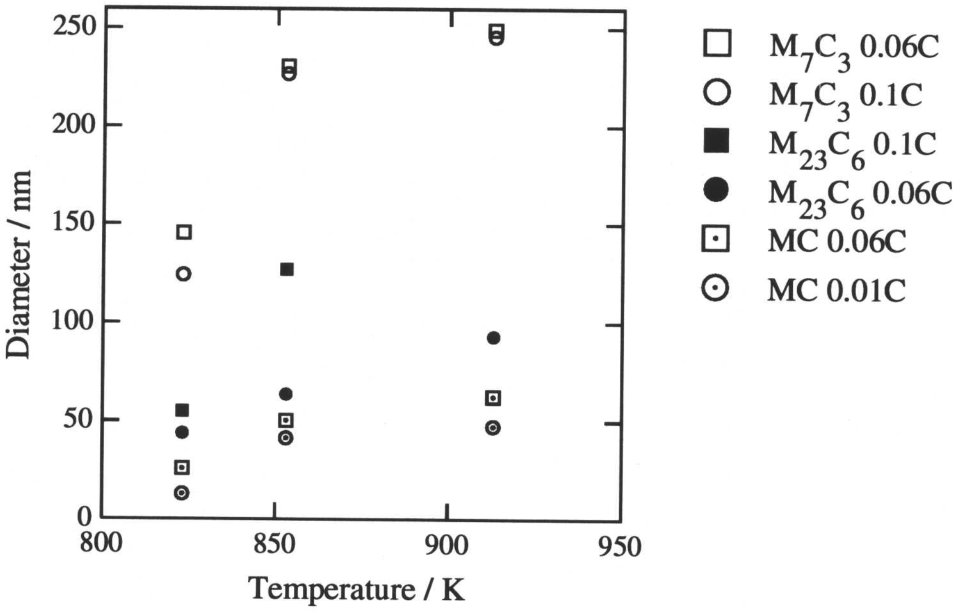

Fig. 2.22 Dependence of average sizes of carbide particles on tempering temperature and C content (wt%) (Janovec *et al.*, 1994). The steel examined was of the composition 2.6Cr-0.7Mo-0.3V and all steels were tempered for 150 hours.

Sikka *et al.* (1984) examined the effect of varying tempering temperature on the creep rupture strength of a 9Cr-1Mo alloy. It was shown that tempering above a nominal temperature of 760 °C produced insignificant effects on creep rupture strength, but tempering below this temperature significantly improved it. Iseda *et al.* (1989) also found that tempering at over 780 °C for a 9Cr-1Mo should be avoided. They found that varying the tempering temperature produced differing short-term creep properties but these became similar in the long-term.

In practice two tempering heat treatments are quite often applied to the alloys after normalisation. One reason for this could be the retention of austenite in the microstructure and this can influence dimensional stability. An initial temper of 500 °C can induce the decomposition of the austenite so machining can be carried out accurately. A higher temperature tempering treatment may then be applied as normal for stress-relief. Also, a second temper may be required as a post-weld heat treatment.

The heat treatments applied to these steels have to be carefully chosen and controlled to produce a suitable microstructure. The choice has to take into account the composition of the alloy and the phases which will be formed. Normalising at too low a temperature or tempering at a temperature too high could have a deleterious effect on the creep rupture strength.

2.3.5 Microstructural Changes during Creep Deformation

All of the variables described so far effect the microstructure of power plant steels. The microstructure is not at equilibrium at the start of service and the changes which occur through service affect the creep rupture strength. This process ultimately limits the performance of the steel. These changes, which involve the dislocation structure as well as the precipitation and dissolution of carbides and nitrides, are strongly dependent on temperature and stress.

The schematic strength of a 9Cr-1Mo steel is shown in Fig. 2.23, indicating the basic strengthening mechanisms contributing to the overall creep strength of the alloy (Orr & Woollard, 1995). Chromium provides solid solution strengthening with elements such as tungsten and molybdenum. The precipitates found to form in this system include $M_{23}C_6$, VN and NbC. The drop in the strengthening effect of precipitate hardening is due the coarsening of these precipitates.

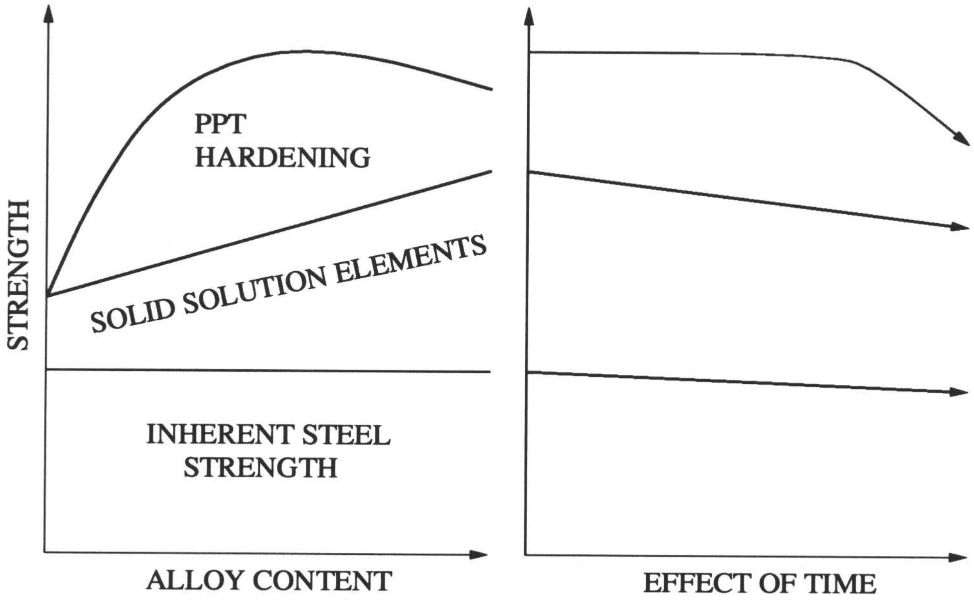

Fig. 2.23 Schematic strength of 9Cr-1Mo steels (modified from Orr & Woollard, 1995).

Work has been carried out by a number of researchers to relate microstructural properties to creep strength in 9-12 wt% Cr steels (*e.g.* Vanstone, 1994; Spiradek *et al.*, 1994; Abe, 2000a). The changes in microstructure experienced by a 10Cr-2W-0.3Mo-0.2V wt% alloy after creep testing at 600 °C and 150 MPa for 25 000 hours were examined in the Cooperation in Science and Technology programme in Europe (COST). The microstructure prior to creep was found to consist of $M_{23}C_6$ and MX. The changes in dislocation structure and particle distribution were examined.

The movement of dislocations is initially resisted by other dislocations in the matrix, due to a reasonably high dislocation density within the martensite laths. Motion is also restricted by intra-granular particles such as MX and the strain fields caused by substitutional solutes. As the microstructure undergoes creep, the dislocation structure within the laths changes with the formation of sub-grains which then grow (Fig. 2.24). This is also accompanied by a reduction in the dislocation density (Nickel *et al.*, 1995). As the sub-grains grow the creep rupture strength is reduced and becomes more dependent on resistance to sub-grain growth than movement of individual dislocations.

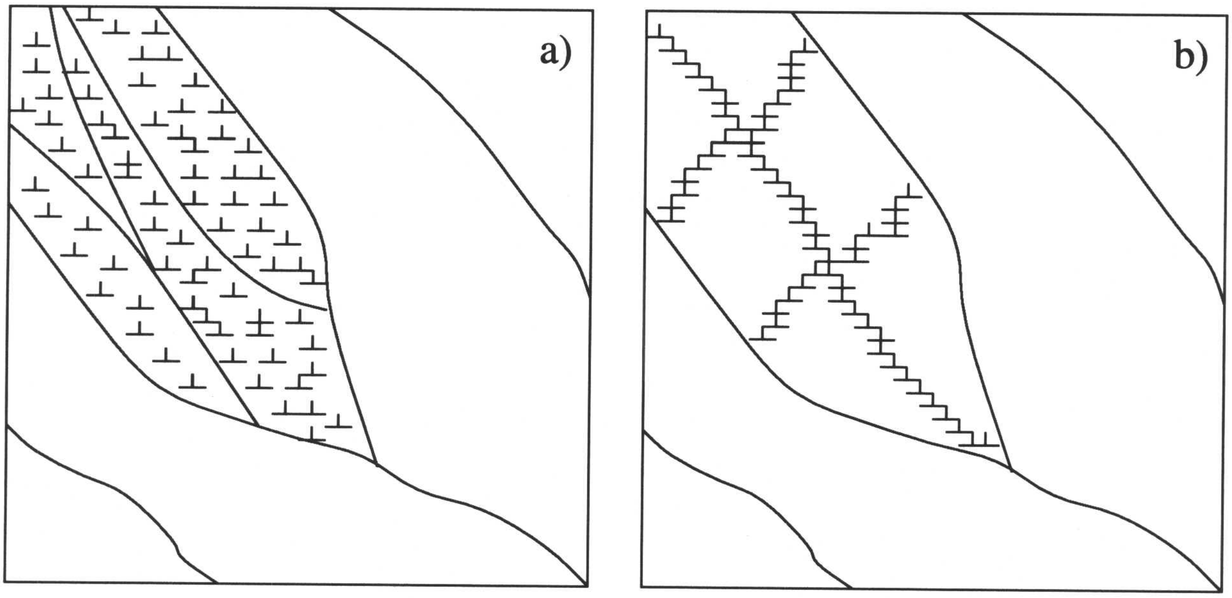

High Dislocation Density in Laths

Dislocations Form Sub-grains which grow

Fig. 2.24 Changes in dislocation distribution during creep testing of a 10Cr-2W-0.3Mo-0.2 wt%V steel at 600 °C. a) Microstructure prior to creep testing; b) after 25 000 hours at 150 MPa (adapted from Robson, 1996a).

After typical heat treatments, the microstructure of the 10Cr-2W-0.3Mo-0.2V steel consists of $M_{23}C_6$ precipitates located on lath and block boundaries and smaller precipitates, such as MX and M_2X, within the laths. M_2X was found to dissolve rapidly during creep exposure and so this phase, which plays a dominant role in the strengthening of $2\frac{1}{4}$ wt% Cr steels, is less important for the creep properties of this higher chromium alloy. As creep occurs, small $M_{23}C_6$ precipitates on lath boundaries dissolve and the larger, on block boundaries, coarsen. The MX precipitates are resistant to coarsening and remain as a fine dispersion within the laths. This process is shown schematically in Fig. 2.25. As the precipitates dissolve, coarsening of the martensite laths can occur.

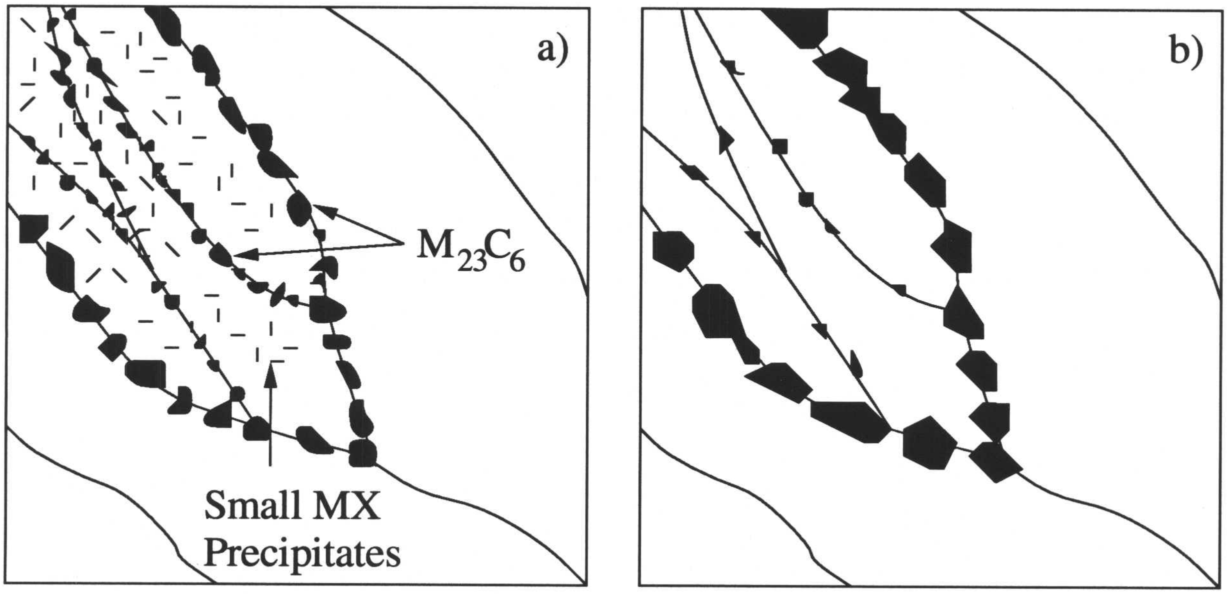

Fig. 2.25 Changes in particle size and distribution during creep testing of a 10Cr-2W-0.3Mo-0.2 wt%V steel at 600 °C. a) Microstructure prior to creep testing; b) after 25 000 hours at 150 MPa (adapted from Robson, 1996a).

Abe (1999) examined the coarsening of martensite laths in 9Cr-W steels during creep testing at 550-650 °C for up to 15 000 hours, with varying tungsten content. Before creep, the steels consisted of martensite laths of 0.3-0.5 μm in width, which grew in size during creep. $M_{23}C_6$ precipitates were also found to coarsen, growing in size from 0.07 μm after tempering to about 0.3-0.5 μm during creep. Increases in the amount of tungsten were found to reduce the coarsening of $M_{23}C_6$ and the laths and to cause the precipitation of Laves phase. The conclusion drawn is that $M_{23}C_6$ precipitates are the most effective in this system for pinning lath boundaries and reducing the coarsening rate of the laths.

Disappearance of lath boundaries was found to not be the process by which lath coarsening occurred. Instead, the sideways movement of lath boundaries and the coalescence of two boundaries resulted in the observed coarsening. The main process for this was considered to

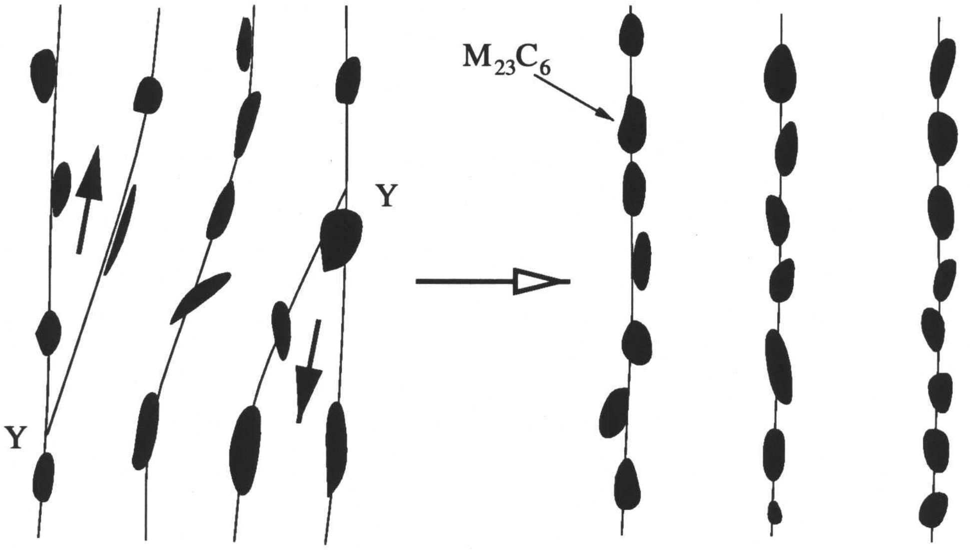

Fig. 2.26 Schematic of coarsening of martensite laths by the movement of Y-junctions (Abe, 1999).

be the movement of Y-junction or triple points of lath boundaries (Fig. 2.26).

Prior austenite grain boundaries have been recently been found to be an important factor in terms of the recovery of martensite laths (Abe, 2000a). Examination of 9Cr-1Mo steels which had been creep tested showed preferential recovery of the microstructure in the vicinity of prior austenite grain boundaries. This mechanism is caused by carbides forming and coarsening preferentially at the prior austenite grain boundaries, removing solutes and dissolving smaller precipitates in the surrounding region. This loss of pinning precipitates allows the recovery of the martensitic microstructure. This process is shown schematically in Fig. 2.27 for a 12Cr alloy (Kushima *et al.*, 2000).

These mechanisms account for the loss in long-term creep strength often experienced by 9-12 wt% Cr steels, caused by the coarsening of the microstructure. Fig. 2.28 shows this occurring after 10 000 hours for a modified 9Cr-1Mo steel at 873 and 923 K. For the improvement of long-term creep rupture strength the dissolution of small precipitates and the coarsening of large ones needs to be retarded. Recovery of the microstructure also needs to be delayed, especially in the vicinity of prior austenite grain boundaries.

2.4 Summary

Information presented in this chapter is essential knowledge when designing power plant steels. However, the large number of variables and the complicated interactions between them make such design extremely difficult without carrying out many creep tests. Unfortunately,

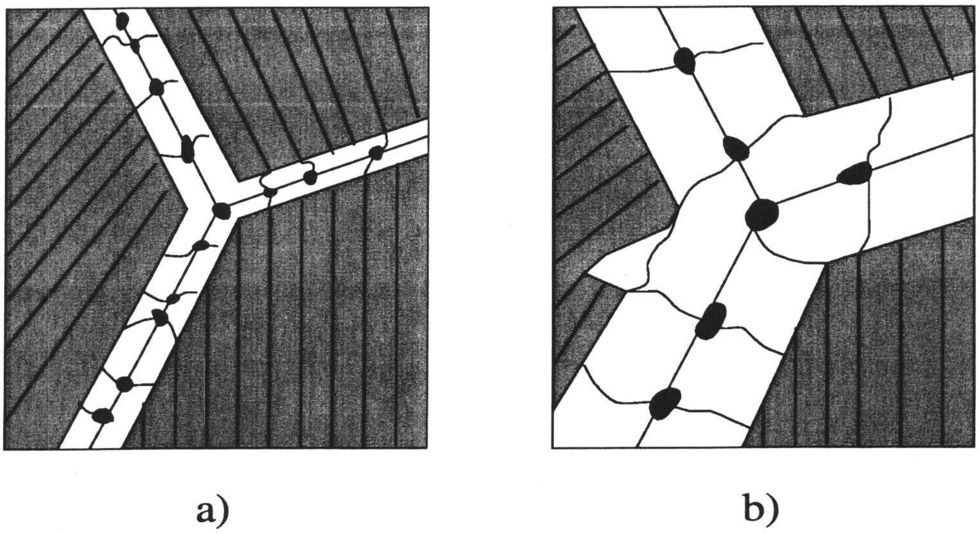

Fig. 2.27 Schematic illustration of the degradation mechanism of a 12Cr-0.4Mo-2W-Cu-V-Nb steel. a) shows the microstructure prior to creep testing and b) illustrates the microstructure after long-term creep deformation (adapted from Kushima *et al.*, 2000).

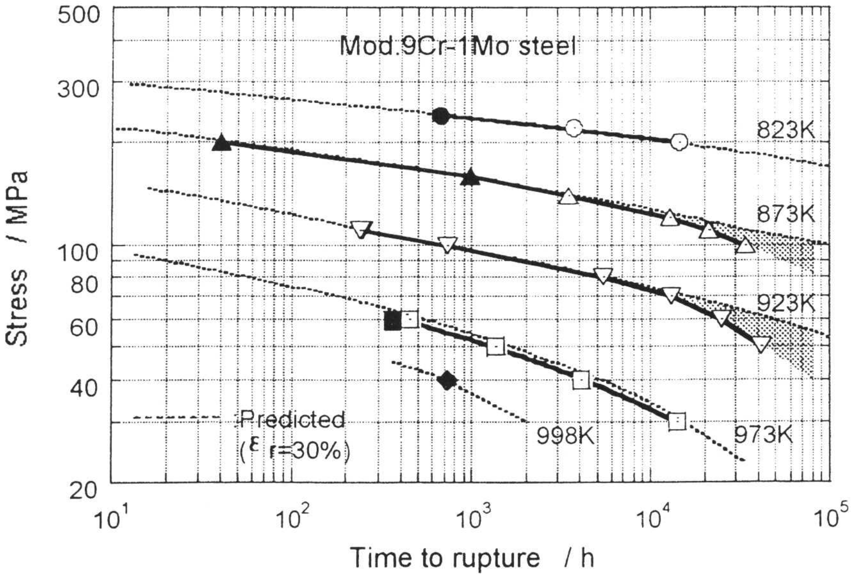

Fig. 2.28 Degradation in creep rupture strength for a modified 9Cr-1Mo steel (Abe, 2000a).

useful creep tests take a long time and are very expensive.

One way of predicting long-term creep rupture strength of power plant steels, involving variable interaction, is the use of thermodynamic, kinetic and neural network models.

CHAPTER 3

Neural Network Analysis

The difficulty in predicting the mechanical properties of a power plant steel alloy can now be seen, given the large number of interacting variables including chemical composition, heat treatments and carbide formation. Neural network models are outstanding in such circumstances, where the problem is extremely complex from a fundamental perspective and when simplification is not acceptable. A neural network is a general form of regression analysis in which a very flexible non-linear function is fitted to experimental data. This method gives considerable advantages over linear regression.

3.1 Linear Regression

In ordinary regression analysis, data are best-fitted to a specific relationship which is usually linear. The result of this process is an equation in which each of the inputs x_j is multiplied by a weight w_j. The estimate of the output is then given by the sum of the product of the weights and the inputs and the addition of a constant θ, where y is the output.

$$y = \sum_j w_j x_j + \theta \tag{3.1}$$

These weights and the bias θ are then given values in order to minimise the difference between the prediction of the model and the real data. To achieve this, an error function can be used:

$$E(w) = \sum_m [y^m(w) - t^m]^2 \tag{3.2}$$

In this equation, t^m are the target values for the analysis, *i.e.*, the real data, and $y^m(w)$ are the predicted values of the model. The lower the value of $E(w)$, the better the model is for the given data. The relationship formed tends to be linear or pseudo-linear with the addition of non-linear terms, reducing its ability to model complicated relationships. Also, once the regression relation has been derived it applies across the entire input space, which may not be reasonable.

3.2 Neural Networks

Neural networks are a general form of regression which can overcome these problems. We shall begin by examining linear regression as a network, the representation of which is illustrated in Fig. 3.1. The inputs x_j define the input nodes and each of these is multiplied by a random weight w_j. Each of these products is summed with a bias θ to give the output y. The summation process is said to be ***hidden***. As the weights and bias are randomly chosen, the output of the model will not match experimental data. Therefore, the weights and bias are systematically changed until the error is minimised. This operation is the ***training*** of the network.

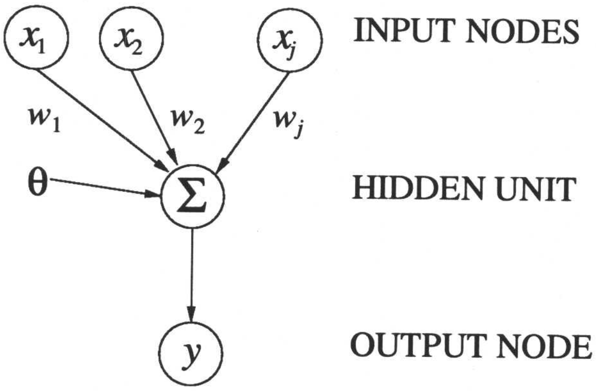

Fig. 3.1 A neural network representation of linear regression.

The network can be made non-linear by changing the mathematical operation in the hidden unit. Instead of a simple summation we shall now utilise a *hyperbolic tangent* function. The new hidden unit now contains two functions, as shown in Eqns 3.3 and 3.4.

$$y = \sum w^{(2)} h + \theta^{(2)} \tag{3.3}$$

$$h = \tanh\left(\sum_j w_j^{(1)} x_j + \theta^{(1)}\right) \tag{3.4}$$

As before, the input data x_j are multiplied by weights $w_j^{(1)}$, but now the sum of all these products form the argument of a hyperbolic tangent. The output y is the described by the function h multiplied by another weight, $w^{(2)}$, the product of which is then added to a second bias $\theta^{(2)}$. Combining these equations gives the output y as a non-linear function of $w_j^{(1)}$, because the hyperbolic tangent is non-linear. The strength of the hyperbolic tangent transfer function is determined by the set of weights $w_j^{(1)}$. Varying the weights will also change the shape of the hyperbolic tangent (Fig. 3.2a).

A further advantage of using hyperbolic tangents is that they may be combined to introduce greater degrees of non-linearity (Fig. 3.2b). This can be achieved by increasing the

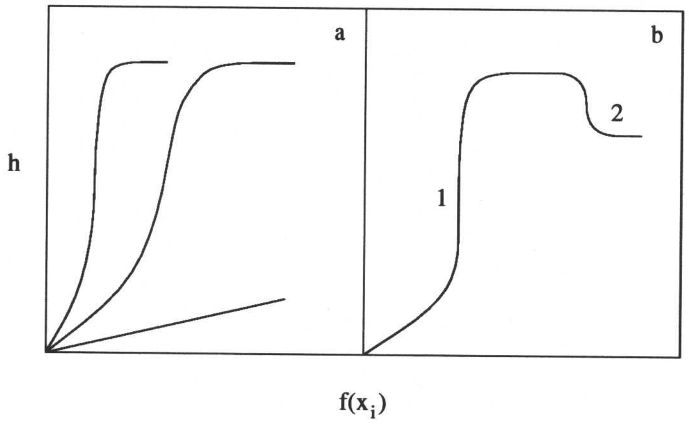

Fig. 3.2 (a) Three different single hyperbolic tangents, the shape of each is determined by the weights. (b) A combination of two hyperbolic tangents to create a more complex model.

number of hidden units in the neural network. The number of tanh functions then increases with the number of hidden units. The structure of a two hidden unit network is illustrated in Fig. 3.3. There are no theoretical limits on the number of inputs, hidden units and outputs in a model but availability of data and computing power will reduce model size along with other considerations such as overfitting, which will be examined later. This concept will allow the neural network method to capture almost arbitrarily non-linear relationships.

The equations for a multiple hidden unit network are the same as for a single unit one, but now the parameters have to be summed over all the hidden units as well as the inputs. There are j inputs in the neural network structure relating to i hidden units. As shown in Fig. 3.3 the function for a neural network is given by

$$y = \sum_i w_i^{(2)} h_i + \theta^{(2)} \tag{3.5}$$

where

$$h_i = \tanh\left(\sum_j w_{ij}^{(1)} x_j + \theta_i^{(1)}\right) \tag{3.6}$$

The weights $w_{ij}^{(1)}$ run over the links between the inputs and the hidden units and each has its own weight. There is a bias or constant, $\theta_i^{(1)}$, attached to each hidden unit h_i. All the hidden units perform the operation shown in Eqn 3.6 and then contribute to the output as shown in Eqn 3.5. The weights $w_i^{(2)}$ and bias $\theta^{(2)}$ are a second set of coefficients for the linear operation in Eqn 3.5.

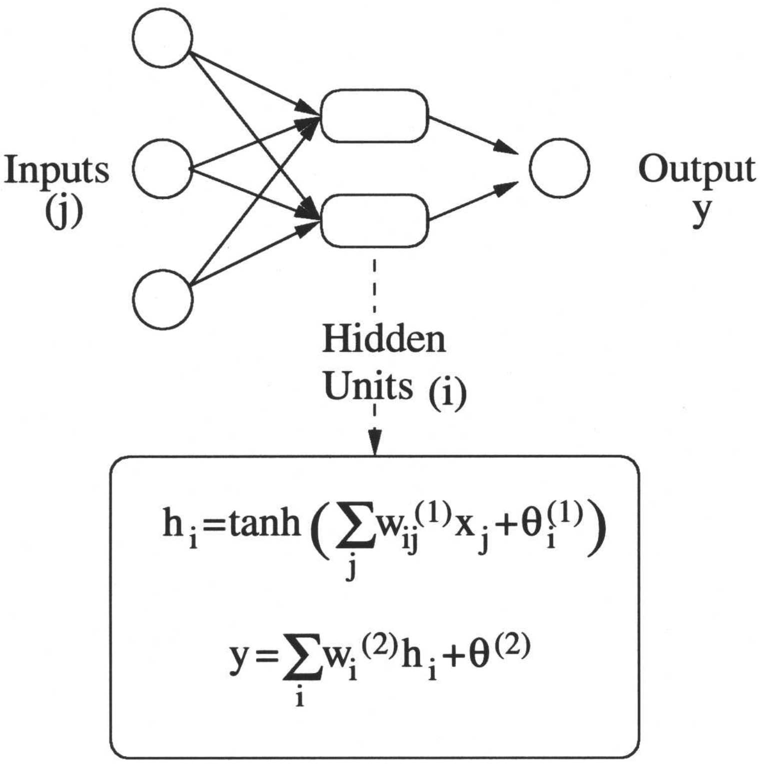

Fig. 3.3 Neural network structure, model shown has 2 hidden units.

3.2.1 Training and Complexity Control

The weights and biases are unknowns and have to be determined through *training* using a set of data. Each of the variables is first *normalised* in the range ±0.5 as follows:

$$x_N = \frac{x - x_{min}}{x_{max} - x_{min}} - 0.5 \tag{3.7}$$

In this equation x_{max} and x_{min} are the respective maximum and minimum value of x and x_N is the normalised value. This normalisation allows the comparison of the relative importance of individual inputs in the analysis.

The normalised data are then used to determine the values of the weights, w, and the biases, θ, by minimising the following function:

$$M(w) = \beta E_D + \alpha E_w \tag{3.8}$$

In this equation, E_D is the error function and E_w provides regularisation, α and β are the regularisation constants (discussed later). E_D is the sum of the squared errors:

$$E_D(w) = \frac{1}{2}\sum_m [y(x^m; w) - t^m]^2 \tag{3.9}$$

In this case, x^m represents the inputs of the database and t^m represents the targets of the database, *i.e.* the outputs. The coefficient m relates to the particular part of the dataset is being examined. The error function is reduced to minimise the difference between the output of the model and the target values. However, if this is unchecked the total error may be reduced to a point where an excessively complex model has formed. This will lead to a model which generalises badly due to the *overfitting* of the training data.

Overfitting is one of the main problems with such a powerful non-linear technique as neural network analysis. This problem is addressed in two ways, by controlling the regularisation of $M(w)$ and by randomly splitting the data available into two sets. Overfitting is illustrated in Fig. 3.4, showing three attempts to model noisy data.

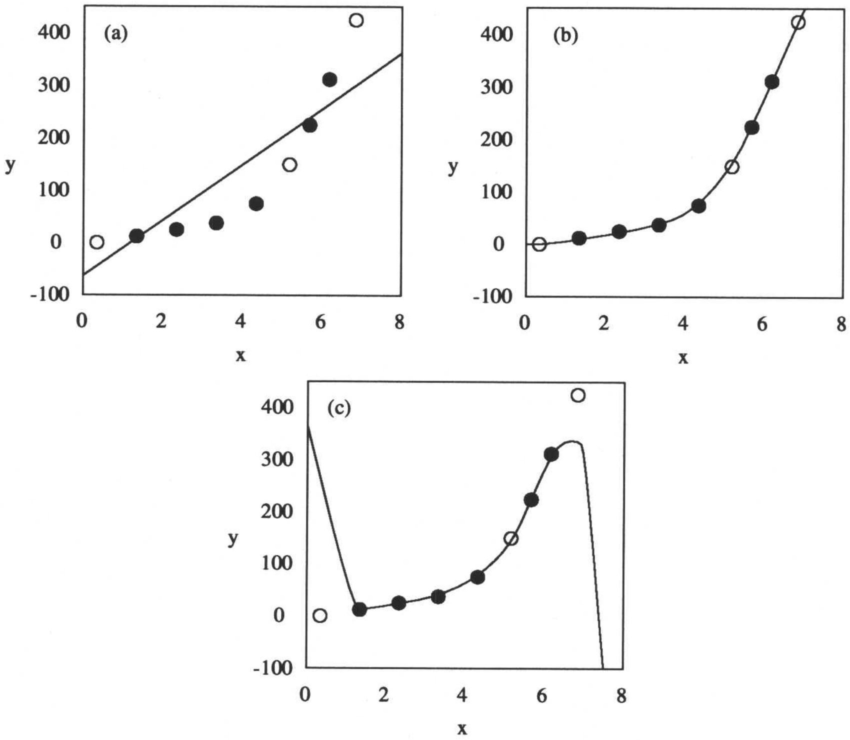

Fig. 3.4 Attempts to model y from noisy data. Filled circles represent data used to create the models and the open circles show the test data. (a) Demonstrates a linear solution which is too simple. (b) Shows a solution which fits the seen and unseen data very well. (c) Shows an over-complicated solution which fits the training data but is unable to adequately represent the unseen data (adapted from Bhadeshia, 1999b).

A linear model as shown in Fig. 3.4a is far too simple in that it does not capture the real complexity in the data. Fig. 3.4b shows the optimum model which generalises well on the unseen data and Fig. 3.4c shows a model which is too complex, fitting the training data but generalising badly. Splitting the available data into two sets allows one set to be used for training the model and one to be used in testing the model. The test data, which are unseen by the model, are used to see whether the model generalises satisfactorily.

The training and test errors are shown schematically in Fig. 3.5, compared with the increasing complexity of the model. The training error decreases as model complexity increases and it is able to fit the training data more and more accurately. However, as the complexity increases the model is less likely to be able to generalise well and so the error associated with predicting the test data reaches a minimum and then increases. The ideal model in this situation is obviously of the level of complexity found at the minimum of the test error. The complexity of the model is not only controlled by the number of hidden units, but also by E_w, α and β from Eqn 3.8.

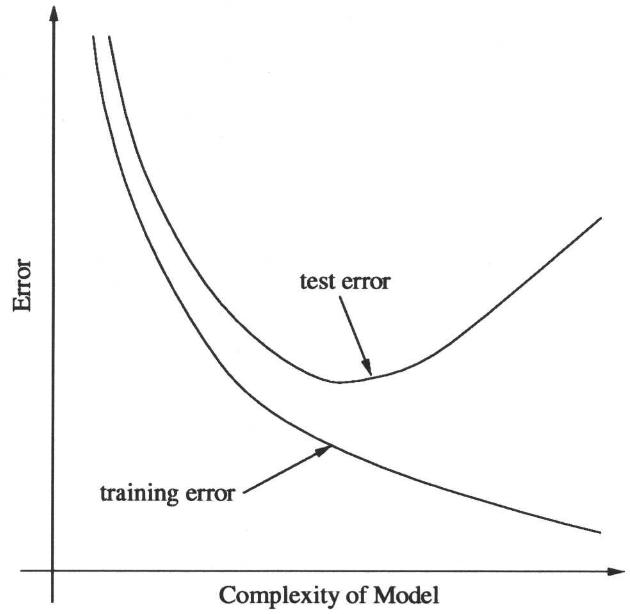

Fig. 3.5 Comparison of training and test error with increasing model complexity.

Weights in a network may have a large influence on the outcome of the model or little or no influence on the outcome. The latter may take arbitrary values and reduce the training error by modelling noise in the data. The term E_w is added to the error function in order to control the size of the weights. E_w may take the form:

$$E_w = \frac{1}{2}\sum_i {w_i}^2 \tag{3.10}$$

The minimisation of this term discourages weights from becoming excessively large and causing a model to be overcomplex. The regularisation constants α and β also control the complexity of the model. Increasing the value of α increases the influence of E_w, penalising the formation of large weights and a simple model which may not fit the data well is formed. Reducing the magnitude of α allows the model to fit the data better but if α becomes too small the model will become highly flexible and fit noise in the data. β controls the influence of the error function E_D on the model. This constant may be seen as a measure of the noise in the training data. The larger the magnitude of β the more precisely the model will fit the data. If β is too large, noise in data may be modelled.

The network size and regularisation constants are optimised to produce a model which fits the data well and is capable of good generalisation. The application of a Bayesian Framework by MacKay (1992a, 1992b, 1995) has allowed networks to be trained efficiently and successfully. This process selects the simplest model which is able to predict the data without modelling noise. In this analysis the regularisation constants are described as σ_w and σ_ν where:

$$\sigma_w = \sqrt{\frac{1}{\alpha}} \tag{3.11}$$

and

$$\sigma_\nu = \sqrt{\frac{1}{\beta}} \tag{3.12}$$

σ_w describes the distribution of the weights, larger values allowing a more complex model. σ_ν gives the noise level allowed in the model output. The influence of a particular input variable on the output of a model may vary in a many input variable problem. Inputs with only a small influence on the solution could be detrimental to the model output by taking values which reduce the test error by modelling noise. This may be particularly important if there are many input variables. To overcome this problem, a set of weights related to one input node may be assigned its own value of σ_w, with a less relevant input having a small value of σ_w. In this way the relevance of each input to the problem can be qualified.

3.2.2 Log Predictive Error

As previously shown, selection of a neural network model based on the minimum of the test error helps to avoid overfitting. Models can also be chosen based on a quantity termed the *log predictive error* (LPE). Unlike the test error, the LPE attaches less importance to points which are outliers, *i.e.*, points which are, for some reason, very badly predicted. A good example would be an erroneously reported data point. The LPE is of the form:

$$LPE = \sum_m \frac{1}{2}(t_m - y_m)^2/\sigma_y^{m2} + log(\sqrt{2\pi}\sigma_y^m) \tag{3.13}$$

where σ_y^m is an error bound calculated by MacKays treatment of neural networks, using Bayesian statistics. Therefore, the penalty from the LPE for making wild predictions is much less if that prediction is accompanied by appropriately large error bars.

3.2.3 Error Bar Analysis

MacKays treatment of neural networks in a Bayesian framework is particularly useful in that it allows the calculation of error bars representing the uncertainty in the fitting parameters. Fig. 3.6 illustrates the advantages of this method when describing uncertainties in regions of the input space which are lacking in data or where the data are scattered. In these areas the error bars are large but the fit in regions where there are plenty of accurate data remains uncompromised.

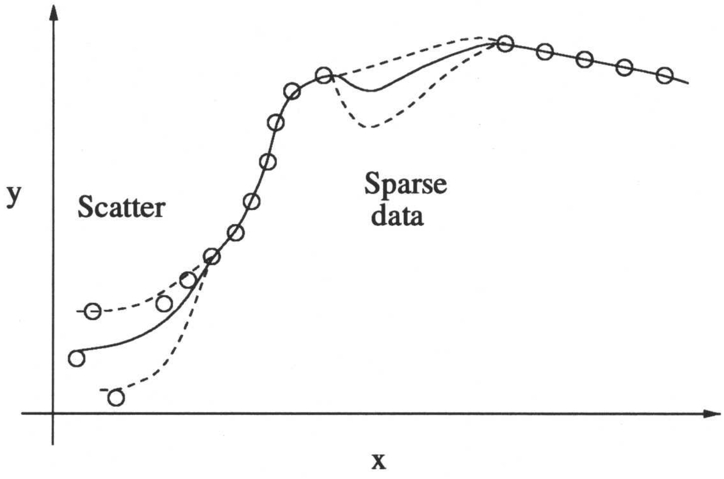

Fig. 3.6 Illustration of uncertainty of defining a relationship in areas of noisy data or where data are sparse. The dashed lines represent the error bars produced by this type of analysis.

This analysis is extremely useful since it gives the user clear warning when there are uncertainties in the predictions being made.

3.2.4 Forming a Committee

The neural network method can be further improved by combining the predictions of multiple good models instead of just using one. A collection of models whose outputs have been combined is called a *committee.* A committee of models can give more reliable predictions in regions where individual models perceive quite different relationships due to sparse or very noisy data.

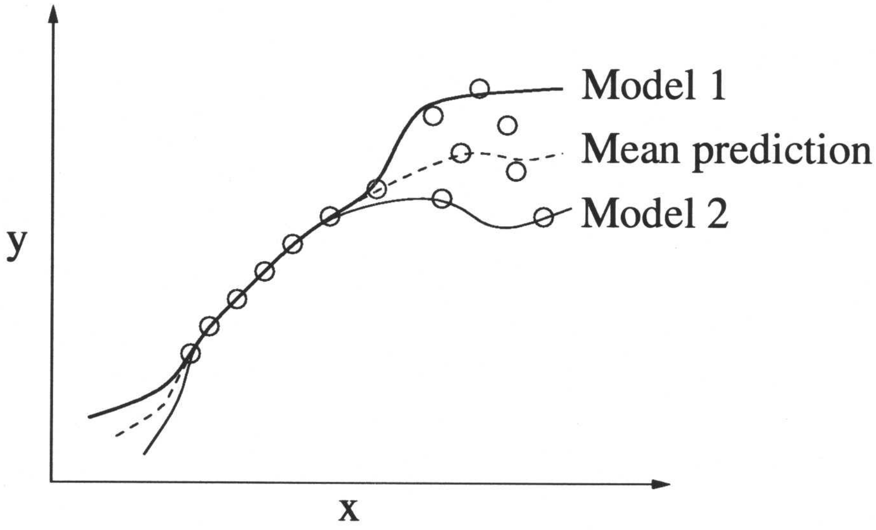

Fig. 3.7 Illustration of a committee of models compared to the predictions of single models.

This is illustrated in Fig. 3.7, showing the the mean prediction of the committee may give more reasonable results in problem data areas but where data are good, the models perform identically and so does the committee.

To create a committee, the best models are ranked according to the magnitude of the log predictive error. The committee is formed by combining the best N models (where N=1,2,3...) such that the mean prediction $\bar{y}$ of the committee is:

$$\bar{y} = \frac{1}{N}\sum_{i=1}^{N} y_i \tag{3.14}$$

The associated error σ in $\bar{y}$ is given by:

$$\sigma^2 = \frac{1}{N}\sum_{i=1}^{N}\sigma_i^2 + \frac{1}{N}\sum_{i=1}^{N}(y_i - \bar{y})^2 \tag{3.15}$$

In this case y_i is the predicted value of each model and σ_i is the error associated with the ith model. The test error of committees of increasing size are then compared to each other to determine the optimum number of models in the committee.

Finally, once the complexity of the models and the size of the committee have been chosen, the neural network can be retrained on the entire database (it having been split up for training and testing). This does not change the complexity of the network other than fine tuning the weights.

3.3 Why use a Neural Network?

It has already been mentioned that neural networks are extremely useful when the intricacy of the problem is overwhelming from a fundamental perspective and where simplification is unacceptable. In terms of the task undertaken here, to predict the creep rupture strength of heat-resisting steels, other modelling techniques have been previously applied. These methods include the Larson-Miller parameter, the Manson-Haferd model, θ-projections and various parametric techniques. Evans (1999) took a number of these models and compared their ability to extrapolate the creep rupture life of a 2.25Cr-1Mo steel with the capabilities of a neural network. It was found that the neural network was able to extrapolate well outside the range of training data, with an average extrapolation error of 6%. This compares extremely well with the average extrapolation error of 20% for Larson-Miller based techniques and 45% for certain Soviet models.

This confirms that neural network models are currently one of the best techniques for modelling complex problems, good at extrapolation and interpolation. They are of particular use in areas of materials science where adequate physical models are rare, such as mechanical properties and welding.

3.4 Summary

The central idea of the neural network method is as follows: given examples of a relationship between inputs x and a target t the neural network can 'learn' and model the relationship. A successful neural network will, for any given x, give an output y, which is close to t, the target. The neural network allows the opportunity to model complicated non-linear problems.

In this research we wish to predict the creep rupture strength of any given ferritic heat-resisting steel.

CHAPTER 4

Experimental Data on Novel Steels A and B

Brun and co-workers (1999) used a combination of thermodynamic phase stability calculations, kinetic theory and a neural network model for the creep rupture strength of ferritic steels to propose two steels which ought to have good creep resistance, even at 650 °C. This chapter begins with a presentation of their design methods (§4.1) and then with a presentation of new experimental data which are compared against the original work. The phase diagram calculations were used to ensure the alloys could be made fully austenitic over a temperature range in which they are hot-worked into the required form. The calculations also provide free energy data of use in a kinetic theory capable of estimating the evolution of the carbide and Laves phases as a function of time and temperature. It was possible therefore to postulate compositions which included tungsten but avoided Laves phase precipitation during the life time of component (>250 000 h). With these design constraints it was possible to use the neural network model not only to provide quantitative estimates of the creep rupture strength but the alloy design was conducted along pathways which minimised uncertainty.

The work led to the theoretical design of two alloys, designated A and B, the details of which were published; at the time there were no financial or time resources available to actually make and test the steels. As a result of the publication, both Nippon Steel and Mitsubishi Heavy Industries agreed to manufacture and test the steels on our behalf. the work presented in this chapter is a detailed comparison of the experimental results against original predictions, and against the new models.

The reason why two alloys were proposed by Brun *et al.* is that one of them contains cobalt, which to makes the steel difficult to recycle; cobalt-containing steels have a very low scrap value. Thus, steel B was designed to be free from this element. The proposed chemical compositions are given in Table 4.1. Other noteworthy features of the alloy design include attention to the silicon, aluminium, nickel, copper, boron and tungsten. Si, Al and Ni have been shown to have detrimental effects on the creep rupture strength and were consequently avoided. As will be seen in a later chapter, the reduction of silicon neglected its beneficial effect on the oxidation resistance of the steels. The desired concentration of copper was low since this element promotes the nucleation of Laves phase (Schwind *et al.*, 1996). The level of boron had been kept low to reduce uncertainty in the neural network predictions as creep data available on high wt% boron steels is limited. Other changes from the basic 10 CrMoW alloy examined in the published work include an increase in the tungsten content and a reduction in manganese and chromium concentrations. Alloy A differs from alloy B in that it has increased amounts of Mo and Co. This was done to determine if these changes made a useful difference to the creep rupture strength of the alloy.

Steel	A	B
C (wt%)	0.12	0.13
Si	0	0
Mn	0.48	0.5
P	0.0016	0.0016
S	0.001	0.001
Cr	9	8.7
Mo	0.75	0.30
W	3	3
Ni	0	0
Cu	0	0
V	0.21	0.21
Nb	0.01	0.01
N	0.064	0.064
Al	0	0
B	0.008	0.008
Co	1.25	0
Ta	0	0
0	0.01	0.01
Re	0	0

Table 4.1: Compositions of novel alloys A and B.

The proposed heat treatments to be applied to steels A and B are shown in Table 4.2. The normalisation temperature is relatively high to increase creep rupture strength from an increasing dissolution of precipitate phases. An increase in austenite grain size during this heat treatment may also be beneficial since creep damage can focus at prior austenite grain boundaries (Evans, 1984; Abe, 2000a).

4.1 Phase Stability and Kinetic Theory

The National Physical Laboratory's Metallurgical and Thermodynamic Data Bank (MT-DATA) was used to calculate the phase quantities for A and B (§2.3.1). The analysis showed

Steel	A	B
Normalisation		
Temperature, K	1473	1453
Duration, h	2	2
Cooling Rate	Air Cool	Air Cool
Tempering		
Temperature, K	1073	1073
Duration, h	4	4
Cooling Rate	Air Cool	Air Cool
Annealing		
Temperature, K	1013	1013
Duration, h	4	4
Cooling Rate	Air Cool	Air Cool

Table 4.2: Heat treatments of novel alloys A and B.

that there is a wide temperature range, about the proposed normalising temperature, over which austenite is the only stable phase (Fig. 4.1). This is important in order to avoid the retention of δ-ferrite during normalisation.

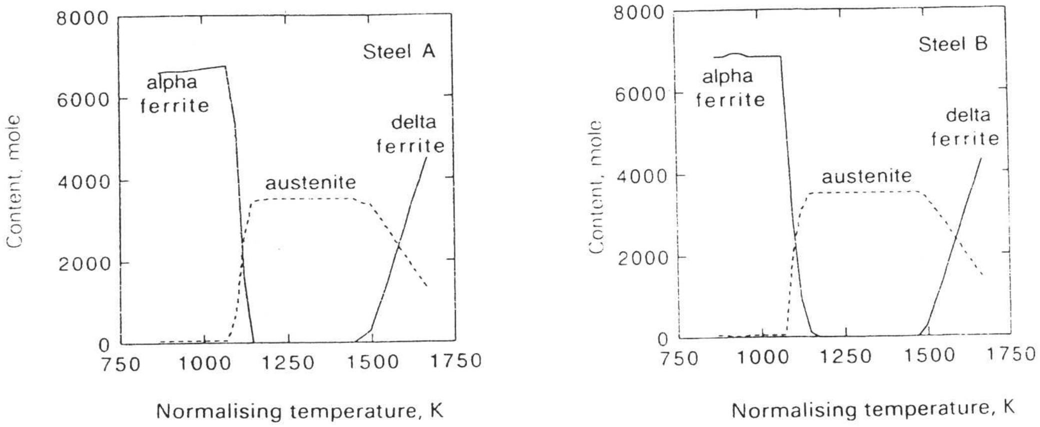

Fig. 4.1 Calculated phase quantities for steels A and B as a function of temperature (K) (Brun *et al.*, 1999). Phase quantities are moles.

MTDATA can only provide information on the phases present in the alloy at equilibrium. To assess precipitation formation during service and to check whether Laves phase will form requires kinetic calculations. There has been recent progress in calculating the precipitation reactions in power plant steels (Robson & Bhadeshia, 1996b, 1997a, 1997b). The basic theory on which the calculations are formed will be examined here.

The problem is further complicated by a number of solid-state transformations occurring concurrently from the same parent phase. These transformations may occur at different rates but the resulting competition for space can be very important to the development of the alloy microstructure. Power plant steels frequently form a variety of phases since the equilibrium precipitate is often difficult to nucleate. Consequently, decomposition starts with the formation of one or more metastable phases which are kinetically favoured. These phases will then dissolve as equilibrium is approached. The formation of the metastable phase is accompanied by a reduction in free energy causing an exaggerated retardation of the stable phase.

A model for a single transformation calculates the nucleation and growth rates using classical theory. However, an estimation of the volume fraction requires impingement between particles to be taken into account. This can be done using the extended volume concept as illustrated in Fig. 4.2 (Kolmogorov, 1937; Avrami, 1939; Johnson & Mehl, 1939). Consider two particles which exist at a time t in the parent phase. A small interval δt later, new regions a, b, c and d are formed assuming that they are able to grow unrestricted in space, regardless of whether the region has already been transformed or not. However, only those components of a, b, c and d which lie in the untransformed matrix can contribute to a change in the real volume of the product phase (the subscript '1' identifies the product phase):

$$dV_1 = (1 - \frac{V_1}{V})dV_1{}^e \tag{4.1}$$

where it is assumed that the microstructure develops randomly. V is the total volume, V_1 is the volume of 1 and the superscript e refers to the extended volume. Multiplying the change in extended volume by the probability of finding untransformed regions has the effect of excluding regions like b, which cannot affect the real change in the volume of the product. For a random distribution of precipitated particles Eqn 4.1 can be integrated to obtain the real volume fraction:

$$\frac{V_1}{V} = 1 - \exp\left\{-\frac{V_1{}^e}{V}\right\} \tag{4.2}$$

These equations can be modified for two precipitates, 1 and 2:

$$dV_1 = (1 - \frac{V_1 + V_2}{V})dV_1{}^e \qquad \text{and} \qquad dV_2 = (1 - \frac{V_1 + V_2}{V})dV_2{}^e \tag{4.3}$$

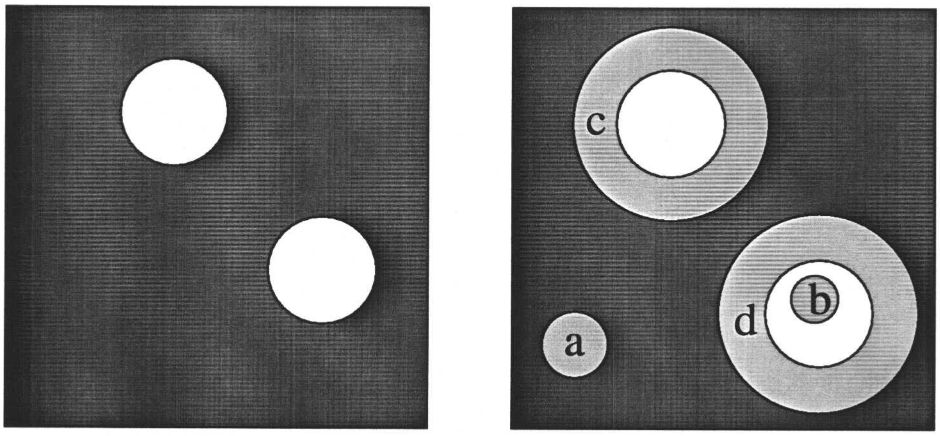

time = t   time = t + Δt

Fig. 4.2 Illustration of the concept of extended volume. Two precipitate particles have nucleated and grown to a finite size in time *t*. New regions *c* and *d* are formed as the original precipitates grow, but *a* and *b* are new particles, of which *b* has formed in a region which is already transformed.

This method can then be used for any number of precipitation reactions occurring together (Robson & Bhadeshia, 1997a, 1997b). In the case of power plant steels the calculations must allow for the simultaneous precipitation of M_2X, $M_{23}C_6$, M_7C_3, M_6C and Laves phase. These phases will interfere with each other by reducing the volume of the matrix available for transformation and also removing solute from the matrix, hence changing its composition. M_3C is assumed to nucleate instantly with the paraequilibrium composition. Subsequent enrichment of M_3C as it approaches equilibrium is accounted for. All the other phases are assumed to form with compositions close to equilibrium. The compositions and the driving forces of the precipitating phases are calculated using MTDATA.

Plots showing the predicted variation of volume fraction of each precipitate as a function of time at 650 °C for steels A and B are shown in Fig. 4.3 (Brun *et al.*, 1999). Steels A and B were not found to exhibit Laves phase formation. This was attributed to the formation of a large fraction of M_2X precipitates which reduced the driving force available for the subsequent formation of Laves phase. $M_{23}C_6$ precipitates rapidly since there is a considerable excess of solute in the matrix due to the high alloying content of chromium and other elements.

4.2 Experimental Results

The steels were manufactured and then creep-tested by Nippon Steel and Mitsubishi Heavy Industries (MHI) in Japan. The actual compositions of the alloys produced were determined by Nippon Steel and MHI and are recorded in Table 4.3. It can be seen that the actual alloy

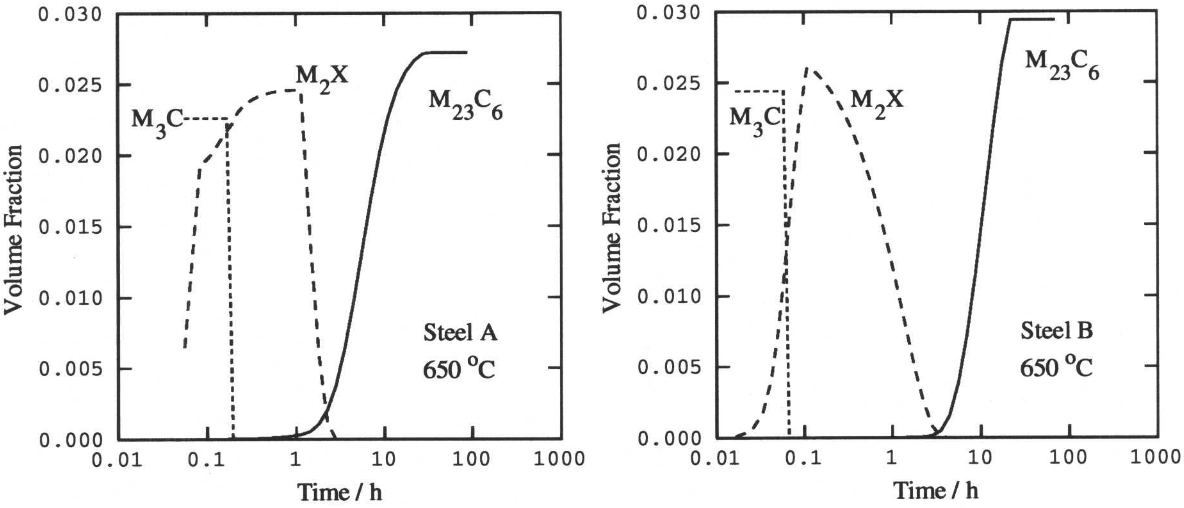

Fig. 4.3 Calculated variation in fraction of precipitates as a function of time at 650 °C for steels A and B (Brun *et al.*, 1999).

composition compares very well with the desired composition reported previously (Brun *et al.*, 1999). The results of the Charpy tests and tensile tests carried out by Nippon Steel are shown in Table 4.4.

The Charpy tests were carried out at 0, 20 and -20 °C and the absorbed energy and crystallinity of the specimens were measured. The absorbed energy of steel B was consistently greater than that of a steel A at the three temperatures. This is naturally reflected in the assessed "crystallinity" of the fracture surface, a measure of the brittleness. Charpy test results for the steel P91 (T91) are from Brühl *et al.* (1989). The average impact energy for P91 at 0 °C was 205 J, which is somewhat higher than the values reported for steels A and B although the toughness levels obtained are more than acceptable. However, the mechanical properties of these alloys vary with the heat treatments applied and during service the material characteristics tend to even out. The main concern is that brittle fracture is unlikely during service and when turning the turbine on and off. The 0.2 % proof stress and tensile stress for P91 at 600 °C are reported as 312 and 410 MPa respectively. The test results for A and B compare well with these data.

4.3 Neural Network Predictions and Creep Test Results

The neural network model created by Brun was trained on a database containing 2066 lines of data, containing information on composition, heat treatment and test conditions. Most steels in the database were of the composition 2.25Cr-1Mo and 9-12Cr. The results of the predictions for steels A and B are shown in Fig. 4.4 (Brun *et al.*, 1999).

Steel	A(Nippon)	B(Nippon)	A(MHI)	B(MHI)
C (wt%)	0.116	0.127	0.11	0.13
Si	0.014	0.012	<0.01	<0.01
Mn	0.47	0.48	0.49	0.50
P	0.004	0.003	0.003	0.002
S	0.0005	0.0005	0.001	0.001
Cr	8.96	8.66	9.04	8.75
Mo	0.71	0.30	0.74	0.30
W	3.01	2.96	2.99	2.99
Ni	0.02	<0.01	0.01	<0.01
Cu	0.004	0.003	<0.01	<0.01
V	0.22	0.21	0.20	0.20
Nb	0.013	0.015	0.011	0.011
N	0.0682	0.0705	0.064	0.068
Al	<0.002	<0.002	0.004	0.003
B	0.007	0.0064	0.0070	0.0078
Co	1.23	0.003	1.25	<0.01
Ta	<0.001	<0.001	<0.001	<0.001
0	0.0103	0.0089	0.003	0.002

Table 4.3: Actual compositions of novel alloys A and B, manufactured by Nippon Steel and Mitsubishi Heavy Industries (MHI).

At the beginning of the research reported here a new neural network was created. The database was increased to 2250 lines of data and the complexity of the model was different after training. The data added consisted predominantly of alloys of 9Cr composition. The results of this model produced predictions significantly lower than that of Brun's model (Fig. 4.5).

The predictions were made before the creep test results were available. The results could only validate one of the models or prove them both wrong and so were extremely important in showing the quality of the models. The creep data from Nippon Steel are shown in Table 4.5.

Plotting the test results against the neural network predictions showed excellent agreement with the neural network based on 2250 lines of data. The results of the tests carried out on steel A are shown in Fig. 4.6. Predictions made by Brun are higher than the actual creep data.

This trend is repeated when the results of the creep tests on steel B are examined (Fig. 4.7). Once again, the predictions of Brun's model are higher than the actual results, which are

Steel A		
Temp./ (°C)	Absorbed energy/ (J)	Crystallinity/ (%)
0	107.6	49
0	87.1	58
0	70.2	60
20	105.1	41
20	164.6	22
20	157.9	21
-20	27.9	74
-20	46.5	67
-20	42.7	71
Steel B		
Temp./ (°C)	Absorbed energy/ (J)	Crystallinity/ (%)
0	166.5	15
0	173.9	12
0	141.7	21
20	172.0	14
20	189.5	0
20	194.2	0
-20	97.1	36
-20	160.1	26
-20	159.6	25

Steel	Temperature / (°C)	0.2%PS / (MPa)	TS / (MPa)	El / (%)	RA / (%)
A	Room Temp.	424	638	33.0	69.0
A		427	641	33.3	69.4
B		429	641	31.5	69.6
B		438	648	31.3	69.1
A	600	309	356	30.1	85.5
A		309	357	31.6	83.4
B		311	354	28.2	86.1
B		306	350	31.7	85.7
A	650	237	292	32.4	89.2
A		233	293	41.2	92.4
B		238	295	37.9	93.0
B		235	293	36.1	90.4

Table 4.4 Charpy and tensile test results for steels A and B.

modelled well by the later network. This is an excellent demonstration of the importance of data in the production of a neural network. A neural network relies on knowledge and

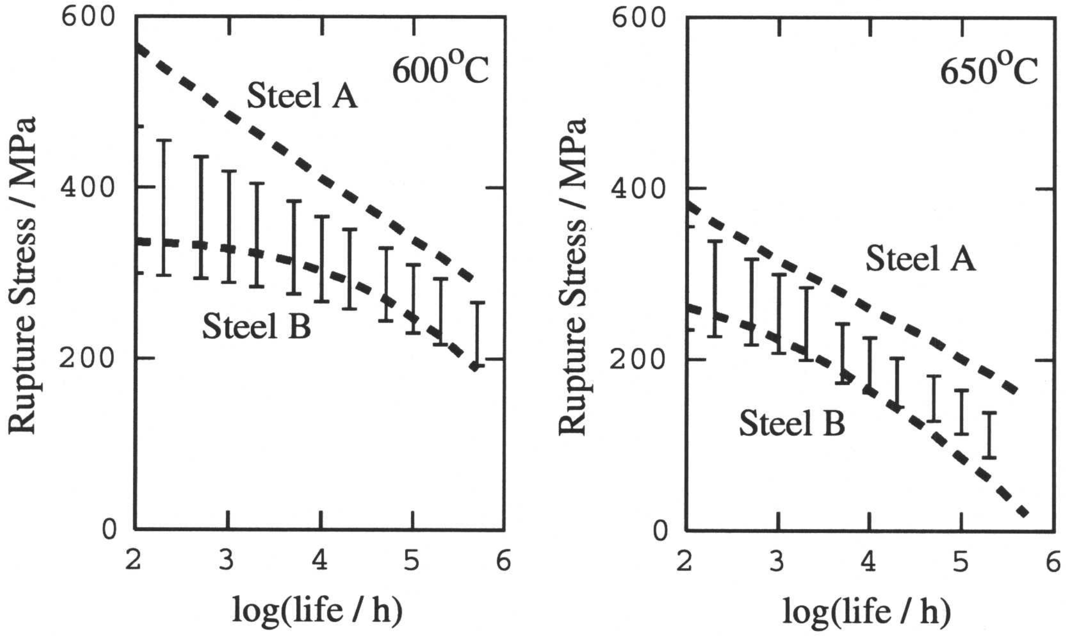

Fig. 4.4 Calculated creep rupture strength as a function of time at 600 and 650 °C for steels A and B using neural network based on 2066 lines. Only the error bounds are shown for each prediction (Brun *et al.*, 1999).

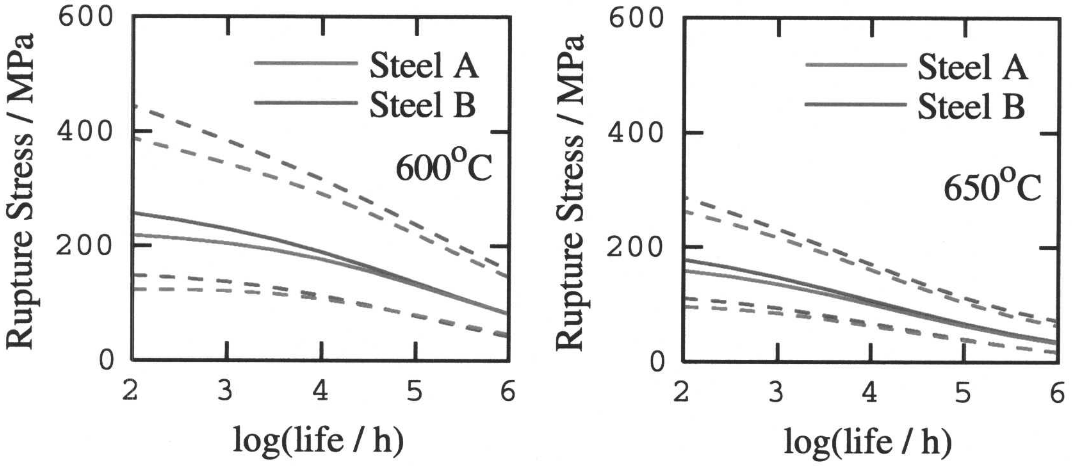

Fig. 4.5 Calculated creep rupture strength as a function of time at 600 and 650 °C for steels A and B using neural network based on 2250 lines. The error bounds are represented by dashed lines and the solid line indicates the mean prediction.

hence improves as the dataset becomes large and better distributed over the input space. The complexity of the model, *i.e.* the number of hidden units, values of the regularisation constants *etc.*, also affect the model behaviour. It is also interesting to note that the error bounds associated with the predictions are large since these are novel alloys which are not

Steel	Test Temperature (°C)	Stress (MPa)	Rupture Time (h)	El (%)	RA (%)
A	600	331.17	0.1	27.6	80.7
		322.96	0.0	217.7	76.4
		302.08	0.3	32.2	82.4
		290.07	0.1	29.8	83.2
		252.57	4.8	34.1	82.6
		202.05	187.2	38.5	84.6
	650	232.36	0.4	38.9	84.2
		202.05	1.8	38.9	84.6
		120.04	2015.1	22.5	76.6
B	600	350.06	0.0	24.4	82.8
		332.28	0.2	20.1	79.0
		303.09	0.4	31.3	83.3
		290.04	0.8	34.3	81.6
		252.57	4.8	34.1	82.6
		201.38	231.4	34.1	84.6
	650	232.36	0.6	32.1	80.9
		201.38	3.4	36.4	83.8
		120.05	2058.1	46.2	68.8

Table 4.5: Creep test results for steels A and B (Nippon Steel).

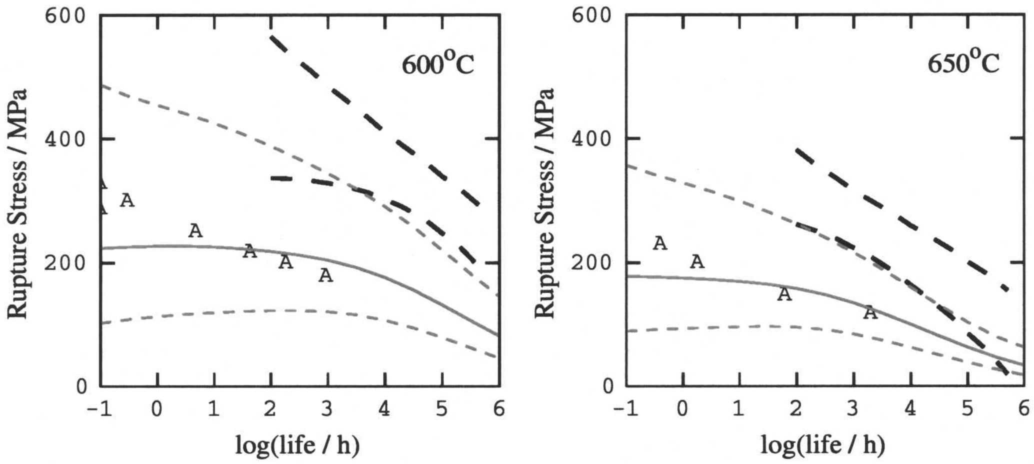

Fig. 4.6 Comparison of neural network predictions with creep test data for steel A (Nippon Steel). The monochrome error bars represent the predictions made by Brun *et al.* (1999). The red results show the predictions made by the later network based on 2250 lines.

represented in the database.

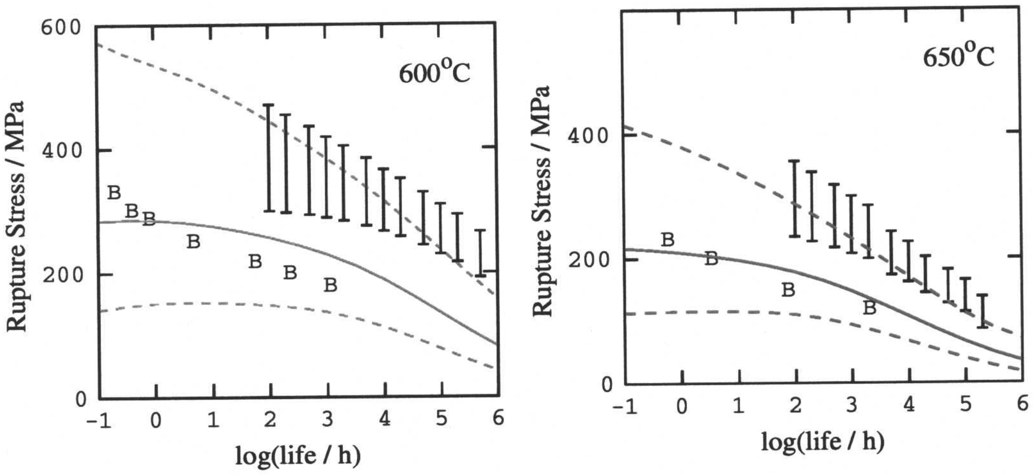

Fig. 4.7 Comparison of neural network predictions with creep test data for steel B (Nippon Steel). The monochrome error bars represent the predictions made by Brun *et al.* (1999). The green results show the predictions made by the later network based on 2250 lines.

An indication of the problems with the Brun model predictions is given by the rupture strength given at short times. These could be approximated to the hot tensile strength of the alloy and are extremely high. However, even though the alloys failed to meet Bruns expectations, their creep rupture strength is still quite high. They compare very well to the creep rupture strength of NF616, the current leader in creep-resistant ferritic steels. A best fit line was created using a large amount of data reported by Buchanan *et al.* (1992) and the creep test results were compared to this line (Fig. 4.8). It is also interesting to note the creep rupture strength of A and B is greater than E911, an alloy which emerged from a huge European effort to design an alloy which beats the NF616 patent whilst enhancing NF616 properties. The compositions of A and B are radically different from NF616.

4.4 Further Predictions

This model was used to predict the creep rupture strength of the steels A and B manufactured by Mitsubishi Heavy Industries (MHI). A 10 CrMoW steel (N) was also manufactured and tested by MHI. The creep test results for steel N are recorded in Table 4.6 and the results for A and B are in Table 4.7. Some more tests are still running so creep times greater than 5000 hours will be available for comparison. The results of the analysis are shown in Fig. 4.9 and again show good agreement. Some of the short term data is of a rupture strength much higher than the prediction but these do lie within the error bounds. These creep data and those produced by Nippon Steel will be compared again with the predictions of an improved neural network in §5.7.

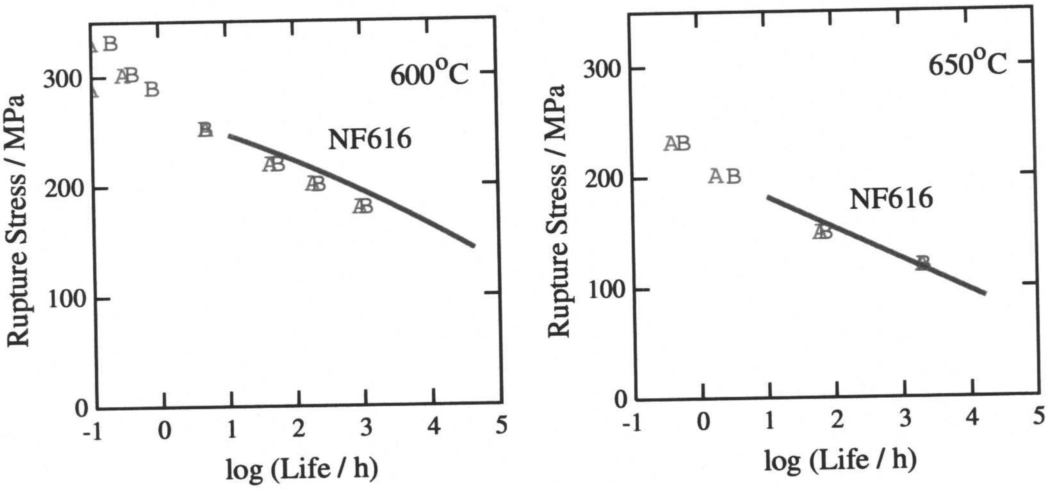

Fig. 4.8 Comparison of creep test results of A and B with a best fit line of creep results of alloy NF616.

Steel	Test Temperature (°C)	Stress (MPa)	Rupture Time (h)	El (%)	RA (%)
N	600	310	0.2	36.9	79.6
		260	2.0	38.2	81.0
		230	9.5	41.5	82.0
		190	177.4	33.2	80.8
		171	1030.8	41.5	81.0
		155	5635.7	22.4	43.2
N	650	205	0.6	58.9	87.8
		165	6.3	36.9	85.6
		140	74.6	46.3	84.4
		120	629.2	38.4	70.8
		100	3401.1	25.9	47.1
N	700	125	1.2	56.2	88.7
		105	5.4	49.6	89.8
		80	47.6	46.7	87.0
		70	163.2	43.4	82.5
		60	665.3	44.2	73.1

Table 4.6: Creep test results for steel N (Mitsubishi Heavy Industries).

4.5 Summary

This work showed that it was possible to design, at the first attempt and without doing any experiments, alloys with excellent properties. The capabilities of the neural network technique were also demonstrated, successfully predictiong the creep rupture strength of novel alloys.

Unfortunately, the design of a good alloy for high temperature service requires more than

Steel	Test Temperature ($^\circ$C)	Stress (MPa)	Rupture Time (h)	El (%)	RA (%)
A	600	370	0.2	36.0	88.3
		280	1.7	40.3	87.7
		250	7.3	36.8	84.1
		200	246.4	43.4	82.9
		185	1433.5	34.3	79.6
		170	6551.8	24.8	56.8
A	650	214	0.6	42.2	84.3
		175	8.0	36.6	86.3
		145	95.0	43.6	84.3
		140	254.6	42.4	81.9
		130	1093.3	25.1	36.8
		115	4278.8	12.8	33.7
A	700	140	1.1	52.3	91.7
		110	11.3	46.9	89.0
		90	82.8	39.5	79.5
		70	1058.5	15.8	21.4
		80	356.3	38.2	65.7
B	600	379	0.0	22.3	77.8
		350	0.1	27.0	79.8
		330	0.4	30.6	84.0
		280	3.4	34.6	82.3
		250	21.6	38.2	84.7
		200	880.0	38.1	75.2
		185	2371.3	22.6	59.5
B	650	250	0.1	42.2	86.4
		225	0.5	40.9	85.5
		195	4.3	38.5	86.5
		170	60.7	43.7	83.0
		145	292.7	41.4	70.8
		130	1423.5	20.0	45.3
		115	2980.8	15.3	37.3
B	700	179	0.2	56.4	91.6
		160	0.5	54.9	91.2
		130	4.5	40.2	89.6
		100	83.4	40.9	78.8
		90	251.6	24.4	50.5
		70	1198.3	17.5	20.4

Table 4.7 Creep test results for steels A and B (Mitsubishi Heavy Industries).

just a high creep rupture stress. In this case, steels A and B showed a susceptibility to oxidation and corrosion, due to the low levels of silicon and chromium. This will be discussed in a later chapter.

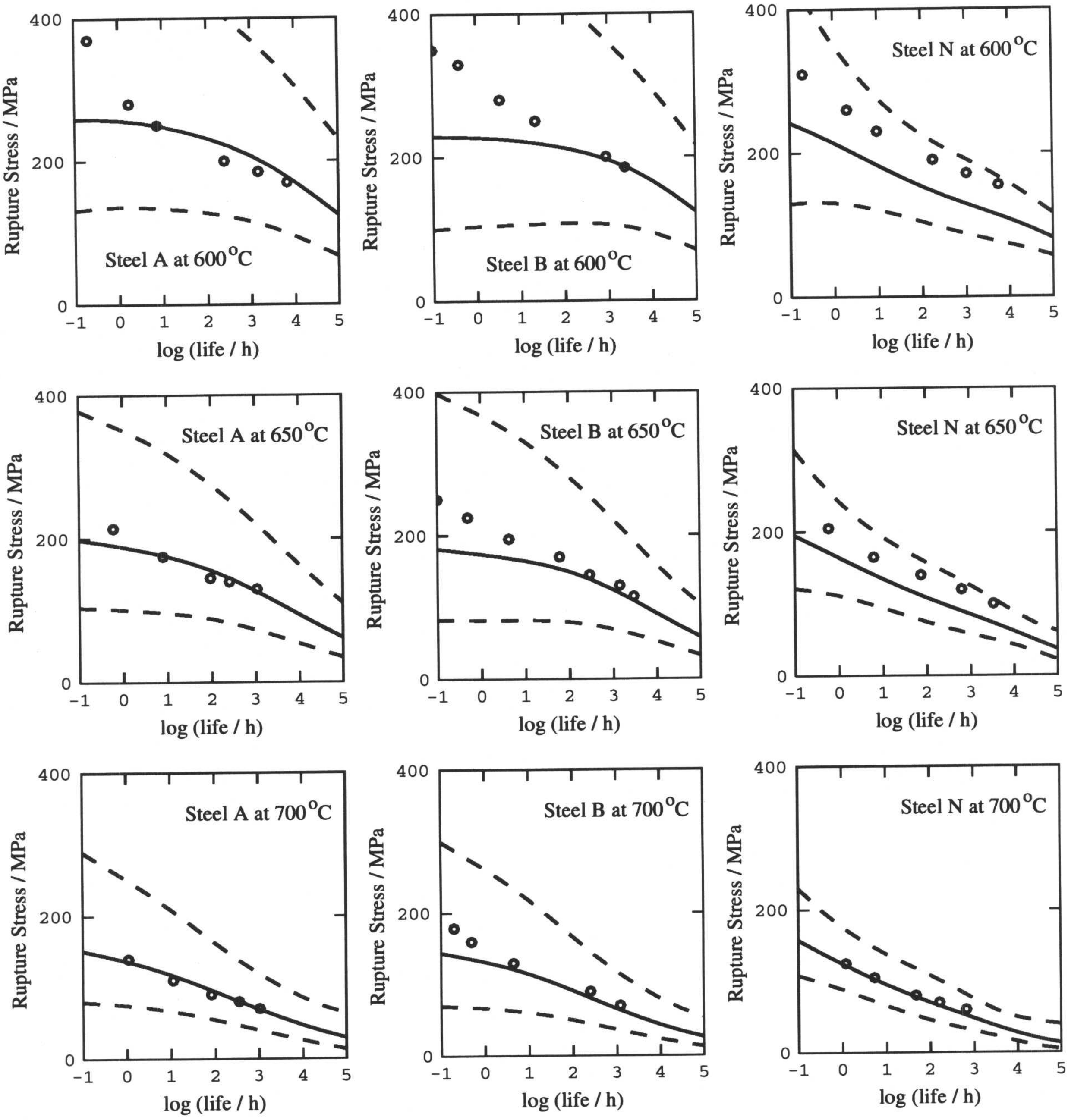

Fig. 4.9 Predictions of creep rupture strength of steels A, B and N compared with the creep data. The steels were manufactured by Mitsubishi Heavy Industries.

Neural networks may be improved by increasing the size of the database upon which they are trained to include a wider variety of accurate data. This will be demonstrated in the next chapter where the network will also be applied to a diiferent problem: the welding of power plant steels.

CHAPTER 5

Modelling Creep Rupture Strength of Ferritic Steel Welds

The creep rupture life is frequently a fundamental limit on the design of steam turbines for power plant. During steady operation, the steam turbine casing achieves the live steam temperature; the steam pressure is contained within a casing; this gives rise to a steady state stress which at elevated temperatures can cause the casing to fail by a creep mechanism.

This chapter is concerned with small steam turbines ($< 40\,\mathrm{MW}$), of the kind described by Sheard and Raine (1998). This utilises a single casing made in two halves which fit around the turbine rotor; the two halves are connected at a horizontal joint using bolts. This bolting limits the pressure differential (*i.e.* the difference in pressure across the wall of the casing) which can be tolerated to about 70 bar. It is possible to overcome this limitation by using multiple casings but there is then a dramatic increase in the manufacturing cost.

The conditions currently desired of small steam turbines, 90 bar at 540 °C (Listman, 1997) are beyond the capability of even the most aggressive horizontal joint bolt design, making it necessary to use an expensive double casing. Fortunately, an alternative to this design was implemented recently by Mason and Sheard (1997) for a 30.4 MW steam turbine. The details of this single–casing design (Fig. 5.1), which permits the higher pressure differential, are beyond the scope of this chapter, but there are two points which need to be emphasised in the context of the present work:

(i) As for the usual design, the steam is fed into the appropriate part of the casing via a steam pipe. This pipe is conventionally joined to the casing with a vertical flange joint which is bolted together. The flange has had to be upgraded to tolerate the higher steam pressures involved.

(ii) The large flange of the steam pipe and its associated bolting causes considerable steric hindrance, making it difficult to assemble the turbine unit.

To overcome these difficulties, it has been decided to replace the bolted vertical joint by a welded joint. For reasons which are proprietary, the heat affected zone of the weld is expected to behave identically in creep to the region of the steel far away from the weld. Therefore, it is the creep properties of the weld metal itself which become an issue. The work presented in this chapter demonstrates a method by which these properties may be estimated.

The methodology involves the creation of neural network models which adequately capture the complexity of the creep rupture phenomenon. Such models rely for their training on

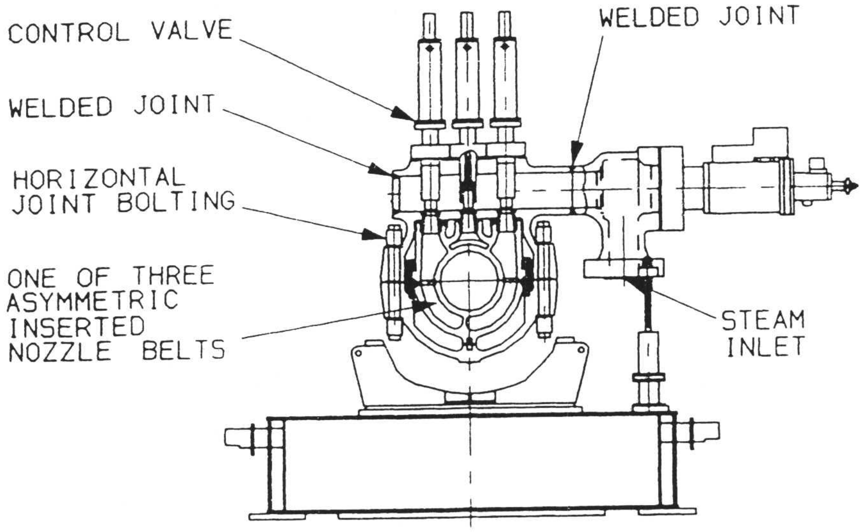

Fig. 5.1 A cross section of the advanced high–pressure inlet of the Sheard and Mason (1997) design of steam turbine.

experimental data, which are available in large quantities for wrought power plant steels, but not for the actual weld metals. For this reason, we shall begin by justifying the idea to use wrought steel data to estimate weld metal properties. The model itself is validated later in the chapter.

5.1 Comparison of Weld Metal and Wrought Plate

Weld metals and steels of matching composition seem to have similar creep rupture properties. In fact, the chemical compositions of weld metals and corresponding steel plates are not very different (Fig. 5.2). Of course, weld metal will, in general, have a higher oxygen and nitrogen concentration but the former should not affect creep resistance. Although differences in the nitrogen concentration are important, they can easily be taken into account both in predicting carbonitride formation and in the neural network model where nitrogen is an input.

The microstructure of an as–deposited weld metal is naturally radically different from that of a wrought steel. However, even this is unimportant because the severe tempering heat treatments used following the welding procedure essentially wipe out the original microstructure and replace it with one which is tempered and similar to that of the steel plate. It is probably for this reason that the welding process itself is found not to influence the creep rupture life (Lundin *et al.*, 1986).

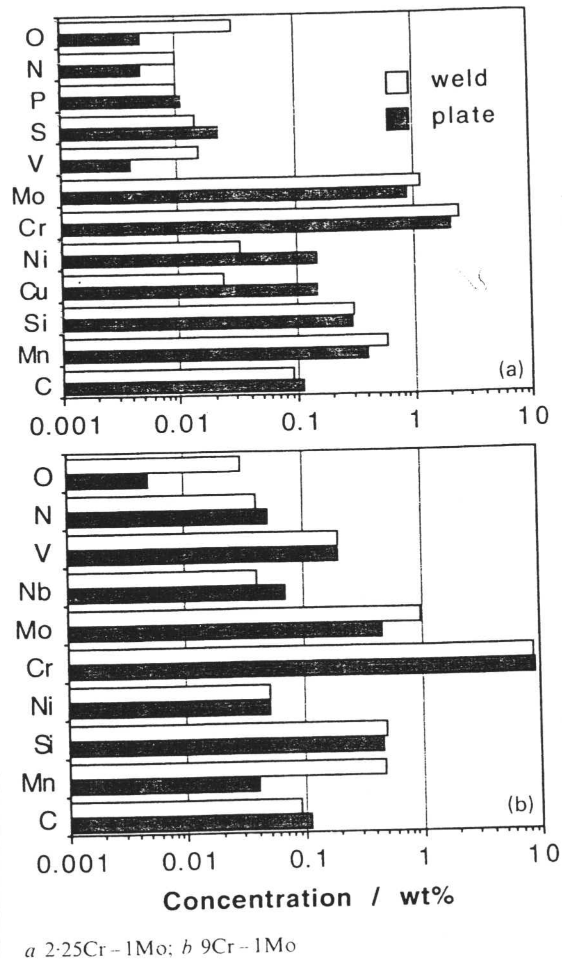

Fig. 5.2 A comparison of the chemical compositions of wrought plates and corresponding weld metals of the kind used in power plant industry (Bhadeshia, 1999c).

5.2 Creep Rupture Strength: The Variables

The basic principles of alloy design for creep resistance are well–established and well–founded on experience. The steels must have a stable microstructure which contains fine alloy carbides to resist the motion of dislocations; however, changes are inevitable over the long service time so that there must be sufficient solid solution strengthening to ensure long term creep resistance. There may be other requirements such as weldability, corrosion and oxidation resistance. It is nevertheless difficult to express the design process quantitatively given the large number of interacting variables.

The variables taken into account in the present work are listed in Table 5.1 , a and b. We note that the entire information about microstructure and properties is in principle to be found in this set of parameters since the chemical composition and heat treatment are comprehensively included. There may, of course, be many other independent variables that might be considered important in creep analysis, but these are for the moment neglected for two reasons. Firstly, an empirical analysis requires experimental data; an over ambitious list would simply reduce the dataset since publications frequently do not report all of the necessary parameters. Secondly, the effect of any missing variables would simply be reflected in the uncertainties of prediction. If the predictions are noisy then they can be improved with carefully designed experiments at a future date. Bearing this in mind, the results to be presented are based on some 5420 sets of experiments obtained from the published literature (Appendix 1, Ref. for database). This compares to earlier work on the creep rupture stress of wrought steels by Brun *et al.* (1999), which used a total of 2066 experiments. The methodology of neural network models has been previously described in Chapter 3.

Variable	Range	Mean	Standard deviation
Test Conditions			
log(life/h)	-0.22-+5.29	3.00	0.28
Temperature (K)	723-977	867	60.97
Composition			
Carbon (wt%)	0.004-0.23	0.11	0.044
Silicon (wt%)	0.01-0.86	0.28	0.17
Manganese (wt%)	0.01-0.92	0.50	0.12
Phosphorus (wt%)	0.001-0.029	0.013	0.0074
Sulphur (wt%)	0.001-0.02	0.0074	0.0048
Chromium (wt%)	2.17-12.9	8.20	3.46
Molybdenum (wt%)	0.04-2.99	0.84	0.53
Tungsten (wt%)	0.01-3.93	0.50	0.79
Nickel (wt%)	0.01-2.00	0.23	0.28
Copper (wt%)	0.01-0.87	0.069	0.099
Vanadium (wt%)	0.01-0.28	0.13	0.10
Niobium (wt%)	0.005-0.312	0.037	0.045
Nitrogen (wt%)	0.001-0.165	0.030	0.027
Aluminium (wt%)	0.001-0.057	0.011	0.012
Boron (wt%)	0.00-0.051	0.0013	0.0041
Cobalt (wt%)	0.00-3.09	0.13	0.49
Tantalum (wt%)	0.00-0.1	0.0007	0.0066
Oxygen (wt%)	0.003-0.035	0.0099	0.0031
Rhenium (wt%)	0.00-1.69	0.014	0.12

Table 5.1: (a) - Details of inputs in database - test data and composition.

Variable	Range	Mean	Standard deviation
Normalising			
Temperature (K)	1123-1453	1283	69.16
Duration (h)	0.17-33	2.05	3.75
Cooling rate			
in furnace	0-1	0.060	0.24
in air	0-1	0.58	0.49
oil quenched	0-1	0.25	0.43
water quenched	0-1	0.11	0.31
Tempering			
Temperature (K)	823-1133	979	74.88
Duration (h)	0.50-32	3.64	6.17
Cooling rate			
in furnace	0-1	0.060	0.24
in air	0-1	0.88	0.33
oil quenched	0-1	0.030	0.17
water quenched	0-1	0.032	0.18
Annealing			
Temperature (K)	300-1023	465.7	282.5
Duration (h)	0.5-50	4.38	8.37
Cooling rate			
in furnace	0-1	0.054	0.226
in air	0-1	0.946	0.226

Table 5.1: (b) - Details of inputs in database - heat treatments.

5.3 Creation of Neural Network

The aim of the neural network in this case was to predict the creep rupture stress as a function of the variables shown in Table 5.1. Those variables include a comprehensive description of chemical composition and three heat treatments (each characterised by a temperature, duration and cooling rate from the treatment temperature). If the steel had only undergone two heat treatments, the annealing heat treatment was set to 300 K to correspond to room temperature. The time to rupture was expressed in logarithmic form, along with the output creep rupture stress, to improve the accuracy of the model.

All the 37 different input variables and the output were normalised within the range ±0.5 as follows:

$$x_N = \frac{x - x_{min}}{x_{max} - x_{min}} - 0.5$$

where x is the original value from the database, x_{max} and x_{min} are the respective maximum and minimum of each variable in the original data and x_N is the normalised value. This step is not essential to the running of the neural network but later allows a convenient way to compare the results of the output.

For several runs of the neural network, Fig. 5.3 shows the model perceived noise σ_ν in the creep rupture stress. As expected, σ_ν decreases as the fitting function becomes more flexible with larger numbers of hidden units. By contrast, Figure 5.4 shows the test error at first decreases and then levels out, with minima at 18 to 22 hidden units.

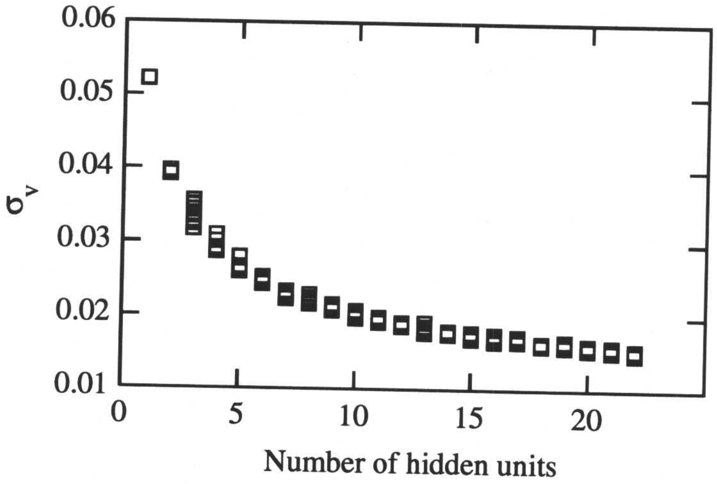

Fig. 5.3 Variation in σ_v as a function of the number of hidden units. Several values are presented for each set of hidden units because the training for each network started with a variety of random seeds.

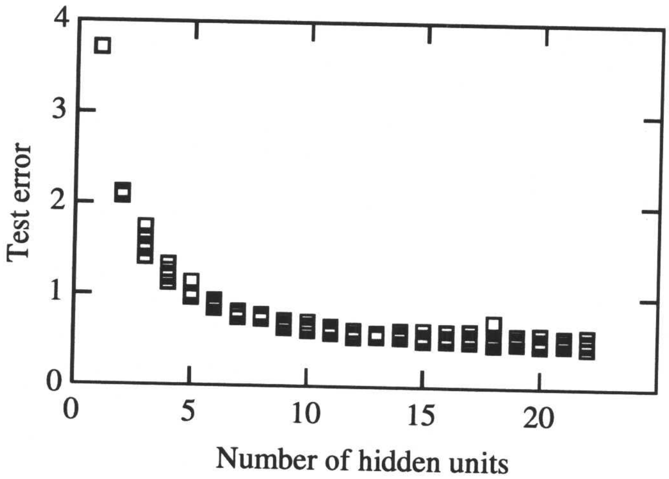

Fig. 5.4 The test error as a function of the number of hidden units.

Fig. 5.5 shows the comparisons made for the best model, consisting of 22 hidden units, on the split database. The comparison for the seen data with the model shows very good agreement as should be expected. The analysis of unseen data by the neural network also shows good agreement.

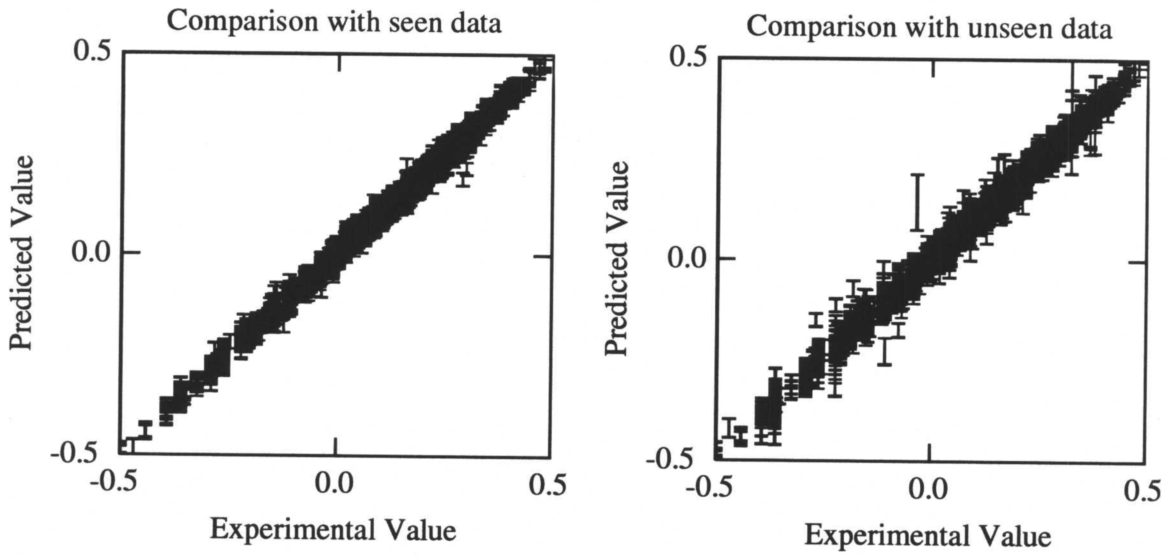

Fig. 5.5 Comparisons between seen and unseen data.

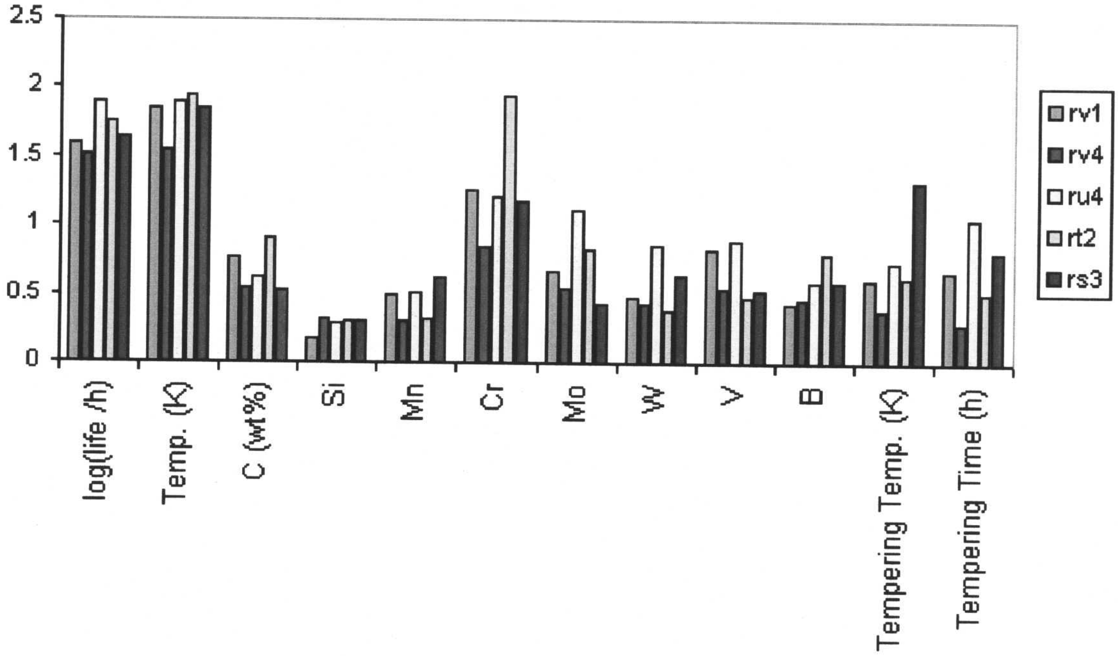

Fig. 5.6 Comparison of values of σ_w for the top five models.

The parameter σ_w indicates the importance of an input in terms of its variation having an effect on the output of the model. Fig. 5.6 compares the value of σ_w for a selection of inputs for the top five models. A high value of σ_w for a specific input can be caused by the corresponding variable inducing a large variation in the output, but it can be seen from Fig. 5.6 that different models can assign varying significance to the same input. In such cases, it is possible that a committee of models can make a more reliable prediction than an individual model. The best models are ranked using the values of the test errors. Committees are then formed by combining the predictions of the best L models, where $L = 1, 2, \ldots$; the size of the committee is therefore given by the value of L. A plot of the test error of the committee versus its size gives a minimum which defines the optimum size of the committee, as shown in Fig. 5.7.

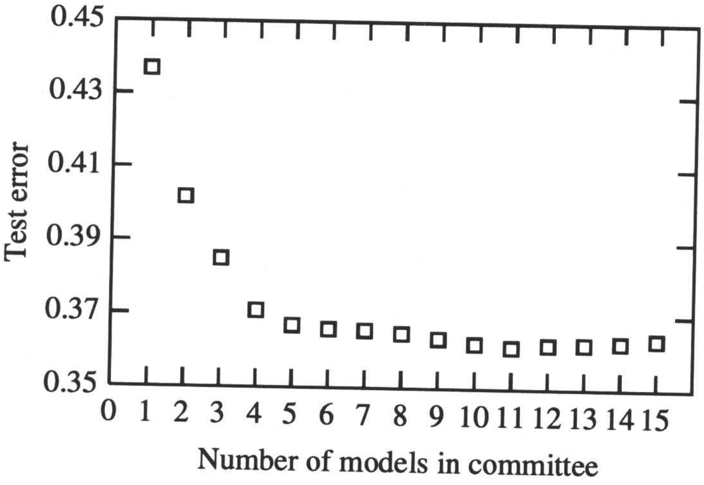

Fig. 5.7 Comparison of test error of increasing size of committees.

The test error associated with the best single model is clearly greater than that of any of the committees. It was determined in this case that a committee of eleven models would be the best choice, being the committee of the lowest test error. The committee was then retrained on the entire data set without changing the complexity of any of its members.

The predictions of the committee trained on the entire data set can be compared with the original dataset as shown in Fig. 5.8. It can be seen that there is excellent agreement between the values and that the error bars are extremely small.

5.4 Application of Model

Fig. 5.9 shows predictions using the neural network in examining the creep rupture strength of a standard 2.25CrMo steel and a modern 10CrMoW heat resistant steel (Table 5.2). The error bounds represent the uncertainty in fitting the non-linear function to the training data, as 65% confidence limits with the σ_ν added quadratically. The calculated lifetime of each steel was examined at temperatures of 550, 600 and 650 °C. The network correctly predicted that the creep strength of the two steels would reduce with increasing lifetime and temperature and also that the 10CrMoW steel is more creep resistant than 2.25CrMo. The error bars, represented by dashed lines, are smaller when the neural network is confident of the predictions

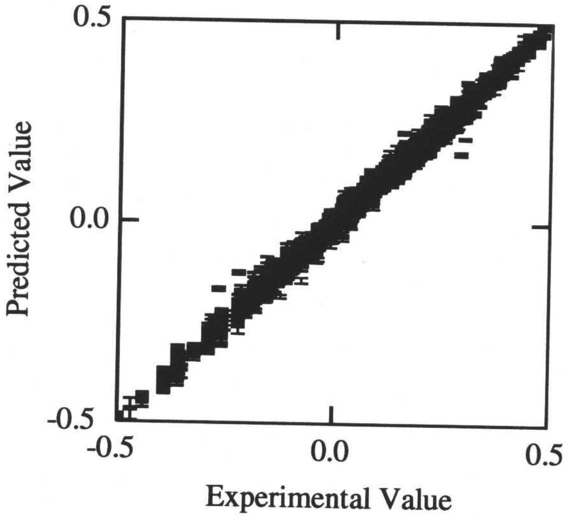

Fig. 5.8 Comparison of predicted values and experimental values for the committee.

that it is making. Increases in error bar size, such as at long life for the 2.25CrMo alloy at 650°C, indicate that a lack of experimental data is restricting the accuracy of the predictions.

Steel	2.25Cr	10Cr	Steel	2.25Cr	10Cr
Norm temp	1203K	1338K	Cr	2.4	10.61
Duration	6h	2h	Mo	1.01	0.44
Cooling rate	water q.	in air	W	0.01	1.87
Tempering	908K	1043K	Ni	0.14	0.32
Duration	6h	4h	Cu	0.16	0.86
Cooling rate	in air	in air	V	0.01	0.21
Annealing	873K	1013K	Nb	0.005	0.01
Duration	2h	4h	N	0.0108	0.064
Cooling rate	in air	in air	Al	0.018	0.022
C wt%	0.15	0.12	B	0.0003	0.0022
Si	0.21	0.05	Co	0.05	0.015
Mn	0.53	0.64	Ta	0.0003	0.0003
P	0.012	0.016	O	0.01	0.01
S	0.012	0.001	Re	0.0003	0.0003

Table 5.2: Heat treatments and compositions of two common power plant steels.

The behaviour of the model can be assessed further by examining creep rupture strength of a variety of steels and determining if the predictions made by the neural network agree with practical results or microstructural theory. In one case the creep rupture stress of an uncommon 3Cr steel was examined using the neural network and then compared to the results

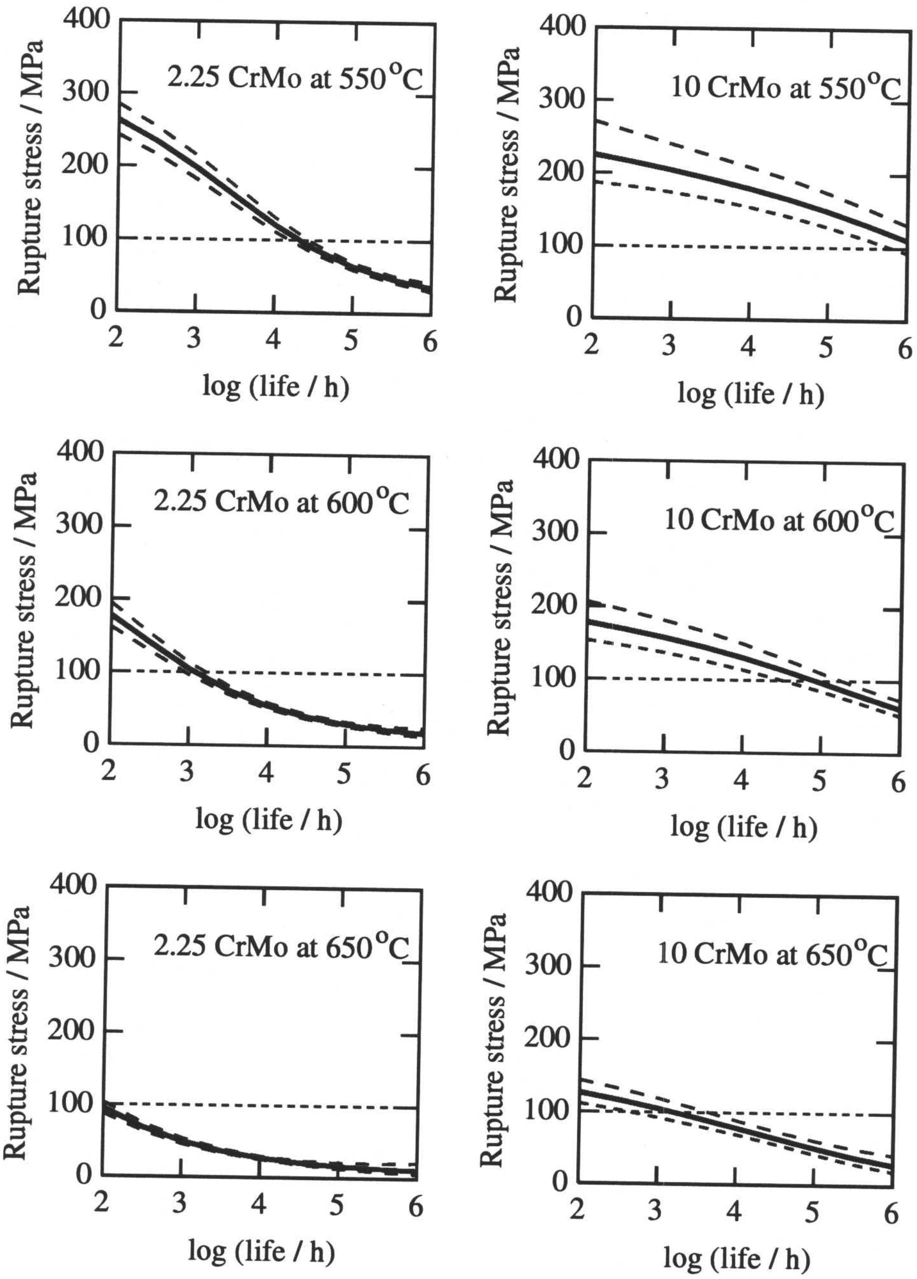

Fig. 5.9 Neural network results for well known power plant steels.

for the 2.25Cr steel previously examined. It could be expected that the 3Cr steel should have a consistently higher creep rupture stress than the 2.25Cr steel due to the increase in chromium content, but it can be seen from Fig. 5.10 that they have comparable creep rupture lives. Fig. 5.10 also shows that the uncertainty for the 3Cr steel is much greater than that of the 2Cr, this being due to the amount of information in the database on 3Cr steel being much less than the amount of data on 2Cr.

This phenomenon can be explained by microstructural theory and is an excellent result for the neural network. The microstructural trends were examined by Robson and Bhadeshia

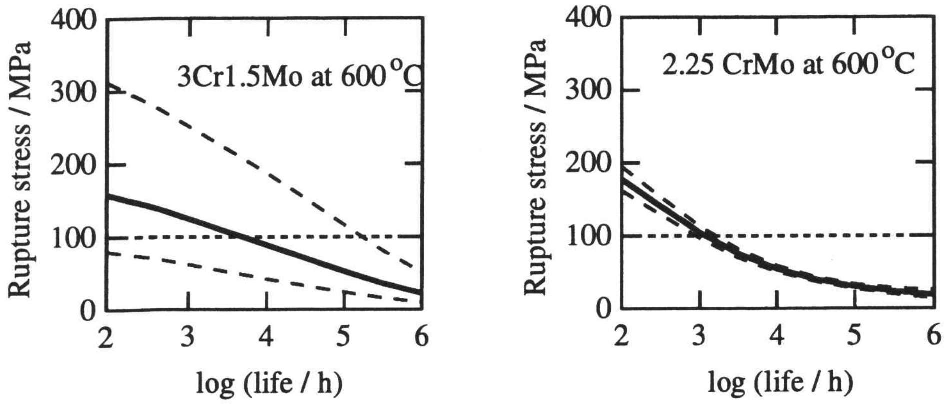

Fig. 5.10 Comparison of a 3Cr steel and a 2.25Cr steel at 600°C.

(1996b) and the results of this research are represented in Fig. 5.11, showing plots of carbide volume fraction versus time for 3Cr steel and for 2.25Cr steel.

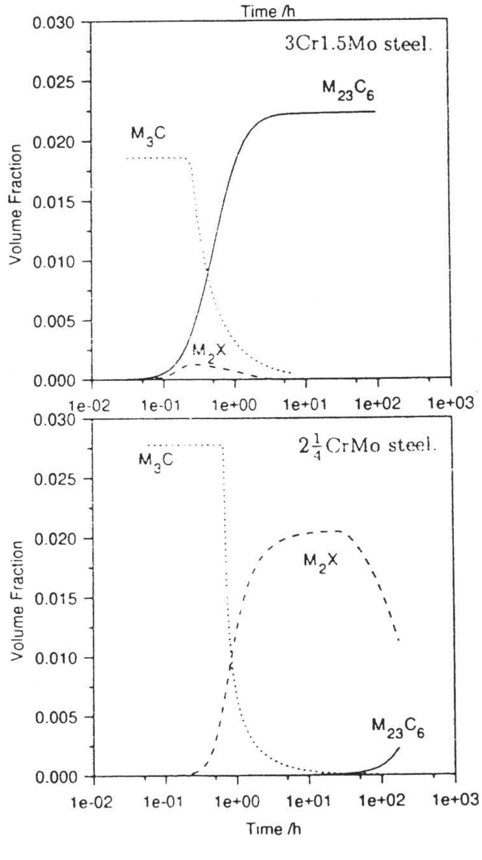

Fig. 5.11 Plot of calculated carbide volume fraction versus time at 600°C for the 2.25Cr alloy and the 3Cr alloy (Robson and Bhadeshia, 1996b).

It is apparent that the rate at which $M_{23}C_6$ precipitates in 3Cr steel is very much greater than that of the 2.25Cr steel. It can also be seen that the maximum volume fraction of M_2X

obtained by the 3Cr alloy is much less. These plots show that, in the 2.25Cr steel, M_2X starts to precipitate well before $M_{23}C_6$, forming a large volume fraction which then suppresses $M_{23}C_6$ formation. However, in the higher chromium steel both carbides tend to precipitate at similar times, and both phases are then competing for solute. The $M_{23}C_6$ phase dominates and M_2X dissolves. The M_2X precipitate is considered to be a factor in improving creep rupture strength, whereas $M_{23}C_6$ is considered less effective in resisting creep deformation due to its large size. This then explains why the 3Cr steel is not as creep resistant as expected.

The neural network model may be used to examine the influence of any of the input variables on the output. Hence, the effect of varying composition in a particular alloy at certain conditions may be determined. Fig. 5.12 shows trends with increasing tungsten content, with a maximum at approximately 3wt% for the 10Cr alloy examined previously. Although the uncertainty of the predictions is large, the decline at greater than 3wt% is expected due to the formation of δ-ferrite which is generally considered detrimental to creep properties. The National Physical Laboratory's Metallurgical and Thermochemical data Bank (MTDATA) was used to determine at what concentration of tungsten that δ-ferrite started to form. The result was that at 2.7wt% tungsten, δ-ferrite formation commenced, agreeing well with the neural network results.

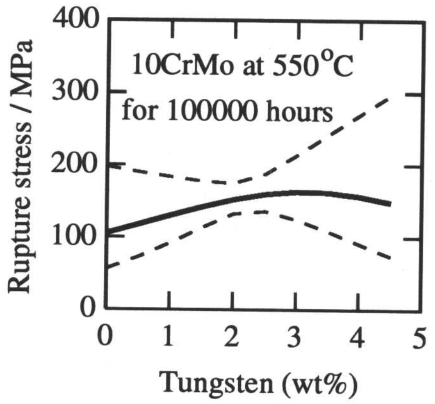

Fig. 5.12 Rupture stress for 10Cr alloy with varying tungsten.

5.5 Application to Weld Metals

It has already been argued that weld metals and steels of matching composition may have similar creep rupture properties. The hypothesis can be proved by examining the relatively limited data on all–weld metal tests in published literature (Bhadeshia, 1999c; Naoi *et al.*, 1995). Fig. 5.13 shows the encouraging agreement between the calculated creep rupture stress and the measured values of 2.25CrMo welds (Table 5.3) (Lundin *et al.*, 1986). The predictions were made without any adjustment to the model, which did not interrogate any weld data during its creation.

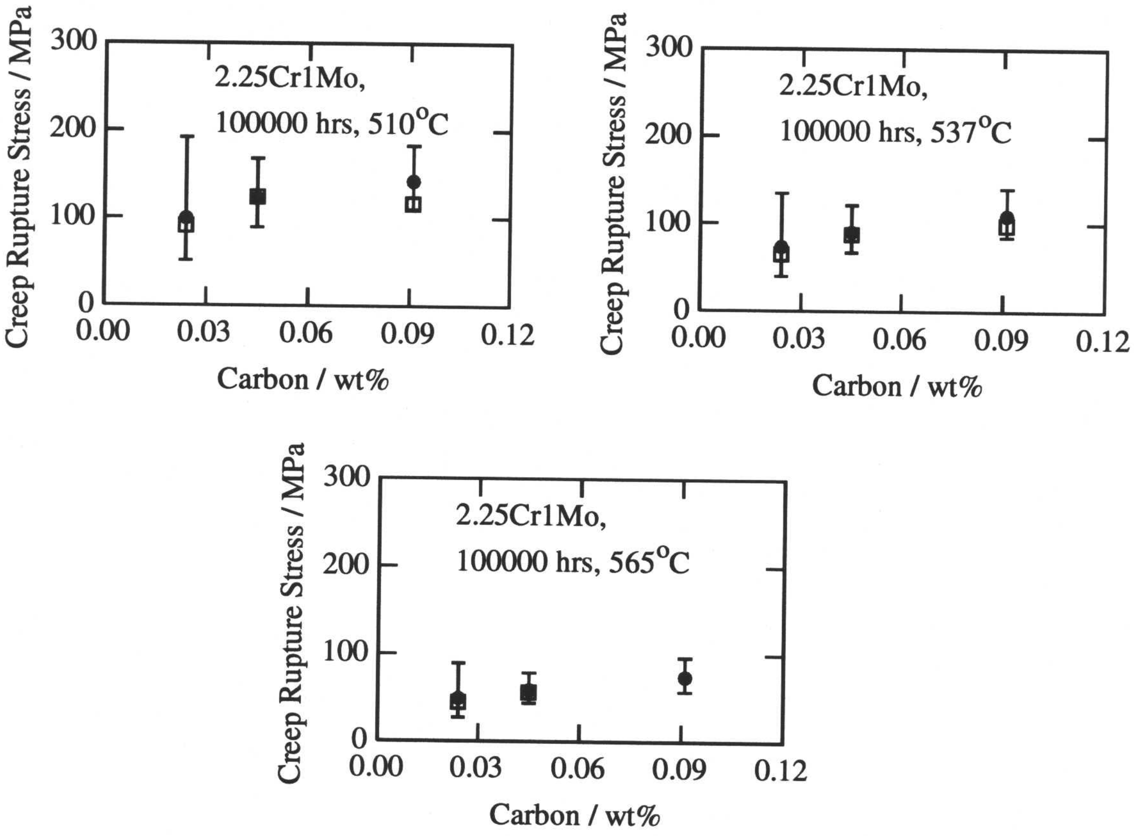

Fig. 5.13 Calculated (filled circles) and measured (open squares) stress rupture data for 2.25CrMo weld metal versus wt% carbon.

Composition (wt%)	C	Si	Mn	P	S	Ni	Cr	Mo	V	Cu
Low carbon	0.024	0.75	0.96	0.019	0.024	0.09	2.39	1.20	0.006	0.11
Medium carbon	0.045	0.31	0.66	0.013	0.018	0.08	2.31	1.11	0.014	0.08
High carbon	0.091	0.39	0.59	0.010	0.014	0.033	2.48	1.17	0.015	0.024

Table 5.3: Chemical composition of weld metals with varying carbon content, wt% (Lundin *et al.*, 1986).

The heat treatments were changed to represent the welding process and the post weld heat treatment (PWHT). It was determined, by trial and error, that setting the normalising process to 1200 K for 6 hours was a fair representation of the welding process itself. The tempering heat treatment was then set to the conditions of the PWHT and the annealing heat treatment was set to 300 K to show that no further heat treatments had been carried out.

Fig. 5.13 confirms that it is reasonable to assume that the creep rupture life of weld metals can be modelled on the basis of wrought steels. The results are plotted with varying carbon since the literature from which these data were taken was, in part, examining the effect of varying carbon wt% on weld metals.

The model may also be used to determine creep rupture stress of modern modified 9Cr-MoW weld metals. There is much less open literature available on this type of weld metal in terms of creep data and so there is less opportunity of testing the model. Naoi *et al.*(1995) have carried out creep tests on a 9CrMoW gas tungsten arc weld metal, the composition of which is shown in Table 5.4.

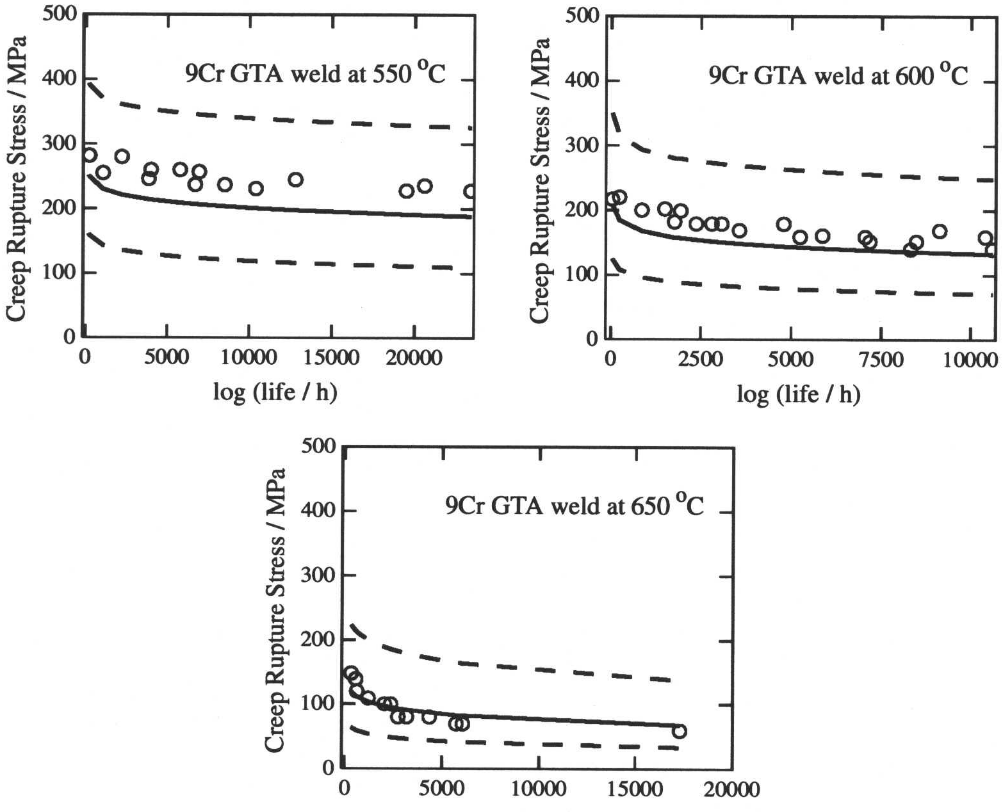

Fig. 5.14 Calculated (filled circles) and measured (open squares) stress rupture data for 9CrMoW weld metal versus creep rupture life (Naoi *et al.*, 1995).

Fig. 5.14 shows that the model is also capable of predicting the creep rupture life of modified 9CrMoW weld metals. The ability to predict the creep properties of these welds has

Composition (wt%)	C	Si	Mn	P	S	Ni	Cr	Mo	W	V	Nb	N
Weld Metal	0.07	0.20	1.01	0.006	0.004	0.36	8.94	0.48	1.62	0.09	0.04	0.032

Table 5.4: Chemical composition of gas tungsten arc weld metal, wt% (Naoi *et al.*, 1995).

direct industrial implications, as discussed previously.

5.6 Further Predictions of Weld Metals

The model was applied to a number of sets of weld data for different alloys to determine the quality of the predictions. Weldments of a 9Cr alloy were tested by Morimoto *et al.* (1996). The composition of the weld metal is given in Table 5.5 and the results of the neural network are shown in Fig. 5.15. Especially impressive is the fact that the model has successfully predicted creep rupture strength up to 40,000 hours.

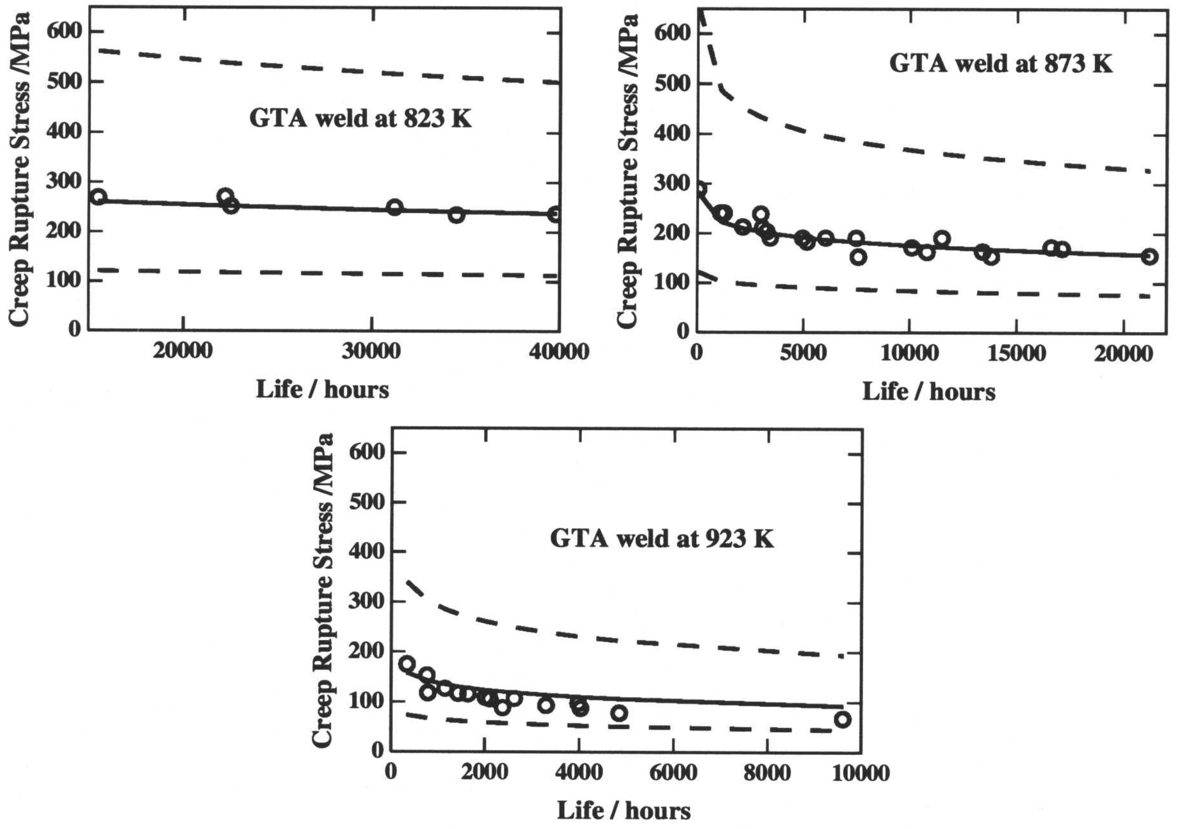

Fig. 5.15 Calculated and measured (open circles) stress rupture data for 9Cr weld metal versus creep rupture life (Morimoto *et al.*, 1996).

Composition (wt%)	C	Si	Mn	P	S	Ni	Cr	Mo	W	V	Nb
Weld Metal	0.08	0.21	0.96	0.007	0.002	0.32	9.01	0.49	1.58	0.11	0.05

Table 5.5: Chemical composition of 9Cr weld metal, wt% (Morimoto *et al.*, 1996).

Previous research at the University of Cambridge with Oerlikon Welding Limited and Siemens Power Generation Limited produced a novel composition 9Cr weld alloy (Cool, 1996; Conroy, 1999). The neural network model was used to predict the creep rupture strength of the alloy and the results are compared with the creep data in Fig. 5.16. Once again we can see excellent agreement between creep data and the model prediction. The composition of the alloy is shown in Table 5.6.

Composition (wt%)	C	Si	Mn	P	S	Ni	Cr	Mo	V	Nb	N	O
Weld Metal	0.093	0.15	0.40	0.010	0.006	0.071	8.70	0.98	0.16	0.007	0.042	0.070

Table 5.6: Chemical composition of 9Cr weld metal, wt% (Cool, 1996; Conroy, 1999).

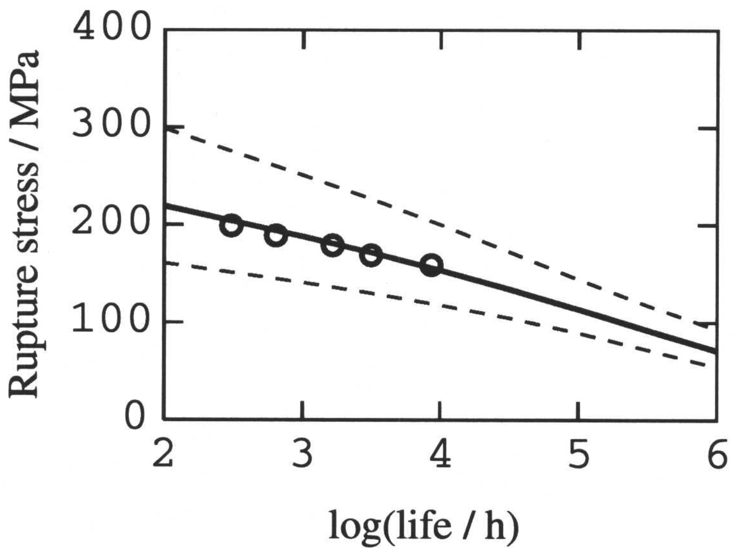

Fig. 5.16 Creep data (open circles) for novel 9Cr alloy compared to neural network predictions (Cool, 1996; Conroy, 1999).

The influence of vanadium on creep properties of low alloy creep resistant steels was examined by Sobotka *et al.* (1999). Three weld metals were creep tested and their compositions

Composition	Weld 1	Weld 2	Weld 3
C (wt%)	0.12	0.15	0.10
Si	0.23	0.32	0.28
Mn	0.61	0.53	0.49
Cr	0.61	0.72	2.17
Mo	0.42	0.46	0.92
V	0.28	0.60	0.01

Table 5.7: Chemical compositions of low alloy welds creep tested by Sobotka *et al.* (1999).

are shown in Table 5.7. The results of the creep tests are shown in Fig. 5.17.

The comparison between predictions and data are good for weld 1, even though the error bounds associated with the prediction are large. The comparison for weld 2 is not as good. The vanadium content in weld 2 is high at 0.6 wt%, the maximum vanadium content in the database on which the neural network has been trained is 0.3 wt%. This affects the result of the neural network as shown, the prediction is well below the actual creep data. However, the error bounds reflect the uncertainty of the neural network in this extrapolation and it is pleasing to note that the creep data are within the upper error limits. Analysis of weld 3, a more common 2.25 Cr type alloy, shows good agreement between model and data.

5.7 Further Predictions using Advanced Neural Network

The neural network used in this chapter is based on data from 5420 experiments, as compared to the network used in the previous chapter which was based only on 2250 experiments. This additional data included the creep test results from Nippon Steel (§4.3) but not those from Mitsubishi Heavy Industries (§4.4), which were received at a later date. Fig. 5.18 shows the predictions of the latest neural network against the creep test data from Mitsubishi, showing an improvement in the capabilities of the model when compared with the results in §4.4.

This neural network was also used to predict the hot tensile strength of these alloys. This was achieved by reducing the test time of the prediction to a low value, in this case 0.01 hours. Fig. 5.19 shows that the model adapted well to this task. The comparison with data was extremely good for Nippon steel A, with the model even accurately predicting the room temperature tensile strength accurately (the error bounds are not included for the room temperature prediction since they are very large). This is impressive since the lowest test temperature in the database is 450 °C, much higher than room temperature. The room

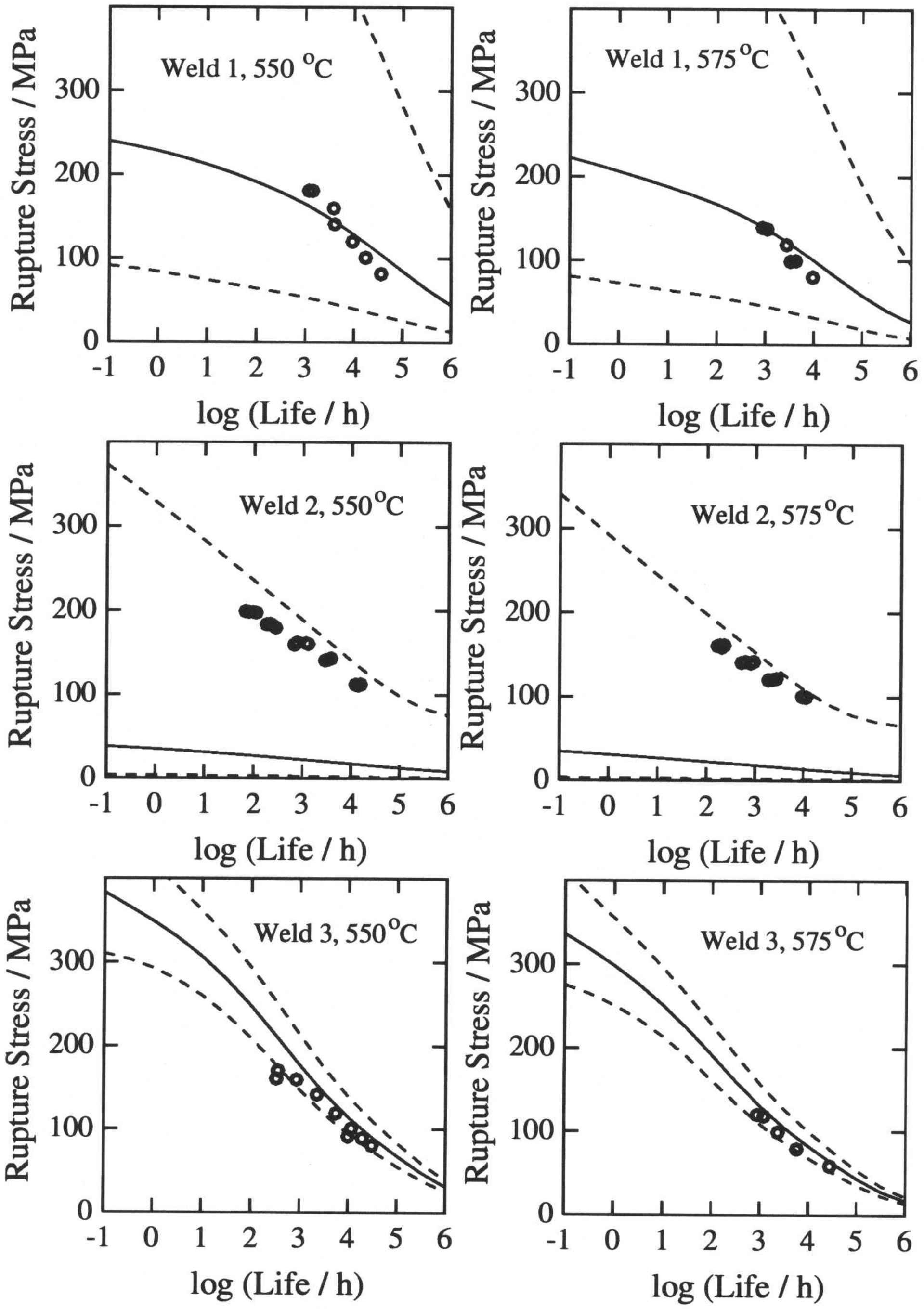

Fig. 5.17 Creep data (open circles) for low alloy weld metals compared to neural network predictions (Sobotka *et al.*, 1999).

temperature results for the other steels are not so accurate but the large error bounds indicate that caution should be taken if relying on these predictions. The worst predictions are shown by Mitsubishi steel N, but the error bounds still include the test data.

Creep tests were also carried out in France by Manoir Industrie on a 9Cr steel designated Z1092. The details of this steel, *i.e.* the composition and heat treatments are recorded in

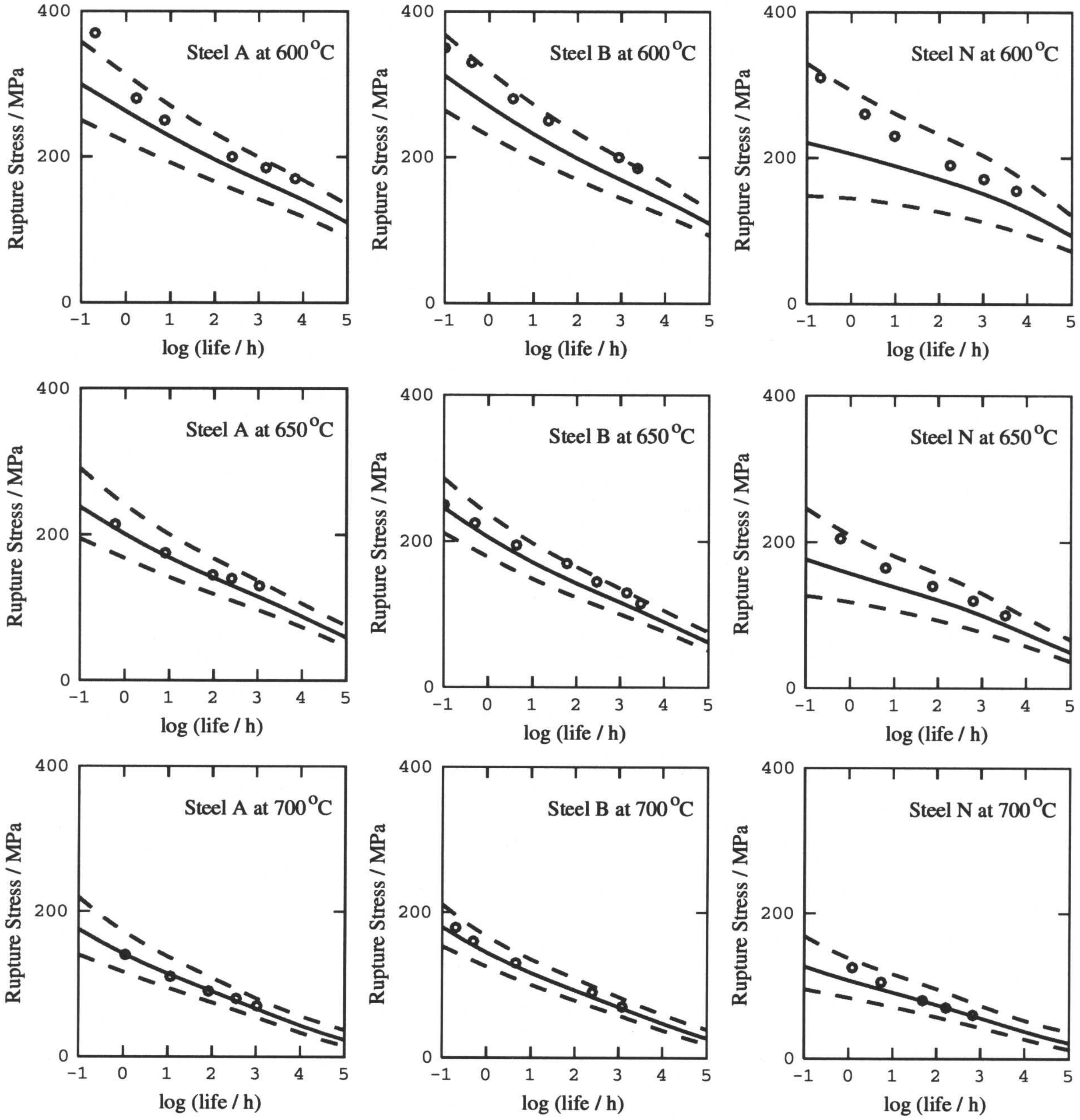

Fig. 5.18 Predictions of creep rupture strength of steels A, B and N compared with the creep data. The steels were manufactured by Mitsubishi Heavy Industries.

Chapter 8, where the steel has undergone metallographic study. Two specimens were creep tested at 600 °C at a stress of 105 MPa and they lasted for 3025 and 3073 hours. The comparison with the neural network predictions are shown in Fig. 5.20. There is excellent agreement between the prediction, which was made prior to the test results, and the data.

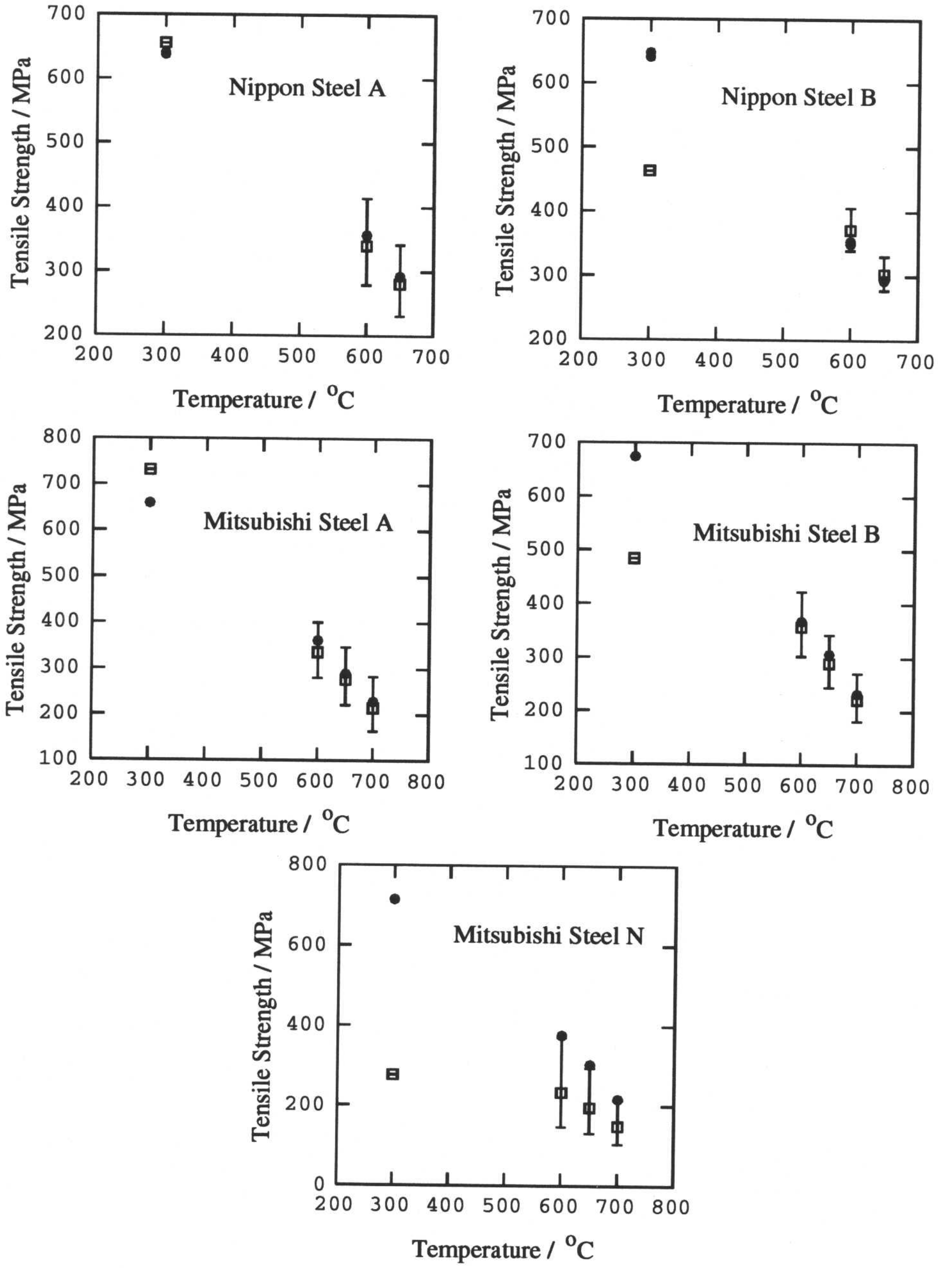

Fig. 5.19 Prediction of tensile strength of steels manufactured by Nippon Steel and Mitsubishi Heavy Industries. Filled circles show the model predictions and the open squares represent the tensile test data.

5.8 Summary

A neural network model has been created to study the influence of chemical composition and heat treatment on the creep rupture strength of ferritic steels. The model is based on a very large set of experimental data accumulated from published literature.

The neural network model has been successfully applied to weld metal data reported in

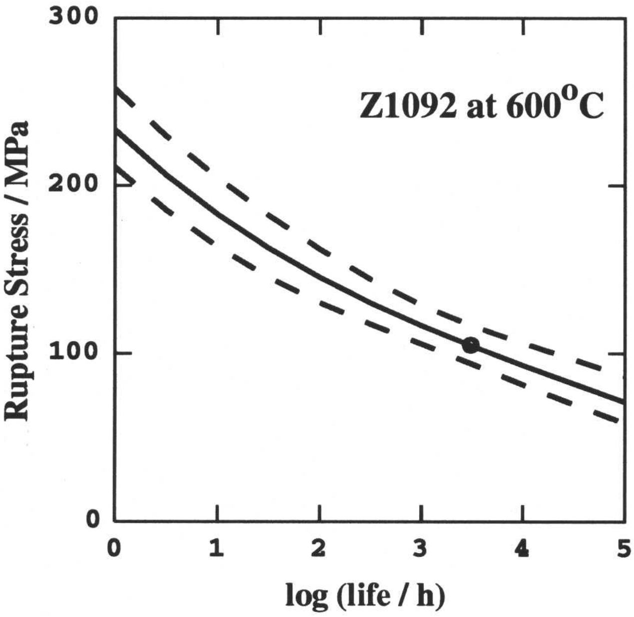

Fig. 5.20 Prediction of Z1092 (Chapter 8), a 9Cr steel creep tested by Manoir Industrie. There are two data points, represented by circles.

the literature, even though these were not used in the creation of the model.

It was also possible to demonstrate that the capabilities of a neural network could be significantly improved by increasing the amount of accurate data on which it can be trained. The model was also applied to predicting, with success, the hot tensile strength of power plant steels.

CHAPTER 6

Oxidation of Ferritic Steels

It was emphasised in Chapter 4 that during the design of steels A and B, Brun *et al.* (1999) did not consider their oxidation properties. It is useful therefore, to examine this topic to enable an improved alloy design procedure.

The problems associated with steels A and B in terms of oxidation resistance can be demonstrated simply by examining the condition of the creep test specimens, the test conditions for which are presented in Table 6.1. The specimens were tested in air.

Specimen	Temperature (°C)	Stress (MPa)	Rupture Time (h)
A-10	600	202	187
A-9	600	253	4.8
A-8	650	202	1.8
A-5	650	120	2015
B-10	600	201	231
B-9	600	253	8.7
B-8	650	201	3.4
B-5	650	120	2058

Table 6.1: Test conditions of selected creep specimens of alloys A and B.

The creep test specimens of steel A are shown in Fig. 6.1 and those of steel B in Fig. 6.2. The specimens tested at 600 °C, A-10, A-9, B-10 and B-9 do not show signs of any serious oxidation problems, as would be expected. However, A-10 and B-10 were only tested for 187 and 231 hours respectively. A-9 and B-9 were tested at a higher stress of 253 MPa but only for a short time, 4.8 and 8.7 hours respectively. The higher stress test specimens appear to have developed a more significant oxide layer than the lower stress tests, despite the large difference in test time.

Specimens A-8, A-5, B-8 and B-5, which were tested at 650 °C and hence show exaggerated oxidation. A-8 and B-8 were tested at a stress of approximately 200 MPa for around 200 hours. By contrast, A-5 and B-5 lasted for over 2000 hours at 120 MPa.

Creep data from experiments conducted in air are generally extrapolated with the assumption that there is no influence on the mechanical properties by the service environment. For

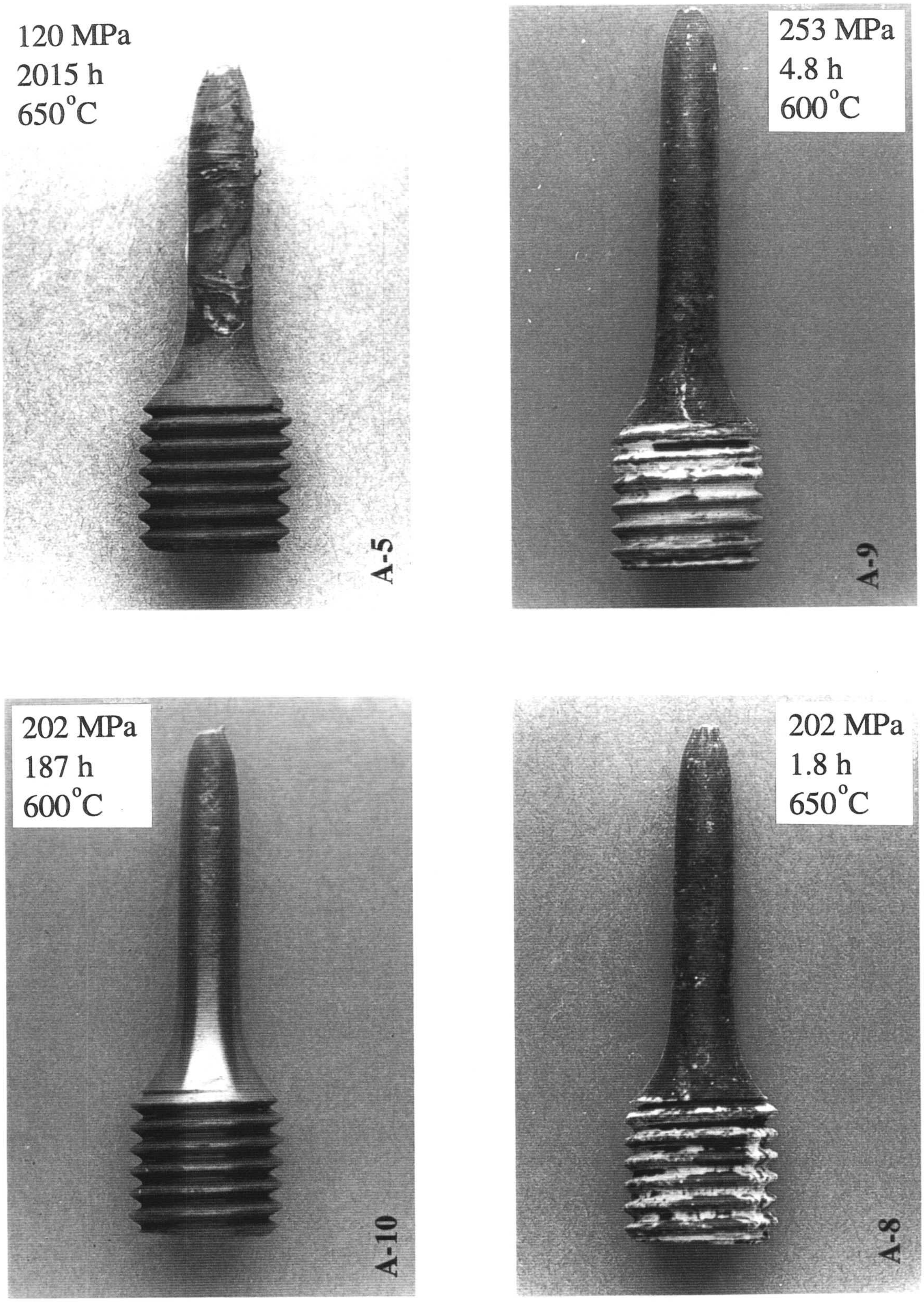

Fig. 6.1 Creep test specimens of steel A. Specimen A-5 shows bad oxidation damage.

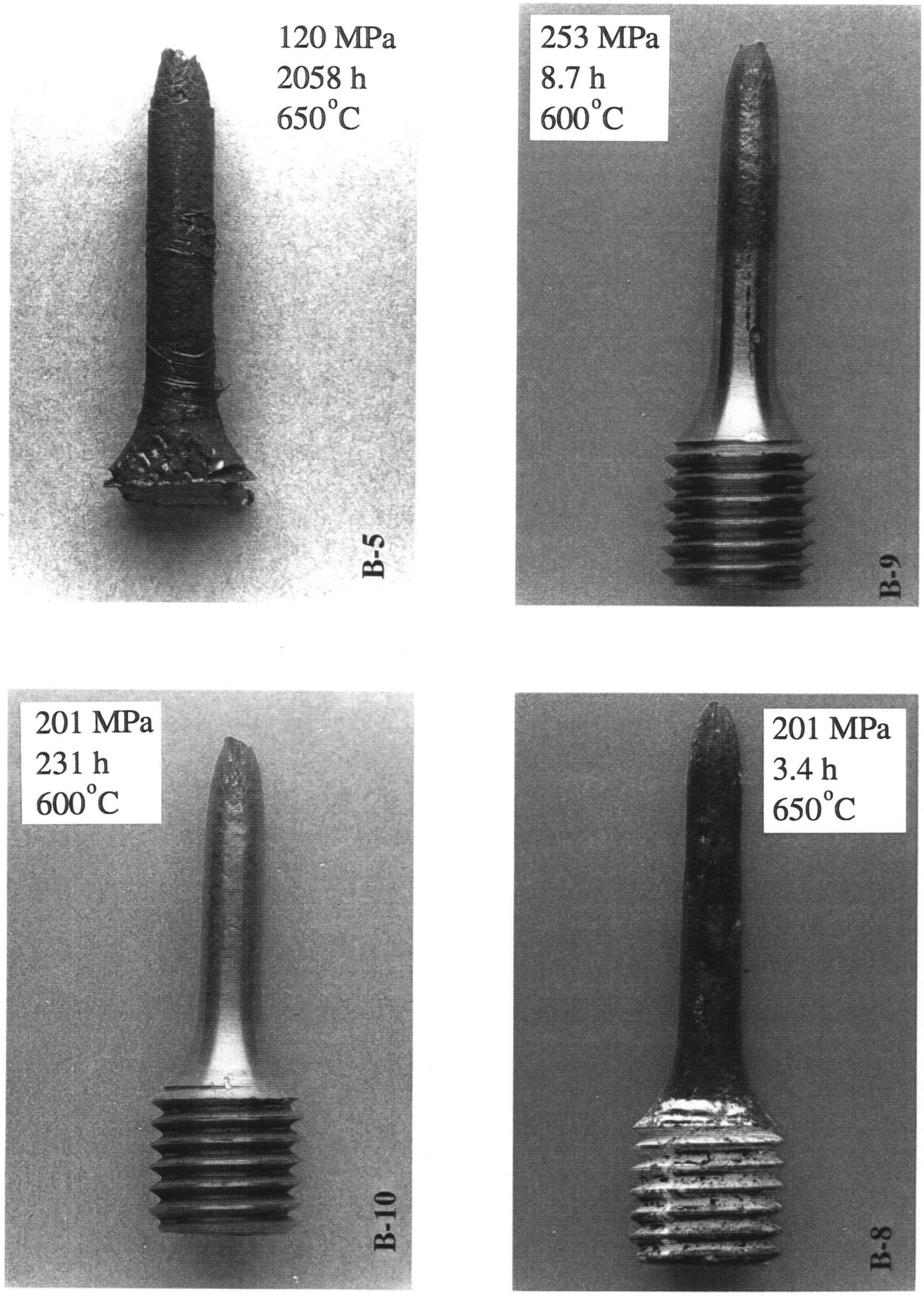

Fig. 6.2 Creep test specimens of steel B. Specimen B-5 shows bad oxidation damage.

long-service components, especially ones which are thin-walled, oxidation effects may become limiting. The formation of a thick oxide scale which spalls will cause a loss in the load-bearing cross-section. The resulting increase in the stress on the component must reduce its service life. Spalling itself can cause problems such as blockage or turbine erosion due to the movement of solid particles through the turbine system. Also, a thick oxide scale in boiler tubes can act as a thermal insulating layer which induces overheating and tube failure.

It is therefore useful to review and understand the mechanism by which oxidation occurs in steels A and B. The formation of an oxide scale on a steel surface is determined by a number of factors, including the alloy properties, the environment, the service temperature and the length of service. The metal components are also subjected to stresses throughout their service life and this may cause the oxide layer to form multilayer scales or spall. This is important for ferritic steels where the loss of oxide layer adherence occurs at the metal/oxide interface, leading to increased rates of oxide growth.

Steam oxidation of low chromium ferritic steels causes the formation of a duplex oxide scale, consisting of an iron-rich oxide over an iron-chromium oxide (Armitt *et al.*, 1978; Metcalfe, 1989). The outer iron-oxide layer is made up of coarse columnar grains of magnetite, Fe_3O_4. These coarse grains become small and equiaxed near the base of the outer layer. The inner layer has a very fine grain size and contains iron and the main alloying elements such as chromium. There is a distinct boundary between the outer and inner layers which corresponds to the original metal surface. A layer of haematite, Fe_2O_3, may also form on the surface of the outer layer. The morphology described here is shown in Fig. 6.3.

In air, 9 wt%Cr steels form protective oxide scales consisting of $Fe_2O_3$with small amounts of Cr in solution. In a steam-containing atmosphere this type of scale is destroyed and a much thicker scale is formed, based on Fe_3O_4 (Williams *et al.*, 1996). This is of a form similar to that illstrated in Fig. 6.3 and it is likely that the inner scale will contain more alloying elements such as manganese.

Cross sections were taken of the creep specimens shown in Table 6.1 in order to determine the thickness of the scale formed. The sections were cut very slowly under a low force in order to minimise any loss of the oxide scale during preparation. They were then cold mounted in clear epoxy resin so that the scale was not effected by a hot mounting press method and was also clearly visible in the mount.

The micrographs of the specimens of steel A are shown in Fig. 6.4. Specimen A-5, which was tested at 650 °C for over 2000 hours shows a thick oxide scale which has spalled, allowing new material to be oxidised. The unspalled section is approximately 0.7 mm thick and after

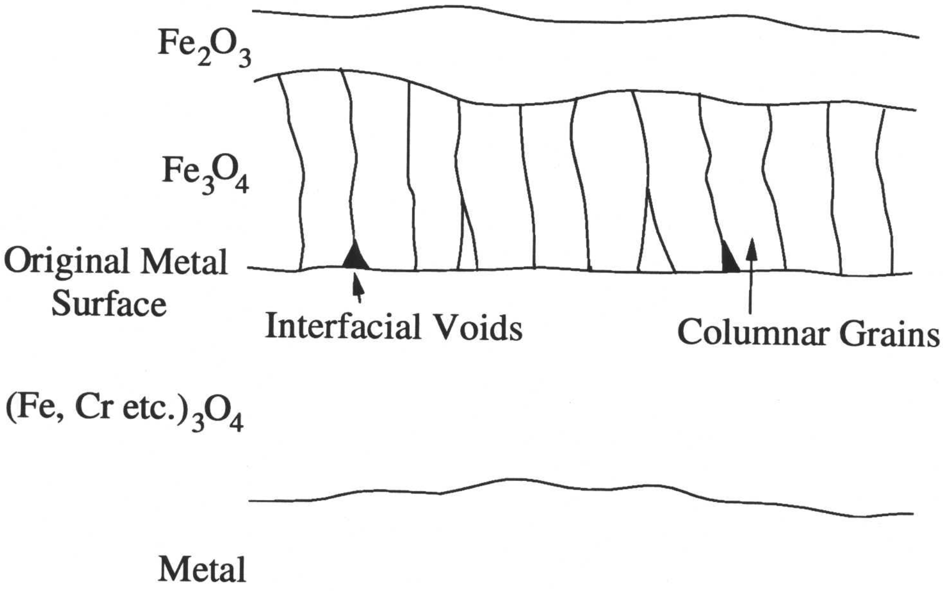

Fig. 6.3 Schematic of duplex oxide scale forming on low chromium ferritic alloy (adapted from Metcalfe, 1989).

spalling there remains a layer approximately 0.25 mm thick. The straight line in the oxide layer indicates the original metal surface, as shown schematically in Fig. 6.3. Specimen A-10 (200 h at 600 °C) has a much thinner oxide layer of about 0.025 mm.

Specimen B-5 (650 °C for over 2000 h) has an oxide scale around 1 mm thick (Fig. 6.5). This is thicker than the scale which forms on the comparative A-5 sample. The main difference between the two alloys is that steel A contains cobalt and more molybdenum. The effects of cobalt additions on oxidation resistance are currently being investigated in the Cooperation in Science and Technology programme in Europe (Ennis, 1999). It is thought that cobalt promotes the formation of a stable oxide layer. The oxide film formed on B-10 (231 h at 600 °C) is about 0.025 mm thick.

6.1 Effect of Chromium Content

The addition of chromium to ferritic steels has been shown to improve the oxidation resistance. This was demonstrated by Solberg *et al.* (1942) who compared the metal loss of a series of ferritic steels at 593 and 649 °C. The steels listed in Table 6.2 were tested in bar form in contact with steam for 200, 500, 1000 and 2000 hours. The results of the tests carried out are shown in Table 6.3. The original average penetration results have been converted from inches to microns.

These results have been plotted in Fig. 6.6 to show the general trend that the corro-

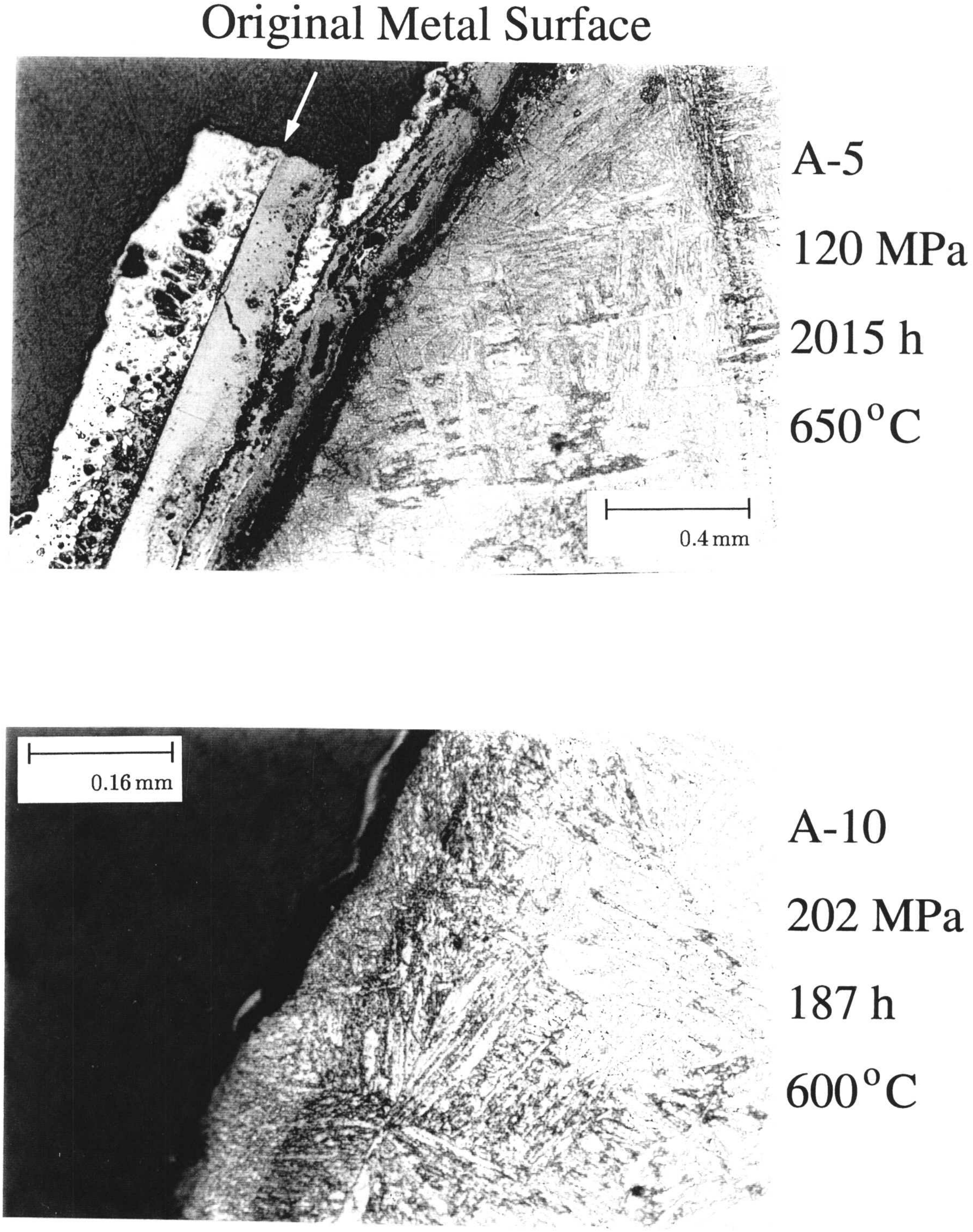

Fig. 6.4 Microstructure of oxide scale on specimens A-5 and A-10.

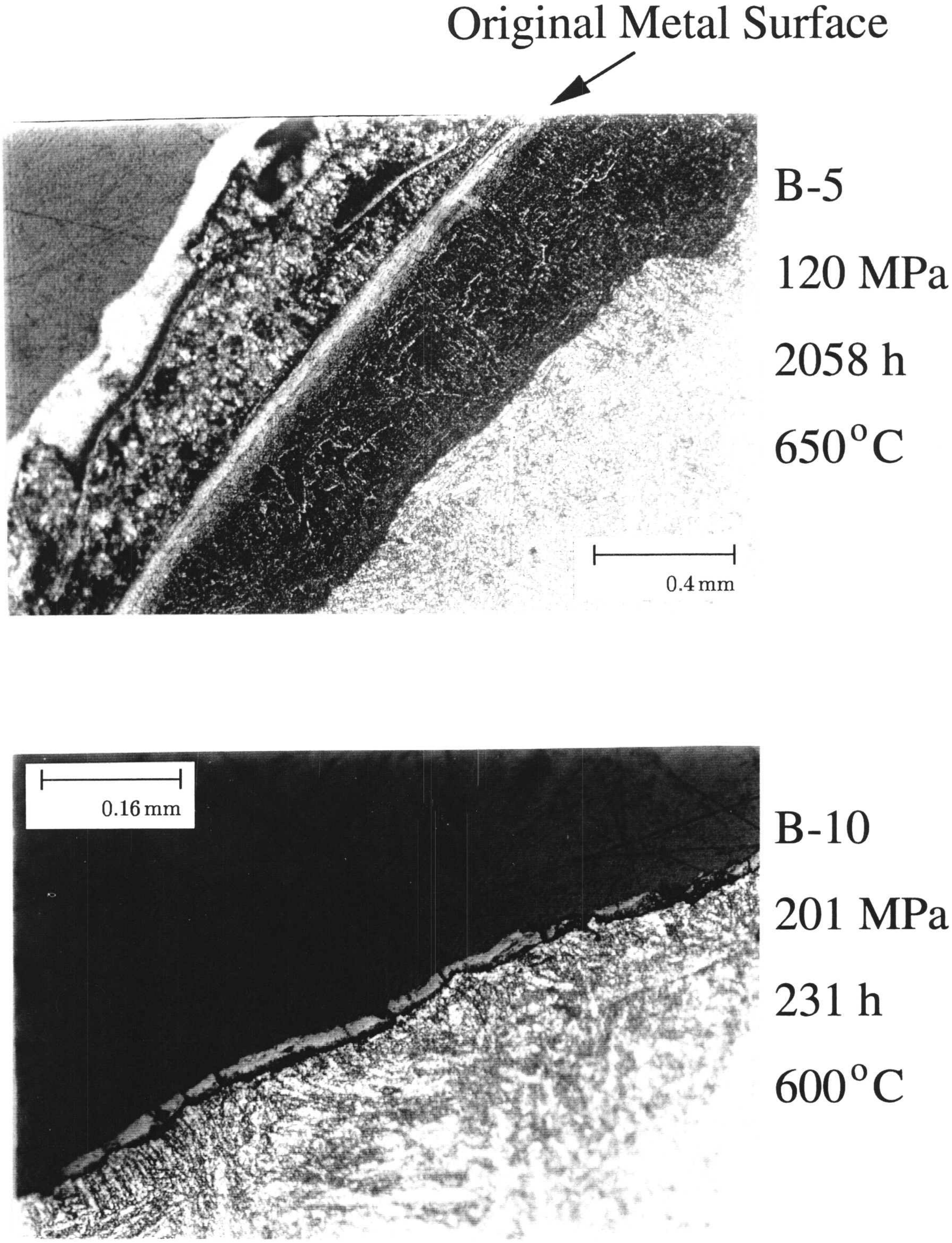

Fig. 6.5 Microstructure of oxide scale on specimens B-5 and B-10.

Steel	C	Mn	P	S	Si	Cr	Ni	Mo
SAE 1010	0.08	0.30	0.017	0.034	-	-	-	-
1.25 Cr-Moly	0.11	0.43	0.012	0.012	0.80	1.22	-	0.53
2 Cr-Moly	0.11	0.47	0.017	0.016	0.40	1.98	-	0.51
3 Cr-Moly	0.11	0.51	0.014	0.016	0.36	2.95	-	0.98
4.6 Cr-Moly	0.12	0.41	0.017	0.016	0.28	4.60	-	0.54
9 Cr-Moly	0.11	0.38	0.010	0.016	0.27	9.00	-	1.22
12 Cr-Moly	0.05	1.19	0.021	0.025	0.38	11.92	-	-
18 Cr 8 Ni	0.07	0.36	0.015	0.012	0.39	18.62	9.9	-

Table 6.2: Compositions (wt%) of steel bars tested in contact with steam at 593 °C (Solberg *et al.*, 1942).

Steel	200 hours		500 h		1000 h		2000 h	
	No. of Samples	Ave. Pen. (μm)	No.	Ave. Pen. (μm)	No.	Ave. Pen. (μm)	No.	Ave. Pen. (μm)
SAE 1010	18	20.98	8	31.45	13	34.24	16	43.18
1.25 Cr-Moly	6	20.02	4	20.22	-	-	8	29.69
2 Cr-Moly	8	18.75	8	20.60	5	34.26	8	29.54
3 Cr-Moly	7	19.00	5	20.62	8	34.24	8	28.73
4.6 Cr-Moly	6	15.34	-	-	5	23.95	8	24.28
9 Cr-Moly	3	8.23	4	11.66	7	12.32	4	17.63
12 Cr-Moly	8	2.41	3	3.10	8	2.31	4	1.143
18 Cr 8 Ni	8	0.56	4	0.48	8	2.01	8	0.30

Table 6.3 Average penetration of corrosion of steel bars tested in contact with steam at 593 °C (Solberg *et al.*, 1942). These data have been plotted in Fig. 6.6.

sion decreases as the chromium content increases. The high chromium steels are extremely corrosion-resistant but the lower chromium steels are susceptible to corrosion. The corrosion experienced is very rapid during the first 100 hours after which the layer of the corrosion products retards the oxidation rate. Therefore the majority of the corrosion in this case takes place in the first 500 hours.

Tests at 649 °C on cast steels of varying chromium content were also carried out by Solberg *et al.* (1942). The composition of these steels and the average penetration are listed

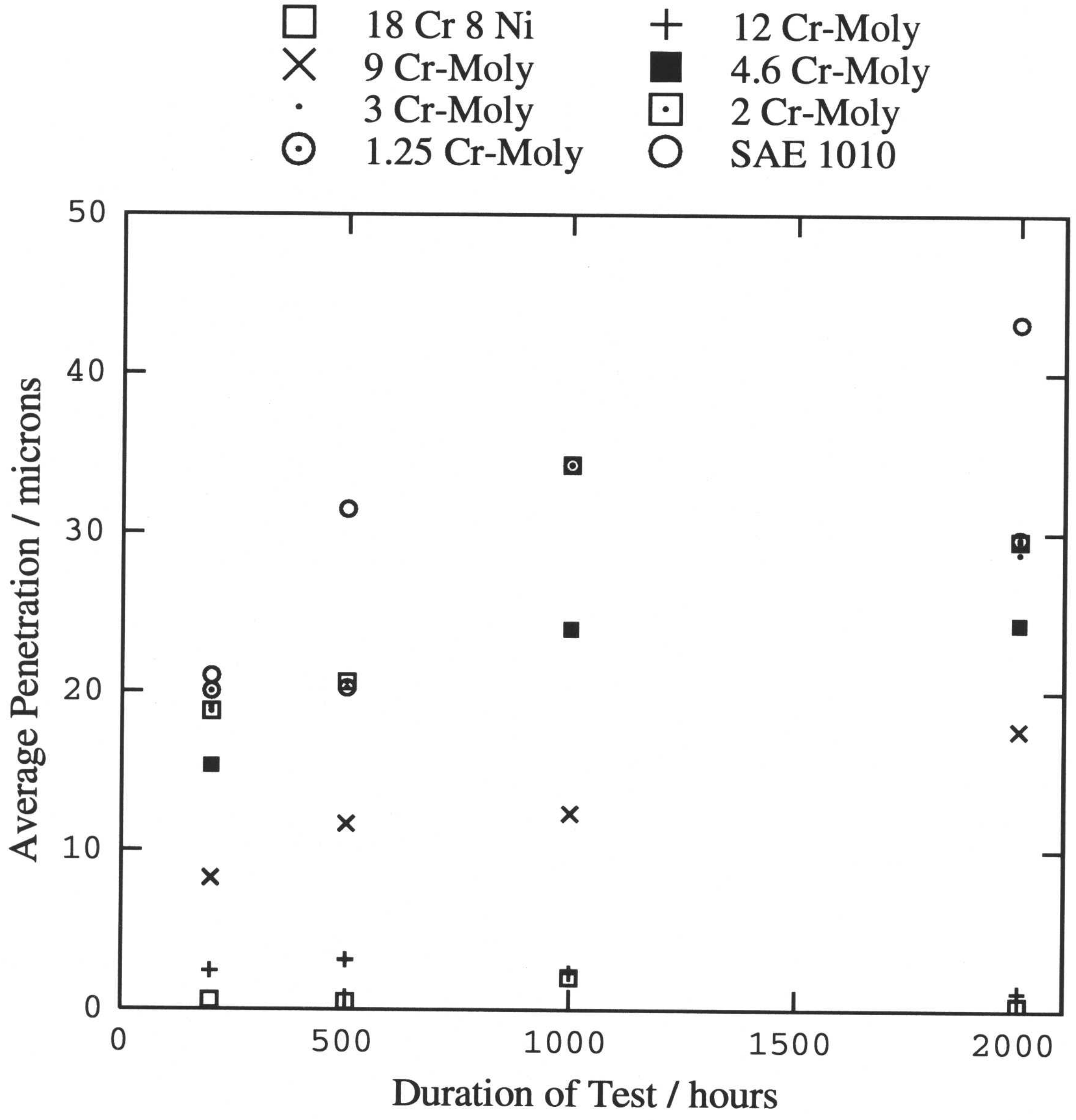

Fig. 6.6 Corrosion of steel bars in contact with steam at 593 °C.

in Table 6.4. The tests were carried out for 570 hours. It can be clearly seen from the average penetration of corrosion that the increase in temperature has a severe effect on the oxidation rate. Comparison of the 9 wt%Cr steels tested at 593 and 649 °C for 500 hours and 570 hours respectively show that the average penetration has almost doubled from 11.66 μm to 22.35 μm. The rate of corrosion is shown to reduce with increasing chromium content again.

Rohrig *et al.* (1944) also showed that addition of chromium improves the steam oxidation resistance of ferrous alloys and that ferritic alloys with high chromium weight percents were adequately resistant at 593 °C.

The improvement of these steels with chromium addition is less apparent when corrosion

C (wt%)	Mn	P	S	Si	Cr	Ni	Mo	No. of Samples	Ave. Pen. (μm)
0.24	0.95	0.020	0.010	0.44	-	-	-	2	299.72
0.25	0.75	0.022	0.018	0.44	-	-	-	2	289.31
0.21	0.64	0.020	0.012	0.43	-	-	0.49	2	318.01
0.20	0.71	0.020	0.015	0.37	-	-	0.49	2	266.45
0.35	0.61	0.021	0.010	0.45	0.64	2.13	0.26	2	251.97
0.28	0.62	0.018	0.010	0.44	0.73	2.25	0.26	2	257.05
0.22	0.65	0.032	0.010	0.77	5.07	-	0.47	1	108.97
0.27	0.63	0.025	0.010	0.87	5.49	-	0.43	2	100.33
0.11	0.43	0.012	0.011	0.92	7.33	-	0.59	2	43.94
0.23	1.05	0.032	0.015	0.84	9.09	-	1.56	5	22.35

Table 6.4: Compositions of cast steels tested in contact with steam at 649 °C for 570 hours (Solberg *et al.*, 1942).

is evaluated in terms of scale thickness rather than metal loss. Eberle *et al.* (1964) used this evaluation on the scaling of eight ferritic superheater steels in steam at 554 °C and 160 atm. for 36 000 hours. Although a slight trend towards decreasing scale thickness with increasing chromium content was observed, the scale thicknesses of the eight steels varied little. The results of the analysis are shown in Table 6.5.

Steel	Scale Thickness μm	Scale Thickness Range, μm
SA-210 C-Steel	160	125-160
$\frac{1}{2}$Mo	150	125-150
$\frac{1}{2}$Cr$\frac{1}{2}$Mo	125	125-165
1$\frac{1}{4}$Cr$\frac{1}{2}$Mo	135	135-165
2$\frac{1}{4}$Cr$\frac{1}{2}$Mo	135	125-145
5Cr$\frac{1}{2}$Mo	125	110-150
7Cr$\frac{1}{2}$Mo	120	120-125
9Cr1Mo	120	120-145

Table 6.5: Metallographically measured scale thicknesses on exposure to steam at 554 °C and 160 atm. for 36 000 hours (Eberle *et al.*, 1964).

The scale thickness presented in Table 6.5 was only measured at one location and the range represents measurements from a number of locations. SA-210 C-Steel and $\frac{1}{2}$Mo are chromium free steels. These observations are also confirmed by Ennis *et al.* (1998) who have plotted the parabolic rate constants determined at 600 and 650 °C as a function of chromium content. The parabolic rate constant is the gradient of the straight line formed by plotting the weight gain against the square root of time. The tests were carried out in a simulated combustion gas on the steels summarised in Table 6.6.

Steel	C (wt%)	Mn	Si	Cr	Ni	Mo	W
12Cr1MoV (high-Cr)	0.20	0.56	0.28	11.60	0.69	0.87	-
12Cr1MoV (low-Cr)	0.20	0.5	-	10.2	0.7	0.9	-
P91	0.10	0.46	0.8	8.10	0.33	0.92	-
P92 (NF616)	0.11	0.45	0.04	8.96	0.06	0.7	1.84
E911	0.12	0.51	0.20	8.85	0.24	0.94	0.96
AISI 316LN	0.02	1.66	0.38	16.48	12.8	2.25	-

Table 6.6: Composition of alloys examined by Ennis *et al.* (1998).

The results of the analysis are shown in Fig. 6.7. There is no large change in the rate constant until the amount of chromium in the steel exceeds approximately 9 wt%. There is then a large decrease in the rate constant between 9-12 wt% Cr at 600 and 650 °C. This is an important factor when the composition ranges of steels are considered, such as that of HCM12A for which the defined range for chromium is 10.00-12.50 wt%. If an alloy is made with a chromium content less than 11 wt% a nominal 12 wt% Cr steel may display similar oxidation properties as a 9 wt% Cr steel.

In summary, from the evidence presented here the design of a steel for use at 650 °C requires a chromium content of at least 11 wt%. This is simply demonstrated by the work carried out by Iseda *et al.* (1989). Fig. 6.8 shows the comparison of scale thickness between three alloys of varying chromium content. The $2\frac{1}{4}$Cr1Mo steel forms the thickest scale with increasing temperature. The 9Cr1Mo scale appears to increase thickness at a greater rate with temperatures above 650 °C. HCM12 has the thinnest oxidation scale.

6.2 Effect of Silicon Content

The effect of silicon additions to ferritic alloys also has consequences on oxidation. Silicon additions are beneficial to oxidation resistance but, as pointed out by Brun *et al.* (1999), can

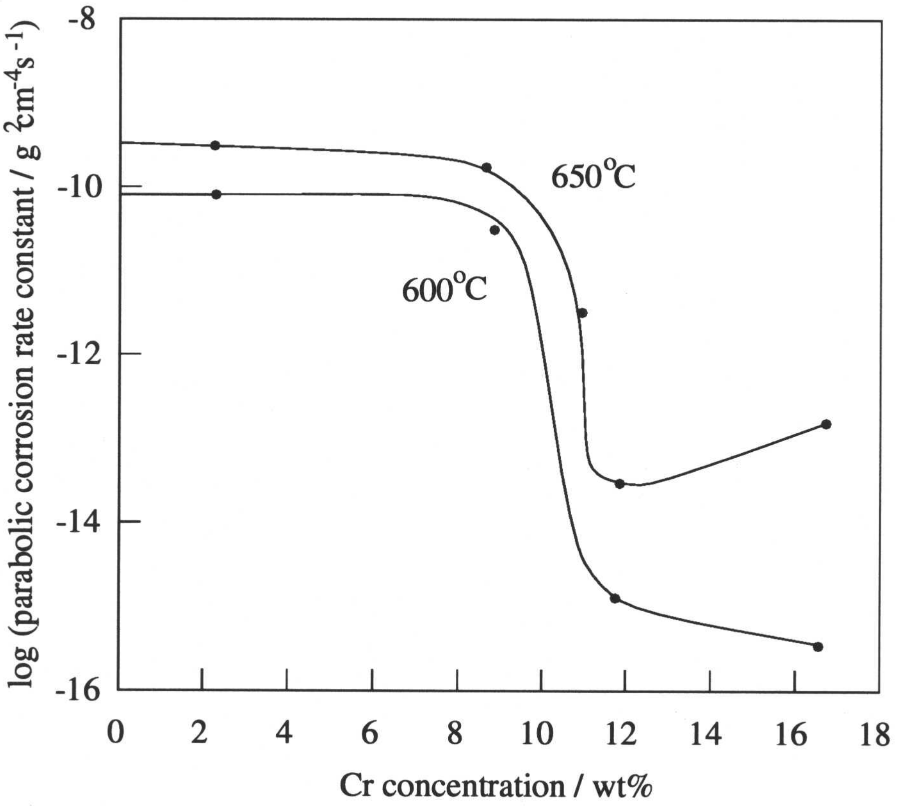

Fig. 6.7 The effect of chromium content on the oxidation rate of steels at 600 and 650 °C in simulated combustion gas (adapted from Ennis *et al.*, 1998).

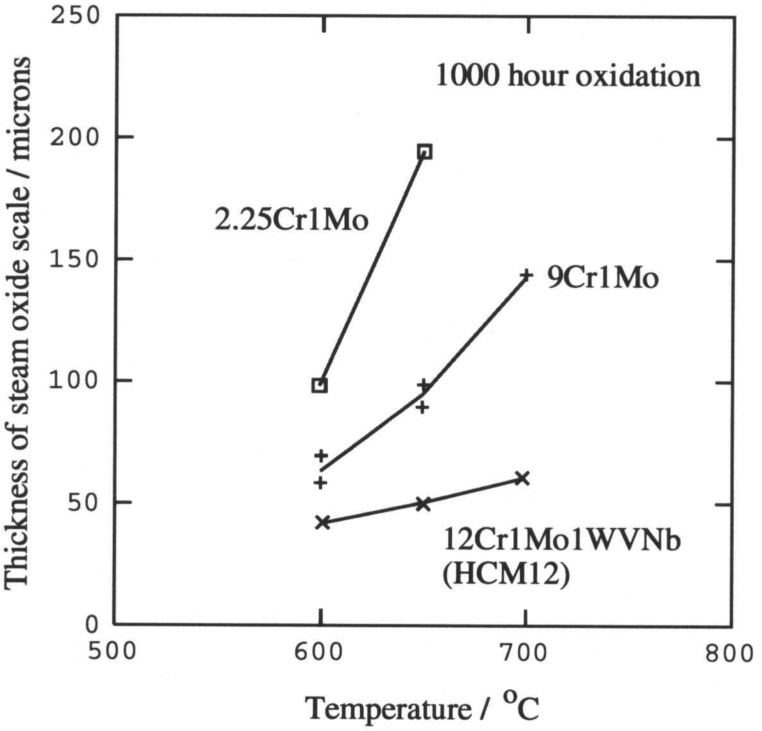

Fig. 6.8 Steam oxidation of various ferritic steels after 1000 hours at various temperatures (adapted from Iseda *et al.*, 1989).

also be detrimental to the creep properties of the alloy due to δ-ferrite formation. Robertson *et al.* (1989) reported on the silicon concentrations required to form a protective scale at 650 °C for ferritic steels. The requirements were stated as 0.8 and 0.4 wt% Si for 9 and 12 wt% Cr steels respectively.

A selection of modified NF616 alloys of varying silicon content were subjected to steam oxidation at 1 atm. and 650 °C by Tamura *et al.* (1995). The oxide scale thickness followed a parabolic rate law, the thickness decreasing with increasing silicon content (Fig. 6.9). There was an optimum silicon content of approximately 0.3 wt% Si to give acceptable corrosion resistance and mechanical strength. This is because a silicon content above 0.4 wt% lead to a deterioration in tensile strength, creep rupture strength and toughness due to δ-ferrite formation. For comparison, the scale thickness which forms on a $2\frac{1}{4}$Cr1Mo steel is also represented in Fig. 6.9.

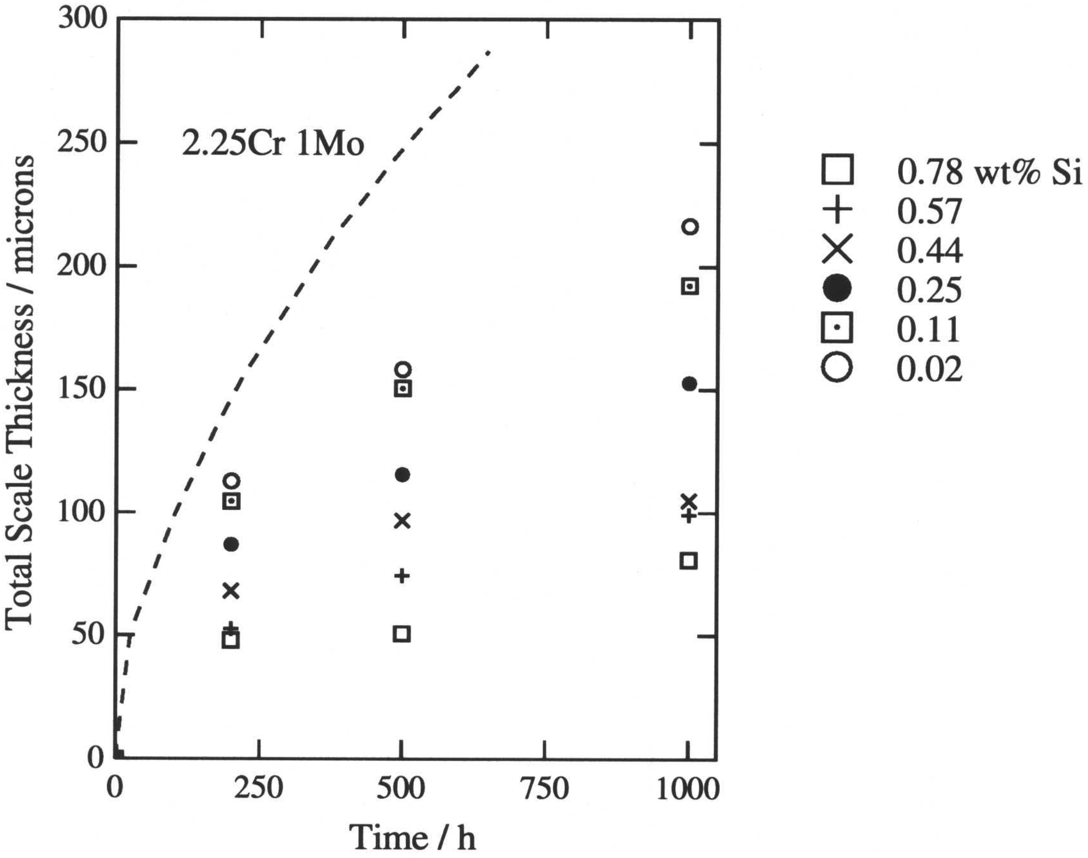

Fig. 6.9 Scale thickness of NF616 with varying Si additions after 650 °C steam oxidation tests (adapted from Tamura *et al.*, 1995).

The main problem with silicon additions is the formation of δ-ferrite, which has been examined by Cool and Bhadeshia (1997) and Abe *et al.*, (1998). A phase diagram was calculated using Thermo-Calc for a model steel, comparing the amount of δ-ferrite which forms during austenitisation with chromium and silicon content (Abe *et al.*, 1998). The results of this analysis are shown in Fig. 6.10. This clearly shows that the addition of high chromium or silicon content will provide problems with δ-ferrite formation during austenitisation around 1100 °C. To combat this, the addition of austenite stabilising elements are required.

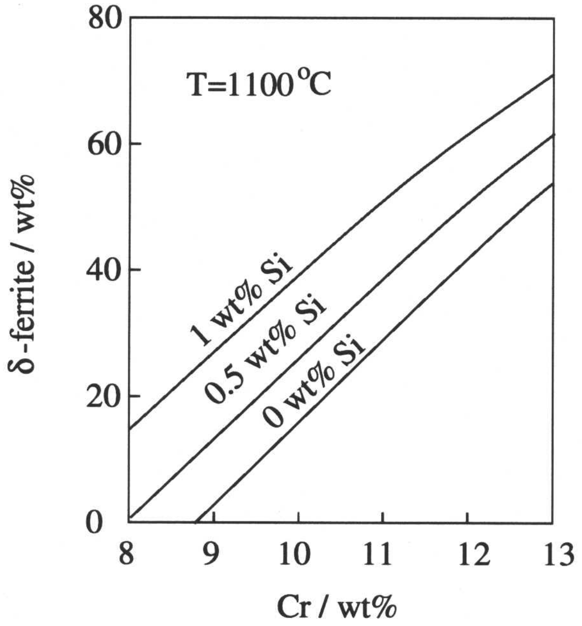

Fig. 6.10 δ-ferrite volume as a function of Cr wt% for a steel of composition 0.08C 0/1Si 0.5Mn 8/13Cr 3W 0.2V 0.05Nb 0.005B 0.05N wt% (adapted from Abe *et al.*, 1998).

The effect of silicon on oxidation was also reported by Abe in his review paper (2000a). The weight gain of a base metal 0.15C 8.5Cr 2W 0.2V 0.05Nb was investigated for varying silicon contents and also titanium and yttrium additions (Fujitsuna *et al.*, 1998). The results are shown in Fig. 6.11 and confirm the beneficial effect silicon has on oxidation resistance. The composition of the steels used in this analysis are recorded in Table 6.7.

Once again, the increase in silicon additions reduces the weight gain of the steels in question. This beneficial effect is substantially reduced at 650 °C which is particularly demonstrated by the alloy tested with 1.0 wt% Si. Titanium and yttrium additions were tested as alternatives to silicon. They both improved the oxidation resistance at 600 °C but the effect was markedly smaller at 650 °C.

It is argued that silicon improves oxidation resistance because it somehow changes the oxide layer from one which is porous to a more compact form (Abe, 2000), but further research is needed.

Steel	C (wt%)	Cr	W	Mo	V	Nb	Si	Ti	Y	Mn
Base	0.15	8.5	2	-	0.2	0.05	-	-	-	-
0.5 Si	0.15	8.5	2	-	0.2	0.05	0.5	-	-	-
1.0 Si	0.15	8.5	2	-	0.2	0.05	1	-	-	-
12 Cr	0.15	12	2	-	0.2	0.05	0.5	-	-	-
0.5 Si-0.05 Ti	0.15	8.5	2	-	0.2	0.05	0.5	0.05	-	-
0.5 Si-0.05 Y	0.15	8.5	2	-	0.2	0.05	0.5	-	0.05	-
Mod. 9 Cr	0.08	8.34	-	0.9	0.23	0.07	0.34	-	-	0.49

Table 6.7: Composition of alloys tested for oxidation weight gain by Fujitsuna *et al.* (1998) and Abe (2000a).

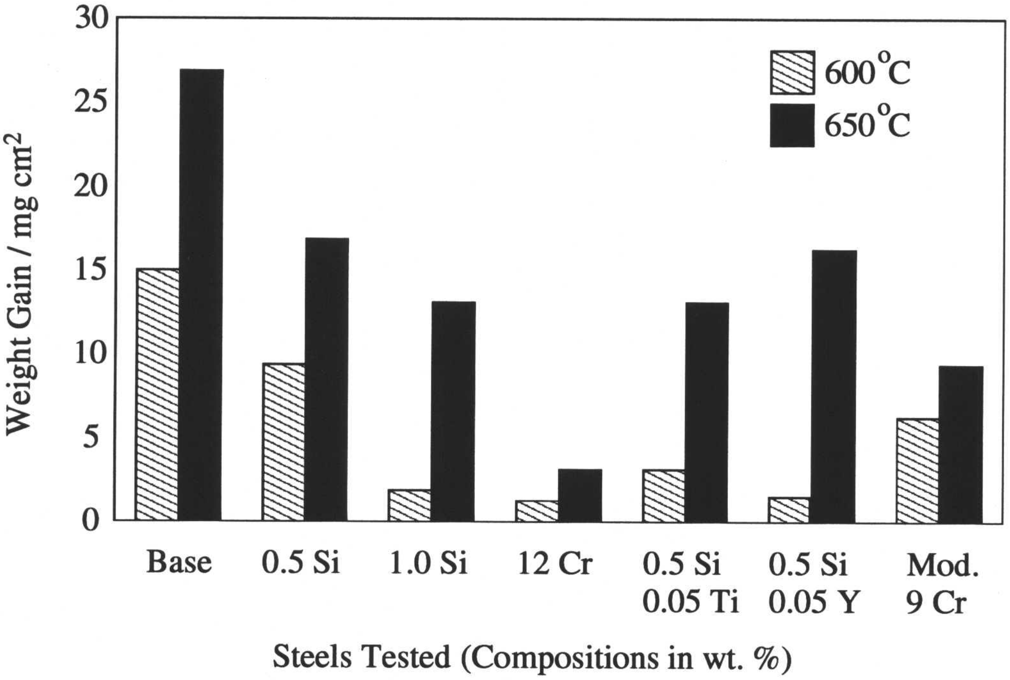

Fig. 6.11 Weight gain of steels tested during oxidation in steam for 600 hours. The base metal tested was of the composition 0.15C 8.5Cr 2W 0.2V 0.05Nb (Fujitsuna *et al.*, 1998; Abe 2000a).

6.3 Other Factors Effecting Oxidation

The parameters affecting oxidation are many and the purpose of this chapter is to explore the basics in order to design a corrosion resistant material. With this in mind, a few more interesting points concerning the oxidation of ferritic steels stand out from the published literature.

The effects of applied stress were examined by Rajendran Pillai *et al.* (2000). Oxidation under stress is important for power plant steels since they will be loaded in service. Specimens of the composition in Table 6.8 were tested at 600 °C under stresses in the range 0-40 MPa for up to 140 h.

Element	Cr	Mo	Mn	Si	P	C	S
wt%	8.9	1.05	0.6	0.4	0.034	0.079	0.005

Table 6.8: Composition of alloy tested for oxidation resistance under stress (Rajendran Pillai *et al.*, 2000).

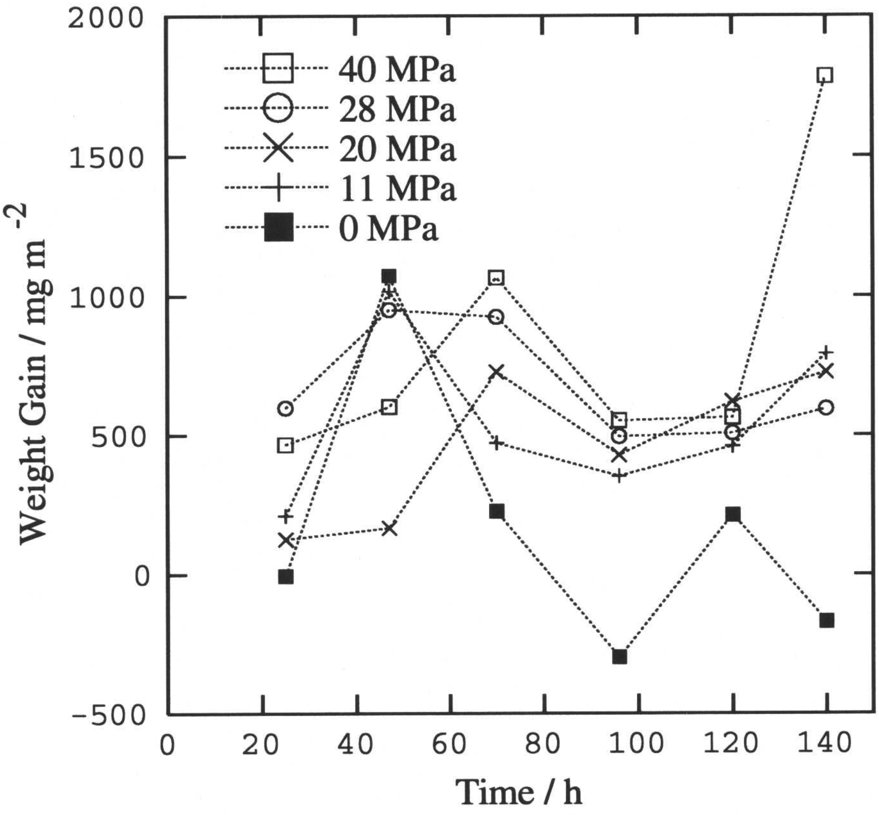

Fig. 6.12 Weight gain versus time for a 9Cr-1Mo steel at 600 °C (adapted from Rajendran Pillai *et al.*, 2000).

The results are shown in Fig. 6.12; all the specimens gained weight up to 47 hours. After this time the weight gain was reduced or there was even a weight loss due to oxide spalling. Specimens stressed at 11, 20 and 28 MPa show very similar weight gain patterns. There is an increase in weight up to 70 hours followed by spallation. The specimen subjected to 40 MPa shows similar behaviour to the lower stress specimens up to 120 hours, after which time the weight gain increases abruptly. This was attributed to cracking of the oxide scale because of the elongation of the specimen under the applied stress. This exposed fresh surfaces for oxygen to react with, causing the weight gain.

Another interesting point raised by Rajendran Pillai *et al.* (2000) was that the spalling of the oxide scale occurred mainly on cooling. This was determined by examining acoustic-emission activity, which was absent when the specimens were held at 600 °C. This is relevant for steam turbines which are often turned on and off during their service life.

The effect of tempering heat treatment temperature on oxidation resistance was examined by Singh Raman *et al.* (1993). A normalised $2\frac{1}{4}$Cr1Mo steel (Table 6.9) was tempered for 10 hours at temperatures between 600 and 750 °C. The oxidation resistance was then tested in air between 500 and 700 °C.

Element	C	Mn	Si	S	P	Cr	Mo	Ni
wt%	0.07	0.42	0.19	0.025	0.19	2.28	0.95	0.09

Table 6.9: Composition of alloy tested for oxidation resistance following a variety of tempering heat treatments (Singh Raman *et al.*, 1993).

The results for the oxidation at 700 °C are shown in Fig. 6.13, the tests at lower temperatures showed the same trends. The steels which were tempered at 600 °C and 650 °C for 10 hours show very little difference in oxidation weight gain. However, increasing the tempering heat temperature above 650 °C does cause a deterioration in the oxidation resistance. This can be explained by the degree of precipitation of chromium-based carbides such as $M_{23}C_6$ and M_7C_3 during the tempering heat treatment. At the higher temperature tempers there is substantial depletion of the chromium in the alloy matrix to form precipitates. This leads to the formation of less protective scales during service. The steel tempered at lower temperatures had less chromium removed from the matrix and so could form more stable oxide scales on testing.

6.4 Summary

The creation and testing of novel alloys A and B had distinctly highlighted the severe problem of oxidation of these steels in air. This would also be problematic in the aggressive steam environments encountered in a steam turbine.

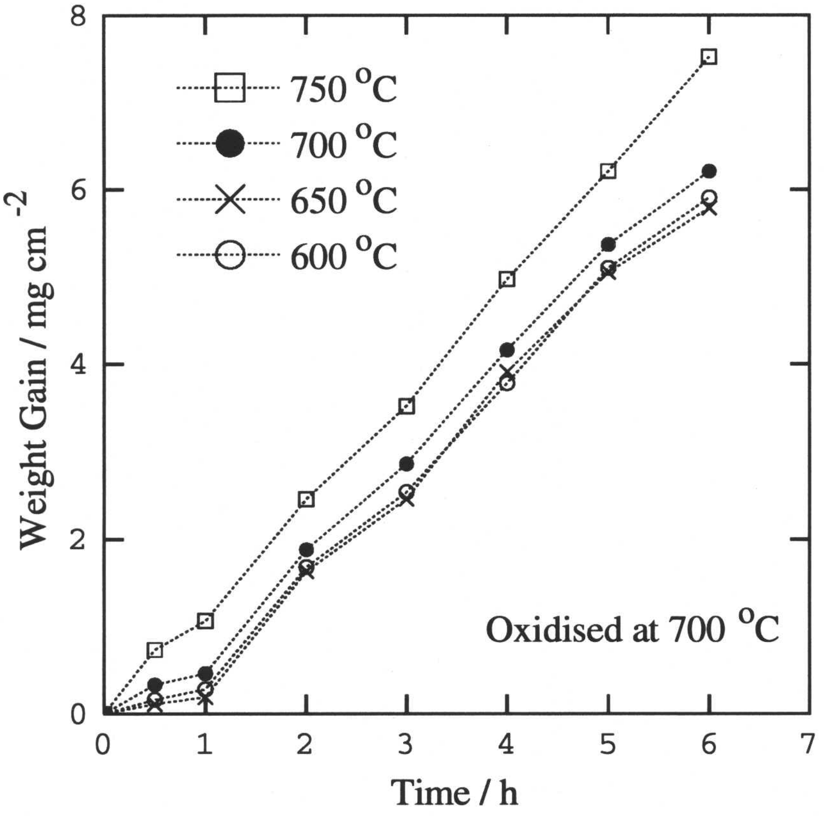

Fig. 6.13 Weight gain versus time for a $2\frac{1}{4}$Cr1Mo steel at 700 °C (adapted from Singh Raman *et al.*, 1993).

This chapter has illustrated the morphology of the oxide scales which can form on ferritic steels and the problems which may occur due to the spallation of these layers causing a loss in component section and solid particle erosion of the turbine.

Additions of chromium and silicon have be shown to be beneficial to oxidation resistance but this has to be balanced with the effect on the mechanical properties of the alloy. The main problem is caused by additions of silicon, which promotes the formation of undesirable δ-ferrite phase. Other factors shown to effect the oxidation properties were applied stresses and tempering heat treatments.

The following chapter will describe the design of a novel alloy. Information reported in this chapter will be taken into account to produce an alloy with satisfactory oxidation resistance.

CHAPTER 7

Design of Novel Alloys

We have already shown that alloys with excellent properties can be designed without resorting to experimental analysis, which is a lengthy and expensive process. The work reported in this chapter ustilises the improved models described in chapters 4 and 5, combined with knowledge of the physical metallurgy and oxidation properties of power plant steels, to propose novel alloys which should have a creep rupture strength of 100 MPa at 650 °C after 100 000 hours.

7.1 Alloy Design Philosophy

Designing an alloy, in terms of the chemical composition and pre-service heat treatments, is an extremely complicated task. Changing one parameter will invariably change the effect of one or more of the others. This problem is illustrated by a simple schematic (Fig. 7.1) of philosophy used by Abe (2000a) in the design of high chromium ferritic steels for use in steam power plant at 650 °C.

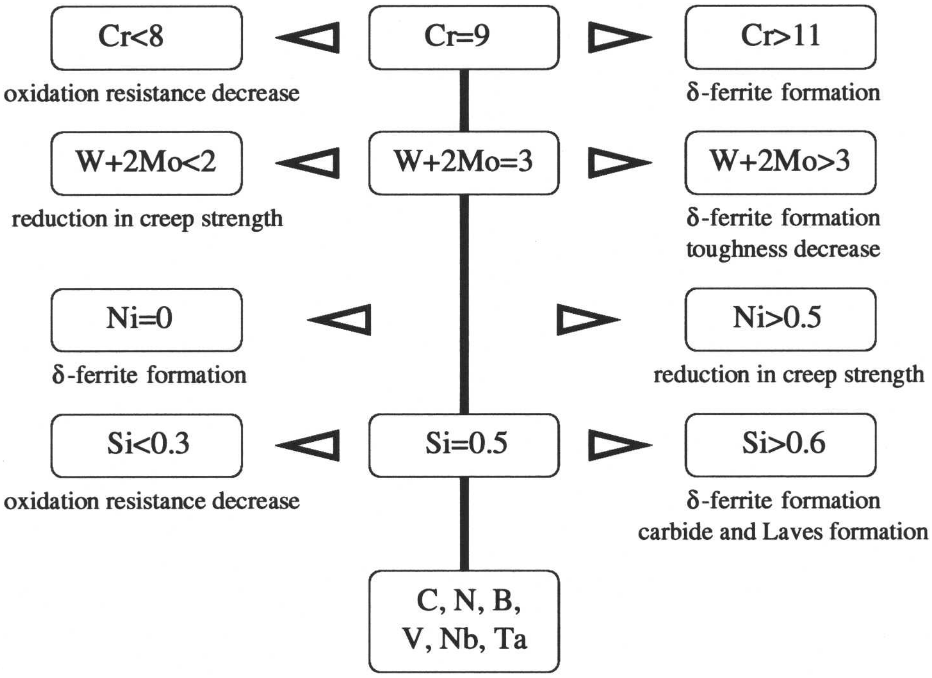

Fig. 7.1 Alloy design philosophy for high-Cr ferritic steels for service in steam power plant at 650 °C (Abe, 2000a).

It is immediately clear that many elements affect δ-ferrite formation, an important factor for creep strength. One of the fundamental problems of this design is the desirable increase in chromium and silicon concentrations to enhance oxidation resistance. Unfortunately, these increases can lead to the formation of disastrous amounts of δ-ferrite. To overcome this problem, austenite stabilising elements such as nickel can be added, but this element can have a deleterious effect on creep properties. The content of tungsten and molybdenum are also highlighted as important factors on alloy properties. Both are strong carbide formers and have to be carefully balanced to avoid the formation of undesirable phases. The optimisation of C, N and B is extremely important in terms of the phases formed and the long-term creep rupture strength.

It can be seen from Table 5.1 that many elements can be reasonably included in any analysis of power plant steels, and this list is by no means exhaustive. Elements such as titanium and neodymium could be added as well as hafnium, iridium and palladium (Igarashi *et al.*, 1997; Abe *et al.*, 1998).

In contrast the experiment based approach of Abe and co-workers, the design process used in this research was based on models of creep rupture properties, phase stability and the kinetic evolution of microstructure. The iterative design process followed three basic steps:

1) A neural network model was used to examine the effect of composition and heat treatment on the long term creep rupture strength. The oxidation resistance of the alloy was also taken into account at this stage. Once the required conditions had been achieved, step 2 was applied.

2) This step involved the examination of the process window using phase stability calculations (MTDATA), *i.e.* to ensure the alloy is fully austenitised during normalisation, that unreasonable amounts of δ-ferrite do not form and that precipitates such as VN dissolve (§2.3.4). If these criteria were not satisfied step 1 was repeated. If a suitable alloy had been found step 3 was applied.

3) Determination of the evolution of phases during service. This gave some idea of the rate of formation of certain precipitates such as M_2X and $M_{23}C_6$ and also if Laves phase would form. This was achieved using the kinetic theory due to Robson and Bhadeshia (1997a, 1997b). If the results of this stage were acceptable the alloy could be considered to be a strong candidate to achieve the desired properties.

These steps are combined in a flow chart in Fig. 7.2, illustrating the iterative process. This design process requires a starting point. Alloys A and B, which had performed so well seemed an obvious choice.

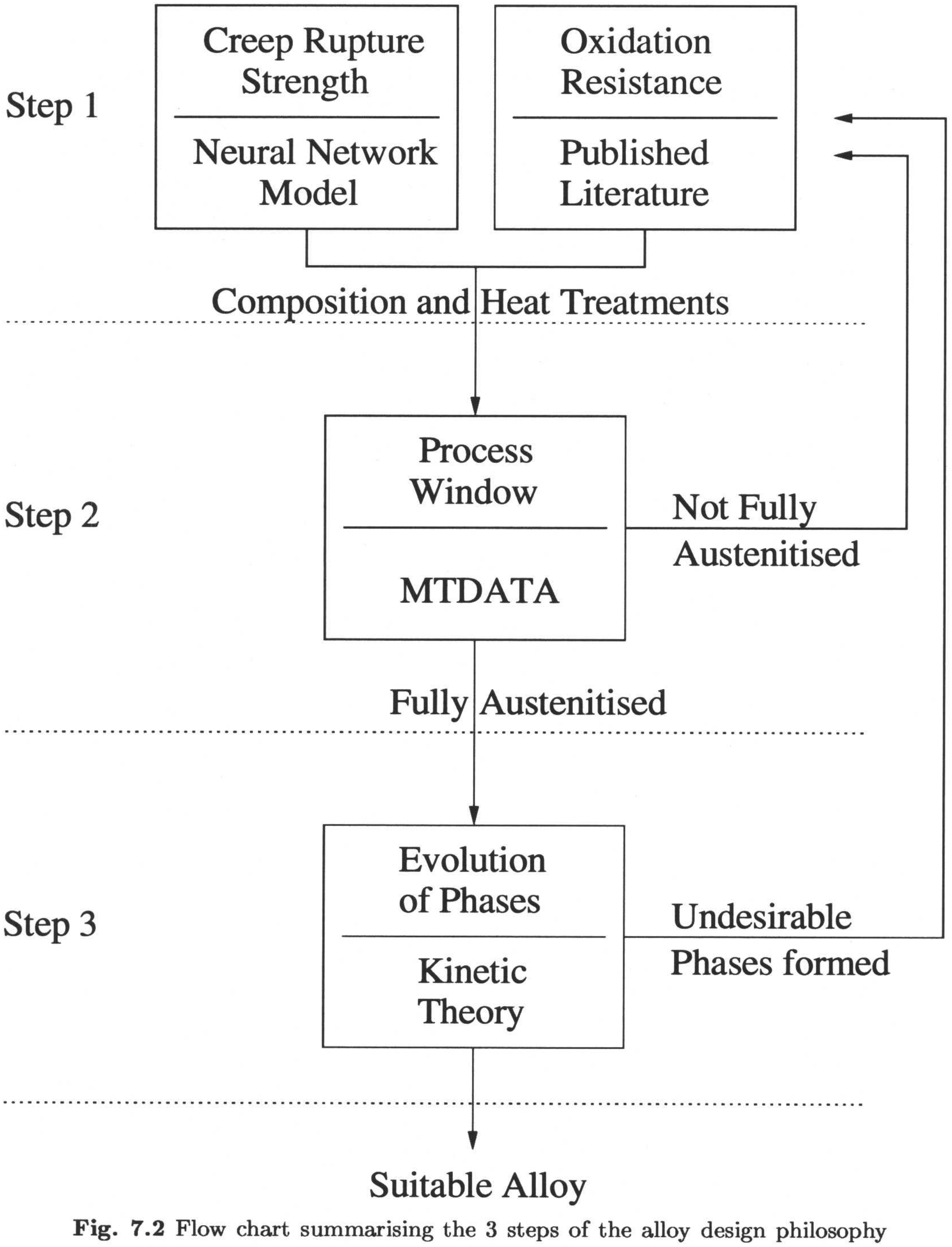

Fig. 7.2 Flow chart summarising the 3 steps of the alloy design philosophy applied in this chapter.

7.2 The Design of a Novel Alloy

Applying step 1 to A and B was carried out by first varying individual elements to examine the effect that they have on the creep rupture strength. Fig. 7.3 shows the model perceived effects of boron and carbon on the creep rupture strength of steel A at 650 °C after 100 000 hours. Increasing boron content gives a steady rise in creep rupture strength up to 0.025 wt% but the error bounds associated with the prediction above 0.01 wt% are very large, due to the sparsity of data on high boron concentrations. Carbon also shows a steady increase in creep rupture strength as a function of concentration.

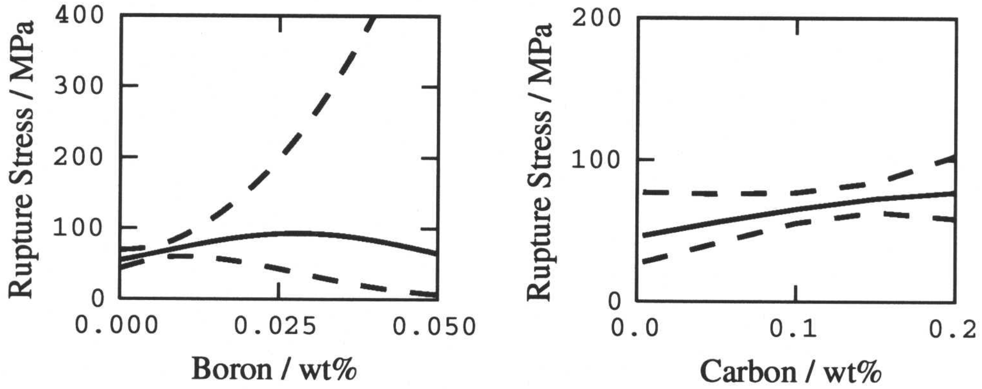

Fig. 7.3 Effect of aluminium and boron on the creep rupture strength of steel A at 650 °C after 100 000 hours. Predictions made by neural network analysis.

Further examples of this elemental analysis for steel A are shown in Fig. 7.4 and Fig. 7.5, illustrating some interesting points for the alloy design. The creep rupture strength is insensitive to cobalt. This is expected - after all, steel A is richer in Co than steel B and yet they have similar creep strength. The creep rupture strength reaches a maximum at about 9-10 wt% Cr but the drop at higher concentrations is gradual. Copper shows a definite increase in the creep strength whereas manganese and molybdenum both reduce $\sigma_{100000h}$. There are geat uncertainties with nickel and experimental evidence (§2.3.3) indicates that it has a detrimental effect on creep properties.

Niobium additions are optimum at 0.1 wt% and nitrogen at about 0.06 wt%. However the nitrogen content has been varied with 0.01 wt% niobium, an increase in this or other nitride forming elements may change the effect of nitrogen. The ability to examine this possibility with the neural network model highlights the power of this technique when dealing with interacting variables. Silicon does not affect the creep strength but the addition of sulphur shows a decrease within large error bounds. Tungsten shows no real improvement in creep strength in this system. Vanadium is a key element due to the stability of its nitride, so it is encouraging that it is found to improve the creep rupture strength.

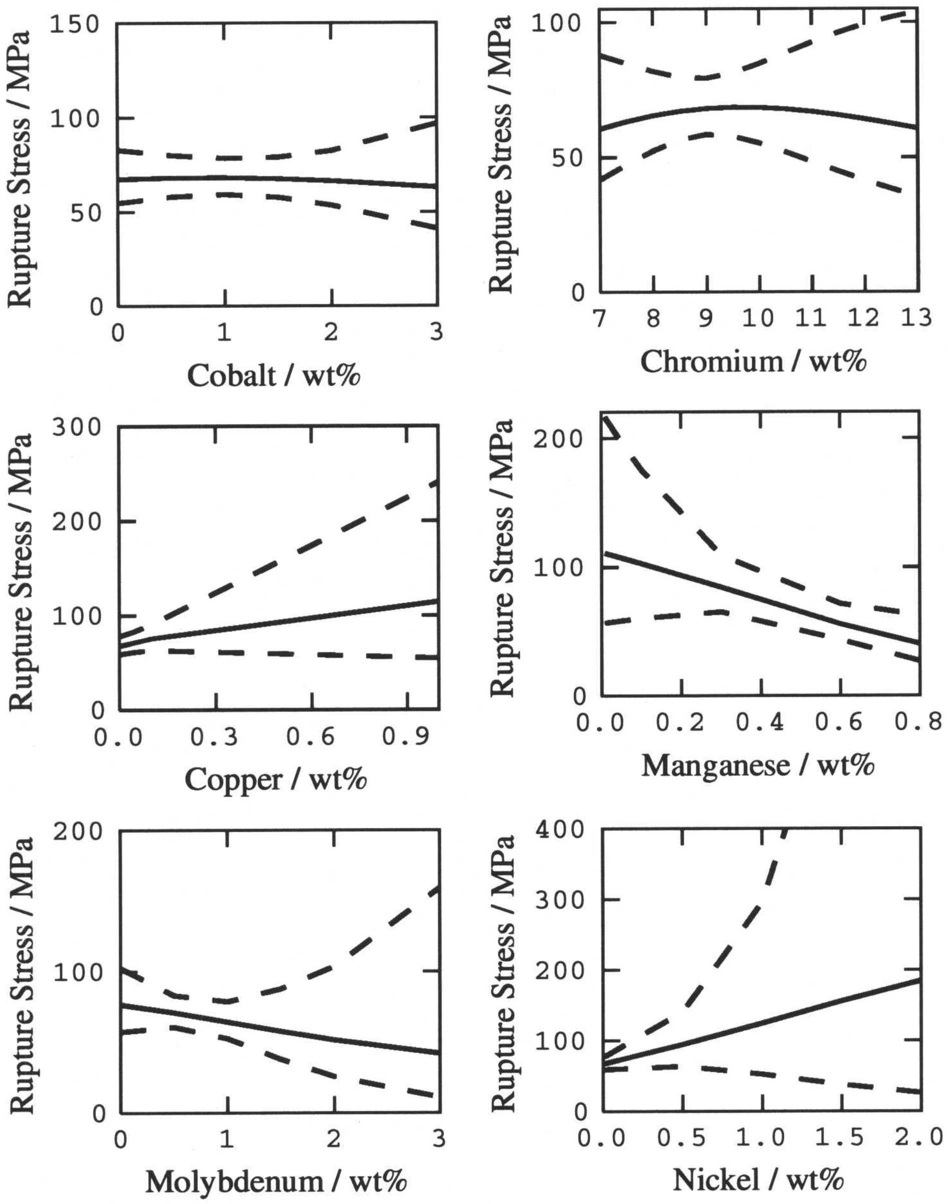

Fig. 7.4 Variation in the creep rupture strength of steel A at 650 °C after 100 000 hours, with changes in the alloy content of certain elements.

With these results in mind, a number of composition changes were hypothesized with the goal of improving the long-term creep rupture strength. These changes were made with a specific intention of keeping error bounds as small as possible (Fig. 7.6). In the context of steel A, the boron and niobium contents were increased and manganese and molybdenum were reduced to improve creep rupture strength. The chromium content was boosted to enhance the oxidation resistance and tungsten has been lowered to retard δ-ferrite formation.

A comparison of creep strength of steel A and the proposed alloy C is illustrated in Fig. 7.7. The predicted creep rupture strength meets the 100 MPa at 100 000 h requirement. The error

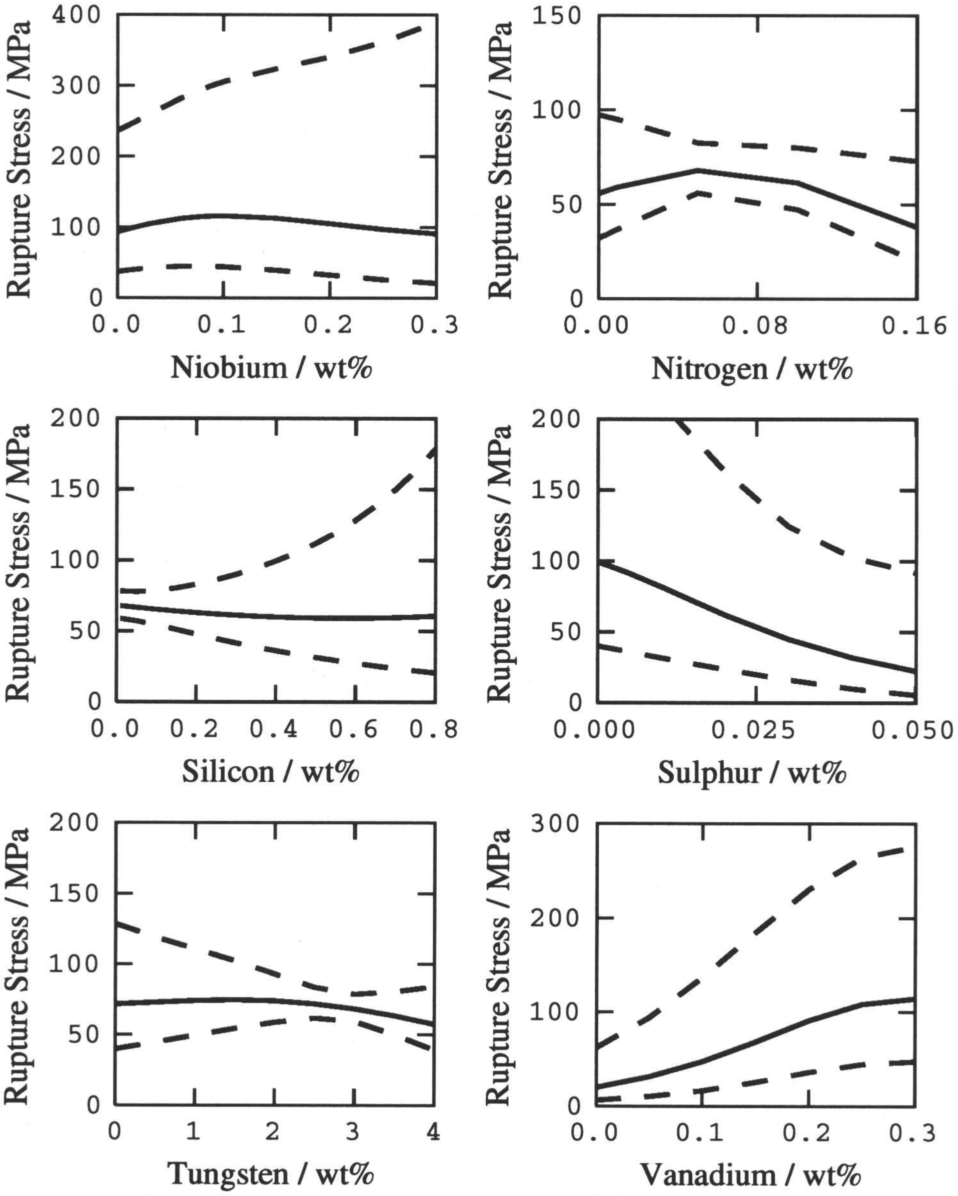

Fig. 7.5 Variation in the creep rupture strength of steel A at 650 °C after 100 000 hours, with changes in the alloy content of certain elements.

bounds also show that the worst case scenario for this alloy is that its predicted creep rupture strength would be the same as that of steel A.

MTDATA was then used to determine the available process window for the normalisation heat treatment to be applied to the steel. The phases allowed in this analysis are listed in Table 7.1, with a view to estimating the temperature at which δ-ferrite forms and VN dissolves. This is illustrated in Fig. 7.8. The austenitisation heat treatment for steel A is carried out at 1475 K (Table 4.2) which is suitable for alloy C since δ-ferrite does not begin to form until 1475 K and VN was found to dissolve at 1300 K.

Boron	0.008 wt%	▻	0.01 wt%
Chromium	9 wt%	▻	10 wt%
Manganese	0.48 wt%	▻	0.3 wt%
Molybdenum	0.75 wt%	▻	0.3 wt%
Niobium	0.01 wt%	▻	0.1 wt%
Tungsten	3 wt%	▻	2 wt%

Fig. 7.6 Compositional changes applied to steel A to improve the creep rupture strength. The original composition of steel A can be found in Table 4.1.

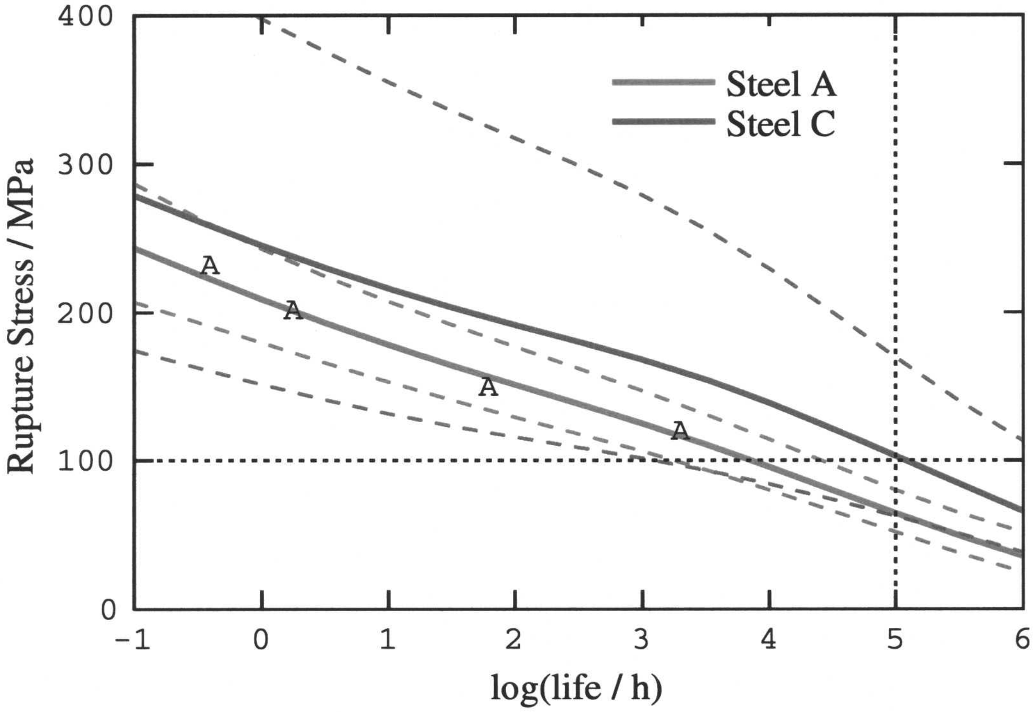

Fig. 7.7 Comparison of creep rupture strength predictions for steel A and steel C with the changes shown in Fig. 7.6.

Ferrite	$M_{23}C_6$
Austenite	VN
Laves phase	

Table 7.1: Phases included in MTDATA analysis for step 2 of design process.

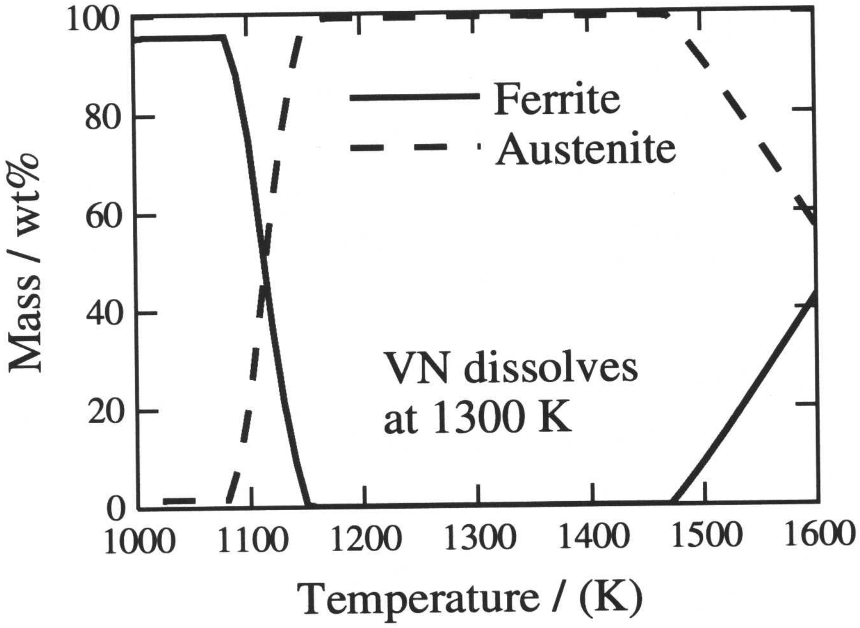

Fig. 7.8 MTDATA analysis of novel alloy C. δ-ferrite is found not to form until 1475 K.

However, the increase in silicon content to improve oxidation resistance was yet to be applied and this would affect the austenitisation. The silicon content was increased from 0.014 wt% to 0.2 wt% and the analysis using MTDATA was repeated (Fig. 7.9). This increase made it impossible to make the alloy fully austenitic. It was therefore necessary to stabilise the austenite. Nickel is excluded because it is detrimental to the creep strength. This leaves elements such as copper, cobalt and nitrogen.

Fig. 7.10 shows the results on manganese and cobalt. Increases in the content of Mn are detrimental to creep properties but Co stabilises austenite without leading to a deterioration in $\sigma_{100000h}$. Increases in nitrogen and copper were also found to be acceptable in terms of the

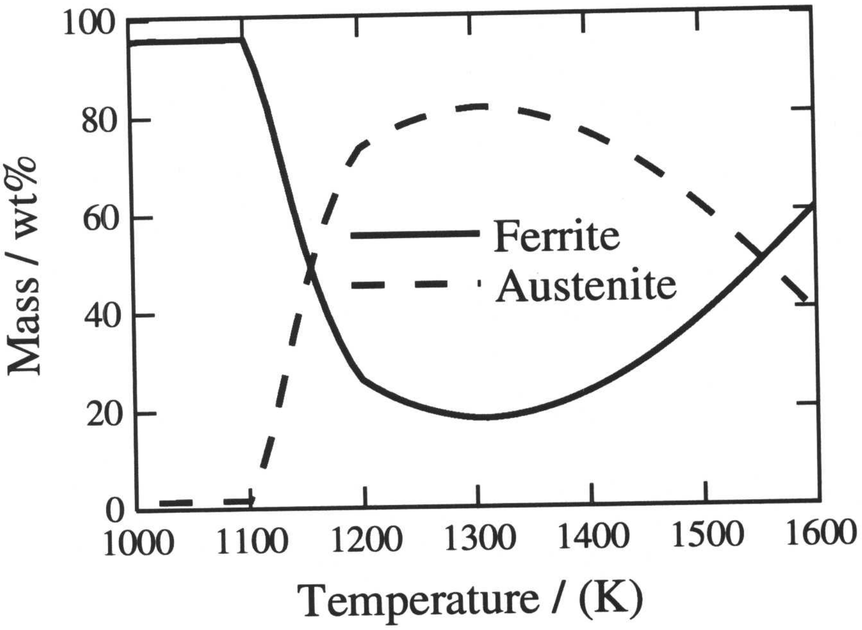

Fig. 7.9 MTDATA analysis of novel alloy C with silicon content increased from 0.014 wt% to 0.2 wt%. It is now not possible to fully austenitise the alloy.

creep rupture strength. The effect of these elements on the austenitisation of the steel was then fully investigated using MTDATA. As a result of this analysis a number of changes were made to the alloy composition, listed in full in Table 7.2.

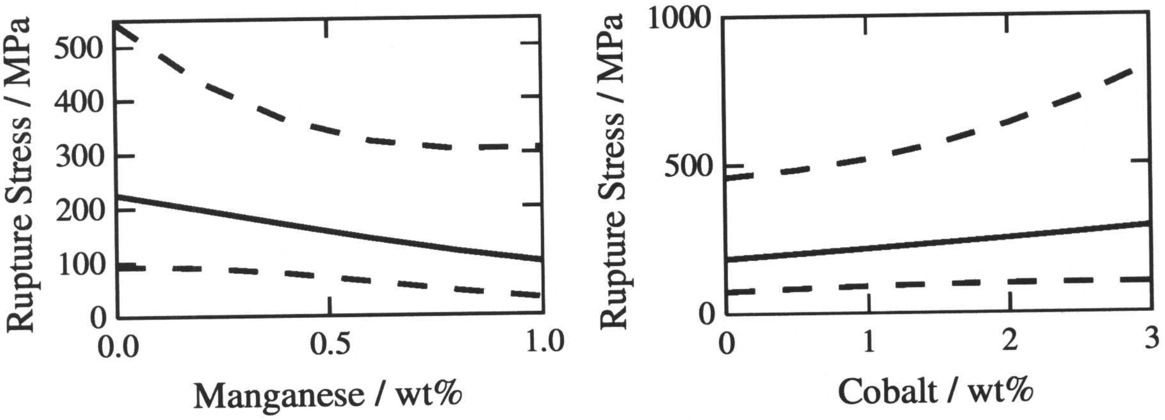

Fig. 7.10 Neural network predictions showing the effect of manganese and cobalt on the creep rupture strength of alloy C.

It was found that δ-ferrite would not form until approximately 1450 K, shown in Fig. 7.11. VN precipitates were estimated to dissolve at 1370 K. Therefore a normalisation heat treatment between 1370 K and 1450 K would be acceptable. Analysis of the effect of the normalisation

C	0.12	Ni	<0.02
Si	0.15	Cu	1.5
Mn	0.3	V	0.2
P	0	Nb	0.1
S	0	N	0.1
Cr	11	Al	0
Mo	0.3	B	0.01
W	2	Co	4

Table 7.2: Composition (wt%) of novel alloy C accounting for the formation of δ-ferrite due to increased silicon levels.

heat treatment temperature on creep rupture strength using the neural network for this alloy shows that increasing the temperature to 1450 K would be beneficial.

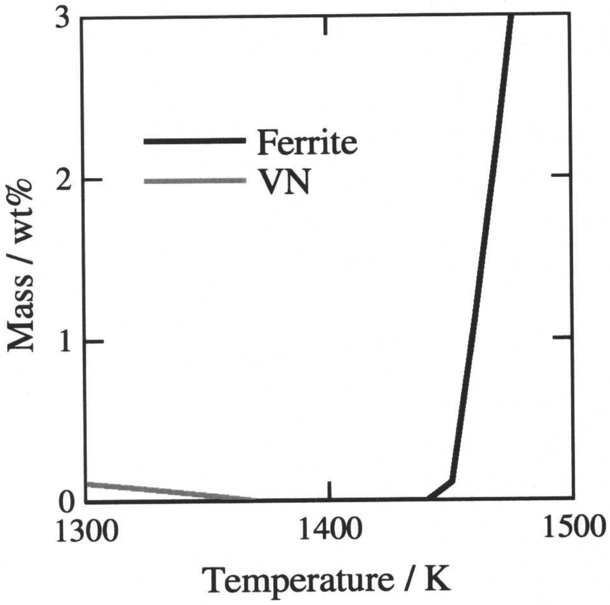

Fig. 7.11 Temperatures of dissolution for VN and formation for δ-ferrite for alloy C presented in Table 7.2. Analysis from MTDATA.

The predicted creep rupture strength for this alloy is shown in Fig. 7.12 but the uncertainties are overwhelming. This is unfortunately expected since the composition being examined is novel. The mean prediction is unlikely to be correct, as evident from the very high strength at short times. The input which contributes most to the uncertainty may be copper. The maximum copper content in any composition in the database is 0.87 wt%, which is much lower than the 1.5 wt% required in this alloy. If it is assumed that copper additions are not detrimental to creep strength, as suggested by physical metallurgy (Tsuchiyama *et al.*, 2000), it can be removed from the set of inputs to the neural network to obtain a more reasonable prediction.

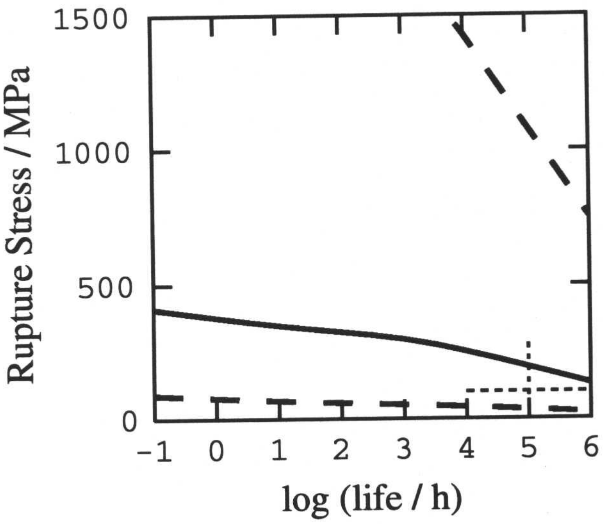

Fig. 7.12 Predicted creep rupture strength of alloy C at 650 °C.

Fig. 7.13 illustrates much more plausible results with copper removed from the analysis. The creep rupture strength is above the design requirements.

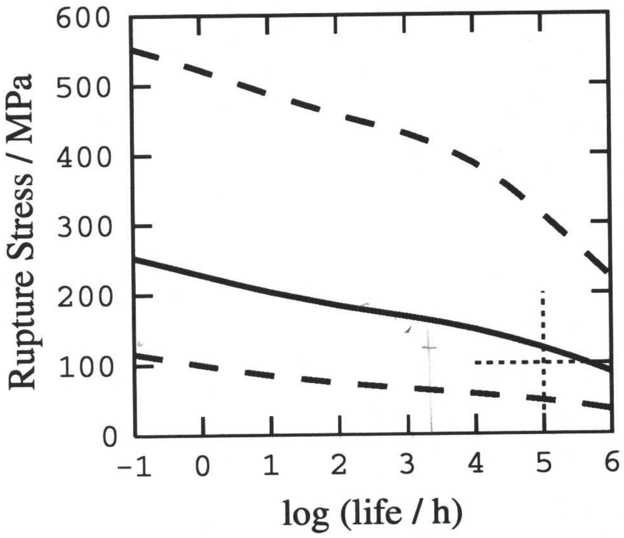

Fig. 7.13 Predicted creep rupture strength of alloy C minus copper content at 650 °C.

The theory described in §4.1 was then used to estimate the evolution of the microstructure in service. Fig. 7.14 illustrates the changes expected at 650 °C; cementite steadily dissolves as M_2X and $M_{23}C_6$ form. M_2X falls to a stable level after formation and its composition is indicated to be Cr_2N by MTDATA. The driving force for the formation of Laves phase was found to be very low for this alloy and consequently was found not to form for at least 10^6 hours.

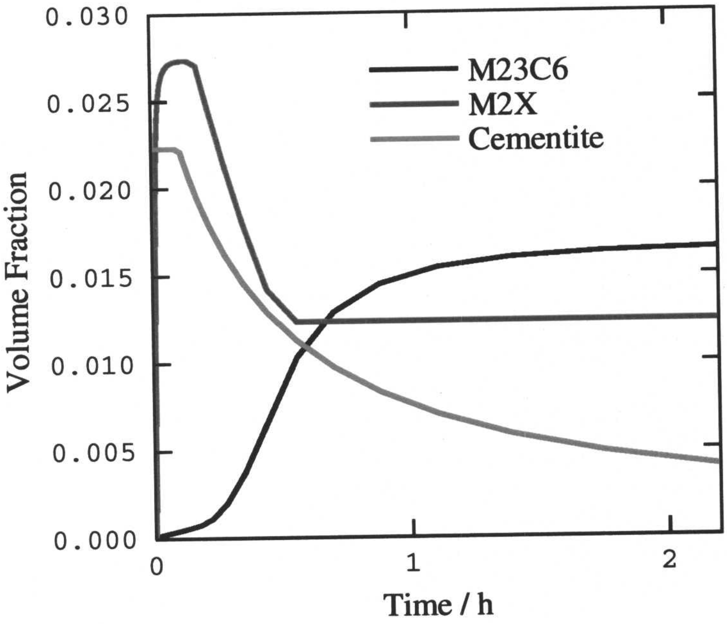

Fig. 7.14 Calculated variation in fraction of precipitates as a function of time for alloy C at 650 °C.

The finalised alloy composition has recently been manufactured by *Corus* as part of the Foresight Technology Project. The alloy is called steel C but two alloys with differing Ni contents (Table 7.3) were produced for commercial reasons, *i.e.*, it may not in industrial practice be possible to keep the Ni as low as <0.02wt%. Thus, both the nickel contents are higher than recommended by the alloy design due to manufacturing difficulties.

As the compositions of these steels differ from that of steel C, MTDATA was utilised again to examine the process window available for normalisation and to finalise the heat treatments to be applied to the steels. It was apparent that these steels could not be fully austenitised (Fig. 7.15). However, an acceptable amount of δ-ferrite would be formed if the alloys were normalised at 1400 K, a temperature which should also cause the dissolution of most of the VN precipitates.

The final heat treatment conditions are that the ingots must be homogenised for two days at 1300 K followed by normalising at 1400 K for 2 hours. They will then be tempered at 940

Steel	C1	C2
C (wt%)	0.14	0.14
Si	0.2	0.2
Mn	0.35	0.35
P	0.011	0.011
S	0.004	0.004
Cr	10.8	10.9
Mo	0.31	0.31
W	2.03	1.96
Ni	0.15	0.35
Cu	1.38	1.4
V	0.2	0.2
Nb	0.11	0.11
N	0.079	0.082
Al	0.013	0.015
B	0.010	0.010
Co	3.90	3.91

Table 7.3: Compositions (wt%) of the two versions of steel C created by *Corus* with differing Ni contents.

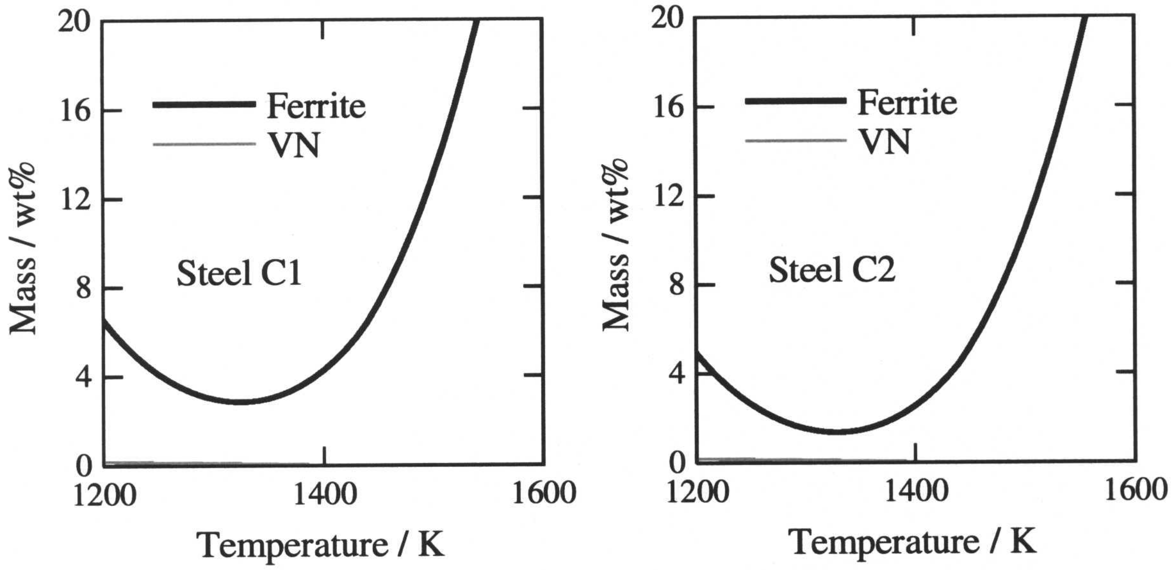

Fig. 7.15 Temperatures of dissolution for VN formation for δ-ferrite for steels C1 and C2.

K for 8 hours. This temperature was chosen from the MTDATA results showing that the alloy would form austenite at temperatures greater than this. However, the tempering temperature is subject to change pending dilatometry results to determine Ac1, the temperature at which austenite forms on heating. Once the steels have been heat treated they will be mechanically tested, including creep tests at Swansea University.

7.3 Further Design

Although an exciting new alloy has been designed, it will take about three years to complete a reasonable set of tests. Therefore, every effort has been made to validate the models, either by proposing new experiments or by testing against the latest published data.

7.3.1 Novel Heat Treatment

As shown in §2.3.4, the tempering temperature and time can have an important effect on the microstructure of power plant steels. High temperatures are required for stress relief but also cause coarsening, particularly at the austenite grain boundaries which then become covered by a locally recrystallized zone which in turn leads to a drastic deterioration in creep rupture life. It is possible that low temperature temper could induce a more homogeneous dispersion of precipitates; this could be followed by a short higher temperature temper for stress relief as illustrated in Fig. 7.16.

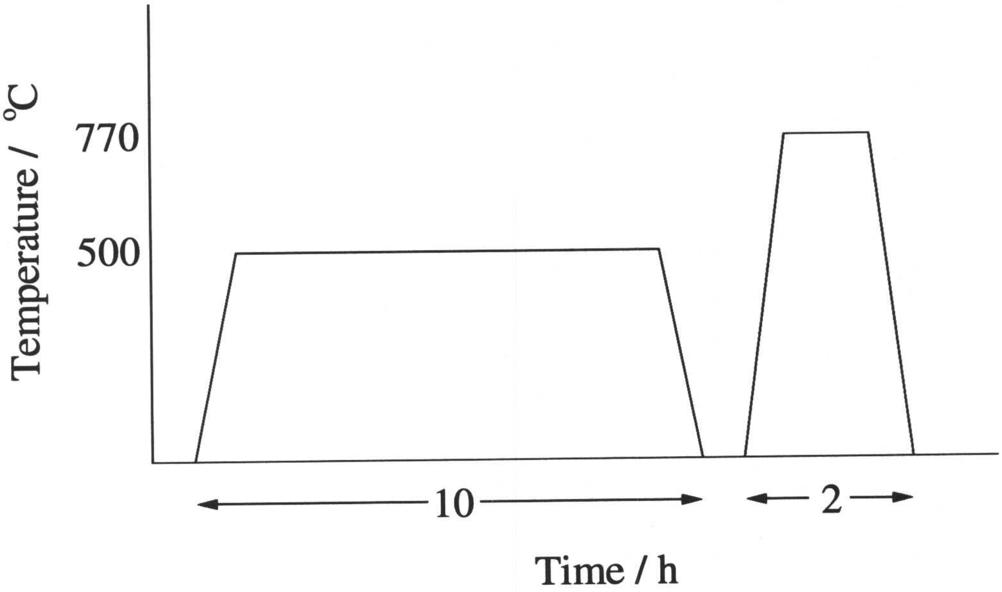

Fig. 7.16 Double tempering heat treatment.

The heat treatment normally applied to NF616 involves a normalisation for 2 h at 1065 °C followed by a short 2 h tempering at 770 °C . The calculated creep rupture strength at 650 °C of NF616 for the dual heat treatment shown in Fig. 7.16 are plotted on Fig. 7.17. It appears that the dual heat treatment should give an improved resistance to creep although the uncertainties are large. The experiments were proposed to Nippon Steel Corporation who conducted the tests; the results are given in Table 7.4.

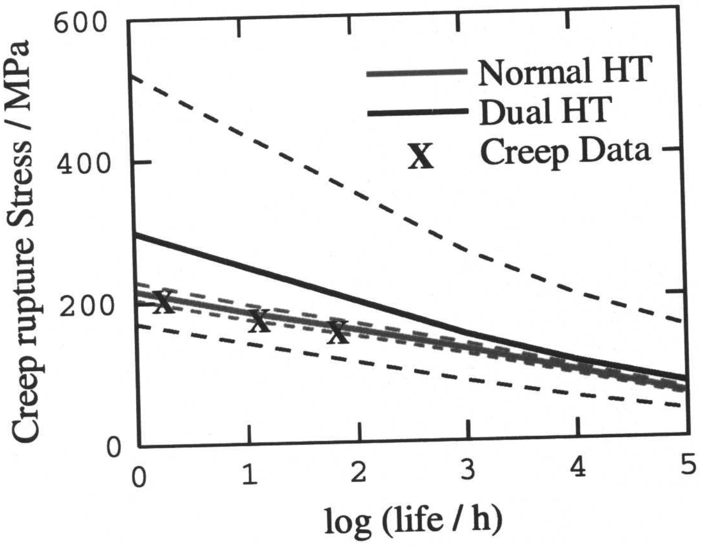

Fig. 7.17 Prediction of creep rupture strength for NF616 at 650 °C comparing the effect of a normal heat treatment (HT) and a dual heat treatment.

Temp. (°C)	Stress (MPa)	Rupture Time (h)
650	200	1.8
650	170	12.9
650	151	65.9

Table 7.4: Creep data obtained on our behalf by Nippon Steel for dual heat-treated NF616.

The data show that there is no discernible improvement in the short term creep rupture strength due to the dual heat treatment. Although disappointing, it could be argued that the effects of a heterogeneous distribution of precipitates, as expected in the conventionally treated samples, are best seen in long term, low stress tests.

7.3.2 Effect of Tungsten

The effect of tungsten and molybdenum on the creep properties of a 9 wt% Cr steel have recently been examined by Abe (2000b). The W-Mo balance was varied as shown in Table 7.5 and then the steels were creep tested at 650 °C. The results are shown in Fig. 7.18. For short-term tests, an increase in the W content whilst reducing Mo content increased the creep rupture strength. However, this effect does not persist at 10 000 hours, the creep rupture strength of the high-tungsten alloys drops markedly.

Steel	C	Si	Mn	Cr	W	Mo	V	Nb	B	N
3W-0Mo	0.076	0.32	0.50	8.95	3.05	<0.01	0.23	0.051	0.003	0.0490
2.8W-0.1Mo	0.076	0.30	0.51	8.94	2.79	0.10	0.22	0.051	0.004	0.0473
2.4W-0.3Mo	0.076	0.30	0.52	9.04	2.51	0.33	0.21	0.053	0.003	0.0498
1.8W-0.6Mo	0.076	0.31	0.52	8.98	1.85	0.62	0.22	0.049	0.003	0.0492
0W-1.5Mo	0.078	0.32	0.50	9.08	<0.01	1.54	0.20	0.045	0.003	0.0487

Table 7.5: Compositions (wt%) of alloys creep tested by Abe (2000b) to examine the effect of W and Mo on the creep rupture strength of a 9 wt% Cr steel. The alloys were normalised at 1100 °C for 30 minutes and air cooled, followed by a tempering at 800 °C for 1 hour and then air cooled.

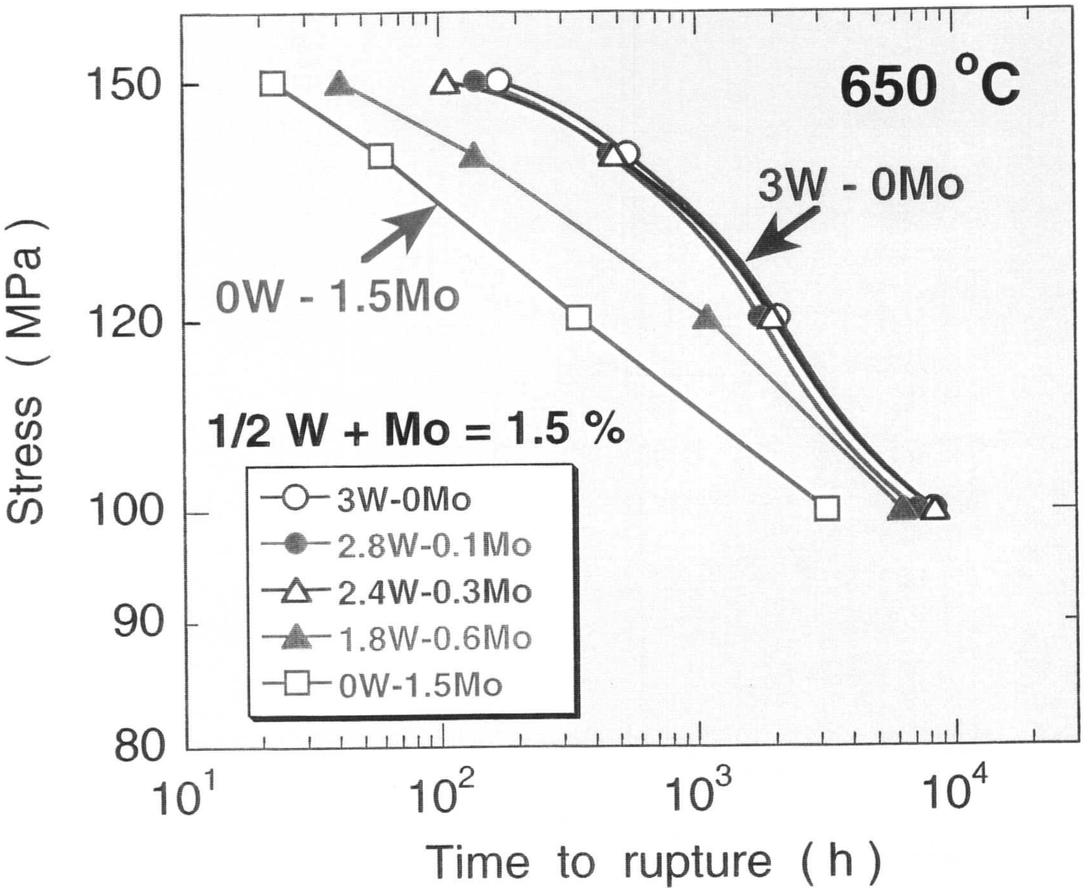

Fig. 7.18 Effect of W-Mo balance on the creep rupture strength of 9 wt% Cr alloys (Abe, 2000b).

Neural network predictions show a remarkable agreement with these new data (Fig. 7.19) both in terms of the quantitative agreement, and with respect to the detailed shape of the creep rupture curves for the high W alloys. This emphasizes an important point, that Abe's creep rupture experiments were not really necessary - the neural network which was made available to him could have been used to produce the results. The small uncertainties in the predictions indicates that experiments are not needed.

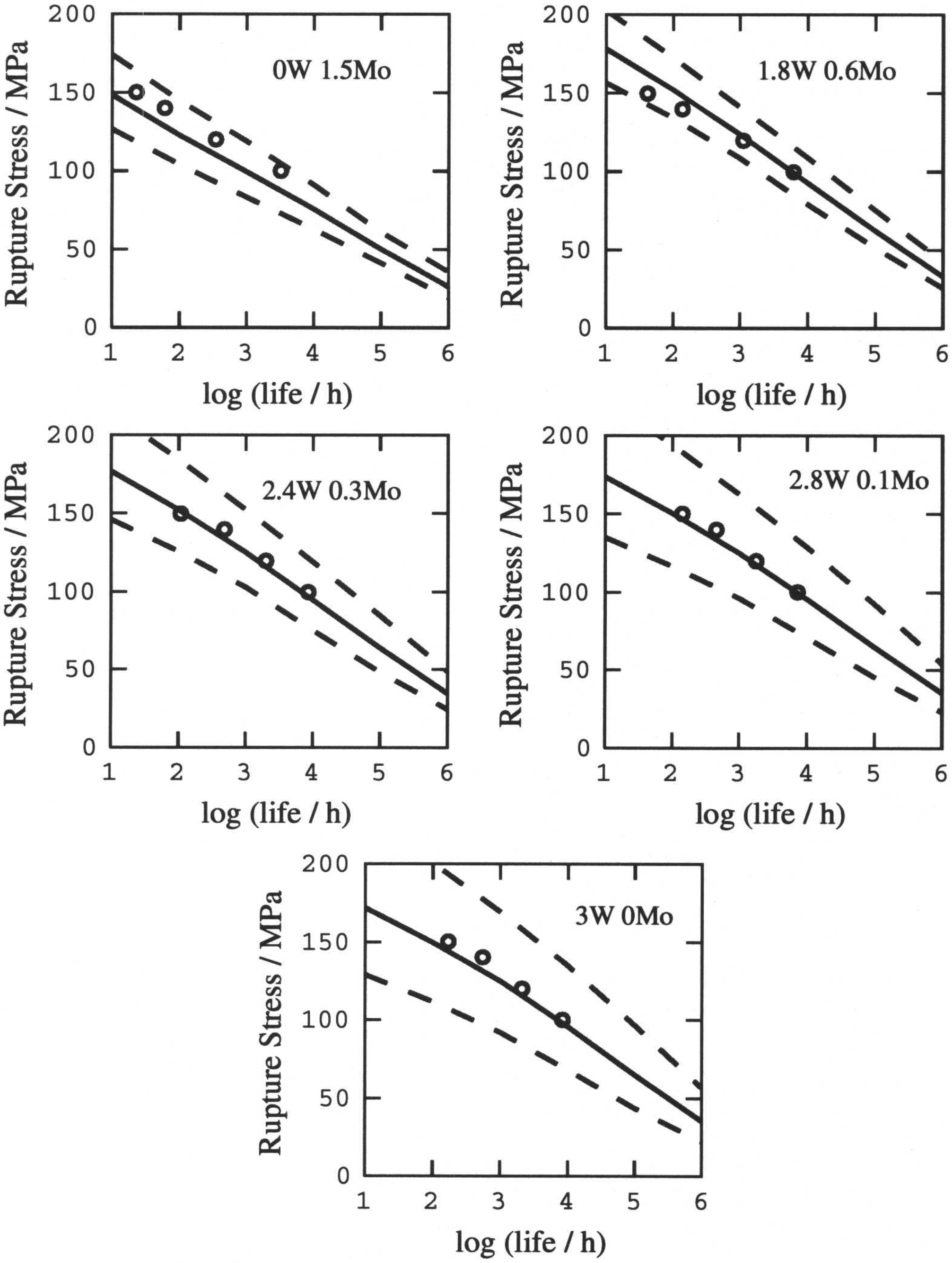

Fig. 7.19 Neural network predictions of effect of W-Mo balance on creep rupture strength of 9 wt% Cr steels at 650 °C.

7.3.3 Some Further Designs

Much of this work has demonstrated the complexity of the these power plant steels and highlighted the fact that there is still much to learn about their properties. Further calculations have been carried out to suggest alternative alloys capable of meeting the 650 °C design requirements.

Our work indicates that tungsten does not add much to the strength of NF616 judging from results presented in Appendix 2. Alloy D, whose composition is listed in Table 7.6, should have better properties when compared with NF616.

Steel	NF616	Alloy D
C (wt%)	0.1	0.12
Si	0.04	0.15
Mn	0.46	0.3
P	0.008	0.001
S	0.001	0.0005
Cr	8.96	11
Mo	0.47	0.5
W	1.84	0.5
Ni	0.06	0.01
Cu	-	1.5
V	0.2	0.25
Nb	0.069	0.05
N	0.051	0.075
Al	0.007	0.001
B	0.001	0.01
Co	-	3
Ta	-	0.1

Table 7.6: Comparison of compositions (wt%) of NF616 and alloy D.

The silicon and chromium contents have been increased to improve the oxidation resistance. Cobalt and copper have also been increased to control the amount of δ-ferrite formed during heat treatment. Manganese, nickel, phosphorus, sulphur and aluminium concentrations have been kept low to improve creep resistance. Tungsten has been reduced to 0.5 wt% to retard δ-ferrite but retain any solid solution strengthening effect. Vanadium has been increased to improve creep strength via the formation of VN precipitates. The tantalum helps improve weldability (Igarashi & Sawaragi, 1997). The predicted creep rupture strength of this alloy is

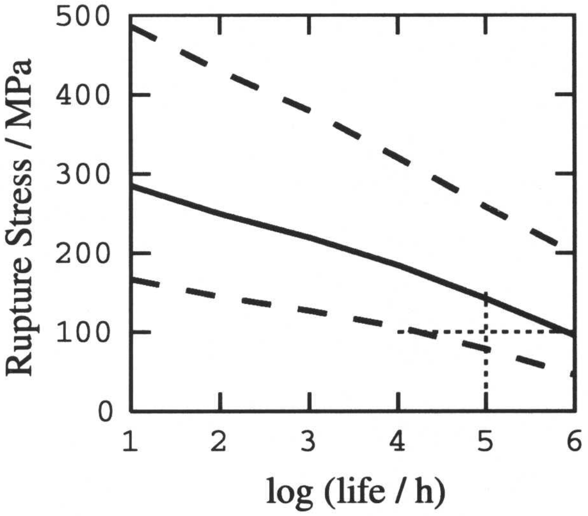

Fig. 7.20 Predicted creep rupture strength of alloy D at 650 °C. As before, copper, although presented in the alloy has been excluded from the calculations to reduce uncertainties.

shown in Fig. 7.20.

The process window of alloy D for heat treatment was also estimated using MTDATA (Fig. 7.21a). The ideal normalisation temperature is 1450 K, dissolving VN precipitates and minimising δ-ferrite formation. The analysis of the normalisation heat treatment, shown in Fig. 7.21b indicates the advantages for creep rupture strength from increasing this temperature to the maximum possible.

It turns out that, because of the smaller tungsten concentration, Laves phase is not an equilibrium phase in alloy D. The equilibrium precipitates at 650 °C are found to be $M_{23}C_6$, BN, NbN and VN.

The complete heat treatment applied to this alloy for this work is very similar to that applied to NF616: normalised at 1450 K for 2 hours and air cooled followed by a tempering at at 1043 K for 2 hours and then air cooled.

Other designs considered include a variation of the previously described steel C. Further analysis using the neural network showed that, in this case, increases in tungsten content had a more pronounced effect on the creep rupture strength of alloy E described in Table 7.7 (Fig. 7.22). As can be seen, an increase in tungsten to 3 wt% does give improved rupture strength but the error bounds associated with this analysis are very large. Also, this increase provides further problems with respect to δ-ferrite content, which has to be compensated with cobalt and manganese together with a reduction in silicon.

The predicted creep rupture strength for alloy E is shown in Fig. 7.23 with the process

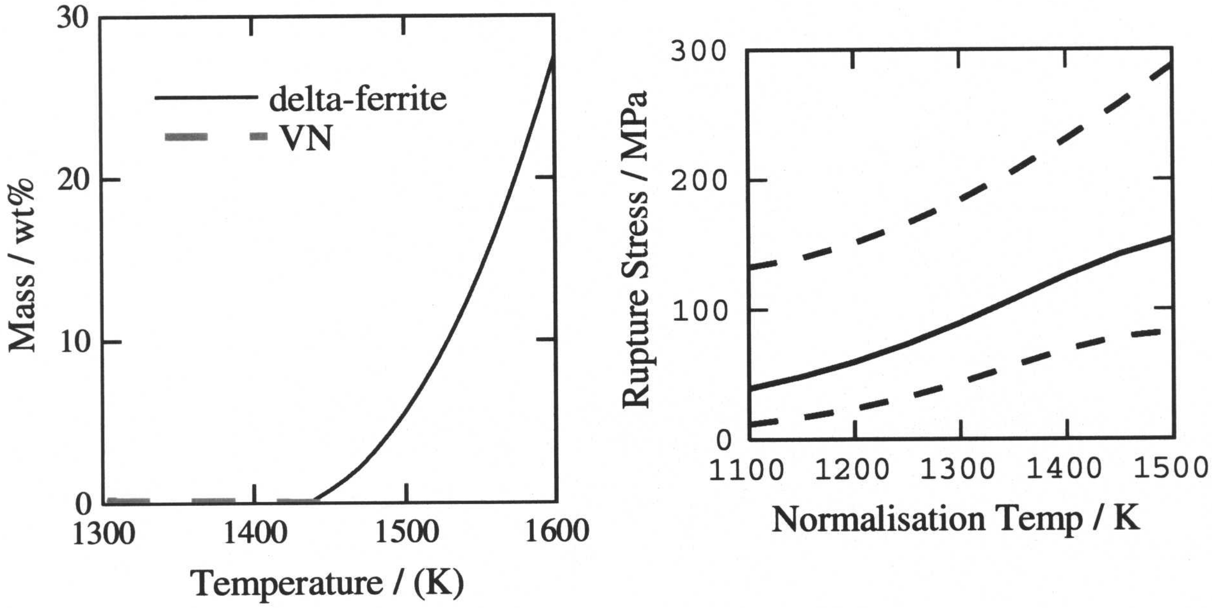

a)

b)

Fig. 7.21 a) Process window for alloy D as calculated using MTDATA. b) Neural network analysis of effect of increasing normalisation temperature on creep rupture strength for alloy D.

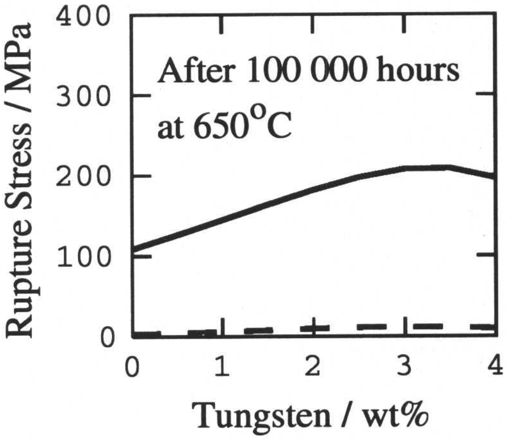

Fig. 7.22 Effect of tungsten on alloy E.

window calculated using MTDATA. The alloy demonstrates a creep rupture strength greater than the required properties but once again the error bounds are very large. The increase in tungsten and other alloy elements will lead to the formation of an increased amount of precipitates such as $M_{23}C_6$ and Laves phase. It may therefore be beneficial to creep properties to apply the dual heat treatment described in §7.3.1 to precipitate a fine dispersion of precipitates

C (wt%)	Si	Mn	Cr	Mo	W	Ni	Cu	V	N	Nb	B	Co	Ta
0.15	0.1	0.5	11	0.5	3	<0.01	1.5	0.2	0.1	0.1	0.01	4	0.1

Table 7.7: Composition of alloy E. Phosphorus, sulphur and aluminium are required to be as low as possible, as for steel C.

at the beginning of service. The heat treatment conditions recommended for this alloy are as follows: normalisation at 1450 K for 2 hours; tempering at 773 K for 10 hours followed by 1 hour at 1073 K (each stage should be followed by air cooling).

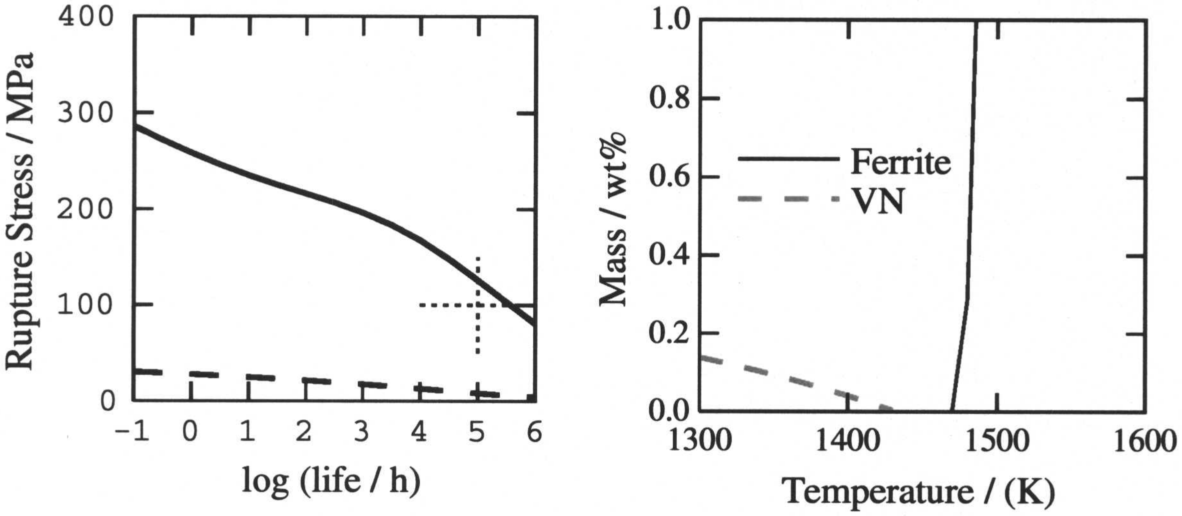

Fig. 7.23 Creep rupture strength of novel alloy as predicted by the neural network for 650 °C. Also shown is the heat treatment process window as calculated using MTDATA.

These steels will be manufactured and tested by Mitsubishi Heavy Industries in the near future.

7.4 Summary

The total design process has been presented in this chapter and used to propose a number of novel alloys. These have and will be manufactured and creep tested to validate the applicability of the process. Confidence is high that these alloys will meet the requirements of this project because of the success of alloys A and B (Chapter 4) and the success of the neural network in tackling a wide variety of problems. The results of these tests will also make extremely useful additions to the neural network database for the next retraining.

CHAPTER 8

Metallographic Studies of New Alloys

A variety of techniques was used to characterise the microstructure of the experimental alloys. These included optical microscopy and analysis using transmission electron microscopy (TEM).

Steels A and B (Chap. 4) and also two steels manufactured by Manoir Industrie in France are examined here. The french steels were used by Allen Power Engineering in the construction of a steam turbine. The compositions of these steels are presented in Table 8.1, they are 9 wt% Cr alloys and are referred to by Manoir Industrie as Y0336 and Z1092. The compositions of A and B are also summarised. The heat treatments applied to these alloys are recorded in Table 8.2.

Steel	Y0336	Z1092	A	B
C wt%	0.088	0.093	0.12	0.13
Si	0.42	0.34	0	0
Mn	0.50	0.53	0.48	0.5
P	0.018	0.018	0.0016	0.0016
S	0.003	0.002	0.001	0.001
Cr	8.28	8.52	9	8.7
Mo	0.95	0.96	0.75	0.30
W	0	0	3	3
Ni	0.18	0.39	0	0
V	0.21	0.20	0.21	0.21
Nb	0.08	0.07	0.01	0.01
N	0.03	0.03	0.064	0.064
Al	0.009	0.01	0	0
B	0	0	0.008	0.008
Co	0	0	1.25	0

Table 8.1: Compositions (wt%) of power plant steels used by Allen Power Engineering. Summaries of the compositions of steels A and B are also presented (Chap. 4).

The practical techniques used will be described followed by the analysis of the microstructures of the alloys described here.

Steel	Y0336	Z1092	A	B
Normalisation				
Temperature	1326 K	1321 K	1473 K	1453 K
Duration	11.35 h	11.6 h	2 h	2 h
Cooling rate	air cool	air cool	air cool	air cool
Tempering				
Temperature	1023 K	1015 K	1073 K	1073 K
Duration	12.67 h	12.5 h	4 h	4 h
Cooling rate	air cool	air cool	air cool	air cool
Annealing				
Temperature	-	-	1013 K	1013 K
Duration	-	-	4 h	4 h
Cooling rate	-	-	air cool	air cool

Table 8.2: Heat treatments applied to the power plant steels presented in Table 8.1.

8.1 Experimental Procedure

8.1.1 Optical Microscopy

Specimens for optical microscopy were hot-mounted in acrylic moulding powder and ground down using silicon carbide paper as fine as 1200 grit. Final polishing was carried using 6 and 1 μm diamond pastes. Specimens were etched with 2 vol.% nital (nitric acid in methanol). Samples were examined using a Laborlux 12 ME 5 optical microscope.

8.1.2 Transmission Electron Microscopy

Two specimen preparation techniques were utilised to produce TEM samples, the creation of thin foils and also carbon film replicas. Two microscopes were also used in this work, a Philips 400T and also a Jeol 200CX, both operated at 200 kV.

Thin foil specimens were created from 3 mm diameter discs cut from a rod using a 250 μm silicon carbide disc and cooling lubricant. The cut discs were of a thickness of approximately 100 μm, which was reduced to less than 60 μm by grinding the discs by hand using a steel holder and 600 grit silicon carbide paper. Great care was taken to not bend or distort the specimens and so reduce mechanical damage. Electropolishing of the specimens was conducted using a twin jet electropolisher, thinning parts of the specimen and rendering them transparent to electrons. The specimens were electropolished at approximately 50 V in a solution containing 5 vol.% perchloric acid, 20 vol.% glycerol and 75 vol.% industrial methanol.

The foils examined in this chapter were all taken from the main body of the creep specimens, away from the point of fracture.

Carbon replicas consist of a thin carbon film in which carbides are embedded. Samples are made as described for optical microscopy and are also etched. A carbon film of 20-30 nm was then applied to the surface of the specimen using vacuum evaporation at 10^{-5} torr. The deposited film was then scored with a sharp blade, dividing it into several smaller squares covering the sample. Electrolytic etching in a solution of 5 vol.% hydrochloric acid in methanol at an approximate potential of 1.5 V was used to remove the carbon film. This film was washed in methylated spirits and then floated off in distilled water, where the carbon replicas could be collected on 3 mm diameter copper grids.

There are some advantages to using replicas as compared to thin foils. The problems encountered with a magnetic specimen in an electron beam are avoided with this technique. Also, a larger area of specimen can be available for examination per sample, since the area transparent to electrons in thin foils can be rather small. The main disadvantage is the loss of information pertaining to the matrix structure when using replicas.

8.2 Practical Examination

8.2.1 Optical Microscopy

The microstructures consisted of fine tempered martensite; a typical microstructure is given in Fig. 8.1 † for steel B. Although this image gives a general overview of the microstructure transmission electron microscopy is essential to reveal the details.

8.2.2 Transmission Electron Microscopy

Z1092 and Y0336

Fig. 8.2 shows an image obtained from a thin foil specimen of Z1092. The microstructure consists of tempered martensite and carbides. The heat treatment, although quite severe, clearly does not destroy the martensite microstructure which retains the essential lath-like morphology. This is because the carbides, which nucleate heterogeneously at the lath boundaries, stabilise the microstructure. Indeed, there are very few precipitates located within the laths themselves. This is illustrated in the micrographs in Fig. 8.3, showing carbides aligned at the laths and also showing dislocations along grain boundaries and building up at obstacles such as carbides.

As can be seen from Fig. 8.4, the carbides are identified to be $M_{23}C_6$ particles. These are the carbides expected from equilibrium phase diagram calculations. Phases allowed in

---

† Due to the large quantity of Figures in this Chapter they have been moved to the end of the text.

this analysis are shown in Table 8.3. The equilibrium phases found for each of the steels are shown in Table 8.4 and $M_{23}C_6$ is a predominant carbide in each case. Their role in the long term stability of the microstructure is extremely important because they constrain the coarsening of the laths, whose boundaries are important obstacles to dislocation motion. Table 8.4 also indicates that, compared to Y0336 and Z1092, a large fraction of equilibrium carbides is expected to be present in steels A and B.

Ferrite	M_7C_3	Laves phase
Austenite	$M_{23}C_6$	BN
Cementite	M_6C	NbN
M_2X	M_5C_2	VN

Table 8.3: Phases allowed in MTDATA analysis to determine equilibrium phases.

Steel	$M_{23}C_6$	Laves phase	BN	NbN	VN
Y0336	1.69	-	-	0.09	-
Z1092	1.80	-	-	0.08	0.009
Steel A	2.36	3.99	0.02	0.01	0.24
Steel B	2.60	2.95	0.18	0.11	0.24

Table 8.4: Equilibrium phases (wt%) obtained from phase diagram calculations for the steels examined in this chapter.

A comparison of Z1092 and Y0336 shows an interesting change in the microstucture as a function of the nickel concentration. The two steels are otherwise essentially identical. Z1092 contains 0.39 wt% nickel which is more than twice as much as Y0336 (0.18 wt%). Fig. 8.5 shows for identical heat treatments that the microstructure of Z1092 is much coarser than that of Y0336. This confirms the alloy design procedures used in Chap. 7 where the nickel concentration was minimised, and indeed is consistent with the discussion in §2.3.3.

These alloys were creep tested and TEM specimens were made of the crept Y0336 samples and examined in order to compare against the samples before they entered service. The comparison of the microstructures is shown in Fig. 8.6. The grain and precipitate size has coarsened slightly as a result of the creep testing. This is the recovery mechanism which causes the loss in creep strength during the service life of components and which needs to be retarded in order to improve creep properties. Areas of large recovery were found in both creep test samples and an example of this is shown in Fig. 8.7. A very large grain has formed next to some much narrower laths; the difference is so large that this is unlikely to be a stereological aberration. Carbides which were previously on grain boundaries can also be seen in the large grain. However, there were also areas where little recovery of the microstructure had occurred. It is also prudent to remember that the area of material which it is possible to examine in a TEM specimen is extremely small so there is a danger of overinterpreting the microstructure.

To summarise, Fig. 8.6 shows that there is not much of a general change in the microstructure compared with the uncrept sample, in spite of the additional heat treatment during the creep test and any possible effects of creep strain in accelerating coarsening. It is likely therefore that creep failure initiates at local regions such as those illustrated in Fig. 8.7 where a small region breaks away and forms a coarse region which is weak. This is rather like the mechanism discovered by Abe *et al.* (1998, 1999) and Kushima *et al.* (2000), and indicates the importance of obtaining a uniform microstructure.

Steels A and B

Fig. 8.8 shows a small area of the microstructures of steels A and B. It is interesting that the lath microstructures appear to be finer than those of Y0336 and Z1092 even though the tempering conditions are comparable (Table 8.2). This could be because the alloys A and B have a lower martensite start temperature (M_s) than Y0336 and Z1092. It is well known that a reduction in the transformation temperature leads to a refinement of the plate size (Singh & Bhadeshia, 1998) because of the greater nucleation rate and the greater strength of the austenite. However Table 8.5, which compares M_s for the four alloys shows no great differences. The experimental values for steels A and B were measured using dilatometry and compare well with those calculated using the thermodynamic method described by Cool and Bhadeshia (1996). The M_s values for Y0336 and Z1092 were calculated using this same model and are similar to those of A and B. Since the finer microstructure is not due to the tempering heat treatments or differences in M_s it is probably due to the larger fraction of

M_s (°C)	Experimental	Predicted
A	330	316
B	318	308
Y0336	-	331
Z1092	-	322

Table 8.5: Comparison of martensite start temperatures (M_s) for steels A, B, Y0336 and Z1092. Values for A and B have been found experimentally using dilatometry and compare well with model results (Cool & Bhadeshia, 1996). Values for Y0336 and Z1092 were calculated and found to be similar to those of A and B.

pinning precipitates in steels A and B (Table 8.4).

TEM foils were made from crept specimens of steels A and B. Details of the specimens examined are shown in Table 8.6. Areas of recovery were found as well as areas of relative microstructural stability. Fig. 8.9 pictures an area where the martensite laths have increased in thickness and a coarse precipitate has formed on the boundary between laths. The width of the coarsened laths are still narrower than those found in steels Y0336 and Z1092 prior to creep testing.

Steel	Temp / °C	Stress / MPa	Rupture Time / h
A	650	120.04	2015.1
B	650	120.05	2058.1

Table 8.6: Results of creep testing of alloys A and B.

However, Fig. 8.10, taken from the same specimen of steel A, shows a stable microstructure where the lath size has not coarsened and many carbides are still relatively small. Such microstructural stability is of great benefit to creep rupture strength and goes some way to explaining the excellent results achieved with steels A and B in creep testing.

Similar properties were found in steel B. Fig. 8.11 shows large recovery in the microstructure where the martensite lath has widened in size considerably. Fig. 8.12 shows an area where the microstructure is found to be stable.

8.3 Summary

One of the important observations in the recent literature is that many ferritic steels are strong in creep in the early stages of creep life , but the strength then deteriorates sharply as a consequence of the development of local regions of recovery where damage is then intensified. The observations reported here confirm that recovery is not homogeneous. A possible solution to this problem has already been presented in §7.3.1, using a dual heat treatment to obtain a more homogeneous dispersion of precipitates and retard localised recovery. The observations also support the design philosophy that the concentration of nickel should be minimised.

The comparisons between the novel steels A and B and the Manoir Industrie alloys highlight how the stability and scale of the microstructure depend on the carbide fraction. Consequently the increased alloy content of A and B was shown to improve the stability of the microstructure during creep.

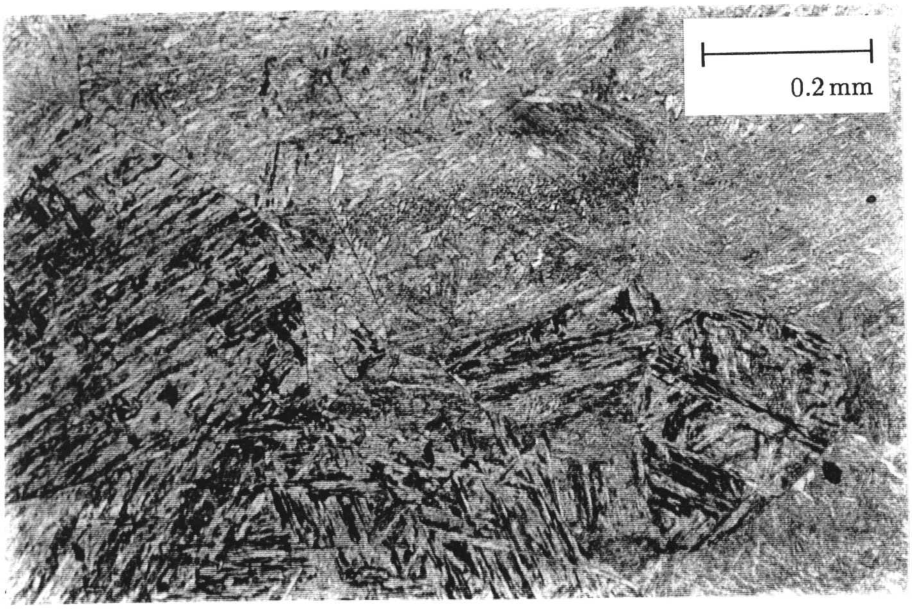

Fig. 8.1 Optical micrograph of steel B after initial heat treatments. The microstructure shown is tempered martensite.

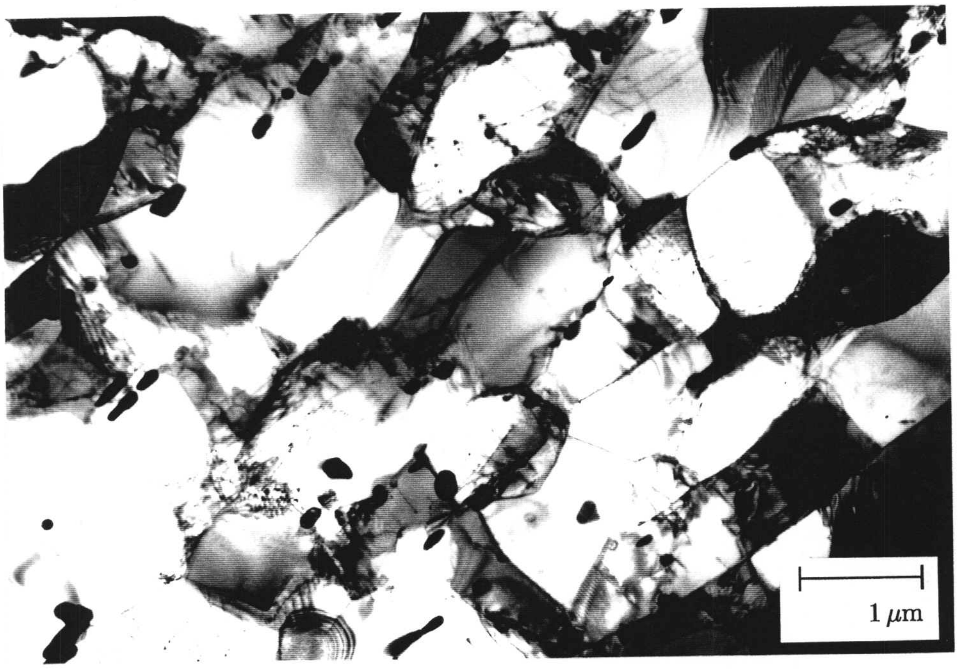

Fig. 8.2 TEM micrograph of Z1092, showing the general microstructure.

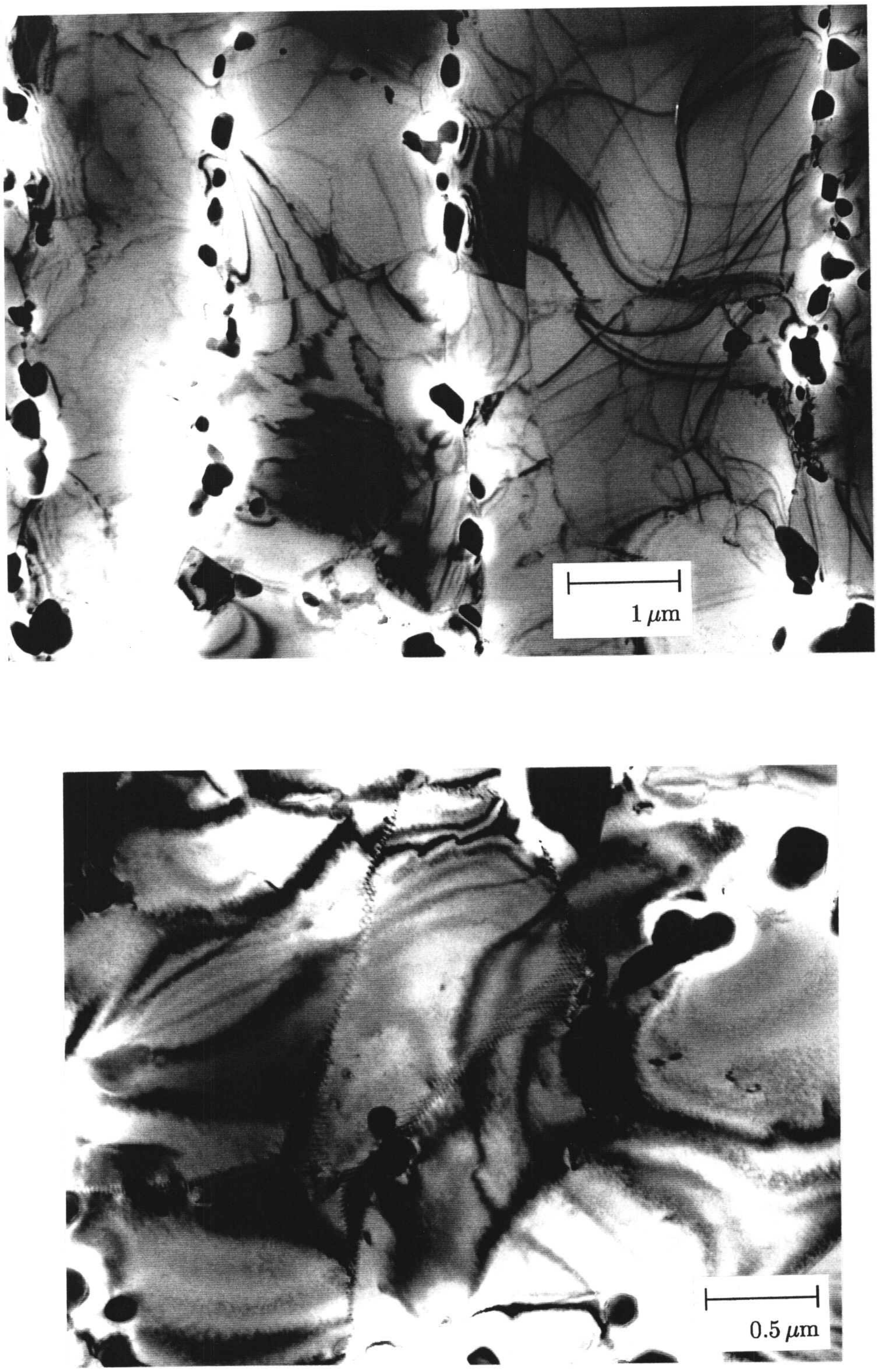

Fig. 8.3 TEM micrographs of Z1092. Firstly showing carbides aligned at the martensite lath boundaries and secondly showing dislocations along grain boundaries and building up at carbides.

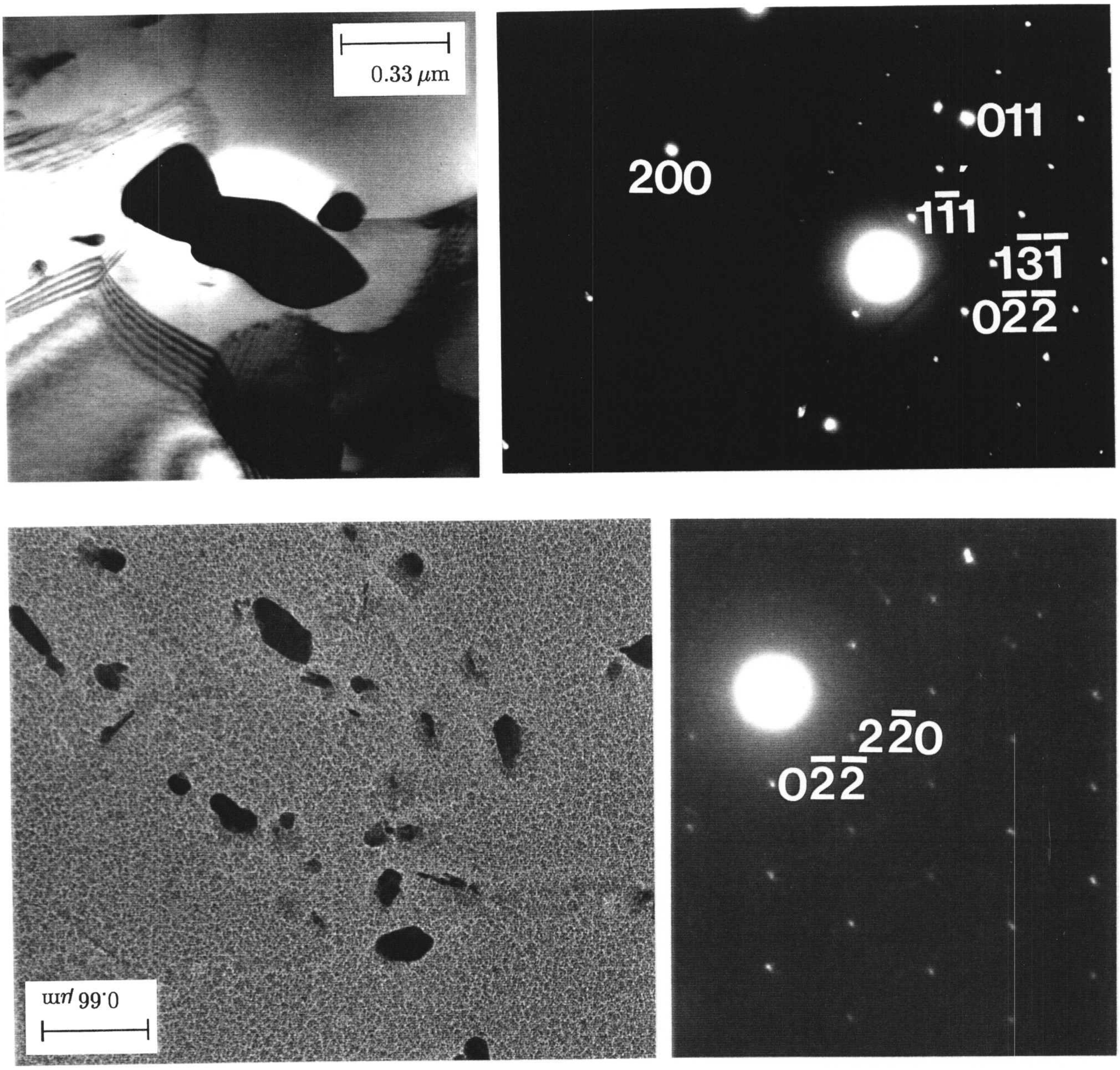

Fig. 8.4 TEM micrographs of carbides obtained from Z1092 and correlating diffraction patterns. The top picture shows a carbide found in a thin foil specimen and the diffraction pattern obtained from the carbide and the matrix. The lower micrograph shows carbides found in a replica sample and also the diffraction pattern obtained from a carbide in the film. In each case the carbide was found to be $M_{23}C_6$. For the foil specimen the matrix was confirmed to be ferrite.

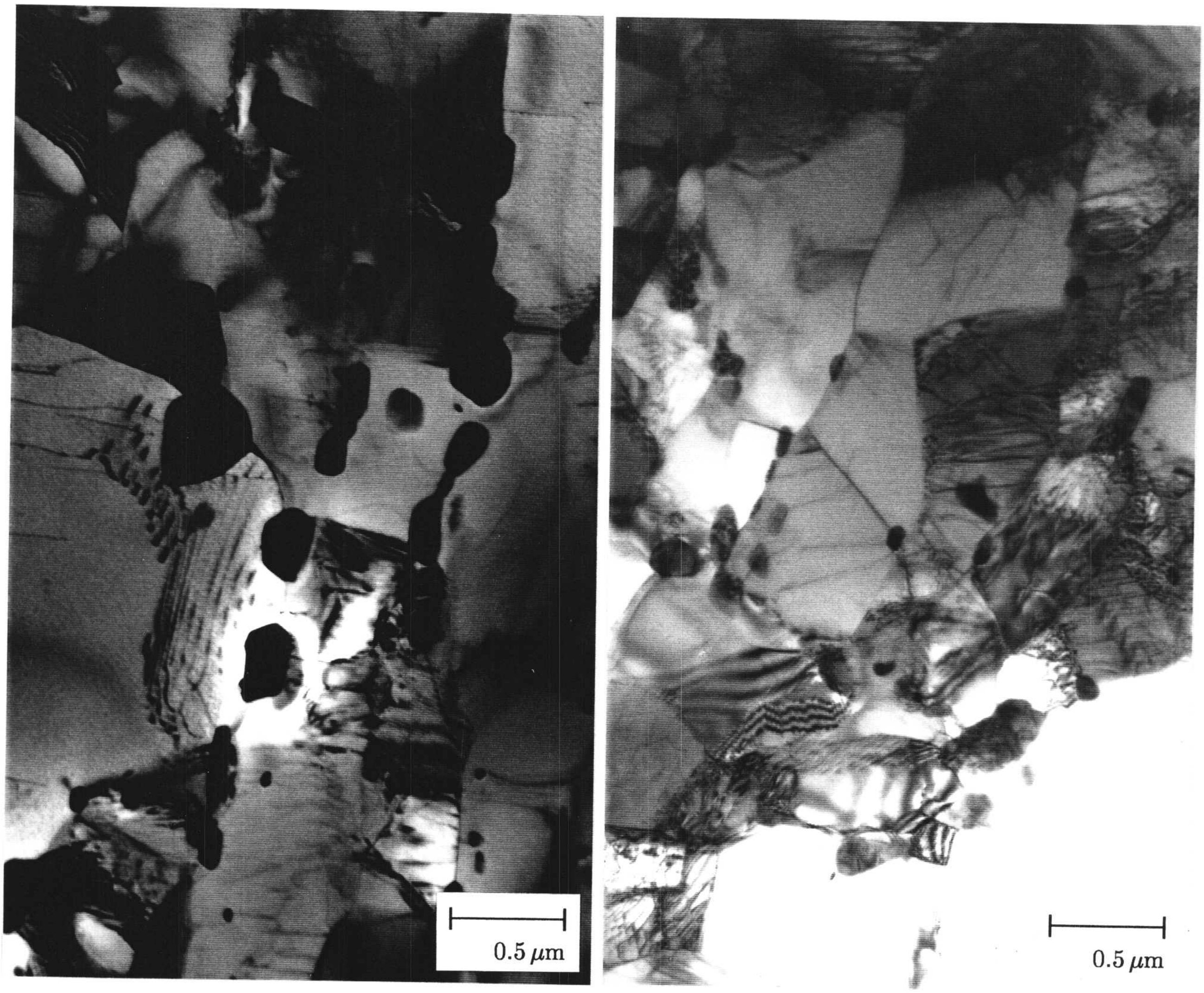

Z1092

Y0336

Fig. 8.5 Comparison of representative TEM micrographs of Z1092 (0.39 wt% Ni) and Y0336 (0.18 wt% Ni) after initial heat treatment. The microstructure of Z1092 was found to be coarser than that of Y0336.

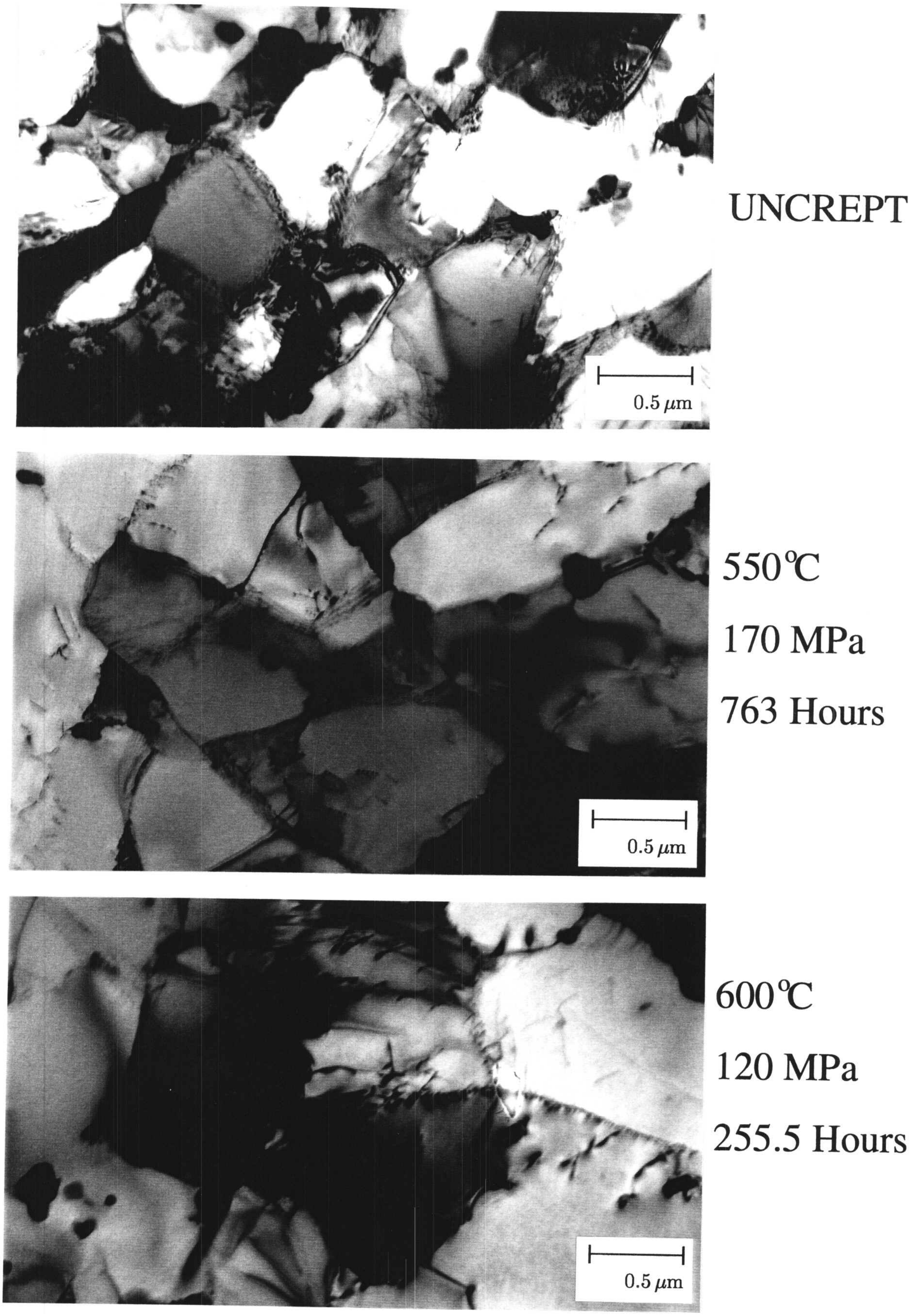

UNCREPT

550℃
170 MPa
763 Hours

600℃
120 MPa
255.5 Hours

Fig. 8.6 TEM micrographs of Y0336, before and after creep testing.

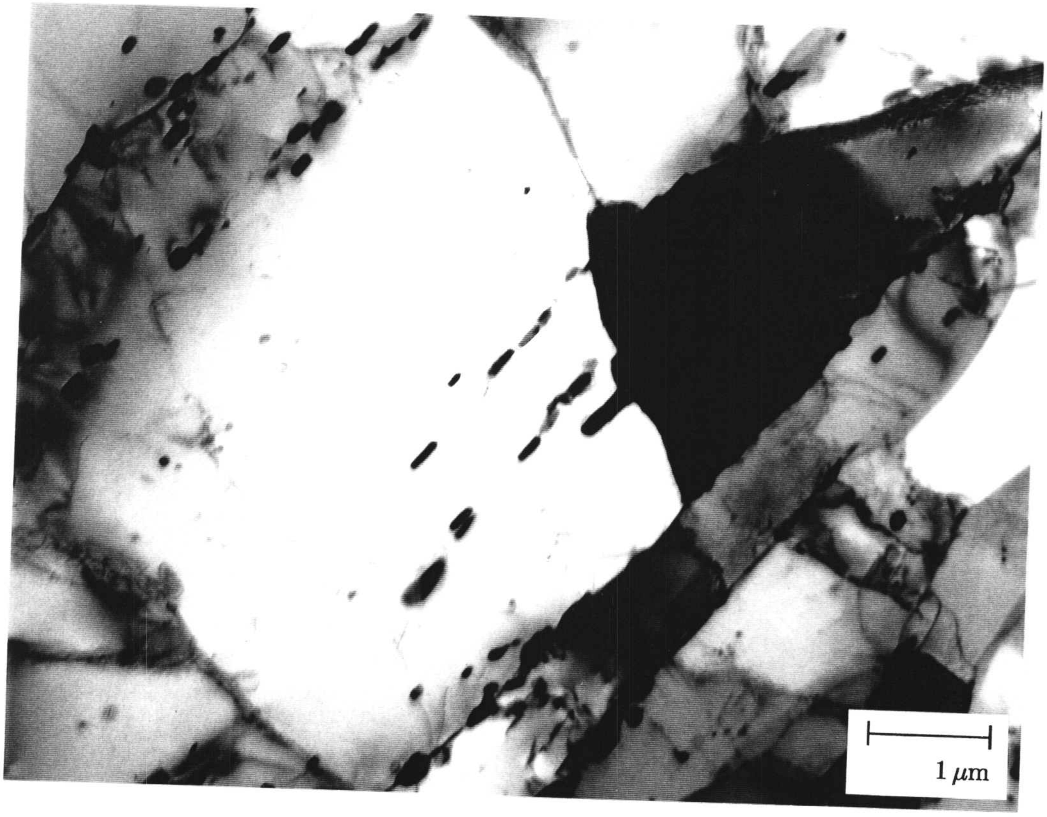

Fig. 8.7 Area of recrystallisation found in Y0336 after creep testing at 600 °C for 255 hours at a stress of 120 MPa.

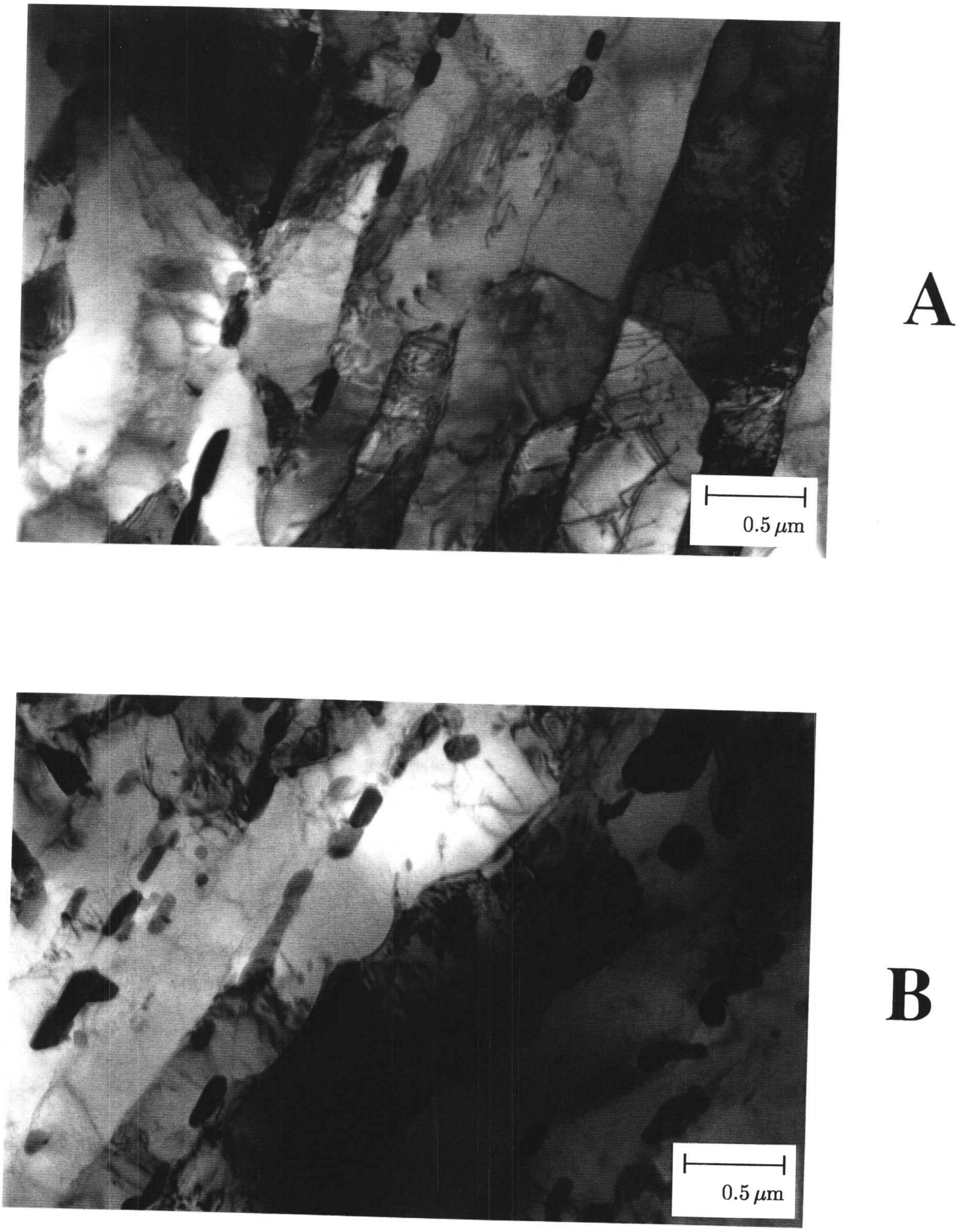

Fig. 8.8 TEM micrographs of steels A and B prior to creep testing.

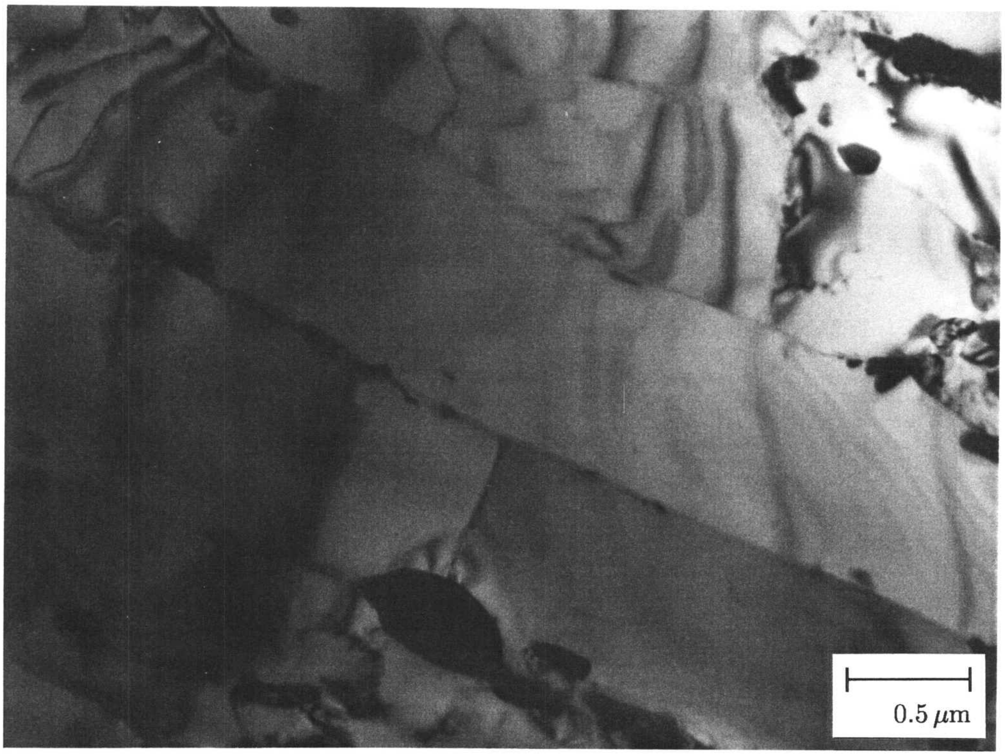

Fig. 8.9 Area of recovery found in a specimen of steel A which had been crept at 650 °C at a stress of 120 MPa for 2015 hours.

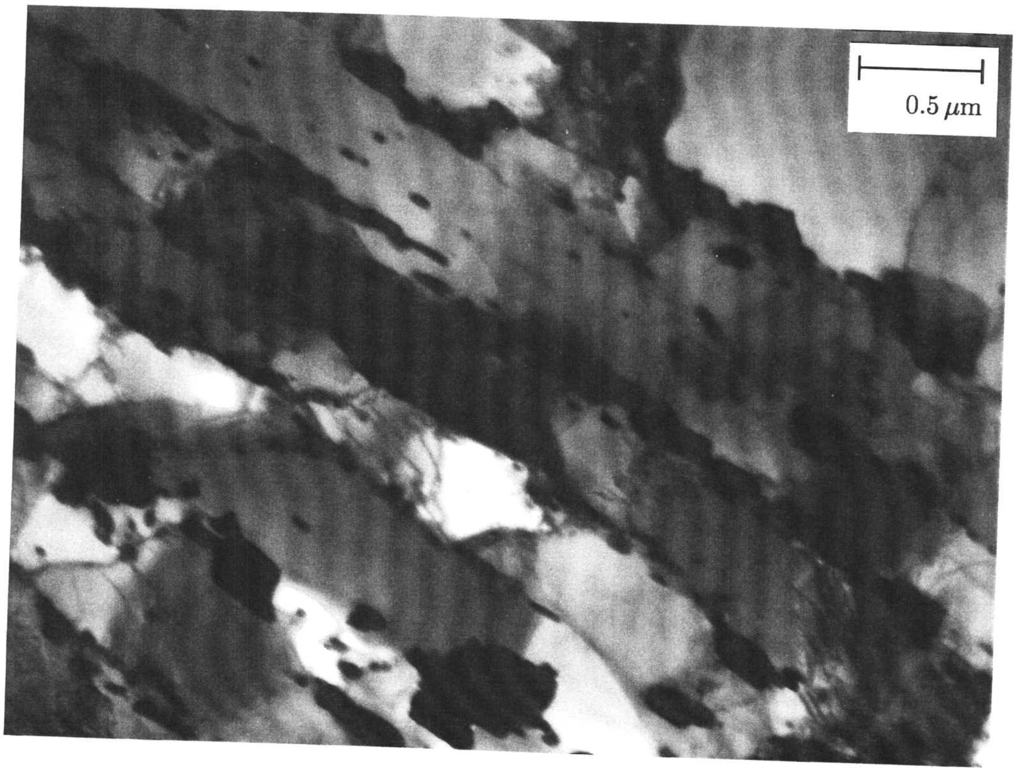

Fig. 8.10 Area of microstructural stability found in a specimen of steel A which had been crept at 650 °C at a stress of 120 MPa for 2015 hours.

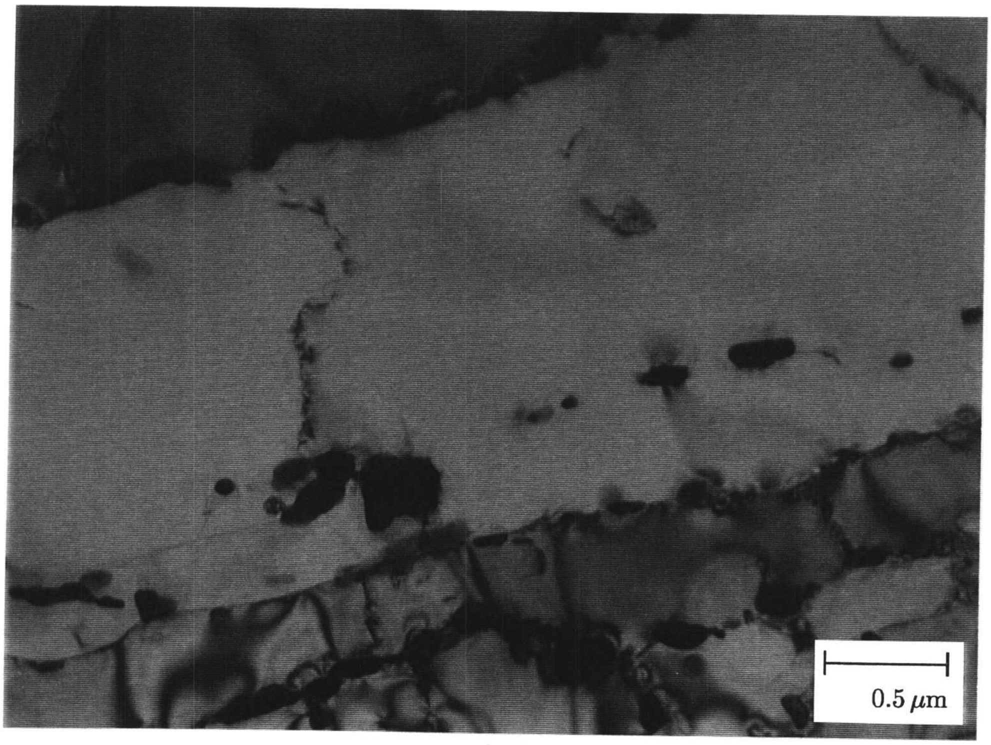

Fig. 8.11 Area of recovery found in a specimen of steel B which had been crept at 650 °C at a stress of 120 MPa for 2058 hours.

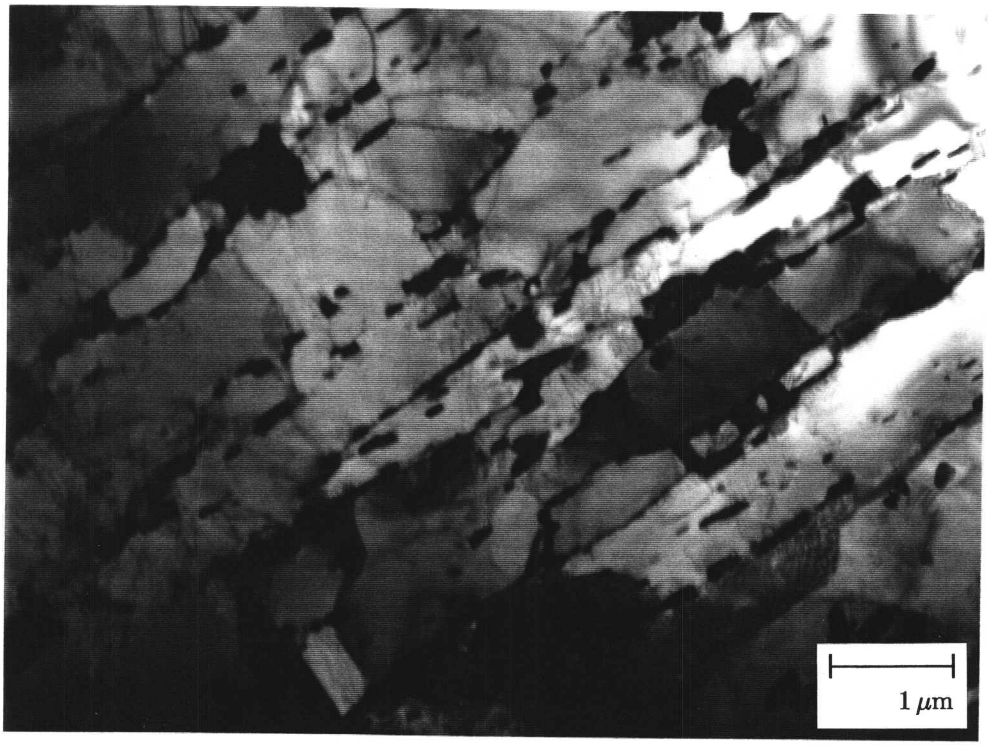

Fig. 8.12 Area of microstructural stability found in a specimen of steel B which had been crept at 650 °C at a stress of 120 MPa for 2058 hours.

CHAPTER 9

Summary and Suggestions for Further Work

It was intended in this research to attempt a quantitative design of heat-resistant steels and welding alloys for small power plant. Although there remain uncertainties and problems, it is now possible to attempt a quantitative design of heat-resistant steels and welding alloys. This is true both with respect to the thermodynamics and kinetics of microstructural evolution and in the estimation of creep rupture life. These methods do not completely solve the problem of alloy design but they do reduce the number of variables which have to be assessed from qualitative knowledge alone.

There have been three important uses of thermodynamic models in the alloy design procedures. Firstly, in the assessment of a processing window where it is necessary to ensure that any proposed alloy becomes fully or almost fully austenitic. This is important in order to allow thermomechanical fabrication treatments at high temperatures and to ensure an ultimate microstructure which is mostly martensitic. The second major application is in the calculation of thermodynamic parameters important in the kinetic theories. For example, the driving force for nucleation, the compositions of the phases in equilibrium and the martensite–start temperatures. Finally, the phase stability calculations have helped to define the maximum temperature at which any proposed steel can be tempered without reverting to austenite.

Kinetic theory has been used to estimate the rates at which precipitate form or dissolve. This is particularly useful in designing against early Laves phase precipitation.

None of these microstructure calculations are, however, sufficiently advanced to be able to estimate the creep properties of the steel. There are just too many complexities in the quantitative definition of creep. For this reason, the neural network approach of MacKay has proved to be extremely powerful in enabling the estimation of creep rupture life as a function of a large number of variables. The method is particularly meritorious in the way in which it provides uncertainties due to sparsity in data or due to extrapolation of trends. Furthermore, the method has proved itself reliable when validated against vast quantities of experimental data, and against known though admittedly simplistic metallurgical trends.

It will be necessary in the longer term for the microstructure models to predict particle size and spatial distributions, and to account for the effects of stress and strain on transformation kinetics. This will require a treatment of multiphase coarsening reactions and a finer study of what is important in creep. It is likely that mechanical property models which use a large number of variables will be the only ones that succeed in bridging the gap between microstructure and complex properties.

The present work has led to the design of a novel steel which has just been manufactured. The steel has yet to be tested; it is expected that this will take a minimum of 10 000 h once the alloy has been fabricated and machined into the correct form. Welding trials will require further resources although those tests can proceed in parallel with creep testing.

References

ABE, F. & NAKAZAWA, S. (1992), Microstructural evolution and creep behaviour of bainitic, martensitic and martensite-ferrite dual phase Cr-2W steels, Mat. Sci. & Tech., Vol. 8, p. 1063–1069

ABE, F., IGARASHI, M., FUJITSUNA, N., KIMURA, K. & MUNEKI S. (1998), Research and Development of Advanced Ferritic Steels for 650 ° USC Boilers, Materials for Advanced Power Engineering, Proceedings of the 6th Liege Conference, Volume 5, part 1, p. 259–268

ABE, F. (1999), Coarsening behaviour of martensite laths in tempered martensitic 9Cr-W steels during creep deformation, Fourth International conference on Recrystallisation and Related Phenomena, The Japan Institute of Metals, p. 289–294

ABE, F. (2000a), R & D of Advanced Ferritic steels for 650 °C USC Boilers, ULTRA-STEEL 2000, Tsukuba, Japan, Sponsored by the Science and Technology Research Agency, National Rearch Institute for Metals, p. 119–129

ABE, F. (2000b), Private communication

ANDREWS, K. W. (1956), J. Iron Steel Inst., **184**, p. 416

ANDREWS, K. W. & HUGHES, H. (1959), Hexagonal carbide and nitride phases and their occurrence in some alloy steels J. Iron Steel Inst., **193**, p. 304–311

ANDREWS, K. W., DYSON, D. J.& KEOWN, S.R. (1967), Interpretation of Electron Diffraction Patterns, Higger and Watts, London

ARGENT, B. B., van NIEKERK, M. N. & REDFERN, G. A. (1970), Creep of ferritic steels, Journal of The Iron and Steel Institute, p. 830–843

ARMITT, J., HOLMES, D. R., MANNING, M. I., MEADOWCROFT, D. B. & METCALFE, E. (1978), The Spalling of Steam-Grown Oxide from Superheater and Reheater Steel Tube Steels, Electric Power Research Institute, EPRI Report No. FP-686

ARMOR, A. F. (1998), Overview of the Power Generation Business in the United States, p. 1–11, Steels for Power Generation, Conference Proceedings, San Sebastian, Spain

ASHBY, M. F. & JONES, D. R. H. (1989), Engineering Materials 1, Pergamon Press, ISBN 0-08-026138-8

AVRAMI, M. (1939), Kinetics of Phase Change, Journal of Chemical Physics, **7**, p. 1103

BAKER, R. G. & NUTTING, J. (1959), The tempering of 2.25Cr1Mo steel after quenching and normalizing, Journal of the Iron and Steel Institute, **192**, p. 257–268

BARRACLOUGH, D. R. & GOOCH, D. J. (1985), Effect of inadequate heat treatment on creep strength of 12Cr-Mo-V steel, Materials Science and Technology, Vol. 1, p. 961–967

BEECH, J. & WARRINGTON, D. H. (1966), J. Iron Steel Inst. **204**, p. 460–468

BERGER, C., BEECH, S. M., MAYER, K. H., STAUBLI, M., & THORNTON, D. V. (1993), International Joint Power Generation Conference, U.S.A.

BHADESHIA, H. K. D. H. (1992), Bainite in Steels, The Institute of Materials, London

BHADESHIA, H. K. D. H., STRANG, A. & GOOCH, D. J. (1998), Ferritic Power Plant Steels: Remanent Life Assessment and Approach to Equilibrium, p. 45–69, International Materials Reviews, Vol. 43, No. 2

BHADESHIA, H. K. D. H. (1999a), Estimation of the Micrstructure of Ferritic Creep-Resistant Steels, p. 15–38, Modelling of Microstructural Evolution,

BHADESHIA, H. K. D. H. (1999b), Neural Networks in Material Science, p. 966–979, ISIJ International, Vol. 39, No. 10

BHADESHIA, H. K. D. H. (1999c), Proc. 5th Int. Conf. on Trends in Welding Research, Ed. J. M. Vitek *et al.*, Materials Park, OH, ASM International, p. 795–804

BHADESHIA, H. K. D. H. (2000), Design of Alloys for the Energy Industries, Charles Parsons Conference 2000

BJÄRBO, A. (1994), Microstructural Changes in 12wt% Cr Steel during Creep, Royal Institute of Technology, Stockholm, Sweden

BRIGGS, J. Z. & PARKER, T. D. (1965), The Super 12wt% Cr Steels, Climax Molybdenum Company, 1st Edition

BRÜHL, F., HAARMANN, K., KALWA, G., WEBER, H. & ZSCHAU, M. (1989), Behaviour of the 9% Chromium Steel P91 in Short and Long Term Tests, VGB KRAFTWERKSTECHNIK, 12, p. 1064–1080

BRUN, F., YOSHIDA, T. ROBSON, J. D., NARAYAN, V., BHADESHIA, H. K. D. H. & MACKAY, D. J. C. (1999), Theoretical design of ferritic creep resistant steels using neural network, kinetic and thernodynamic models, it Mat. Sci. & Tec., Vol 15, p. 547–554

BUCHANAN, L. W., HUNTER, A. N. R. & HOLT A. V. (1992), Materials for ultra-supercritical boilers

CAHN, R. W., HAASEN, P. & KRAMER, E. J. Eds. (1994), Materials Science and Technology, VCH Verlag, Weinheim

CANE, B. J. & MIDDLETON, C. J. (1981), Intergranular creep-cavity formation in low-alloy bainitic steels, Metal Science, Vol. 15, p. 295–301

CERJAK, H., HOFER, P. & SCHAFFERNAK, B. (1999), Influence of Microstructural Aspects on the Service Behaviour of Advanced Power Plant Steels, p. 874–888, ISIJ International, Vol. 39, No. 9

COOL, T. (1996), Design of Steel Weld Deposits, Cambridge University Thesis, Chapter 5, p. 58–60

COOL, T. & BHADSHIA, H. K. D. H. (1996), Materials Science and Technology, **12**, p. 40–44

COOL, T. & BHADSHIA, H. K. D. H. (1997), Science and Technology of Welding and Joining, Vol 2., p. 36–42

CONROY, R. (1999), Private communication

DU, X., WHITEMAN, J. A., THOMSON, R. C. & BHADESHIA, H. K. D. H. (1992), Modelling the carbide composition changes in $\frac{1}{2}\mathrm{Cr}\frac{1}{2}\mathrm{Mo}\frac{1}{4}\mathrm{V}$ steel during long-term tempering Materials Science and Engineering, A155, p. 197–205

EBERLE, F., SEIFERT, J. W. & KITTERMAN, J. H. (1964), Scaling of Ferritic Superheater Steels During 36,000 hours in 980/1030 F Steam of 2350 psi, with Particular Respect to Scale Exfoliation Tendency, Proc. of American Power Conf., Vol. 26, p. 501

EDMONDS, D. V. & HONEYCOMBE, R. W. K. (1973), Structure and properties of isothermally transformed Fe-4Mo-0.2C alloy, Journal of the Iron and Steel Institute, **211**, p. 209–216

EVANS, R. W. & WILSHIRE, B. (1985), Creep of Metals and Alloys, The Institute of Materials, London

ENNIS, P. J., WOUTERS, Y. & QUADAKKERS, W. J. (1998), The Effects of Oxidation on the Service Life of 9-12wt% Chromium Steels , p. 457–467, Advanced Heat Resistant Steel for Power Generation, San Sebastian, Spain, Eds. Viswanathan, R. & Nutting, J.

ERNST, P. N., UGGOWITZER, P. J. & SPEIDEL, M. O. (1986), Improved boron-containing 9 to 12 % chromium steel with high creep rupture strength, journal of Materials Science Letters, **5**, p. 835–839

EVANS, H. E. (1984), Mechanisms of creep fracture, Elsevier Applied Science, Barking

EVANS, M. (1999), Method for improving paramteric creep rupture life of 2.25Cr-1Mo steel using artificial neural networks, Materials Science and Technology, Vol. 15, p. 647–658

ENNIS, P. J. (1999), Private Communication Regarding Oxidation and the COST 522 Action

EVANS, R. W. & WILSHIRE, B. (1993), Introduction to Creep, The Institute of Materials, Book 429, ISBN 0-901462-64-0

FOLDYNA, V., JAKOBOVÁ, A., RIMAN, R. & GEMPERLE, A. (1991), Effect of structural factors on the creep properties of modified chromium steels, Steel Research, **62**, No. 10, p. 453–458

FROST, H. J. & ASHBY, M. F. (1982), Deformation-mechanism maps, The plasticity and creep of metals and ceramics, Pergamon Press, ISBN 0-08-029337-9

FUJITA, T. (1978), Supplement, Transactions of the Japanese Institute of Metals

FUJITA, T. & TAKAHASHI, N. (1979), The effects of V and Nb on the long period creep rupture strength of 12 % Cr heat-resisting steel containing Mo and B, Transactions of the Iron and Steel Institute of Japan, Vol. 18, p. 269–278

FUJITA, T., ASAKURA, K., SAWADA, T., TAKAMATSU, T. & OTOGURO, Y. (1981), Creep rupture strength and microstructure of low C-10Cr-2Mo heat-resisting steels with V and Nb, Metallurgical Transactions A, Vol. 12A, p. 1071–1079

FUJITA, T. & ASAKURA, K. (1986), Effects of carbon on creep rupture strength and toughness of high Cr-Mo heat-resisting steels containing V and Nb, Transactions of the Iron and Steel Institute of Japan, Vol. 26, p. 1073–1079

FUJITSUNA, N., KUTSUMI, H., ITAGAKI, T., IGARASHI, M. & ABE, F. (1998), Report of the Japan Society for the Promotion of Science, 123rd Committee, **39**, 265

FUJITSUNA, N., IGARASHI, M. & ABE, F. (2000), Acceleration of Fe_2W precipitation and its effect on creep deformation behaviour of 8.5Cr-2W-VNb steels with Si Key Engineering Materials, Vols. 171-174, p. 469–476

GOLDSCHMIDT, H. J. (1948), The structure of carbides in alloy steels Journal of the Iron and Steel Institute, **160**, p. 345–362

GOOCH, D. J. (1982), Creep Fracture of 12 Cr-Mo-V Steel, p. 79–89, Metals Science, Vol. 16

GOOCH, D. J. (1993), Turbine Materials for Advanced Steam Cycles, National Power Report

HALD, J. (1995), Material comparison between NF616, HCM12A and TB12M III: Microstructural stability and ageing, The EPRI/National Power Conf. New steels for advanced plant upto 620 °, The Society of Chemical Industry, Ed. E. Metcalfe. p. 152–173

HARVEY, P. D. (1982), Engineering Properties of Steel, Am. Soc. Met.

HÄTTESTRAND, M. & ANDRÉN, H.O. (1999), Boron Distribution in 9-12 wt% Chromium Steels, Materials Science and Engineering, A270, p. 33–37

HIDAKA, K., FUKUI, Y., KANEKO, R. & FUJITA, T. (1997), Development of 9-12 % Cr steels for all-ferrite steam turbine at target temperature of 650 °C, International Conference on Advanced Steam Power Plant, IMechE, ISBN 1 86058 097 1, p. 99–113

HIDAKA, K., FUKUI, Y.,NAKAMURA, S., KANEKO, R., TANAKA, Y. & FUJITA, T. (1998), Development of Heat Resistant 12%CrWCoB Steel Rotor for USC Power Plant, Advanced Heat Resistant Steel for Power Generation, San Sebastian, Spain, Eds. Viswanathan, R. & Nutting, J., p 418–429

HODSON, S. M. (1989), MTDATA-Metallurgical and Thermochemical Data Bank, National Physics Laboratory, Teddingon, U.K.

HONEYCOMBE, R. W. K. & BHADESHIA, H. K. D. H. (1995), Steels, Microstructure and Properties, 2nd Edition, Edward Arnold, ISBN 0-340-58946-9

HOFER, P., CERJAK, H. & WARBICHLER, P. (1998), Qunatitative evaluation of precipitates in the martensitic cast steel G-X12CrMoVNbN10-1-1 Materials for Advanced Power Engineering, Proceedings of the 6th Liège Conference, Eds. Lecomte-Beckers, J., Schubert, F. & Ennis, P. J., p. 549–557, ISBN 3-89336-228-2

HOSOI, Y., WADE, N. & URITA, T. (1986), Effect of Si and Mn on precipitation behaviour of Laves phase and 9Cr-2Mo Steel, Trans. Iron Steel Inst. Japan, Volume 26, Number 1, p. B-30

IGARASHI, M. & SAWARAGI, Y. (1997), Development of 0.1C-11Cr-3W-3Co-V-Nb-Nd-N Ferritic Steel for USC Boilers, ICOPE '97, Tokyo, Vol. 2, p. 107–112

IRVINE, K. J., CROWE, D. J. & PICKERING, F. B. (1960), The physical metallurgy of 12% chromium steels, Journal of the Iron and Steel Institute, p. 386–405

ISEDA, A., SAWARAGI, Y., TERANISHI, H., KUBOTA, M. & HAYASE, Y. (1989), Development of New 12%Cr Steel Tubing (HCM12) for Boiler Application The Sumitomo Search, 40, 41

ISEDA, A., SAWARAGI, Y., KATO, S. & MASUYAMA, F. (1992), Development of a new 0.1C-11Cr-2W-0.4Mo-1Cu steel for large diameter and thick wall pipe for boilers, Creep: Characterisation, damage and life assessments, Proceedings of the Fifth International Conference on Creep of Materials, Lake Buena Vista, Florida, U.S.A.

ISHII, R., TSUDA, Y., YAMADA, M. & MIYAZAKI, M. (1998), The effect of tungsten on creep properties of high chromium steels for steam turbine, Development of Heat Resistant 12%CrWCoB Steel Rotor for USC Power Plant, p 277–287, Advanced Heat Resistant Steel for Power Generation, San Sebastian, Spain, Eds. Viswanathan, R. & Nutting, J.

JACK, D. H. & JACK, K. H. (1973), Carbides and nitrides in steels, Materials Science and Engineering, **11**, p. 386–405

JANOVEC, J., VYROSTKOVA, A. & SVOBODA, M. (1994), Influence of tempering temperature on stability of carbide phases in 2.6Cr-0.7Mo-0.3V steel with various carbon content, Met. Trans. A 25A, p 267–275

JOHNSON, W. A. & MEHL (1939), Trans. Metall. Soc. AIME, **56**, p. 355

KOLMOGOROV, A. N. (1937), Izv. Akad. Nauk., USSR-Ser-Matemat., **1(3)**, p. 355

KOMAI, N., MASUYAMA, F., ISHIHARA, I., YOKOYAMA, T., YAMADERA, Y., OKADA, H., MIYATA, K. & SAWARAGI, Y. (1998), Development and assessment of 2.25Cr-1.6W (HCM2S) steel, Development of Heat Resistant 12%CrWCoB Steel, p 96–108, Advanced Heat Resistant Steel for Power Generation, San Sebastian, Spain, Eds. Viswanathan, R. & Nutting, J.

KUBON, Z., FOLDYNA, V. & VODÁREK, V. (1997), The role of Mo and W on the creep behaviour of 9 and 12 % Cr steels, Advances in turbine materials, design and manufacturing, Proceedings of the fourth international Charles Parsons turbine conference, Eds. A. Strang, W. M. Banks, R. D. Conroy & M. J. Goulette, p. 309–321

KUSHIMA, H., KIMURA, K. & ABE, F. (2000), Degradation behaviour during creep deformation of high-Cr ferritic creep resistant steels, The 10th Iketani Conf. on Materials Research towards the 21st Century, Symposium on Iron and Steel, Karuizawa, Japan, p. 83-84

KUO, K. (1953), Carbides in Chromium, Molybdenum and Tungsten steels, Journal of the Iron and Steel Institute, **173**, p. 363–375

KURZYDLOWSKI, K. J. & ZIELIŃSKI, W. (1984), Mo_2C to M_6C carbide transformation in low alloy Cr-Mo ferritic steels Metal Science, Vol. 18, p. 223–224

KUSHIMA, H., KIMURA, K. & ABE, F. (2000), Degradation behaviour during creep deformation of high-Cr ferritic creep rsistant steels, 10th Iketani Conference on materials research towards the 21st century, Symposium on Iron and Steel, June 26-30, Karuizawa, Japan, Eds. Okubo, T., Kishi, T. & Saito, T.

LISTMANN, R. (1997), Efficient, flexible and economic power generation - the advanced combined cycle technology, Proc. CCGT IV: The Next Generation, IMechE Seminar S502

LUNDIN, C. D., KELLEY, S. C., MENON, R. & KRUSE, B. J. (1986), Weld Research Council Bulletin, **277**, p. 1–66

MACKAY, D. J. C. (1992a), Neural Computation, **4**, 415

MACKAY, D. J. C. (1992b), Neural Computation, **4**, 418

MACKAY, D. J. C. (1995), Networks Computation in Neural Systems, **6**, 469

MANN, S. D., McCULLOCH, D. G. & MUDDLE, B. C. (1995), Identification of M_5C_2 carbides in ex-service 1Cr-0.5Mo steels, Metallurgical and Materials Transactions A, **26A**, p. 509–520

MASON, R. N. & SHEARD, A. G. (1997), Proc. 5th ‘Engineering for profit from waste’ Conf., IMechE, p. 39–53

MASUYAMA, F. & OHGAMI, M. (1993), Creep behaviour of high nitrogen ferritic steels, Proceedings of JIMIS - 7, Nagoya, p. 325–332

MASUYAMA, F. (1999), New Developments in Steels for Power Generation Boilers, Advanced Heat Resistant Steel for Power Generation, San Sebastian, Spain, Eds. Viswanathan, R. & Nutting, J., p 33–48

METCALFE, E. (1989), Oxide Characterisation for Life Prediction, Proc. Seminar on Surface Stability, Oxidation-Corrosion-Erosion-Wear: No. 6 - Characterisation of

High-Temperature Materials, Ed. T. N. Rhys-Jones, Institutte of Metals, London, 145

MIYATA, K., IGARASHI, M. & SAWARAGI, Y. (1999), Effect of Trace Elements on Creep Properties of 0.06C-2.25Cr-1.6W-0.1Mo-0.25V-0.05Nb Steel, ISIJ International, Vol. 39, No. 9, p. 947–954

MORIMOTO, H., OHKITA, S., SAKURAI, H. & MIYAKE, T. (1996), Creep rupture properties of weldments of 9Cr ferritic heat resistant steel, Proc. of the 6th Int. Symp. JWS, Nagoya, Japan

MTDATA (1998), Metallurgical Thermochemistry Group, National Physics Laboratory, Teddington, London

NAOI, H., OHGAMI, M., HASEGAWA, Y. & FUJITA, T. (1994), Mechanical properties of 12Cr-W-Co ferritic steels with high creep rupture strength, Materials for advanced power engineering, Part 1, Eds. D. Coutsouradis *et al.*, p. 425–434

NAOI, H., MIMURA, H., OHGAMI, M., MORIMOTO, H., TANAKA, T., YAZAKI, Y. & FUJITA, T. (1995), New steels for advanced plant up to 620 °C, Palo Alto, CA, EPRI, Ed. E. Metcalfe

NICKEL, H., ENNIS, P. J. & WACHTER, O. (1995), The Effect of Heat Treatment on the Microstructure and Properties of 9Cr0.5Mo1.8W Steel, p. 237–243, Am. Soc. Met./JSME, Pressure Vessels and Piping Conference

NOBLE, F. W., SENIOR, B. A. & EYRE, B. L. (1990), The effect of phosphorus on the ductility of 9Cr-1Mo steels, Acta Metall., Vol. 38, No. 5, p. 709–717

NORTON, J. F. & STRANG, A. (1969), Improvement of creep and rupture properties of large 1% Cr-Mo-V steam turbine rotor forgings, Journal of The Iron and Steel Institute, p. 193–203

NUTTING, J. (1999), The Structural Stability of Low Alloy Steels for Power Generation Applications, p 12–30, Advanced Heat Resistant Steel for Power Generation, San Sebastian, Spain, Eds. Viswanathan, R. & Nutting, J.

OHGAMI, M., MIMURA, H., NAOI, H. & FUJITA, T. (1992), Creep rupture properties and microstructures of a new ferritic W containing steel, Proceedings of the Fifth International Conference on Creep of Materials, Lake Buena Vista, Florida, U.S.A., p. 69–73

OHGAMI, M., HASEGAWA, Y., NAOI, H. & FUJITA, T. (1997), Development of 11CrMoWCo Heat Resistant Steel for Fossil Thermal Plants, p. 115–124, IMechE International Conference on Steam Power Plant

ORR, J., BURTON, D. & RASCHE, C. (1993), Sensitivity of microstructure and mechanical properties of Steel 91 to initial heat treatments Ironmaking and Steelmaking, Vol. 20, No. 6, p.415–423

ORR, J. & WOOLLARD, L. (1995), The development of 9%Cr-1%Mo steels from steel 91 to E911, Microstructural development and stability in high chromium ferritic power plant steels, Robinson College, Cambridge University

PARK, I & FUJITA, T. (1982), Long-term creep rupture properties and microstructure of 12 % Cr heat resisting steels Transactions of the Iron and Steel Institute of Japan, **22.2**, p. 830–837

PETTY, E. R. (1968), Physical Metallurgy of Engineering Materials, Publ. George Allen and Unwin, p. 116

PICKERING, F. B. (1997), Microstructural Development and Stability in High Content Chromium Ferritic Power Plant Steels, p. 1–29, The Institute of Materials, London

PICKERING, F. B. & VASSILOU, A. D. (1980), Effect of austenitizing temperature on constitution, transformation and tempering of 9Cr-1Mo steel, Metals Technology, p. 409–413

PILLING, J., RIDLEY, N. & GOOCH, D. J. (1982), The effect of phosphorus on creep in 2.25%Cr-1%Mo steels, Acta Metall., Vol. 30, p. 1587–1595

PILLING, J., RIDLEY, N. & GOOCH, D. J. (1983), The effect of titanium on creep rupture strength in 2.25%Cr-1%Mo steels, Metallurgical Transactions A, Vol. 14A, p. 1443–1449

RAJENDRAN PILLAI, S., SIVAI BARASI, N. & KHATAK, H. S. (2000), Behaviour of Oxide Scale on 9Cr-1Mo Steel Under Varying External Stresses, Oxid. Met., Vol. 53, p. 193–220

RAYNOR, D., WHITEMAN, J.A. & HONEYCOMBE, R. W. K. (1966), Precipitation of Mo and V carbides in iron alloys, Journal of the Iron and Steel Institute, p 349–354

ROBERTSON, J., KHAN, M. A. M. & MANNING, M. I. (1989), CEGB Report, RD/L/3433, R88

ROBSON, J. D. (1996a), Ph.D Thesis, Cambridge University, Department of Materials Science and Metallurgy

ROBSON, J. D. & BHADESHIA, H. K. D. H. (1996b), Kinetics of precipitation in power plant steels, Calphad, Vol. 20, No. 4, p. 447–460

ROBSON, J. D. & BHADESHIA, H. K. D. H. (1997a), Modelling precipitation sequences in power plant steels, Part 1 - Kinetic theory, Materials Science and Technology, **13**, p. 631–639

ROBSON, J. D. & BHADESHIA, H. K. D. H. (1997b), Modelling precipitation sequences in power plant steels, Part 2 - Application of kinetic theory, Materials Science and Technology, **13**, p. 640–644

ROHRIG, I. A., VAN DUZER, R. M. & FELLOWS, C. H. (1944), High Temperature Steam Corrosion Studies at Detroit,p. 277–290, Transactions of the American Society of Mechanical Engineering, 66

SANDERSON, S. J. (1983), Mechanical Properties and Metallurgy of 9Cr1Mo Steel, Ferritic Steels for High Temperature Applications, Am. Soc. Met.

SANDERSON, S. J. (1977), Secondary hardening and tempering processes for a 9Cr-1Mo steel austenitized in the $\gamma + \delta$ phase field Metal Science, Short Communication from The Metals Society

SCHWIND, M., HÄTTESTRAND, M. & ANDREN, H. (1996), High Resolution Microanalysis of Ferritic Steel HCM12A, Sweden

SENIOR, B. A. (1989), The precipitation of Laves Phase in 9Cr1Mo steels Mat. Sci. Eng. 119A, p. L5–L9

SHAW, S. W. K. & QUARRELL, A. G. (1957), The formation of carbides in low-carbon chromium-vanadium steels at 700 °C, Journal of the Iron and Steel Institute, **185**, p. 10–22

SHEARD, A. G. & RAINE, M. J. (1998), Proc. Conf. 'International joint power generation', New York, ASME, p. 701–712

SIKKA, V. K., COWGILL, M. G. & ROBERTS, B. W. (1984), Creep properties of modified 9Cr-1Mo steel, Met. Soc. AIME, Proceedings of topical conference on ferritic alloys for use in nuclear technologies, p. 413–423

SINGH, S. B. & BHADESHIA, H. K. D. H. (1998), Estimation of Bainite Plate Thickness in Low-Alloy Steels, Materials Science and Engineering A, Vol. A245, p. 72–79

SINGH RAMAN, R. K., GNANAMOORTHY, J. B. & ROY, S. K. (1993), Oxidation Behaviour of 2.25Cr-1Mo Steel with Prior Tempering at Different Temperatures, Oxid. Met., Vol. 40, p. 21–36

SOBOTKA, J., THIEMEL, K., BÍNA, V., HAKL, J. & VLASÁK, T. (1999), Influence of vanadium on creep rupture strength reduction factor of boiler tubes made of low-alloy creep-resistant steels, Graz-Seggau Seminar on Welding,

SOLBERG, H. L., HAWKINS, G. A. & POTTER, A. A. (1942), Corrosion of Unstressed Steel Specimens by High Temperature Steam, Transactions of the American Society of Mechanical Engineers, 64, p. 303–316

SPIRADEK, K., BAUER, R. & ZEILER, G. (1994), Materials for advanced power engineering, Liege, Belgium, p. 251–262

STRANG, A. & VODAREK, V. (1996), Z Phase Formation in Martensitic 12 CrMoVNb Steel, Mat. Sci. and Tech., Vol. 12, p 552–556

TAKEDA, Y. & MASUYAMA, F. (1991), 1st International Conference on Heat Resisting Materials, U.S.A.

TAMURA, K., SATO, T., FUKUDA, Y., MITSUHATA, K. & YAMANOUCHI, H. (1995), High-Temperature Strengths and Steam Oxidation Properties of New 9-12 wt.% Cr Ferritic Steel Pipes for USC Boilers, Proc. 2nd Intl. Conf. on Heat-Resisting

Materials, Gatlingburg, Tenessee, ASM International, Materials Park, Ohio, 33

TAYLOR, M. & THORNTON, D. V. (1997), Experience in the manufacture of steam turbines in advanced 9-12 wt% Cr steels, IMechE Conference on Advanced Steam Plant, London,

TILLMAN, C. J. & EDMONDS, D. V. (1974), Alloy carbide precipitation and aging during high-temperature isothermal decomposition of an Fe-4Mo-0.2C alloy steel Metals Technology, p. 456–461

THOMSON, R. C. & BHADESHIA, H. K. D. H. (1994a), Changes in chemical composition in 2.25Cr-1Mo power plant steel, Part 1 - Bainitic microstructure Materials science and Technology, **10**, p. 193–203

THOMSON, R. C. & BHADESHIA, H. K. D. H. (1994b), Changes in chemical composition in 2.25Cr-1Mo power plant steel, Part 2 - Mixed microstructure Materials science and Technology, **10**, p. 205–208

THOMSON, R. C. & BHADESHIA, H. K. D. H. (1992a), Carbide precipitation in 12Cr1MoV power plant steel Metallurgical Transactions A, Volume 23A, p. 1171–1179

THOMSON, R. C. (1992b), Ph.D. Thesis, University of Cambridge, p. 65–68

TSUCHIDA, Y., YAMABA, R., TOKUNO, K., HASHIMOTO, K., OGAWA, T. & TAKEDA, T. (1990), Internal Report, Nippon Steel Corporation

TSUCHIYAMA, T., FUTAMURA, Y. & TAKAKI, S. (2000), Strengthening of Heat Resistant Martensistic Steel by Cu Addition, Creep and Fracture of Engineering Materials and Structures, Key Engineering Materials Vols.171-174, Eds. T.Sakuma and K.Yagi, p. 411-418

VANSTONE, R. W. (1994), Microstructure and Creep Mechanisms in Advanced 9-12 wt% Creep Resisting Steels, Materials for Advanced Power Engineering, Liege, Belgium

VANSTONE, R. W. & THORNTON, D. V. (1997), New Materials for Advanced Steam turbines,p. 87–98, IMechE International Conference on Steam Power Plant, London

VANSTONE, R. W. (1999), Private Communication

VANSTONE, R. W. (2000), Private Communication

VISWANATHAN, R. (1989), Damage Mechanisms and Life Assessment of High Temperature Components, Metals Park, ASM International

VODÁREK, V. & STRANG, A. (1997), Int. Conf. Microstructural Stability of Creep Resistant Alloys for High Temperature Plant Applications, Sheffield, U. K.

VODÁREK, V. & STRANG, A. (1998), Effect of Nickel on the Precipitation Processes in 12CrMoV Steels During Creep at 550 °C, p. 101–106, Scripta Materialia, Vol. 38, No. 1

WACHTER, O. & ENNIS, P. J. (1995), Ph.D. Thesis, p. 6–16, Teshniche Hohschule, Aachen, Germany

WILLIAMS, C. R., QUADAKKERS, W. J. & MEADOWCROFT, D. B. (1996), Assessment of steam oxidation and fireside corrosion of 9-12 wt.%Ct steels, Components for advanced steam cycles, COST 501/3 - WP11, Draft Paper

WOODHEAD, J. H. & QUARREL, A. G. (1965), Role of carbides in low-alloy creep resisting steels, Journal of the Iron and Steel Institute, **203**, p. 605–620

YAKEL, H. L. (1985), Crystal structures of stable and metastable iron-containing carbides, International Metals Reviews, **30(1)**, p. 17–40

YANG, J. R., HUANG, C. Y., YANG, C. N. & HORNG, J. L. (1993), Microstructural examination of 2.25Cr-1Mo steel steam pipes after extended service Materials Characterization, Vol. 30, No. 2. p. 75–88

YONG WEY, M., SAKUMA, T. & NISHIZAWA, T. (1981), Transactions of the Japan Institute of Metals, Vol. 22, No. 10, p. 733-742

Appendix 1 - References for Database

1. National Research Institute for Metals: NRIM Creep data sheets 36A (1991), 3B (1986), 13B (1994), 10A (1979), 19A (1981), 46 (1998), 10B (1998), 43 (1996), 19B (1997), 44 (1997), 12B (1992), 21B (1994), 31B (1994), 35A (1990), 11B (1997), 20B (1994), 2A (1976), 1B (1996), 9B (1990). (1976-1998)
2. F. Masuyama and M. Ohgami: Proc. JIMIS–7, Nagoya, Japan 325-332.(1993)
3. F. Abe and S. Nakazawa: Metallurgical Transactions A **23A** 3025–3034.(1992)
4. V. SkleničKa, K. Kuchařova, A Dloughý and J Krejčí: Materials for advanced power engineering, Part I, Kluwer Academic Publishers, Netherlands 435–444.(1994)
5. F. Masuyama and T. Yokoyama: Materials for advanced power engineering, Part I, Kluwer Academic Publishers, Netherlands 301–308.(1994)
6. L. Kunz, P. Lukaš and V. Sklenička: Materials for advanced power engineering, Part I, Kluwer Academic Publishers, Netherlands 445–452.(1994)
7. T. Fujita: Future ferrite steels for high-temperature service New Steels for Advanced Plant up to 620 C, ed. E. Metcalfe, EPRI, California 190–200.(1995)
8. B. S. Greenwell and J. W. Taylor: Institute of Mechanical Engineering Conference C386/041 283–296.(1990)
9. J. Hald: Future ferrite steels for high-temperature service New Steels for Advanced Plant up to 620 C, ed. E. Metcalfe, EPRI, California 152–173.(1995)
10. G. A. Honeyman: Future ferrite steels for high-temperature service New Steels for Advanced Plant up to 620 C, ed. E. Metcalfe, EPRI, California 70–83.(1995)
11. F. Brühl, K. Haarmann, G. Kalwa, H. Weber and M. Zschau: VGB Kraftwerkstechnik **69** 1064–1080.(1989)
12. P. J. Grobner and W. C. Hagel: Metallurgical Transactions A **11A** 633–642.(1980)
13. H Naoi, H. Mimura, M. Ohgami, H. Morimoto, T. Tanaka, Y. Yazaki and T. Fujita: Future ferrite steels for high-temperature service New Steels for Advanced Plant up to 620 C, ed. E. Metcalfe, EPRI, California 8–29.(1995)
14. M. Morinaga, R. Hashizume and Y. Murata: Materials for advanced power engineering, Part I, Kluwer Academic Publishers, Netherlands

319–328.(1994)

15. V. K. Sikka, M. G. Cowgill and B. W. Roberts: Proc. of Topical Conference on ferritic alloys for use in nuclear technologies, TMS-AIME, Warrendale, Pennsylvania 413–423.(1984)

16. M. L. Shaw, T. B. Cox and W. C. Leslie: J. Materials for Energy Systems **8** 347–355.(1987)

17. Y. Tsuchida, R. Yamaba, K. Tokuno, K. Hashimoto, T. Ogawa and T. Takeda: Internal Report, Nippon Steel Corporation, Japan (1990)

18. C. Coussement, M. de Witte, A. Dhooge, R. Dobbelaere and E. Van der Donckt: Reveue de La Soudure **1** 58–63.(1990)

19. H. Masumoto, H. Naoi, T. Takahashi, S. Araki, T. Ogawa and T. Fujita: EPRI 2nd Conference, Palo Alto, California 40.3–40.10.(1988)

20. V. K. Sikka and R. H. Baldwin: Internal Report Data package for modified 9Cr1Mo alloy, update, Oak Ridge National Laboratories, Tennessee, U.S.A. (1987)

21. A. Iseda, M. Kubota, Y. Hayase, S. Yamamoto and K. Yoshikawa: The Sumitomo Search **36** 17–29.(1988)

22. J. Orr and D. Burton: Materials for advanced power engineering, Part I, Kluwer Academic Publishers, Netherlands 263–280.(1994)

23. Anonymous: Internal report, Nippon Kokan K.K., Japan (1987)

24. T. Fujita, K. Asakura, T. Sawada, T. Takamatsu and Y. Otoguro: Metallurgical Transactions A **12A** 1071–1079. (1981)

25. T. Fujita and N. Takahashi: Trans. ISIJ **18** 269–278.(1979)

26. A. Hizume, Y. Takeda, H. Yokota, Y. Takano, A. Suzuki, S. Kinoshita, M. Kohno and T. Tsuchiyama: Advanced Materials Technology '87, eds R . Carson, F. J. Riel, M. Burg and K. J. Kjoller, SAMPE Publishers, California 143–151.(1987)

27. K. Kuwabara, A. Nitta, T. Ogata and S. Sugai: Advanced Materials Technology '87, eds R . Carson, F. J. Riel, M. Burg and K. J. Kjoller, SAMPE Publishers, California 153–162.(1987)

28. K. Haarmann and G. P. Kalwa: Advanced Materials Technology '87, eds R . Carson, F. J. Riel, M. Burg and K. J. Kjoller, SAMPE Publishers, California 267–273.(1987)

29. R. Vanstone: Private Communication (1999)

30. Anonymous: Development of high strength 2.25Cr steel tube (HCM25) for boiler applications, Sumitomo Metal Industries (1993)

31. Murata, Morinaga and Hashizume: Development of ferritic steels for steam turbine rotors with the aid of a molecular orbital method Charles Parson Conference (1997)

32. Anonymous: Procedures to determine maximum allowable stress values for NF616 ferritic steel Nippon Steel (1993)

33. Anonymous: Procedures to determine stress values for HCM12A ferritic steel tubes and pipe Sumitomo Metal Industries and Mitsubishi Heavy Industries (1992)

34. M. Ohgami, H. Mimura, H. Naoi and T. Fujita: Creep rupture properties of a new ferritic Tungsten containing steel Proc. of the Fifth International Conference on Creep of Materials, Florida 69–73(1992)

35. F. Abe and S. Nakazawa: Microstructural evolution and creep behaviour of bainitic, martensitic and martensite-ferrite dual phase Cr-2W steels Materials Science and Technology **8** 1063–1069(1992)

36. L. W. Buchanan, A. N. R. Hunter and A. V. Holt: Materials for ultra-supercritical boilers (1992)

37. H. Naoi, M. Ohgami, S. Araki, T. Ogawa, T. Fujita, H. Mimura, M. Sakakibara, Y. Sogoh and H. Sakurai: Nippon Steel Technical Report **57** 22–27(1993)

38. D. Cole: Unpublished work (1998–9)

39. N. Komai, F. Masuyama, I. Ishihara, T. Yokoyama, Y. Yamadera, H. Okada, K. Miyata and Y. Sawaragi: Development and application of 2.25Cr-1.6W (HCM2S) steel, large diameter and thick section pipe San Sebastian (1998)

40. T. Fujita: Development of high Chromium ferritic steels for ultra supercritical power plant ISIJ (1990)

Appendix 2 - Neural network analysis of the effects of elemental changes on the creep rupture strength of NF616

This appendix contains the results of a comprehensive analysis of the effects of various elements on the creep rupture strength of NF616. The analysis was performed using the neural network model described in this thesis. Fig. 1 shows the predictions made regarding six different elements.

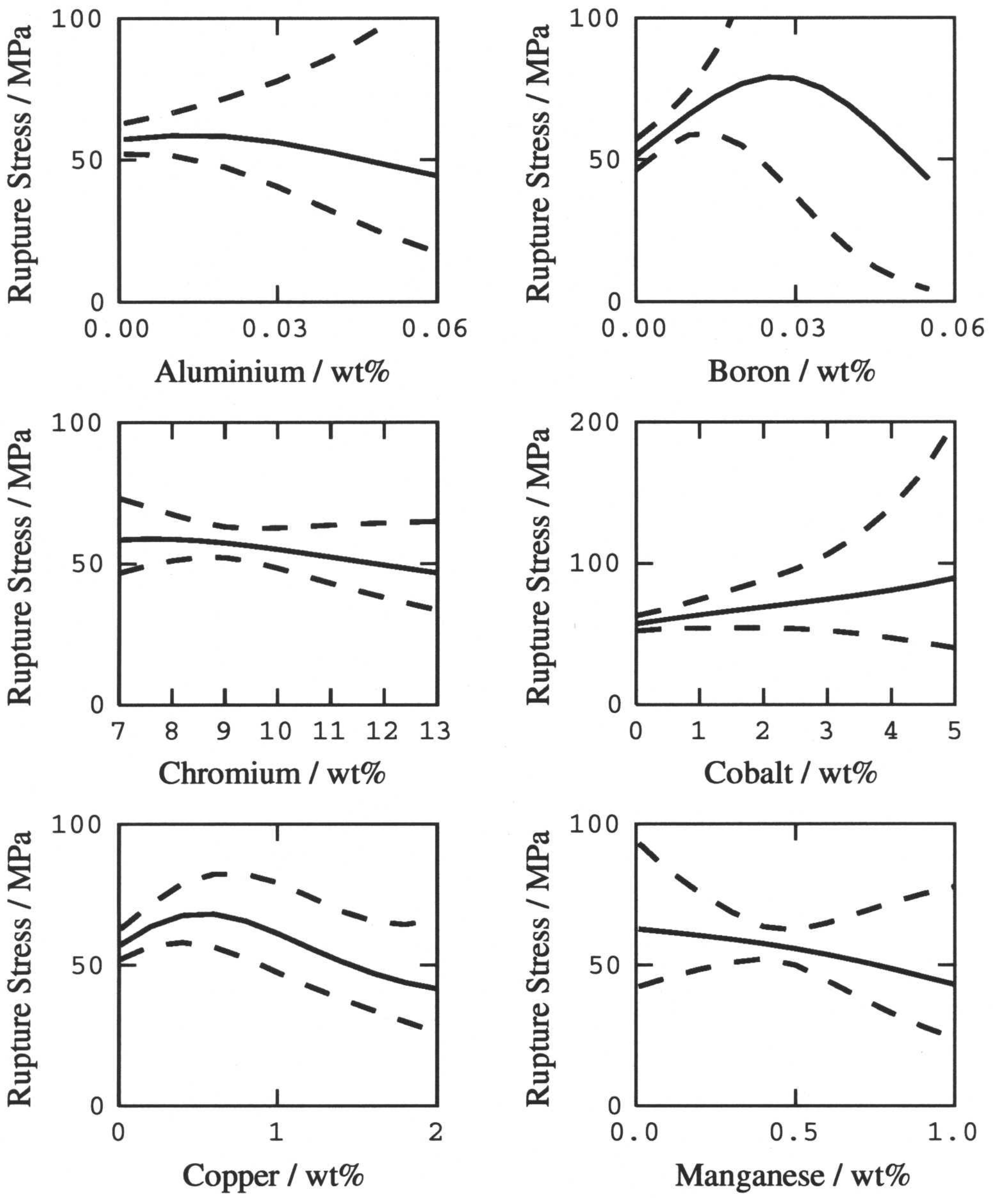

Fig. 1 Neural network predictions of the creep rupture strength of NF616 with varying elements at 650 °C after 100 000 hours.

Al is shown to be detrimental to creep rupture strength. B is beneficial but more data is required with levels greater than 0.01 wt% to improve this analysis. Cr levels greater than 9 wt% show a slight drop in creep rupture strength, probably caused physically by δ-ferrite formation. Co and Mn show expected effects on the creep strength. Cu shows a drop in creep rupture strength at concentrations greater than 0.5 wt%. Fig. 2 shows the analysis of six more elements.

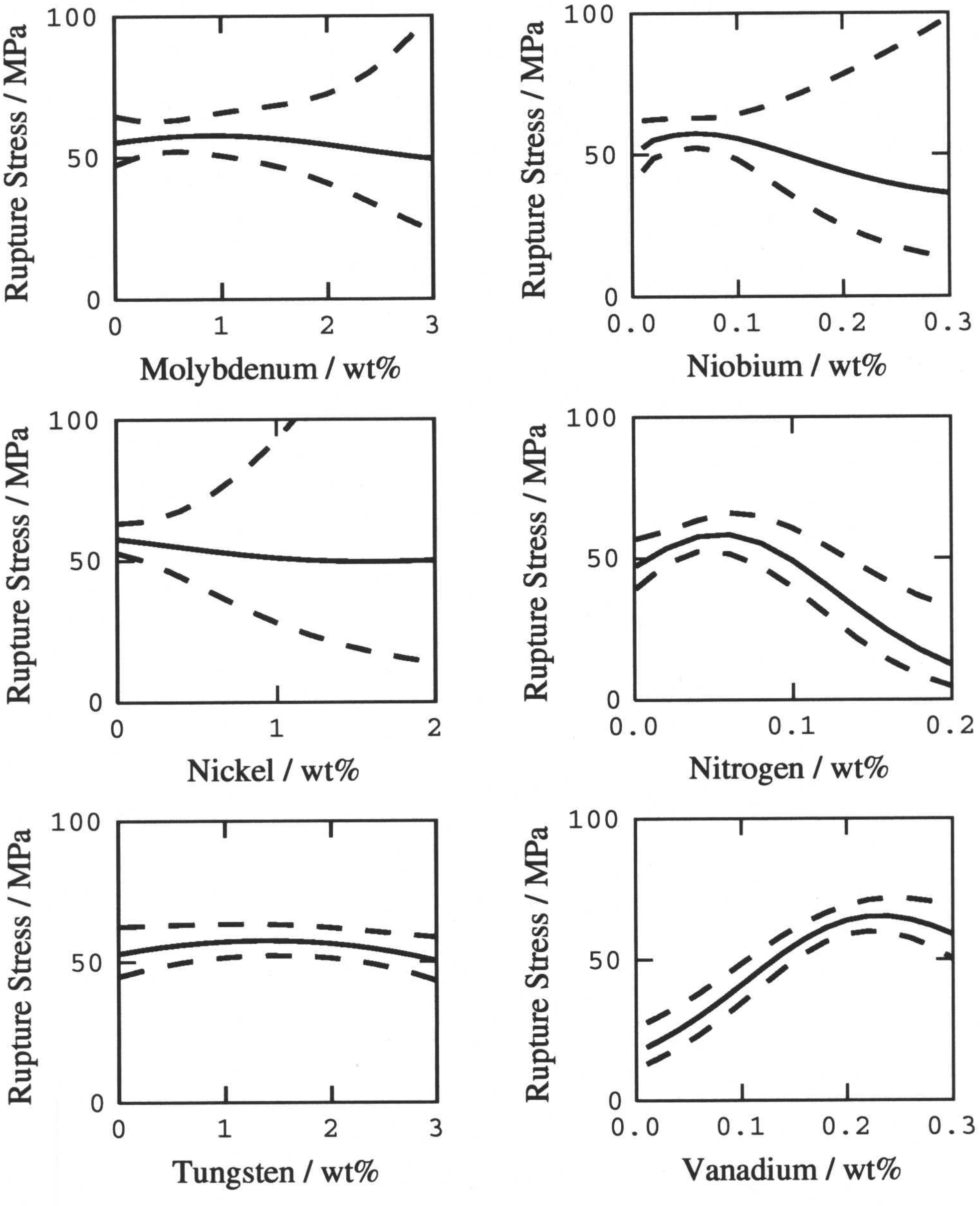

Fig. 2 Neural network predictions of the creep rupture strength of NF616 with varying elements at 650 °C after 100 000 hours.

Mo, Nb and Ni all show decreases in creep rupture strength above certain concentrations but also show that more data would be useful for these predictions. N additions show a distinct maximum at approximately 0.6 wt% in this case. W is seen to have little effect on the creep rupture strength whereas the addition of vanadium has a profound and beneficial effect on creep strength.